

# Non-Proportional Fatigue by Example of Fiber-Reinforced Rotor Blade Adhesive



Supervisors

Prof. Dr.-Ing. Andreas Reuter  
Prof. Dr.-Ing. Martin A. Eder

Michael Kuhn

02 (2023)



# **Non-Proportional Fatigue by Example of Fiber-Reinforced Rotor Blade Adhesive**

Michael Kuhn

## Contact

Leibniz University Hannover  
Institute for Wind Energy Systems  
Appelstraße 9A  
30167 Hannover  
Germany

E-Mail: [research@iwes.uni-hannover.de](mailto:research@iwes.uni-hannover.de)  
URL: [www.iwes.uni-hannover.de](http://www.iwes.uni-hannover.de)

## Cover image

Sander Weeteling, Unsplash, "Early morning windmill sunrise in the mist", 2021

## Bibliographic information of the German National Library

The German National Library has listed this publication in its Deutsche Nationalbibliographie; detailed bibliographic data is available on the internet at: [www.dnb.de](http://www.dnb.de)

## Publication series

Dissertations of the Institute for Wind Energy Systems  
ISSN 2940-2689 (Print)  
ISSN 2940-2697 (Online)

Online access via:



Non-Proportional Fatigue by Example of Fiber-Reinforced Rotor Blade Adhesive © 2023  
by Michael Kuhn is licensed under CC BY 4.0.

To view a copy of this license, visit [www.creativecommons.org/licenses/by/4.0](http://www.creativecommons.org/licenses/by/4.0)

Thesis design and implementation by Michael Kuhn and Pablo Noever Castelos.

Supported by:



on the basis of a decision  
by the German Bundestag

This work was partially funded by the Federal Ministry for Economic Affairs and Climate Action (BMWK) in the frame of the project *ReliaBlade* (funding reference no.: 0324335B).

# Non-Proportional Fatigue by Example of Fiber-Reinforced Rotor Blade Adhesive

Genehmigte Dissertation

Von der Fakultät für Bauingenieurwesen und Geodäsie der Gottfried Wilhelm Leibniz Universität  
Hannover zur Erlangung des Grades Doktor-Ingenieur - Dr.-Ing. - genehmigte Dissertation

Von

Master of Science

**Michael Kuhn**

Geburtsname: Wentingmann

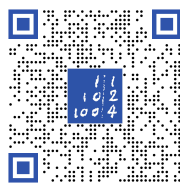
Geb. am 15. November 1990

in Münster, Deutschland

Erscheinungsjahr

2023

PDF Version



Präsentation



## Hauptreferent

Prof. Dr.-Ing.

**Andreas Reuter**

Leibniz Universität Hannover  
Institut für Windenergiesysteme

## Korreferent

Prof. Dr.-Ing.

**Martin A. Eder**

Technical University of Denmark  
Department of Wind and Energy Systems

## Kommissionsmitglied

Prof. Dr.-Ing. habil.

**Raimund Rolfes**

Leibniz Universität Hannover  
Institut für Statik und Dynamik

## Vorsitz

Prof. Dr.-Ing.

**Martin Achmus**

Leibniz Universität Hannover  
Institut für Geotechnik

Tag der mündlichen Prüfung:  
02. Juni 2023

# Vorwort

Die vorliegende Arbeit ist während meiner Tätigkeit als wissenschaftlicher Mitarbeiter am Institut für Windenergiesysteme (IWES) der Leibniz Universität Hannover entstanden und wurde mir durch zahlreiche Personen ermöglicht, bei denen ich mich an dieser Stelle herzlich bedanken möchte.

Meinem Doktorvater Prof. Dr.-Ing. Andreas Reuter danke ich für das in mich und meine Arbeit gesetzte Vertrauen. Durch ihn als Bindeglied zwischen dem universitären und dem Fraunhofer IWES wurde mir die Verbindung von Theorie und Praxis deutlich vereinfacht. Insbesondere durch seine Unterstützung konnten die Experimente am Fraunhofer IWES während der Corona-Pandemie weitergeführt werden.

Bei Prof. Dr.-Ing. Martin A. Eder bedanke ich mich für zahlreiche konstruktive Diskussionen und detailliertes Feedback, das zu einer deutlichen Verbesserung der Arbeit beigetragen hat. Mein Dank gilt ebenfalls Prof. Dr.-Ing. habil. Raimund Rolfes und Prof. Dr.-Ing. Martin Achmus für die Begutachtung meiner Arbeit.

Ganz besonders möchte ich auch Dr.-Ing. Claudio Balzani danken, der mich als Co-Autor meiner Veröffentlichungen und Gruppenleiter am IWES in allen maßgeblichen Schritten unterstützt und diese durch Drittmittelakquirierung überhaupt erst ermöglicht hat. Ebenso bedanke ich mich bei Nikolas Manousides und Prof. Dr.-Ing. Alexandros Antoniou für ihre Mitarbeit an meinen Veröffentlichungen.

Ohne die Unterstützung der Technikerinnen und Techniker wie Martina Karalus, Henning Schnellen und vielen weiteren Kolleginnen und Kollegen am Fraunhofer IWES wäre diese Arbeit zudem nicht möglich gewesen.

Darüber hinaus bin ich allen Kolleginnen und Kollegen vom universitären und Fraunhofer IWES dankbar für jegliche Diskussionen und Anregungen. Die Zusammenarbeit mit euch war mir eine große Freude. Hervorheben möchte ich hier auch die Rolle von Dr.-Ing. Pablo Noever Castelos, der mich während des Masterstudiums für das Thema der multiaxialen Materialermüdung begeistert und fortwährend unterstützt hat.

Meiner Familie und insbesondere meiner Frau Antonia danke ich von Herzen für ihr stetiges Interesse.





## Keywords

Non-Proportional Fatigue, Multi-axial Testing, Fiber-Reinforced Polymers, Wind Turbine, Rotor Blade, Reliability

## Video

Subsequent recording of the defense presentation



# Abstract

Structural optimization relies on precisely known material data and accurate yet computationally efficient damage prediction models. In this regard, non-proportional fatigue represents a major source of uncertainty due to a more complex material behavior. While non-proportional loads are found in a large variety of industries, the associated modeling uncertainties lead to increased levelized cost of energy in terms of wind turbines, an unacceptable condition given the urgency of a sustainable global economy.

In the wind energy industry tests on the coupon, sub-component and full-scale level are predominantly based on uniaxial loads. In addition, the specimen quality in these tests does not always match the mass-production quality. This is particularly true for the design-driving adhesive joints of rotor blades, where hand-mixed specimens are the state of the art even though dosing machines are applied in rotor blade manufacture. The numerical uncertainty regarding non-proportional fatigue is thus amplified based on a deficit of experiments with representative specimens.

This thesis presents a new concept to both accurately *and* efficiently predict the non-proportional fatigue life by example of a fiber-reinforced rotor blade adhesive. In order to achieve this, the influence of non-proportional loads on the cycles to failure of the adhesive needed to be identified with high certainty. Therefore, manufacturing-induced defects such as pores or stress concentrations on account of the specimen geometry were minimized, resulting in the first virtually defect-free rotor blade adhesive specimens that are suitable for multiaxial experiments. A detailed multiaxial material characterization in static and fatigue loading conditions revealed several misconceptions in comparison to literature such as a rather ductile material behavior, associated modeling differences of (elasto-plastic) shear stresses, a more representative yield criterion (Drucker-Prager) and S-N model (Stüssi-Haibach).

Based on the unique experimental data, it was demonstrated that global rainflow-counted equivalent stresses lead to a good fatigue life prediction for proportional loads, while an over-prediction of the fatigue life of up to two orders of magnitude in non-proportional loads is possible. Critical plane algorithms were calibrated using the new experimental data set and found to be substantially more accurate, but impractical due to an extensive computation time and complicated validation. However, a FFT-based re-proportionalization of the stress state in combination with a S-N-based correction factor allows to use global equivalent stresses again in phase shift-induced non-proportional conditions. This way, accurate fatigue life predictions are possible that are *several* orders of magnitude faster than the critical plane approach. Although demonstrated with a rotor blade adhesive, the new approach can be used with any equivalent stress criterion and thus for any material when a phase shift is the main source of non-proportionality.



## Schlagwörter

Nicht-Proportionale Ermüdung, Multiaxiale Tests, Faserverstärkte Polymere, Windenergieanlage, Rotorblatt, Zuverlässigkeit

# Kurzfassung

Strukturoptimierungen beruhen auf präzisen Materialdaten sowie akkuraten und dennoch recheneffizienten Schadensvorhersagemodellen. Diesbezüglich stellt die nicht-proportionale Ermüdung aufgrund eines komplexeren Materialverhaltens eine große Unsicherheitsquelle dar. Während nicht-proportionale Belastungen in einer Vielzahl von Branchen vorkommen, führen die damit verbundenen Modellierungsunsicherheiten bei Windenergieanlagen zu erhöhten Stromgestehungskosten, was angesichts der Dringlichkeit einer nachhaltigen Weltwirtschaft inakzeptabel ist.

In der Windenergiebranche basieren Versuche im Coupon-, Sub-Komponenten- oder Vollmaßstab überwiegend auf uniaxialen Lasten. Hinzu kommt, dass die Probenqualität dieser Tests nicht immer der Serienproduktion entspricht. Dies gilt insbesondere für auslegungskritische Rotorblattverklebungen, für die handgemischte Proben Stand der Technik sind, obwohl in der Rotorblattfertigung Dosiermaschinen eingesetzt werden. Die numerische Unsicherheit bezüglich der nicht-proportionalen Ermüdung wird daher auch durch einen Mangel an Experimenten mit repräsentativen Proben verstärkt.

Diese Arbeit präsentiert am Beispiel eines faserverstärkten Rotorblattklebstoffes ein neues Konzept die nicht-proportionale Lebensdauer akkurat *und* recheneffizient vorherzusagen. Um dies zu erreichen, musste der Einfluss nicht-proportionaler Lasten auf die Versagens-Zyklen des Klebstoffes mit hoher Genauigkeit ermittelt werden. Daher wurden fertigungsbedingte Mängel wie Poren oder Spannungskonzentrationen infolge der Probengeometrie minimiert, was zu den ersten nahezu defektfreien Rotorblattklebstoffproben für multiaxiale Experimente führte. Eine detaillierte multiaxiale Materialcharakterisierung unter statischen und dynamischen Lasten deckte mehrere Fehleinschätzungen seitens der Literatur auf, wie z.B. ein eher duktileres Materialverhalten, damit verbundene Modellierungsunterschiede von (elastoplastischen) Schubspannungen, sowie ein repräsentativeres Fließkriterium (Drucker-Prager) und S-N Modell (Stüssi-Haibach).

Auf der Grundlage der einzigartigen experimentellen Daten konnte gezeigt werden, dass globale rainflow-gezählte Vergleichsspannungen zu einer guten Lebensdauervorhersage für proportionale Belastungen führen, diese bei nicht-proportionalen Belastungen die Lebensdauer aber um bis zu zwei Größenordnungen überschätzen. Critical plane Algorithmen wurden mit dem neuen experimentellen Datensatz kalibriert und führten zu substantiell genaueren Ergebnissen, sind aber aufgrund hoher Rechenzeiten und einer komplizierten Validierung nicht praktikabel. Eine FFT-basierte Re-Proportionalisierung des Spannungszustands kombiniert mit einem S-N-basierten Korrekturfaktor ermöglicht es jedoch, unter Phasenverschiebungs-induzierten nicht-proportionalen Bedingungen, globale Vergleichsspannungen zu verwenden. Auf diese Weise sind genaue Lebensdauervorhersagen möglich, die um *mehrere* Größenordnungen schneller sind als der critical plane Ansatz. Obwohl der neue Ansatz an einem Rotorblattklebstoff demonstriert wurde, kann er mit jedem Vergleichsspannungskriterium und somit jedem Material verwendet werden, solange Phasenverschiebungen der Hauptgrund der Nicht-Proportionalitäten sind.

## Video

Nachträgliche Aufnahme der Verteidigungs-Präsentation





# Contents

<b>1</b>	<b>Introduction</b>	<b>1</b>
1.1	Motivation . . . . .	2
1.2	State of the art. . . . .	2
1.2.1	Non-proportional fatigue. . . . .	2
1.2.2	Rotor blade manufacturing. . . . .	14
1.2.3	Verification of fatigue life prediction methods . . . . .	18
1.3	Research gap and objectives. . . . .	19
1.3.1	Research gap . . . . .	19
1.3.2	Objectives . . . . .	20
1.4	Thesis concept . . . . .	21
1.4.1	Outline . . . . .	21
1.4.2	Declaration on the included publications . . . . .	22
<b>2</b>	<b>1<sup>st</sup> Paper: Design and manufacturing optimization of epoxy-based adhesive specimens for multiaxial tests</b>	<b>27</b>
P1-1	Introduction . . . . .	29
P1-1.1	Bond lines in wind turbine rotor blades . . . . .	29
P1-1.2	State of the art specimen manufacture . . . . .	29
P1-1.3	Aims and outline. . . . .	29
P1-2	Specimen design optimization . . . . .	29
P1-2.1	Optimization objectives . . . . .	29
P1-2.2	Boundary conditions . . . . .	30
P1-2.3	Adhesive system . . . . .	30
P1-2.4	Finite element modelling . . . . .	30
P1-2.5	Sensitivity study . . . . .	30
P1-2.6	Results . . . . .	31
P1-3	Manufacturing optimization. . . . .	32
P1-3.1	Optimal mixing quality . . . . .	32
P1-3.2	Mold design and injection process . . . . .	33
P1-4	Quality assurance. . . . .	35
P1-4.1	Manufacturing performance . . . . .	35
P1-4.2	High-resolution X-ray evaluation . . . . .	36
P1-5	Uniaxial and biaxial static tests . . . . .	36
P1-5.1	Instrumentation . . . . .	36
P1-5.2	Uniaxial tests . . . . .	36
P1-5.3	Biaxial tests . . . . .	38
P1-6	Porosity analysis of industrial dosing machines . . . . .	38
P1-7	Conclusion . . . . .	40

<b>3</b>	<b>2<sup>nd</sup> Paper: Yield surface derivation for a structural adhesive based on multiaxial experiments</b>	<b>43</b>
	P2-1 Introduction . . . . .	44
	P2-1.1 Definition of yielding . . . . .	44
	P2-1.2 Experimental yield point detection. . . . .	44
	P2-1.3 Structural adhesives for wind turbine rotor blades. . . . .	45
	P2-1.4 Aims and outline. . . . .	45
	P2-2 Specimens and test setup. . . . .	45
	P2-3 Elasto-plastic shear stress correction . . . . .	47
	P2-3.1 Shear stress formulae . . . . .	47
	P2-3.2 A practical approach for the elasto-plastic transition . . . . .	47
	P2-4 Yield surface derivation . . . . .	48
	P2-4.1 Yielding in tension . . . . .	49
	P2-4.2 Yielding in torsion and compression . . . . .	49
	P2-4.3 Yielding in biaxial stress states . . . . .	49
	P2-4.4 Yield locus . . . . .	51
	P2-5 Result discussion . . . . .	52
	P2-5.1 Bi-modularity . . . . .	52
	P2-5.2 Viscoelasticity. . . . .	53
	P2-5.3 Comparison to existing yield criteria . . . . .	54
	P2-6 Conclusion . . . . .	54
<b>4</b>	<b>3<sup>rd</sup> Paper: Fatigue properties of a structural rotor blade adhesive under axial and torsional loading</b>	<b>57</b>
	P3-1 Introduction . . . . .	58
	P3-1.1 Fatigue in bond lines of wind turbine rotor blades. . . . .	58
	P3-1.2 Experimental investigations of bond line fatigue . . . . .	59
	P3-1.3 Aims and outline. . . . .	59
	P3-2 Specimens and fatigue test setup. . . . .	59
	P3-2.1 Material system and manufacturing . . . . .	61
	P3-2.2 Fatigue test setup . . . . .	61
	P3-3 Uniaxial S-N curves . . . . .	62
	P3-3.1 S-N models . . . . .	62
	P3-3.2 Conversion from displacement to load control . . . . .	62
	P3-3.3 Experimental results . . . . .	63
	P3-3.4 Engineering approach to gigacycle fatigue . . . . .	66
	P3-3.5 Apparent yield strength separation points . . . . .	68
	P3-3.6 Comparison with literature. . . . .	68
	P3-4 Stiffness degradation . . . . .	70
	P3-4.1 Cycle- and load-dependent modeling . . . . .	70
	P3-4.2 Comparison with residual strength tests . . . . .	73
	P3-4.3 Run-out fatigue life estimation . . . . .	74
	P3-5 Conclusion . . . . .	74

5	<b>4<sup>th</sup> Paper: Effects of non-proportionality and tension-compression asymmetry on the fatigue life prediction of equivalent stress criteria</b>	<b>77</b>
	P4-1 Introduction . . . . .	79
	P4-2 Experimental setup . . . . .	79
	P4-2.1 Material system . . . . .	79
	P4-2.2 Specimen design and manufacturing . . . . .	80
	P4-2.3 Biaxial fatigue testing campaign. . . . .	80
	P4-3 Influence of non-proportional loads . . . . .	81
	P4-3.1 Experimental results . . . . .	81
	P4-3.2 Influence of material ductility. . . . .	82
	P4-3.3 Fracture surface analysis. . . . .	83
	P4-4 Tension-compression asymmetry . . . . .	84
	P4-5 Haigh diagram . . . . .	85
	P4-5.1 Stüssi-Haibach S-N approach . . . . .	86
	P4-5.2 Constant fatigue life model. . . . .	86
	P4-5.3 Model generation and discussion . . . . .	87
	P4-6 Multiaxial fatigue life predictions. . . . .	87
	P4-6.1 Equivalent stress formulations . . . . .	89
	P4-6.2 Hybrid equivalent stress . . . . .	89
	P4-6.3 Influences of non-proportional loads . . . . .	90
	P4-6.4 Comparison of modeling approaches . . . . .	91
	P4-6.5 Discussion of modeling influences . . . . .	92
	P4-7 Conclusion . . . . .	92
6	<b>Non-proportional fatigue life prediction without critical plane analysis</b>	
	– <b>The forced proportional interference approach</b>	<b>97</b>
	6.1 Introduction . . . . .	98
	6.2 Multiaxial fatigue analyses . . . . .	98
	6.2.1 Level of non-proportionality . . . . .	98
	6.2.2 Overview: proportional loading . . . . .	99
	6.2.3 Overview: non-proportional loading . . . . .	99
	6.2.4 Signed equivalent stresses . . . . .	101
	6.2.5 Time dependencies . . . . .	102
	6.3 A new approach to non-proportional fatigue analyses. . . . .	103
	6.3.1 Basis: The LiWI approach . . . . .	103
	6.3.2 Forced proportional interference. . . . .	104
	6.3.3 Fatigue life prediction concept . . . . .	104
	6.4 Implementation of methods . . . . .	105
	6.4.1 Global equivalent stress criteria . . . . .	105
	6.4.2 Critical plane equivalent stress criteria . . . . .	106
	6.4.3 Enclosing surface methods . . . . .	107
	6.4.4 Haigh diagram & S-N curves . . . . .	107
	6.4.5 Filtering & damage sphere discretization . . . . .	107
	6.5 Comparison to experiments . . . . .	107
	6.5.1 Damage prediction quality . . . . .	108
	6.5.2 Fracture surface prediction . . . . .	110
	6.5.3 FPI: Computational efficiency & ease of use . . . . .	111
	6.5.4 FPI: Limitations & Possibilities . . . . .	112
	6.6 Concluding Remarks . . . . .	112

<b>7</b>	<b>Conclusion and Outlook</b>	<b>115</b>
7.1	Conclusion . . . . .	116
7.2	Outlook. . . . .	121
	<b>List of Figures</b>	<b>xvii</b>
	<b>Copyrights of included Pictures</b>	<b>xix</b>
	<b>List of Tables</b>	<b>xx</b>
	<b>List of Abbreviations</b>	<b>xxi</b>
	<b>List of Symbols</b>	<b>xxii</b>
	<b>Bibliography</b>	<b>xxvi</b>



# 1

## Introduction

This chapter establishes the research motivation of this thesis. The state of the art of non-proportional fatigue is presented with an emphasis on adhesive joints of wind turbine rotor blades. Based on that, a research gap and corresponding objectives for this thesis are identified. Hereafter, the cumulative thesis concept is outlined and followed by a declaration of contributions to the incorporated publications.

---

1.1	Motivation .....	2
1.2	State of the art .....	2
1.3	Research gap and objectives.....	19
1.4	Thesis concept .....	21

## 1.1 Motivation

With the overall goal of a sustainable global economy [1, 2], it is key to minimize the carbon footprint of all products and services. In terms of engineering structures and machinery, this also corresponds to a thorough understanding of material degradation processes and cost-effective lightweight design, i.e., structural optimization. However, uncertainties associated with complex loading conditions limit the optimization potential given that the operational safety has to be assured at all times.

It is thus of utmost importance to characterize the degradation behavior of materials under such complex (multiaxial) loading conditions and validate associated damage prediction models, as this enables a safe operation of highly optimized structures [3, 4]. The advent of digital twins [5–7] also relies heavily on reliable material data and computationally efficient models, respectively. Applied to the renewable energy sector, structural optimization and the aforementioned approaches act as a multiplier to reduce carbon emissions, since they can result in lower cost of clean energy, which will accelerate the transition to a sustainable global economy.

Therefore, this thesis analyses the effects of a major source of modeling uncertainty concerning structural optimizations: non-proportional fatigue [8–11]. Numerous studies have shown that the experimental and numerically predicted fatigue life of a material can be substantially different under non-proportional loading compared to proportional conditions. In fact, fatigue life prediction models that were validated for proportional loading can lead to (very) non-conservative predictions in non-proportional scenarios [12–16]. To investigate this phenomenon, new experiments are conducted based on a short fiber-reinforced adhesive [17] which is commonly used in the manufacture of wind turbine rotor blades. As the bond lines are critical design drivers for rotor blades [18–20] and still contribute significantly to blade-related turbine downtimes [20–22], the high-precision material characterization necessary to reliably analyze non-proportional fatigue will also be beneficial for future blade designs. On account of the challenging experimental setup, this work is the first to investigate non-proportional fatigue on rotor blade adhesives.

## 1.2 State of the art

The state of the art of non-proportional fatigue is presented in this Section with a concise summary of typical structures, which are prone to this load state. Rotor blades of wind turbines are among these structures, hence their manufacturing process is presented with an emphasis on the adhesive joints. Hereafter, the typical verification process of fatigue life prediction methods is discussed.

### 1.2.1 Non-proportional fatigue

A load state is classified as non-proportional when the principal stress/strain orientation is a (continuous) function of time [8–11]. Therefore, multiple material planes get loaded and the damage evolution is altered in comparison to a proportional load state with a constant principal stress/strain orientation. The latter, however, is assumed in common fatigue life prediction methods, such as uniaxial rainflow-counted equivalent stresses, leading to a diminished fatigue life prediction quality [8–11]. This will also be demonstrated in detail in Section P4-6.3. The influence of non-proportional loads is generally observed to be material-dependent [23], which adds additional complexity.

### Sources and experimental recreation of non-proportional loads

Non-proportional loads can be caused and experimentally recreated in a variety of ways, which are summarized in Figure 1.1. The minimum requirement is a biaxial load state that, e.g., introduces a time-dependent normal stress  $\sigma(t)$  and shear stress  $\tau(t)$ . A proportional load is generated when the ratio between the normal and the shear stress is constant with respect to time. Any change of this constant relation will lead to a non-proportional load history. Therefore, the general definition of a non-proportional load history is simplified to  $\sigma(t)/\tau(t) \neq \text{const}$  for this biaxial setup.

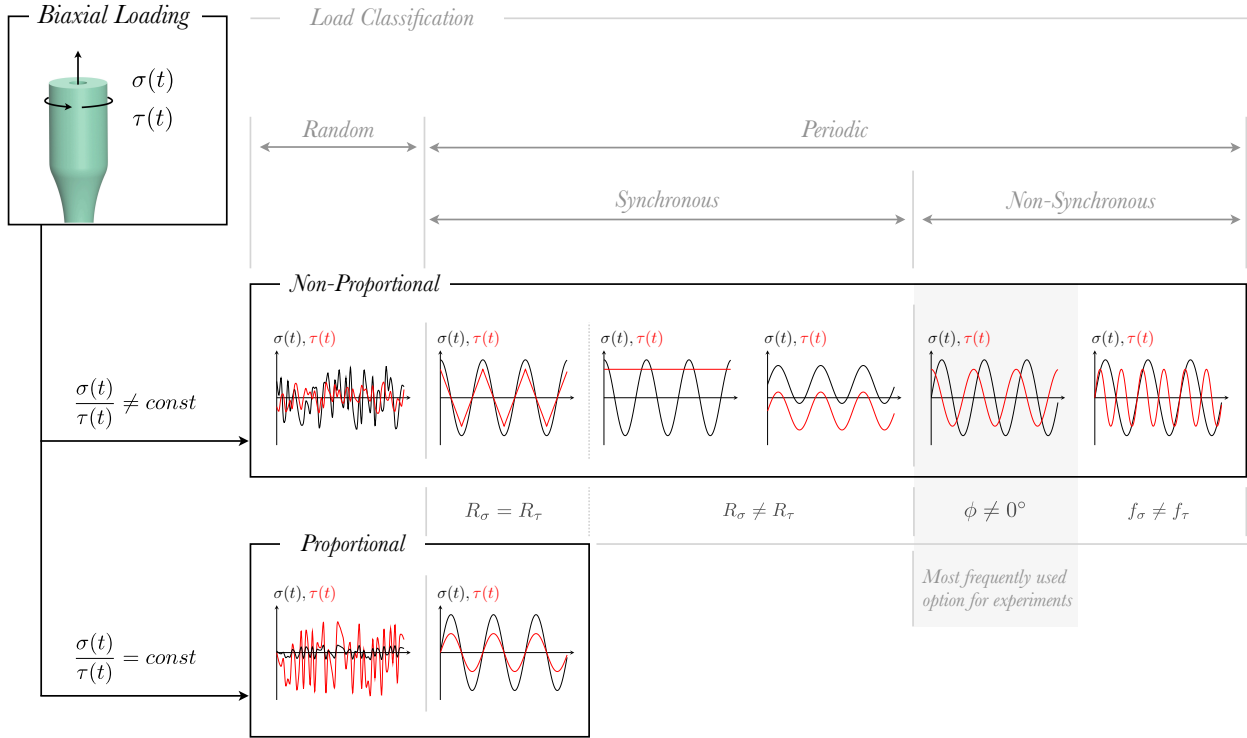


**Figure 1.1:** Sources of non-proportional loads. By example of a biaxial (tension/compression-torsion) load state, a non-proportional load emerges whenever the ratio between the normal and the shear stress history is not constant. With inspiration from [11, 24].

Viable options to trigger a non-proportional load state in experiments are:

- altered signal shapes, e.g., sine wave vs. triangular signal,
- use of different stress ratios for normal stresses ( $R_\sigma = \frac{\sigma_{\min}}{\sigma_{\max}}$ ) and shear stresses ( $R_\tau = \frac{\tau_{\min}}{\tau_{\max}}$ ),
- a phase shift  $\phi$  in between an axial and torsional load,
- different test frequencies of the normal and shear stresses, i.e,  $f_\sigma \neq f_\tau$ .

The implementation of these options should be possible for any programmable multiaxial testing machine and is thus not a decisive factor. However, the evaluation of the respective results and the corresponding verification of fatigue life prediction methods will depend on the available (uniaxial) data that was previously recorded. For instance, the usage of different test frequencies ( $f_\sigma \neq f_\tau$ ) may also introduce additional complexity on account of viscoelastic material behavior. In case this behavior was not previously characterized in detail, the effects of non-proportionality may not be resolvable from the data. In addition, the adjustment of different levels of non-proportionality should be as easy as possible. Hence, the most frequently used option to generate non-proportional loads is a phase shift  $\phi$ , as this option introduces no unintended effects concerning the fatigue life and allows for a straightforward adaption of the required level of non-proportionality. A detailed discussion on the estimation and magnitude of the level of non-proportionality will be given in Section 6.2.1.

It is worth noting that even a multiaxial variable amplitude stress history is proportional when  $\sigma(t)/\tau(t) = const$ , and a superposition of a static load with a varying one is non-proportional. The apparent complexity of the stress history is hence not necessarily an indication for non-proportionality, but rather the independence of the load components. Hence, the presence of a residual or thermal stress in combination with a varying uniaxial load can also lead to a non-proportional load state. The same applies for any rotating system, where a rather constant centrifugal load is superimposed with cyclic (shear) loads or in case a shaft is subjected to a constant torque in combination with cyclic bending loads.

## Overview of structures subject to non-proportional fatigue

Figure 1.2 presents prominent examples of machines and structures that are prone to non-proportional fatigue loads. In all cases the superposition of multiple loads results in a multiaxial and non-proportional load state. Another important aspect that is linked to the fatigue design of machines and structures are maintenance intervals [25–28]. This is because short maintenance intervals, such as those used in aerospace [27, 28], increase the probability to detect fatigue damage initiation and allow for a more precise validation of fatigue life prediction methods under operational loads.



**Figure 1.2:** Examples of multiaxial, non-proportional fatigue across industries, sorted according to the approximate load cycles per maintenance interval.

**Rotor blades** of wind energy turbines face complex fatigue loads due to the rotation of the rotor in a stochastically varying wind field [29–31]. Since non-proportional loads are analyzed by example of a rotor blade adhesive in this thesis, the loads on rotor blades are analyzed in more detail subsequent to this overview.

**Offshore structures & ships** encounter random loads from waves (swell & wind sea), wind, currents and sea pressure [32–38]. Container ships face cargo loads and ballast tank pressure [33]. Ice loads [39] need to be considered alongside residual stresses (in welds) [24, 34–36, 40].

**Cars & trucks** endure multiaxial (non-proportional) loads in powertrain components [41] and the suspension [42], e.g., at the steering knuckle [23, 43–47]. Road-induced loads from surface roughness (vertical) are superimposed with loads from cornering (lateral) and acceleration (longitudinal) [46].

**Aircraft & helicopters** typically face changing load conditions during take-off, cruise and landing [28, 48–53]. Maneuvers likewise change the operational and aerodynamic loads dynamically [50]. Flights at high altitudes introduce temperature and pressure changes [53].

In addition to the aforementioned examples, multiaxial and non-proportional loads are also found in bridges [54–56], railway components [57–59] and other structures [60–64].

### Non-proportional loads on rotor blades of wind turbines

Rotor blades transform the kinetic energy of the wind into a rotation of the rotor system based on arising aerodynamic forces. The magnitude and orientation of these and other resulting forces is governed by the wind speed and is hence linked to the three-dimensional structure of the wind field. Major load sources on wind turbine rotor blades are summarized in the following in addition to a brief description of wind field characteristics and wind turbine control algorithms.

**Wind field characteristics.** The wind field can be described by a height-dependent mean wind speed (wind shear) that is superimposed with a turbulent layer, cf. Figure 1.3 (top). The wind shear is commonly described as a logarithmic or exponential function. However, the turbulent layer can introduce localized changes to this generalization.

**Relative inflow wind speed.** The resulting aerodynamic force at each blade section can be subdivided into a tangential force that leads to the rotation of the rotor and a thrust force parallel to the wind direction, cf. Figure 1.4. On account of the rotation, the inflow direction at each blade section shifts from the wind direction towards the rotational flow velocity. The rotational component of the inflow velocity is proportional to the radial position of the particular blade section and the rotational speed of the complete rotor. Since the aerodynamic forces depend on the square of the inflow wind speed and the inflow angle, the loads also become a function of these quantities and the radial position.

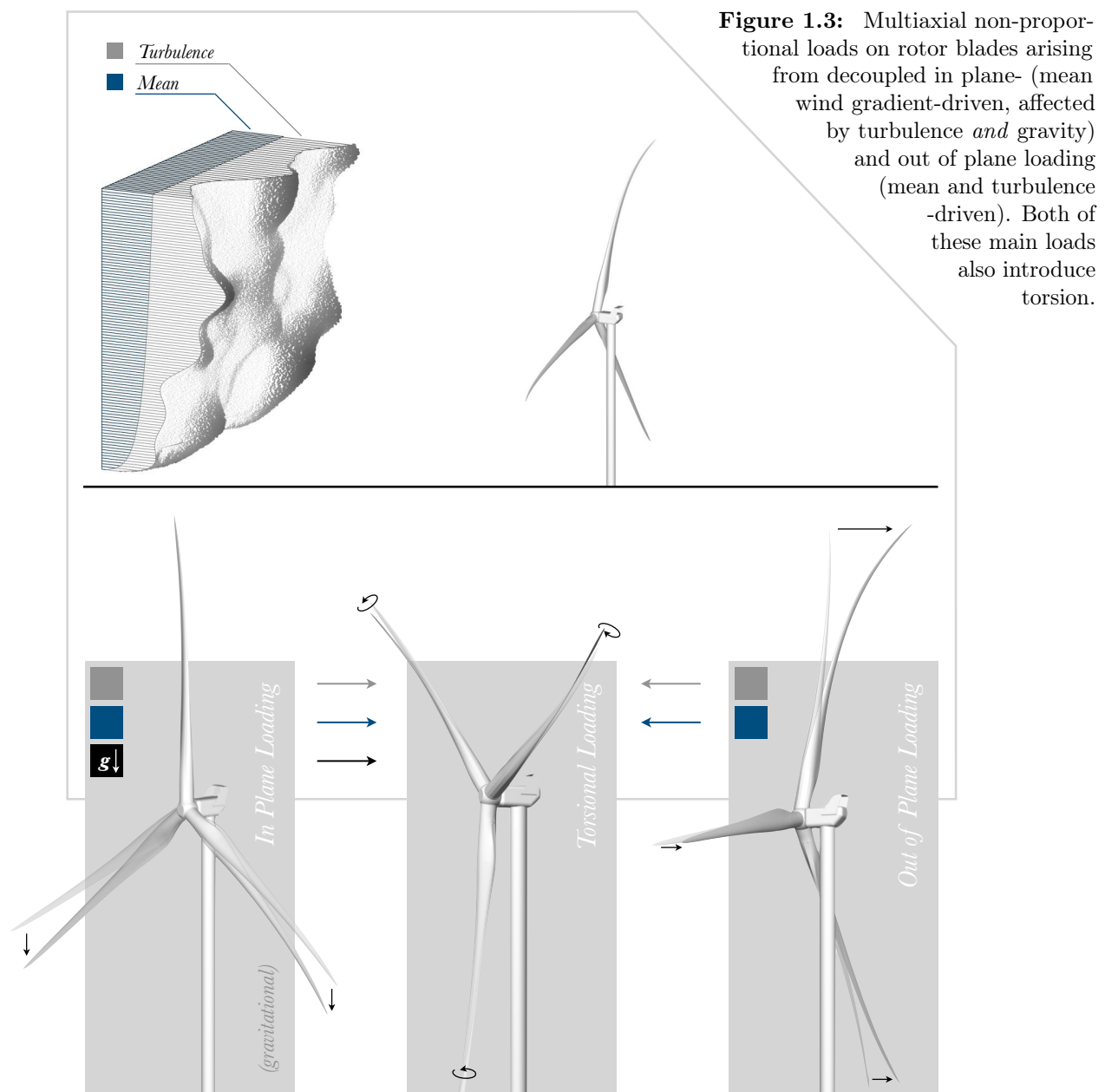


**Figure 1.3:** Multi-axial non-proportional loads on rotor blades arising from decoupled in plane- (mean wind gradient-driven, affected by turbulence *and* gravity) and out of plane loading (mean and turbulence-driven). Both of these main loads also introduce torsion.

**Control of wind turbines.** Modern wind turbines are operated in two basic modes. The first is the partial load regime, where the power output is maximized by adapting the rotational speed of the rotor (via the generator torque) to the wind speed. Once the rated power of the generator is reached, the control strategy is changed to power (and load) limitation via a constant rotational speed of the rotor and by pitching the blades. In this context, pitching the blades refers to a decrease of the angle of attack (indicated as  $\alpha$  in Figure 1.4), i.e., a rotation of the blades leading edge towards the wind direction.

**In plane loading.** Loads that arise parallel to the rotor plane are called in plane loads. These are a combination of the tangential aerodynamic forces and a gravitational component, cf. Figure 1.4. The resulting deformation on account of gravity is shown in Figure 1.3 (left). On account of the large inertia of the complete rotor, the gravitational in plane loads are rather deterministic, meaning that localized turbulence will not significantly alter their magnitude. Only a steady increase of the mean wind speed (in the partial load control regime) will globally change the gravitational in plane loads, as this will change the rotational speed of the rotor. However, turbulence-induced wind speed changes will lead to localized changes of the tangential forces and therefore to localized alterations of the aerodynamic in plane loads. It is important to note that the in plane loads of a particular blade are a function of the azimuth position. This is because the wind gradient generally leads to higher aerodynamic forces at the upward position compared to the downward position, i.e., resulting in a sinusoidal aerodynamic load with each rotation (for steady wind shear conditions). The in plane bending moment on account of gravity is also sinusoidal. However, the maximum and minimum of the gravitational in plane bending moment does not coincide with the aerodynamic one, since, i.e., the maximum is found when the blade is parallel to the ground and not in its upward position. The magnitude of the gravitational bending moment is also independent of the wind speed, only its frequency is affected by a changing rotational speed of the rotor in the partial load regime. To describe the loads on a cross sectional level, the in plane loads are transformed to edge- and flapwise loads, whereat edgewise refers to a direction parallel to the chord line of an airfoil at a particular radius and flapwise refers to a direction perpendicular to the chord line, cf. Figure 1.4. In the partial load regime, the in plane loads mainly contribute to an edgewise load. However, this changes when the blade is pitched and is dependent on the radial position on account of the blade twist (indicated as  $\theta_t$  in Figure 1.4).

**Out of plane loading.** The thrust component of the aerodynamic forces, cf. Figure 1.4, leads to an out of plane deformation which is visualized in Figure 1.3 (right). The resulting bending moment is again a function of the azimuth position on account of the wind gradient. Localized turbulence likewise translates into changing out of plane loads. In direct comparison to the in plane loads, the out of plane loads are practically unaffected by gravity. However, since most wind turbine rotors rotate at an angle (tilt angle of the nacelle and cone angle at the hub), the gravitational load contribution is not zero, even in the un-deformed configuration of the blades or without a pre-bend<sup>1</sup>. Out of plane loads predominantly lead to flapwise loads in the partial load regime and the corresponding displacements are typically significantly larger than their in plane counterparts, cf. Figure 1.3. This is because the blade stiffness in edgewise direction is generally larger than in flapwise direction due to the geometric shape of the airfoils, which leads to a high second moment of inertia in edgewise direction. When the blade is pitched, the impact of out of plane load components on the flapwise loads is reduced and shifted towards the edgewise direction.

---

<sup>1</sup>A pre-bend is introduced to a rotor blade during manufacturing. It is utilized to increase the distance of the blade tip towards the tower (tower clearance) and is therefore an intentional out of plane tip displacement towards the wind direction. This way, the blade stiffness can be lower compared to a blade design without a pre-bend, thus reducing blade weight and cost.

**Torsion.** Both the in plane and the out of plane loads also introduce torsion as the aerodynamic center and the center of gravity of each cross section are usually not found at the same position as the shear center, cf. Figure 1.3 (mid). In addition, the aerodynamic (pitching) moment coefficient of airfoil sections is a source of blade torsion. Some blade designs also utilize a geometrical or structural bend-twist coupling, where peak flapwise loads are lowered by passively pitching the blade, which introduces additional torsion [65, 66]. Even in case a geometrical bend-twist coupling may not be present in a particular blade design, an (unintentional) structural coupling is likely to occur in general, as this is related to the geometrical airfoil shape and the anisotropy of the composite materials used. Moreover, torsion is introduced to the blade when in plane and out of plane loads are superimposed. This is because these load components lead to a second order eccentricity in the deformed state. Therefore, a large out of plane tip displacement represents the lever arm for in plane loads, which inevitably leads to torsion towards the blade root, cf. Figure 1.3. As mentioned, the aerodynamic forces are proportional to the square of the inflow velocity, which itself increases linearly towards the tip. Based on that, the outward part of the blade generates the majority of the aerodynamic forces necessary for a high power output of the turbine. This also means that an eccentricity-based torsion becomes significant for long, flexible blades with large tip displacements. A pre-bend blade design is particularly interesting in this regard, as it introduces a large out of plane eccentricity for small wind speeds, but counteracts the out of plane eccentricity for medium wind speeds when the out of plane loads lead to a rather straitened blade. On account of the different flapwise and edgewise stiffness of rotor blades, pitching will significantly alter the respective eccentricities and therefore change their contribution to blade torsion.

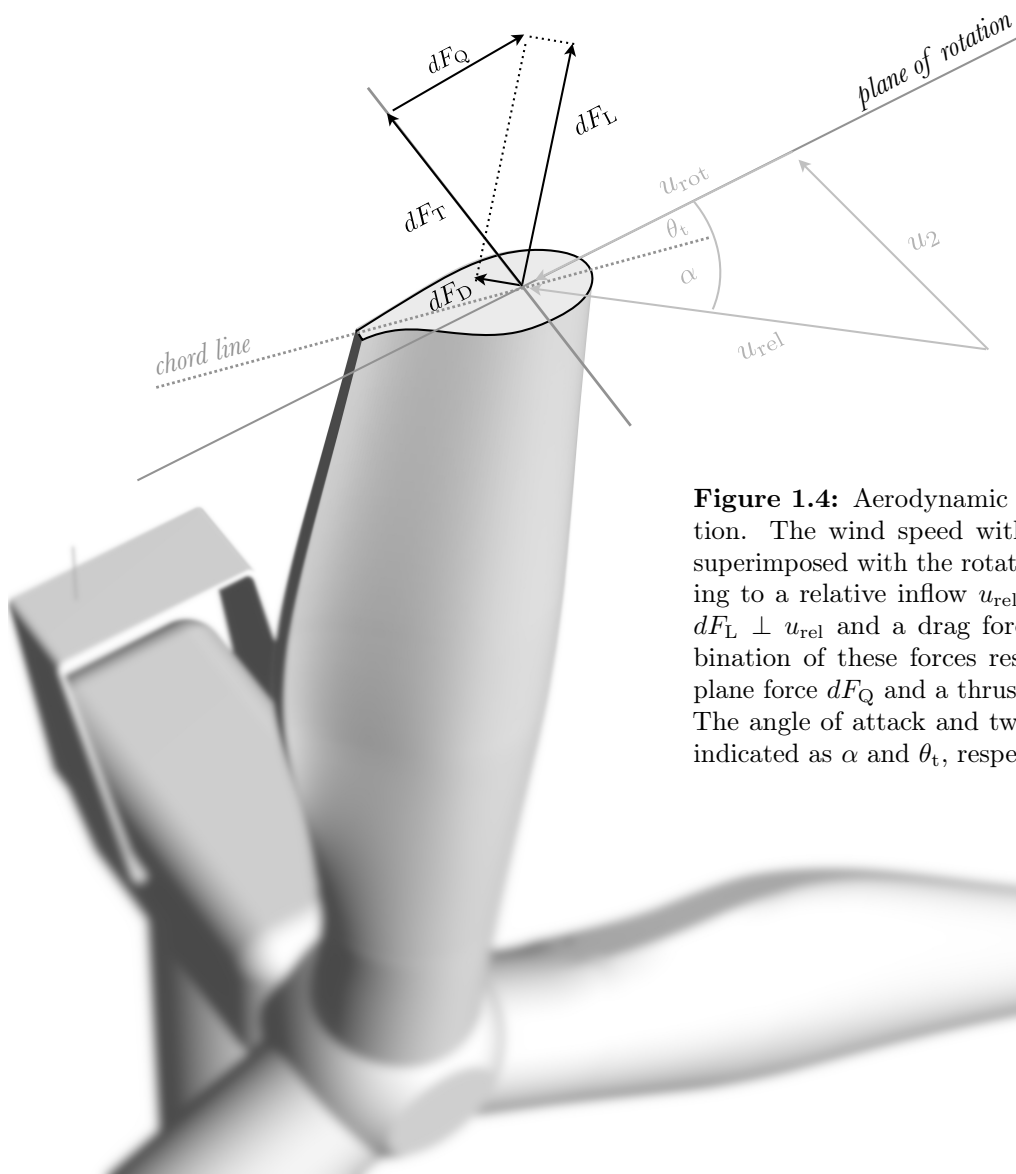


**Figure 1.4:** Aerodynamic loads at a blade cross section. The wind speed within the rotor plane  $u_2$  is superimposed with the rotational component  $u_{rot}$  leading to a relative inflow  $u_{rel}$ . This causes a lift force  $dF_L \perp u_{rel}$  and a drag force  $dF_D \parallel u_{rel}$ . The combination of these forces results in a tangential / in plane force  $dF_Q$  and a thrust / out of plane force  $dF_T$ . The angle of attack and twist angle of the blade are indicated as  $\alpha$  and  $\theta_t$ , respectively.

**Centrifugal loading.** Due to the rotation of the rotor, a centrifugal load is present. The magnitude of this load is dependent on the rotational speed of the rotor and is therefore mainly influenced by the mean wind speed in the partial load regime. Turbulence only has a negligible effect in this case. Since the center of gravity usually does not coincide with the elastic center, the centrifugal load introduces an uneven distribution of (normal) strains in radial direction. In addition, the airfoil geometry and anisotropic material properties lead to coupling effects, so that the extension caused by the centrifugal load may also lead to bending, torsion, etc. Centrifugal loads also lead to a stiffening effect that counteracts flapwise and edgewise tip displacements and therefore affects eccentricity-based torsion.

**Non-linearities.** The vast size of the blades, their complex shape and large deformations lead to a variety of geometric non-linearities such as cross-sectional deformations, e.g., the Brazier effect [67, 68] and local buckling [20, 69]. In addition, material non-linearities are present. These are, for instance, related to the anisotropic behavior of the used materials in combination with non-linear fatigue degradation processes. As these non-linear effects can significantly alter local stresses and strains, they have to be modeled for accurate fatigue life predictions. Therefore, non-linear finite element (FE) analyses are required. On account of the extreme cycle numbers of rotor blades and the fact that non-linear analyses are computationally more expensive than linear ones, accurate fatigue life predictions become challenging. Manufacturing-induced imperfections such as pores, local fiber misalignment or waviness may even require additional local models or local adjustments of the probabilistic material parameters. It is particularly important to note that the mentioned non-linearities are (typically) not included in aeroelastic analyses. However, local changes of the geometry due to non-linear deformations will change the stiffness matrix and may also significantly affect the aerodynamics and hence alter the loads. Concerning the adhesive joints of rotor blades, cf. Section 1.2.2, cross sectional deformations such as transverse shear deformation, trailing edge panel breathing and local buckling introduce additional stresses, which are essential for an accurate fatigue life prediction.

**Residual & thermal stresses.** During the manufacturing of rotor blades<sup>2</sup>, residual stresses may arise from different thermal expansion coefficients and chemical shrinkage of the used materials during curing. While effects such as chemical shrinkage exclusively affect the matrix material and adhesive, they can lead to local fiber waviness and hence indirectly influence the fibers. Viscoelastic material properties also allow for relaxation effects, so that accurate modeling of residual stresses is not trivial. Apart from that, the operation of wind energy turbines in more extreme site conditions, e.g., arising from cold climate or desert regions, may introduce thermal stresses or significantly change the material properties.

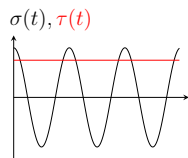
**Dynamic phenomena.** In addition to the aforementioned load sources, wind turbine rotor blades are subjected to a variety of dynamic phenomena, which introduce additional loads. Among other sources, these arise from the tower passage, yaw-misalignment, mass-imbalances of the blades and resulting vibrations from various sources. Unsteady aerodynamics and aeroelastic phenomena also add loads.

---

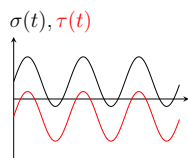
<sup>2</sup>The manufacturing process will be discussed in more detail in Section 1.2.2.



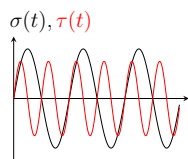
Superimposed and coupled with the non-linear structural behavior, the aforementioned loads result in a multi-axial and non-proportional stress state [19, 70–73], which is transferred to the hub [15, 74] and subsequent components [24, 75, 76]. A variety of examples from Figure 1.1 apply that lead to this non-proportional stress state, which will be discussed in the following to ease understanding of the origin of the non-proportionalities:



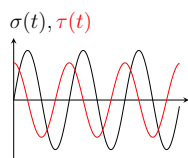
A rather constant centrifugal load introduces a local quasi-static normal stress. Superimposed with cyclic shear stresses from torsion or shear forces, this leads to a non-proportional load state. Note that this holds for any rotating system and in terms of wind turbines applies even in case the wind field is represented by a constant wind speed. In addition, this load case can also be caused by residual stresses.



Residual stresses can distort the stress ratios of different load contributions. So even in case a certain load introduces (in-phase) sinusoidal normal and shear stresses, a superimposed residual stress can introduce a non-proportional load state. Analog to the previous example, this load case can also be caused by a centrifugal load, since the resulting normal stress offset is likely to be higher than the corresponding shear stress offset.



On account of the vast size of the rotor and its large inertia, the contributions of different load sources affect different time-scales and therefore appear at different frequencies. For instance, the sinusoidal in plane load caused by gravity has a different frequency than turbulence-induced out of plane loads or dynamic phenomena.



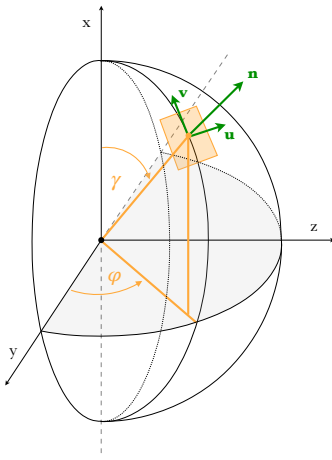
Since the in plane loads are a combination of stochastic aerodynamic loads and deterministic gravitational loads, they are (to a certain degree) decoupled of the (stochastic, mainly aerodynamic) out of plane loads. This also means that normal and shear stresses are introduced to the blade both on a deterministic and stochastic level. Therefore, normal and shear stress components (with a similar frequency) can also be phase-shifted.

It is important to note that the (cross-sectional) design of rotor blades can introduce a geometrical de-coupling of the resulting stresses, e.g., the spar caps will carry the majority of normal stresses. This geometrical de-coupling is blade design-dependent and so is the resulting level of non-proportionality. A study on three different blade designs demonstrated that the level of non-proportionality during normal operation can be substantially different [72]. The radial regions where high levels of non-proportionality are found also change depending on the operational mode of the turbine, i.e., the blade pitch will affect the stress distribution. In addition, the fidelity level of the finite element blade model and the chosen load introduction technique is also likely to affect the observable level of non-proportionality. As mentioned before, a more detailed discussion on the estimation of the level of non-proportionality and its dependencies on various variables will be presented in Section 6.2.1.

### Critical plane approach for non-proportional fatigue life predictions

With time dependent principal stress/strain directions, a non-proportional load causes damages on different material planes. Therefore, the critical plane (CP) approach evolved to individually analyze the damage of the respective material planes in order to find the most damaged one, which is usually referred to as the CP and used for fatigue life predictions [8–11]. This analysis strategy leads to a sequence of complex sub-algorithms on each analyzed plane, which are summarized in the following.

1. The global stress history (complete stress tensor  $\boldsymbol{\sigma}$  as a function of time  $t$ ) is projected onto a particular plane. A half sphere is sufficient to represent all possible (critical) plane orientations, as two diametrically opposite points on a complete sphere define the same plane orientation [77], cf. Figure 1.5. The projection is done using the normal vector  $\mathbf{n}$  of the respective plane and the in-plane vectors  $\mathbf{u}$  and  $\mathbf{v}$ , which are given by



$$\mathbf{n} = \begin{pmatrix} \cos(\gamma) \\ \sin(\gamma) \cos(\varphi) \\ \sin(\gamma) \sin(\varphi) \end{pmatrix}, \quad \mathbf{u} = \begin{pmatrix} 0 \\ -\sin(\varphi) \\ \cos(\varphi) \end{pmatrix}, \quad \mathbf{v} = \begin{pmatrix} \sin(\gamma) \\ -\cos(\gamma) \cos(\varphi) \\ -\cos(\gamma) \sin(\varphi) \end{pmatrix}, \quad (1.1)$$

where  $\gamma$  and  $\varphi$  describe latitude and longitude, respectively. This leads to a normal stress ( $\sigma_{nn}$ ) that is perpendicular to the plane and two shear stresses ( $\tau_{nu}$ ,  $\tau_{nv}$ ) parallel to the plane orientation:

$$\sigma_{nn}(t) = \mathbf{n}^T \cdot \boldsymbol{\sigma}(t) \cdot \mathbf{n}, \quad \tau_{nu}(t) = \mathbf{u}^T \cdot \boldsymbol{\sigma}(t) \cdot \mathbf{n}, \quad \tau_{nv}(t) = \mathbf{v}^T \cdot \boldsymbol{\sigma}(t) \cdot \mathbf{n}. \quad (1.2)$$

**Figure 1.5:** Projection of the stress tensor onto a plane.

The projected stress history is referred to as the CP stress history.

2. Filtering algorithms such as the multiaxial racetrack filter (MRF) [78] can be applied to shorten the CP stress history and increase the computational efficiency of subsequent algorithms. Conventional uniaxial filters such as peak-valley algorithms are not suitable, because different points in time might be filtered out for each stress component, so that the synchronization between the different stress components could get lost [78]. Figure 1.6 visualizes the principle of the MRF. In this two-dimensional example, a circle is moved along the stress path, whereat each point that is not associated with a change of the translation direction of the circle can be filtered. This approach also works for higher dimensions.

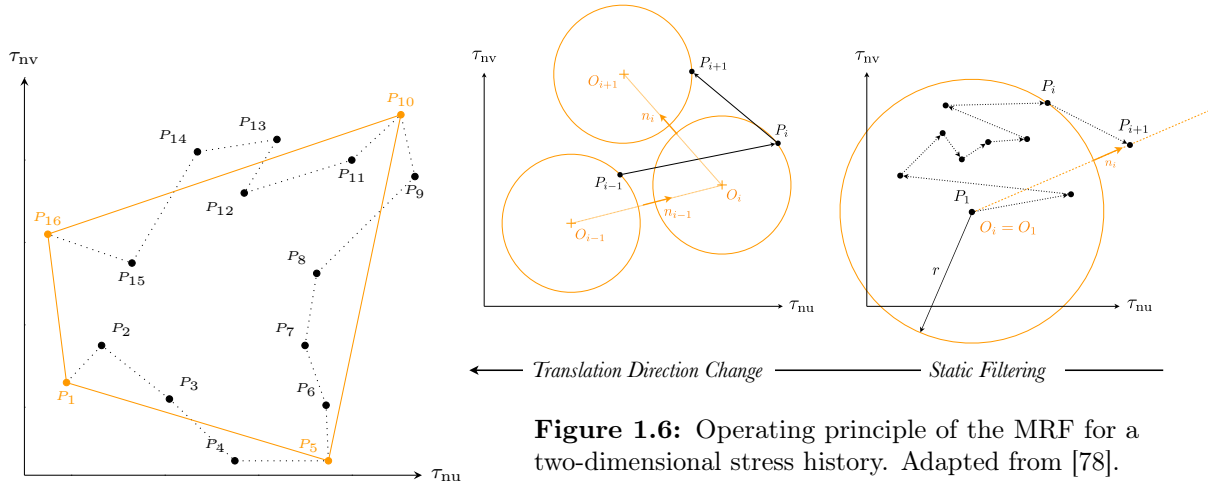


**Figure 1.6:** Operating principle of the MRF for a two-dimensional stress history. Adapted from [78].

3. A multiaxial rainflow count is used to identify cycles for the (filtered) CP shear stress history. Different algorithms for this task are available in literature [79–86], while the Wang-Brown algorithm [79, 80] and particularly its modified version [9, 83] are frequently used. Figure 1.7 depicts the main idea of the modified Wang-Brown algorithm (MWB). Among other rules, the algorithm is based on the search for the (next) point  $P_{j+1}$  that is outside a circle with radius  $\overline{P_i P_{i+1}}$  in ascending order of all points, i.e., the (rearranged) stress history [9, 83]. When such a point is found, the new circle radius is calculated as  $\overline{P_i P_{j+1}}$  and the next point outside the circle needs to be found. All points that were identified this way form a half cycle. A full cycle is identified when the (binned) start and end points of two half cycles match, which is rare for random multiaxial load cases [9]. On account of the sequential search method, it is not a priori known how many points form a half cycle. This leads to the implementation problem that the required memory for a cycle can not be pre-defined, which significantly increases the computation time either by overestimating the memory demand or by repeated re-allocations.

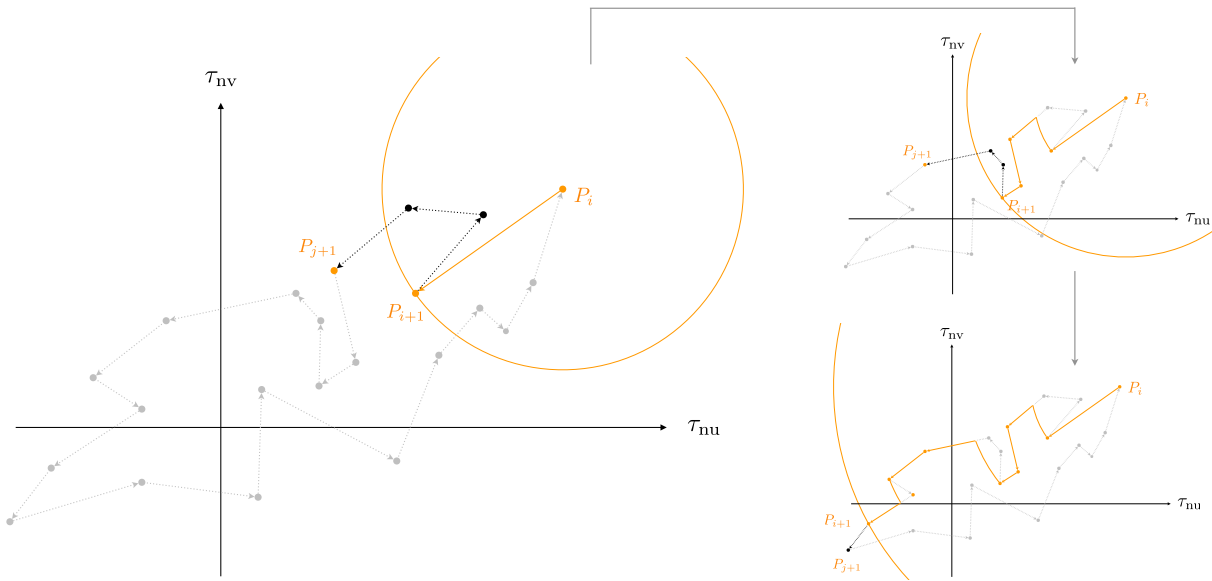


**Figure 1.7:** Multi-axial rainflow counting by example of the modified Wang-Brown algorithm [9, 83].

As briefly mentioned before, the algorithm is performed on a rearranged (filtered) CP shear stress history. The rearrangement of this two-dimensional point cloud is based on the identification of the two most distant points in an Euclidean sense (distance defined as  $d_{ij}$ ). For a history of length  $l$ , this means that  $l \cdot (l - 1) / 2$  distances have to be calculated to find the largest one in a brute-force approach. In wind energy contexts, where a load history is typically 10 min long and sampled with 50 Hz, this means an overhead of approximately  $4.5 \cdot 10^8$  calculations (defined as  $c$ ) before the cycle identification algorithm can start, cf. Figure 1.8 (top).

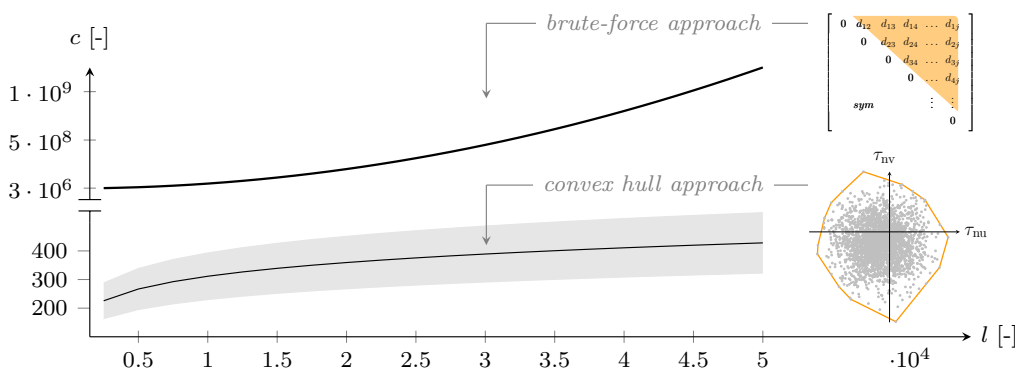


**Figure 1.8:** Convex hull algorithm (lower part) to speed up the rearrangement of the shear stress history in the MWB.

Note that a standard loads assessment for wind turbines results in hundreds of 10 min time series that have to be evaluated in this way. To reduce this additional effort, the author of this thesis proposes to utilize a convex hull algorithm before the Euclidean distances  $d_{ij}$  are calculated, which results in an improvement of several orders of magnitude in computation time, cf. Figure 1.8 (bottom).

4. An enclosing surface method is employed to identify a shear stress amplitude and mean value of the two-dimensional shear stress history of each previously found (multiaxial) cycle. Several methods have been proposed for this step reaching from geometrical simplifications of the shear stress path (minimum ball [87], minimum rectangle [88], minimum ellipsis [89]) to mechanical analogies referring to the polar moment of inertia (PMOI) [90, 91], cf. Figure 1.9.

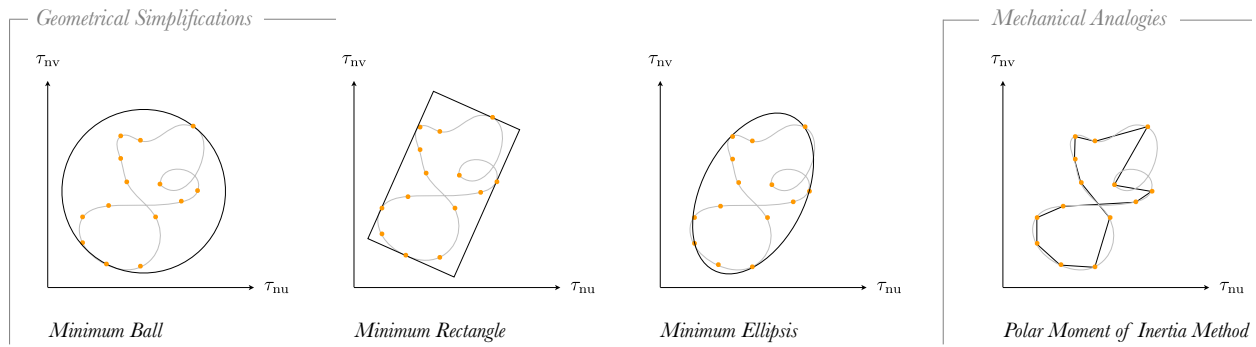


**Figure 1.9:** Overview of enclosing surface methods to calculate the amplitude and mean value of a two-dimensional shear stress path of a particular cycle.

In addition to the accuracy of the respective enclosing surface methods, their computational efficiency is (again) an important factor, as these algorithms will be repeated for potentially thousands of times on each investigated plane. The mechanical analogy of the PMOI methodology is thus also beneficial in this regard as no iterative optimizations are required to fit a certain minimum shape to the shear stress path.

5. Combined equivalent stresses and corresponding damages of each cycle are calculated using CP damage criteria. This step in particular is associated with a large variety of options to account for different material behavior or loading conditions, e.g., [37, 51, 63, 87, 92–109]. Criteria that involve shear stresses are usually coupled with an enclosing surface method, cf. Figure 1.9. This leads to a vast number of overall combinations, since a single damage criterion might lead to different fatigue life predictions depending on the incorporated enclosing surface method. In addition, CP damage criteria involve material parameters, which need to be calibrated based on multiple S-N test results. Most frequently a normal stress- and a shear stress-related S-N curve are required at a stress ratio of  $R = -1$  (ratio between the minimum and maximum stress). While normal stress-related S-N tests are very common, shear stress-related S-N tests are relatively scarce. An experimental campaign may therefore be necessary for an accurate calibration of the chosen damage criterion. The resulting equivalent stress is compared to a single S-N curve to determine the damage of each cycle. Mean stress corrections, e.g., via a constant fatigue life (CFL) / Haigh diagram [110–118], are typically not included in classical CP models, but can be incorporated before the calculation of the equivalent stresses.
6. In the last step, the damage of all cycles is accumulated. Most commonly this is done linearly [119], although non-linear damage accumulation hypotheses have also been proposed [120].

In addition to the aforementioned sub-algorithms for the analysis of a single plane, another global algorithm is required to decide which planes shall be analyzed in the first place. Given that the search space is a half sphere, equal angle increments for both altitude and longitude seem appropriate. However, a dissection of the half sphere based on equal area segments leads to a more homogeneous distribution with less segments especially at the poles [77], as shown in Figure 1.10. Several (adaptive) algorithms were proposed [121–124] to further reduce the number of segments, while maintaining a good precision of the CP location. However, even with these algorithms the number of segments is still considerably high. In combination with the evaluation of complex multiaxial sub-algorithms, this leads to an extensive computational effort. So even in case the CP approach was successfully validated for a certain material, its industrial application in iterative structural optimization processes will be rather limited, e.g., to known stress hot spots of a component.

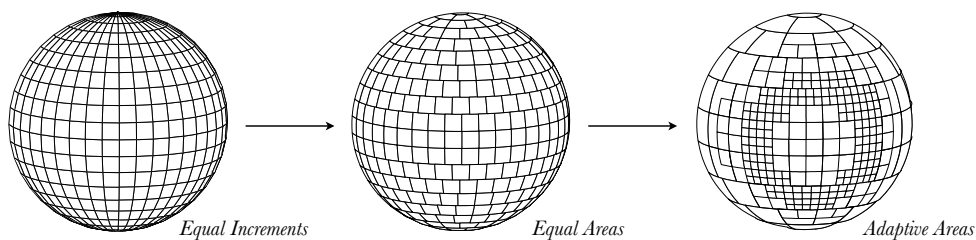
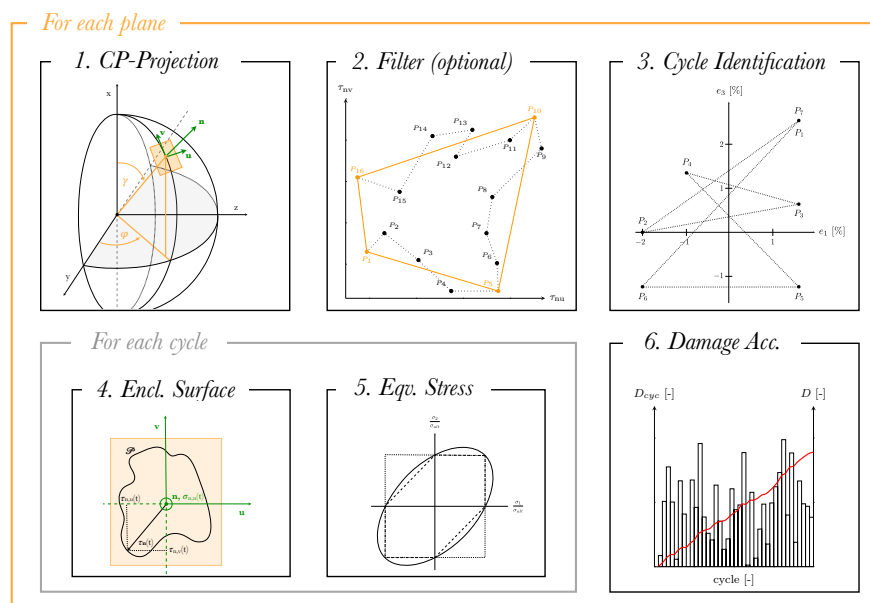


**Figure 1.10:** Damage half sphere discretization based on different strategies. Based on [122].

Although the CP approach was proven to yield good fatigue life predictions for non-proportional load cases, the computationally intense process in combination with the required calibration data and vast number of sub-algorithms leads to a difficult validation and application process. Figure 1.11 presents an overview of the aforementioned algorithms required for a CP analysis. Only in case a very controlled experimental setup, including high-quality specimens and well-known uniaxial material data, is available, it might be possible to identify potential errors of the sub-algorithms with high certainty. A robust, easy-to-use and widely applicable method is not existent (to the knowledge of the author). Recent developments even increased the number of failure criteria [97] and associated methods as most research focused on improving aspects of the CP approach for confined applications or materials. Therefore, the only common agreement found in literature is that such a unified approach is not existent [16, 41, 125–129]. Some researchers even state that this may be impossible to achieve [79].

A detailed comparison of the CP methodology and the global uniaxial equivalent stress-based approach (current state of the art in wind energy) will be given in Chapter 6.

**Figure 1.11:** Critical plane flowchart with exemplary illustrations of typically used sub-algorithms.



### 1.2.2 Rotor blade manufacturing

Modern rotor blades of wind energy turbines are the largest mass-produced composite components of any kind. The manufacturing is typically subdivided into the fabrication of half shells (providing the aerodynamic shape) and shear webs, which are joined using structural adhesives [130–136]. Figures 1.12 and 1.13 summarize the manufacturing steps and depict the typical cross-sectional layout.

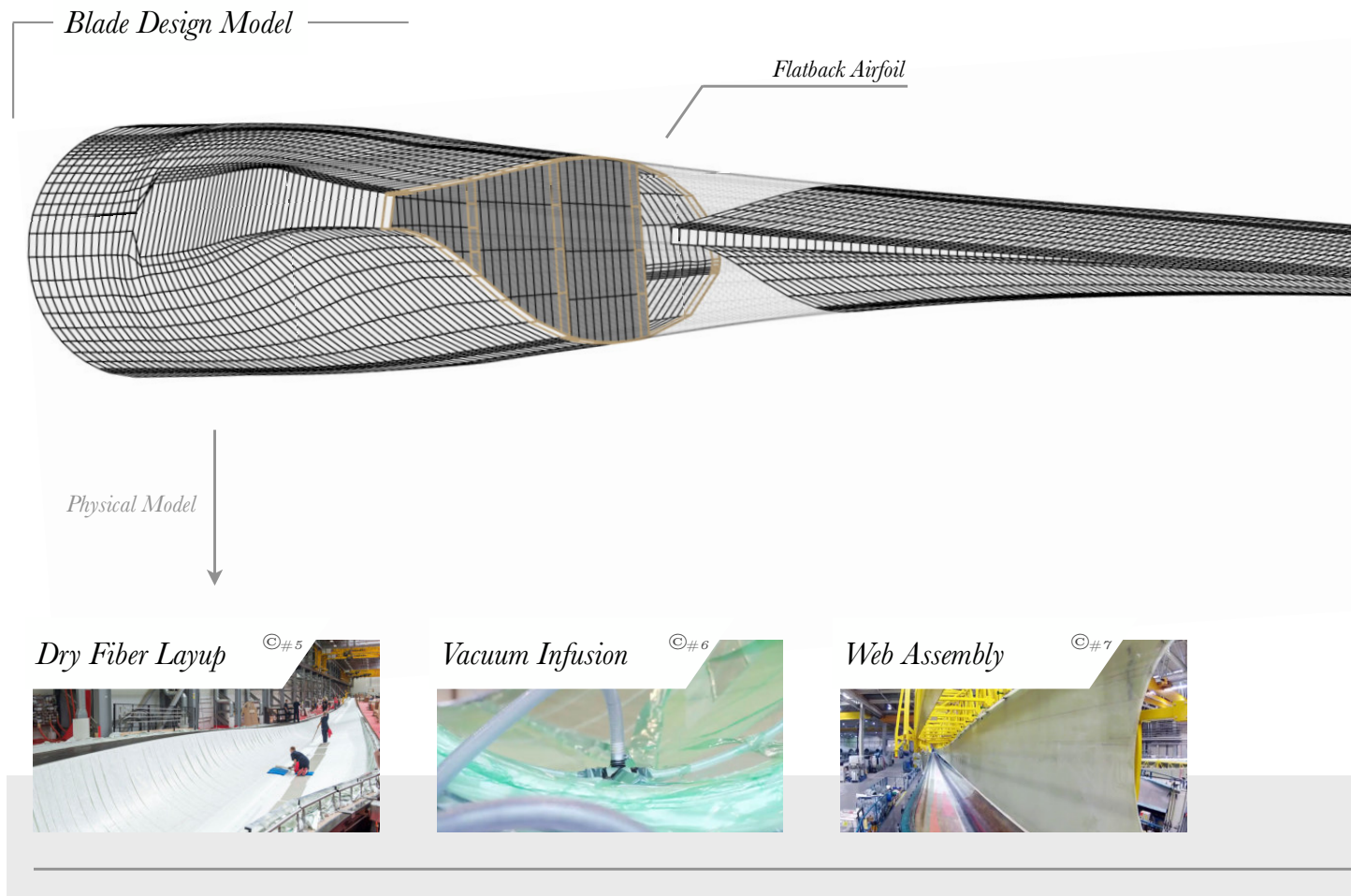


**Figure 1.12:** Rotor blade manufacturing - part 1/2.

The manufacturing process starts with a dry fiber layup of the aerodynamic half shells and shear webs, which are manufactured in parallel. Hereafter, the fibers are infused with resin in a vacuum infusion process. In some cases, planks of the unidirectional spar caps are pre-fabricated in a pultrusion process [137, 138] and included in the aerodynamic shells during the dry fiber placement. The spar caps carry the majority of (flapwise) normal stresses in the blade. To avoid buckling, the shells are sandwich structures, which are made of a rather thick foam or balsa wood core and bi- or triaxial glass fiber face sheets. The same applies for the shear webs, which contribute to the geometrical stability, carry shear loads and divert the cross section into multiple sections to further reduce the risk of buckling and improve shear / torsional stiffness. The joining process is subdivided into the shear web assembly and the full assembly.

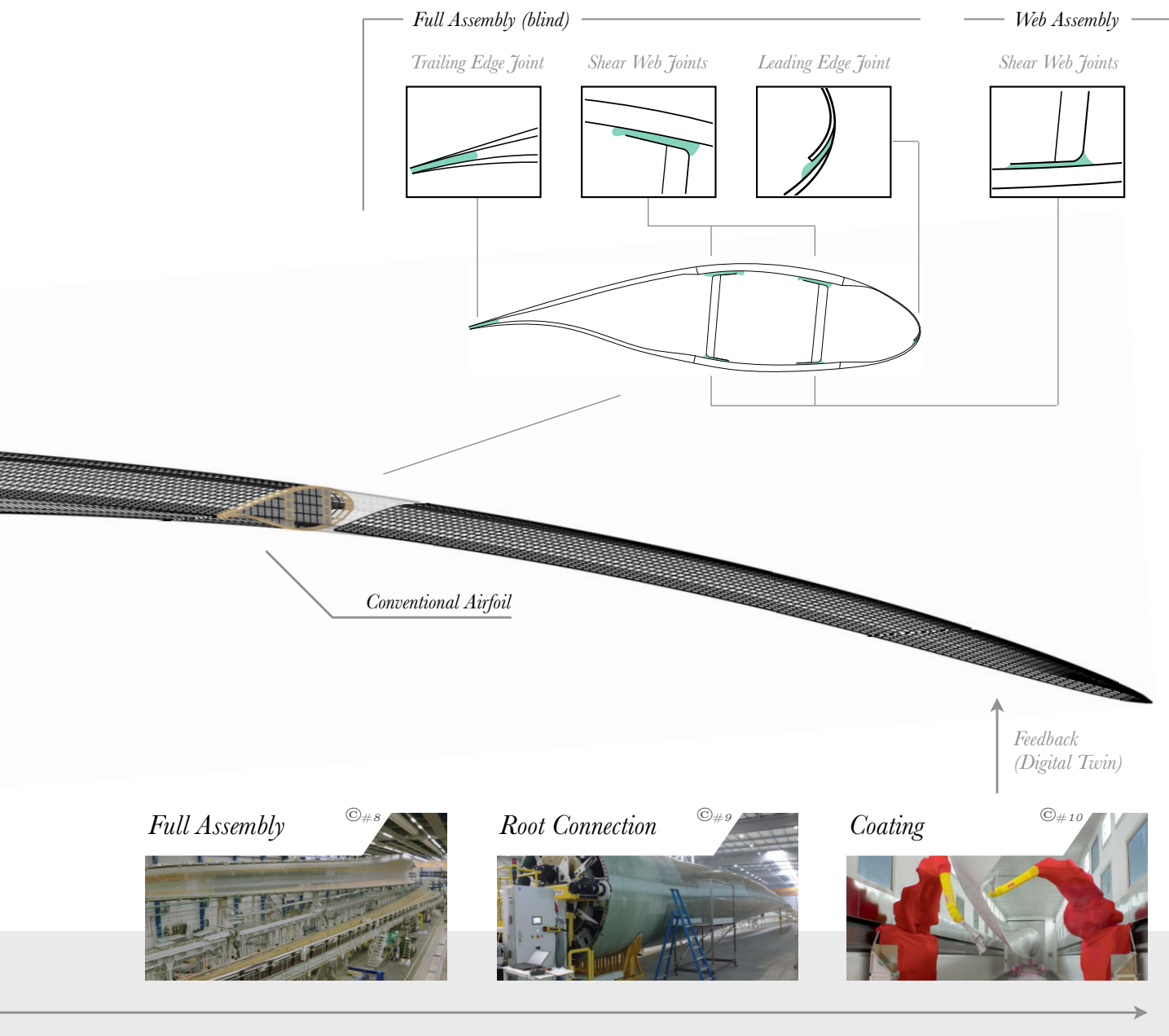


**Figure 1.13:** Rotor blade manufacturing - part 2/2.

In the shear web assembly, the webs are joined with one of the half shells and the bond line can be inspected along the complete length of the blade. Surplus adhesive that is pushed outward of the bonding locations can be removed and the outer surface of the bond line can be shaped with templates. In contrast, the adhesive joints in the full assembly (blade mold closing) can only be inspected and shaped in the accessible regions inside of the complete blade. In this case, surplus adhesive remains in inaccessible regions as dead weight. Subsequent to the adhesive curing process [135, 136] of the full assembly, the root connection is prepared and the blade is grinded and coated for UV protection, aesthetics, etc. [131, 139, 140]. Leading edge protection coating/tapes [140–143] are finally applied to avoid erosion among other optional devices such as vortex generators [144–146].

At all manufacturing steps, cost-effectiveness and hence production efficiency is key to achieve a low levelized cost of energy. Therefore, the material choice is not only based on the material properties of the finished product, but also on the respective manufacturing conditions, such as curing times and drapeability. In this regard, reproducibility of, e.g., the fiber orientation and layup, is essential to minimize uncertainties. However, the degree of automation in the production of blades is low and a matter of research [132–134], so the manufacturing quality of each blade may differ. Digital twins of as-built configurations emerged as an option to estimate the differences between the ideal design model and the real physical model [5]. For both the design optimization and the digital twin modeling, a precise knowledge of the material properties and their standard deviations is essential for good results and low uncertainties.

### Adhesive application

Adhesives in rotor blade manufacture are highly viscous, thixotropic pastes [130]. Most of which are two-component and epoxy-based systems [17, 147–150]. Short fiber reinforcements are also common to enhance, e.g., the fatigue strength [17, 149]. Given the vast size of the blade molds and economic constraints, the thickness of the adhesive joints also serves as a compensation for manufacturing tolerances. Thus, adhesive joints with heights of 10–15 mm are common [130, 136, 151, 152]. This is in stark contrast to other industries, where the bond line thickness is usually in the sub-millimeter range, because strength and stiffness of a bond line usually decrease with increasing thickness [153–157]. To assure a safe bond of the respective components, the width of the bond lines is also considerable and in the order of 100 mm, e.g., at the trailing edge. A typical rotor blade assembly can thus require hundreds of kilos of adhesive.

To meet the industry requirement of an efficient blade mold usage, the adhesive is applied using (several) dosing and dispensing machines [130]. The mixing process is usually vacuum-based, pump-driven and involves a static mixer. The application of the adhesive is done using either a simple hose in combination with a manually operated template or using customized outlet shapes to achieve a specific bond line cross sectional geometry. Recently a versatile adhesive applicator was developed by Fraunhofer IWES, which allows to modify the bond line geometry during the application process [158], cf. Figure 1.14. With this, manual touch-ups or template changes along the blade length become obsolete. At the same time, the material application is more precise and leads to less waste. It is also likely that the orientation of potential reinforcement fibers can be influenced with this device, since the fiber orientation is usually linked to the flow velocity and nozzle shape. However, the mold closing process will still lead to squeezing effects, which may introduce a change in the fiber orientation.

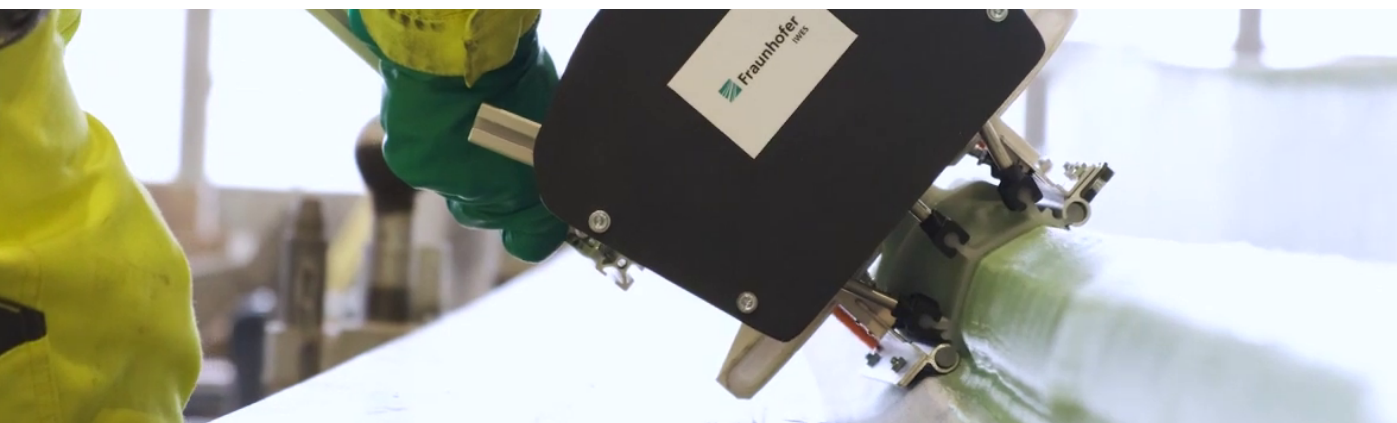


**Figure 1.14:** Demonstration of the Variable Glue Applicator for wind turbine rotor blades [158]. ©#11



### Adhesive specimen

Despite of established vacuum-based mixing processes and semi-automized adhesive application techniques, specimen manufacture involved (predominantly) manual processes in recent publications [152, 159–162] on rotor blade adhesives. This comes at a high cost, as inhomogeneities such as pores will introduce large scatter and prohibit the characterization of the neat material behavior due to effects of defects. Therefore, even the uniaxial material properties at the coupon level are associated with large uncertainties and the variance of the neat material properties remains unknown [3] when the specimen manufacture (especially the mixing process) is done manually. The difference in mixing quality and porosity, respectively, associated with hand- and machine-mixing (laboratory planetary centrifugal mixer) is shown in Figure 1.15. Although the machine-based mixture is not free of pores due to the application process during the specimen manufacture, the overall porosity level is significantly lower compared to a hand-mixing process [163].

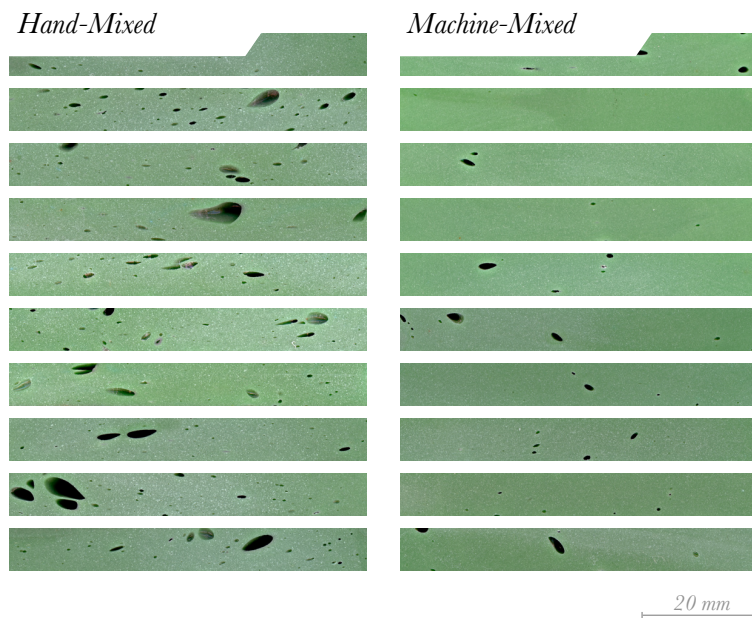


**Figure 1.15:** Demonstration of different mixing qualities achieved with either hand- or machine-mixing, each with 10 samples from plate specimens. While pores are not entirely removed due to the adhesive application process, machine-mixing leads to a higher quality, i.e., lower porosity level. Specifically, the porosity level was  $0.91 \pm 0.60$  % for the machine-mixed samples in contrast to  $4.94 \pm 1.89$  %. Images and porosity estimation based on [163].

Subsequent sub-component and full-scale tests are likely to add additional uncertainties on account of more complex geometries, test setups and a typically lower number of tests, cf. Figure 1.16. The relative merit of more complex tests is thus linked to the quality of prior coupon tests.

The necessity to investigate multiaxial and non-proportional loads generally leads to a more complex experimental setup and specimen geometry. Depending on the available testing machinery, different options such as plates [164, 165], cruciform types [166–170] and tubes [159, 160, 171] can be used on a coupon level. The increased geometrical complexity of the specimens is unfortunately likely to contribute to (even) more manufacturing-induced defects. So far, a virtually defect-free rotor blade adhesive specimen that is suitable for multiaxial and non-proportional tests does not exist. Moreover, the alternative of a detailed characterization of apparent defects such as pores or mixing inhomogeneities is missing in the respective publications of already existing multiaxial adhesive specimens [159, 160]. Hence, a neat material characterization has not been achieved (published), yet.

### 1.2.3 Verification of fatigue life prediction methods

In general, the verification of fatigue life prediction methods starts with tests on generic coupon specimens and simplified (uniaxial) loading conditions [172]. This way, the behavior of a single material or composite can be analyzed for a particular load state and given manufacturing quality. Typically, the test results, e.g., S-N curves, are then used to predict failure for other load cases (Haigh diagram interpolation) or more complex structures. Since tests on uniform and small-scale specimens may not represent the properties on a larger scale, e.g., in terms of manufacturing quality or regarding the load distribution and residual stresses, sub-component tests [19, 152, 173–182] are conducted to quantify potential differences. Structurally very complex components such as rotor blades of wind turbines are required to be tested in full-scale in the context of the certification process [183]. Figure 1.16 visualizes the different verification steps.

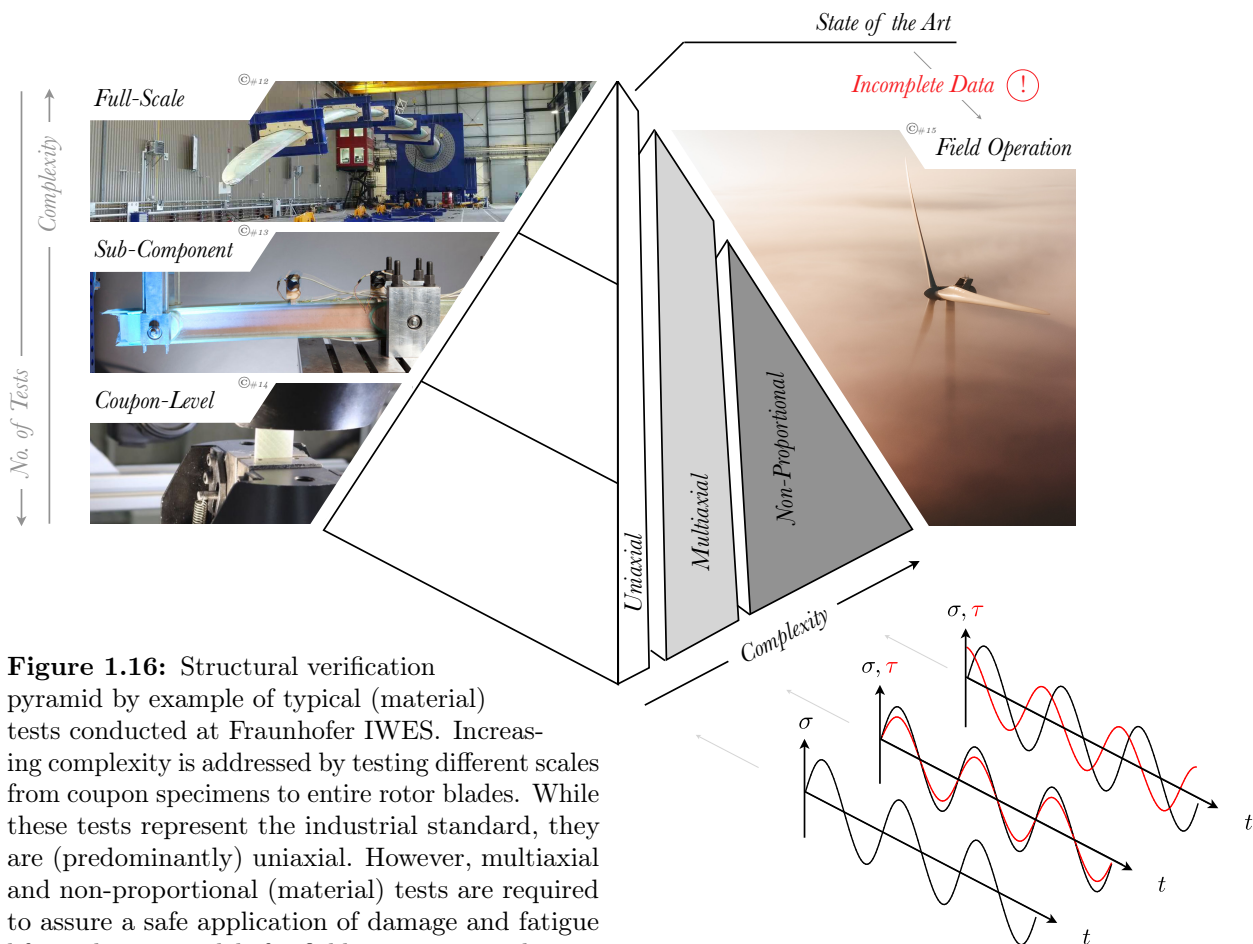


**Figure 1.16:** Structural verification pyramid by example of typical (material) tests conducted at Fraunhofer IWES. Increasing complexity is addressed by testing different scales from coupon specimens to entire rotor blades. While these tests represent the industrial standard, they are (predominantly) uniaxial. However, multiaxial and non-proportional (material) tests are required to assure a safe application of damage and fatigue life prediction models for field operation conditions.

Although the aforementioned verification steps represent the industrial standard, the respective tests are (predominantly) carried out in uniaxial loading conditions. Hence, all resulting model validations are strictly speaking confined to this load state and extrapolations to multiaxial loading are based on additional engineering models. A variety of these additional (multiaxial) models were indeed validated with good precision, however solely for proportional loads [184, 185]. Unfortunately, a model that was successfully validated in proportional loading is not necessarily suitable for non-proportional loading. In fact, a (very) non-conservative fatigue life prediction is likely if non-proportional loads are not accounted for. Given that complex non-proportional loads are found for field operation conditions [20, 72], the (uniaxial) test data leave engineers with an incomplete picture of the structural behavior, i.e., high uncertainties.

In recent years, biaxial rotor blade tests were developed [186–194]. However, the level of non-proportionality in these tests was not quantified in any of the aforementioned publications. With exception of [193] non-proportional loads were not even discussed, which means that there is a general lack of awareness for these load cases. In addition, a precise coupon-level characterization of non-proportional effects is required for ideally all materials used in a blade to be able to validate fatigue models and the blade design in multiaxial and non-proportional load states. Therefore, the relative merit of multiaxial blade tests is limited with respect to (fatigue) model validations in case the respective coupon-level data is missing, even though multiaxial blade tests represent a significant improvement over uniaxial tests regarding the complexity of the loads. Additionally, proportional multiaxial tests might lead to a confirmation bias, because engineering models appear to be validated, but fail in non-proportional conditions, as mentioned before. This will also be shown in Chapter 5.

### 1.3 Research gap and objectives

Based on the presented state of the art, a research gap and associated objectives for this thesis are identified in the following.

#### 1.3.1 Research gap

Concerning the industry standard of structural verification tests, cf. Figure 1.16, the lack of multiaxiality and especially non-proportionality represents an incomplete data set for structural optimization purposes. In addition, the structural integrity of operational turbines is at risk if non-proportional effects are not accounted for.

High uncertainties of basic material parameters due to unrepresentative (hand-mixed) adhesive specimen manufacturing limit the structural optimization potential and do not represent the industrial manufacturing quality. In addition, these uncertainties are transferred to conclusions on best-fit material models such as yield criteria. A high porosity level or mixing inhomogeneity during the material characterization stage may therefore lead to significant errors in the prediction of the structural behavior of components. These errors will likely be amplified when the predictions are done for components with a different manufacturing quality, i.e., in blade manufacture. On the contrary, a defect-free material characterization will lead to significantly reduced scatter and enables to model effects of defects with additional tests of lower quality specimens. Moreover, defect-free specimens are essential to reliably identify influences of multiaxial and non-proportional loads, as these load states might involve additional material degradation effects, which potentially lead to increased scatter on their own.

The fatigue life prediction of rotor blade bond lines in literature was primarily based on rainflow-counted equivalent stress histories, a methodology which is known to be limited to proportional load states. More sophisticated concepts that account for non-proportional loads, such as the CP approach, demand a significant amount of calibration data, which are not available. Additionally, the CP approach is so computationally extensive that an iterative structural optimization process requires significant hardware resources, i.e., CPU time. Even a successful application of the CP approach may therefore be limited to academic research and could be too impractical for industrial applications. A computationally efficient method without loss of accuracy is thus essential to account for non-proportional loads in structural optimization processes, e.g., in future rotor blade design iterations. Such an approach will also be beneficial for other industries, as non-proportional loads are found in a large variety of engineering applications, cf. Figure 1.2.

### 1.3.2 Objectives

The aforementioned research gap leads to the following overall objective of this thesis:

**Accurate and computationally efficient fatigue life prediction under multiaxial, non-proportional loads by example of a fiber-reinforced rotor blade adhesive.**

In order to fulfill this ambitious overall objective, several work packages are defined below, each of which contributing to an improvement of the state of the art.

**1) Specimen Optimization.** To be able to reliably identify the influence of non-proportional loads on the material behavior, defect-free specimens have to be designed and manufactured. Any kind of inhomogeneity or stress concentration might lead to high standard deviations and hence render the influence of non-proportional loads inconclusive. A tubular geometry is required to conduct experiments in combined axial and torsional loads at Fraunhofer IWES. When successful, the optimization will also enable a the characterization of the bulk material, which can then be the basis to model effects of defects, e.g., pores. The achieved manufacturing quality needs to be verified via  $\mu$ CT scans and compared to industrial manufacturing techniques and hand-mixed specimens in order to benchmark the achieved optimization.

**2) Yield Surface Determination.** The material needs to be characterized in tension, compression and torsion and biaxial combinations thereof. This way, the yield surface of the material can be determined and compared to suggestions in literature to assess the influence of manufacturing-induced defects on the yield behavior. A thorough analysis regarding torsion-induced shear stresses is required to account for the wall thickness of the specimens in the test section.

**3) Uniaxial Fatigue Tests.** The material will be subjected to several uniaxial cyclic loads to record S-N curves. Different S-N models need to be discussed to identify the best-fit, which can subsequently be used to provide an engineering approximation for the gigacycle fatigue regime. Additionally, the S-N data will provide the basic parameters necessary for non-proportional fatigue life predictions based on the CP approach. As with the static tests, the results need to be compared to literature to investigate the impact of pores on the material properties, i.e., the fatigue life. Stiffness degradation measurements are required alongside the S-N tests to characterize the continuous degradation in fatigue loading.

**4) Non-Proportional Fatigue Tests.** Biaxial (tension/compression-torsion) fatigue tests need to be conducted with different levels of non-proportionality. By comparison of a proportional baseline configuration and non-proportional scenarios, the influence of non-proportional loads on the cycles to failure can be analyzed. In addition, the previously determined yield criterion will be used to predict the fatigue life in combination with a uniaxial rainflow count. This way, the influence of non-proportional loads can be demonstrated based on experimental results. At the same time, the impact of a tension-compression asymmetry on the fatigue life prediction can be discussed.

**5) Multiaxial Fatigue Life Prediction.** In this last step, all the acquired experimental data shall be used for a detailed comparison of the fatigue life prediction quality of state of the art methods for non-proportional fatigue. An emphasis shall be put on limitations and drawbacks of the respective methods to derive a new computationally efficient and yet accurate method.

## 1.4 Thesis concept

With the definition of the research gap and associated objectives, the cumulative concept of this thesis is summarized in this Section.

### 1.4.1 Outline

The results related to the majority of the aforementioned work packages were published open-access in peer-reviewed, high-quality journals. Since all papers were written in a consecutive manner, they are included in this thesis as its Chapters, cf. Figure 1.17.

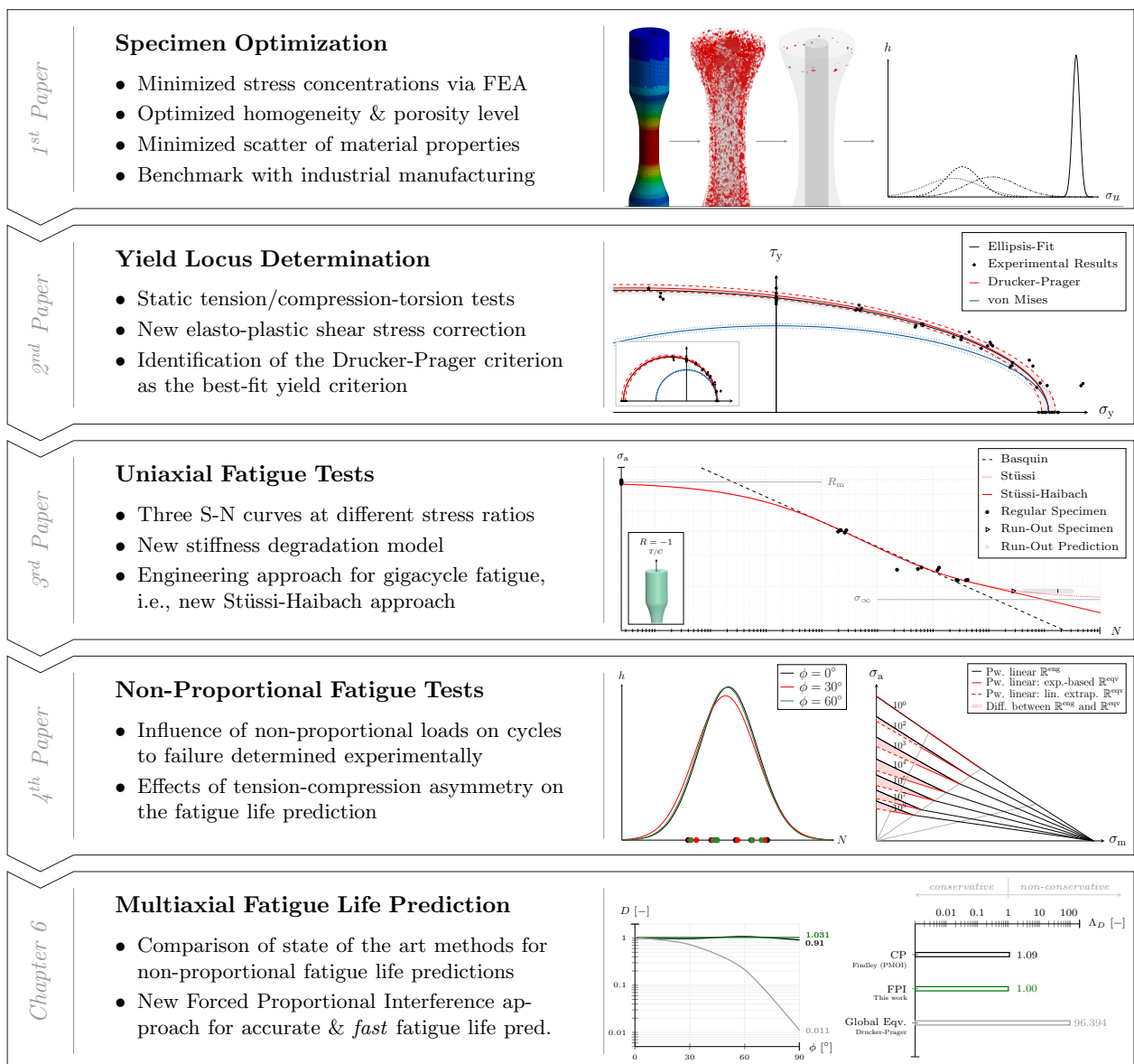
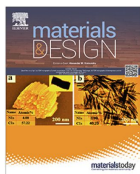


**Figure 1.17:** Cumulative thesis outline. The results of the majority of the work packages are presented in separate, but consecutive journal papers, which are included in this thesis as Chapters.

Subsequent to the presentation of the results of the work packages, the fulfillment of the overall objective is evaluated in the conclusion. New research questions that emerged on the basis of this work are summarized in an outlook.

### 1.4.2 Declaration on the included publications

The large majority of the content of the included publications was prepared by the author of this thesis. However, as with every complex research project, the support of a team is what enables its complexity. This is especially true for projects with a sophisticated experimental background like this thesis. Therefore, the author contributions to the included publications are clarified here. In addition, the contribution of the included publications to the overall objective are stated to emphasize their relevance for this thesis.



#### **Design and manufacturing optimization of epoxy-based specimens for multiaxial tests**

M. Wentingmann, N. Manousides, A. Antoniou, C. Balzani  
Materials & Design, 212:110213, 2021

#### **1<sup>st</sup> Paper**

In the first paper, the foundation for the experimental work is established via a FE-based optimization of the tubular specimen geometry. A subsequential optimization of the manufacturing process is achieved using vacuum mixing and 3D printing to assure a homogeneous and virtually pore-free mixture. These optimizations are essential to the overall objective, as a minimization of specimen-related uncertainties will maximize the possibility to identify the influence of non-proportional loads. Thus, the manufacturing quality, i.e., the level of porosity, is assessed for each specimen via  $\mu$ CT scans. In addition, the porosity level of the optimized specimens is compared to hand-mixed specimens and a sample from an industrial dosing and dispensing machine. The comparison revealed that the porosity level of the dosing machine sample is comparable to the one of the optimized specimens, which indicates that hand-mixed specimens lead to an oversimplified and too conservative estimation of the material properties. The author contributions are described in the following:

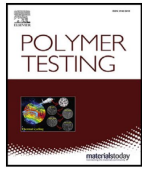
**Michael Kuhn (birth name: Wentingmann)** implemented the FE parametric study and prepared technical drawings for the manufacturing of the molds. He manufactured the specimens and associated 3D printed parts (mixing adapters and mold inserts for injection) and was responsible for the design of the printed parts. He instrumented the specimens (strain gauge rosettes) and performed the static tests. He wrote the paper and made the illustrations, which involved post-processing the  $\mu$ CT scans.

**Nikolas Manousides** applied  $\mu$ CT scanning to assess the porosity of all specimens, pre-processed the scans and provided segmented data.

**Alexandros Antoniou** supervised Michael Kuhn at Fraunhofer IWES and provided scientific advice and support with executing the experiments.

**Claudio Balzani** supervised Michael Kuhn at Leibniz University Hannover and provided conceptual guidance/scientific supervision of all project phases.

All co-authors helped to review the paper before submission and participated in the journal review process. Changes to the manuscript during these revisions were implemented by Michael Kuhn.



## 2<sup>nd</sup> Paper

### Yield surface derivation for a structural adhesive based on multiaxial experiments

M. Wentingmann, N. Manousides, A. Antoniou, C. Balzani  
Polymer Testing, 113:107648, 2022

The second paper describes the results of quasi-static uniaxial tensile, compression and torsion tests and their biaxial combinations. Based on that, the yield surface is identified using a derivative-based yield detection in combination with a new elliptical scaling approach that allows to calculate equivalent stresses and strains for biaxial load cases without an a priori defined yield criterion. In addition, an elasto-plastic approach to estimate shear stresses on account of a torsional load is developed. The Drucker-Prager criterion was found to be in very good agreement with the measurements and more conservative in shear than previously proposed criteria for the adhesive. Both the novel elasto-plastic shear stress estimation and proposed yield surface identification method are important contributions to the overall objective of this thesis, as the accuracy of the yield prediction is improved significantly. In addition, the validation of a yield criterion opens up the possibility to use it for equivalent stress-based fatigue calculations with low uncertainty concerning its applicability to multiaxial stress states. Therefore, this paper finalizes the static material characterization necessary to continue with fatigue testing and modeling. The author contributions are described in the following:

**Michael Kuhn (birth name: Wentingmann)** manufactured and instrumented the specimens (strain gauge rosettes) and performed the static tests. He developed and implemented all proposed methods, wrote the paper and made the illustrations, which involved post-processing the  $\mu$ CT scans of the specimens.

**Nikolas Manousides** applied  $\mu$ CT scanning to assess the porosity of the specimens, pre-processed the scans and provided segmented data.

**Alexandros Antoniou** supervised Michael Kuhn at Fraunhofer IWES and provided scientific advice and support with executing the experiments.

**Claudio Balzani** supervised Michael Kuhn at Leibniz University Hannover and provided conceptual guidance/scientific supervision of all project phases.

All co-authors helped to review the paper before submission and participated in the journal review process. Changes to the manuscript during these revisions were implemented by Michael Kuhn.



### 3<sup>rd</sup> Paper

#### Fatigue properties of a structural rotor blade adhesive under axial and torsional loading

M. Kuhn, N. Manousides, A. Antoniou, C. Balzani

Fatigue & Fracture of Engineering Materials & Structures,  
46:1121-1139, 2023

In the third paper, uniaxial S-N tests were performed. The data from these tests represent the basis for the calibration of CP criteria and provide the opportunity to construct a Haigh diagram to account for mean stress effects in the stress-based fatigue life prediction. Therefore, this work contributes to the overall objective of this thesis by providing the necessary data for a non-proportional fatigue analysis. Different S-N models are compared and the Stüssi model is identified as the best-fit. An engineering approach for the gigacycle fatigue regime is developed on the basis of the Stüssi S-N model and a tangential Haibach extension line, since the maximum number of cycles was limited to  $\approx 10^6$  in the experiments. As with the static tests, the results are compared to literature. It is demonstrated that the porosity content of the respective specimens exhibits a (very) significant influence on the cycles to failure, which again underlines the importance of sophisticated manufacturing techniques. A load level-dependent stiffness degradation model is proposed and used to estimate the residual fatigue life of run-out specimens. The predictions are in good agreement with the sigmoidal-shaped S-N models, e.g., Stüssi, and hence indicate their validity, as the S-N and stiffness degradation modeling is independent from each other. The author contributions are described in the following:

**Michael Kuhn** manufactured the specimens and performed several S-N tests. He developed and implemented all proposed methods, wrote the paper and made the illustrations, which involved post-processing the  $\mu$ CT scans of the specimens.

**Nikolas Manousides** applied  $\mu$ CT scanning to assess the porosity of the specimens, pre-processed the scans and provided segmented data.

**Alexandros Antoniou** supervised Michael Kuhn at Fraunhofer IWES and provided scientific advice and support with executing the experiments.

**Claudio Balzani** supervised Michael Kuhn at Leibniz University Hannover and provided conceptual guidance/scientific supervision of all project phases.

All co-authors helped to review the paper before submission and participated in the journal review process. Changes to the manuscript during these revisions were implemented by Michael Kuhn.

A large majority of the S-N tests and the programming of the biaxial testing machine was done by Martina Karalus and Henning Schnellen, who accompanied the tests as technicians at Fraunhofer IWES.





#### 4<sup>th</sup> Paper

### Effects of non-proportionality and tension-compression asymmetry on the fatigue life prediction of equivalent stress criteria

M. Kuhn, N. Manousides, A. Antoniou, C. Balzani

Fatigue & Fracture of Engineering Materials & Structures, 46:3161-3178, 2023

The fourth paper establishes experimental evidence of the influence of non-proportional loads on the cycles to failure of the investigated adhesive. Therein, the level of non-proportionality is found not to alter the cycles to failure of the adhesive. A state of the art fatigue life prediction using rainflow-counted equivalent stress histories is confirmed to yield good results for the proportional baseline configuration of the experiments. However, an increased level of non-proportionality leads to substantially non-conservative predictions using this method. Since this kind of fatigue life prediction methodology is applied in a variety of, e.g., wind energy-related publications, this work demonstrates the importance of a correct modeling of non-proportional loads in fatigue analyses and is hence directly contributing to the overall objective of this thesis. In addition, the influence of a tension-compression asymmetry on the fatigue life prediction is analyzed. It is found that the stress space representation of the Haigh diagram must be adapted to the equivalent stress space to avoid non-conservative predictions when asymmetric yield criteria such as the Drucker-Prager criterion (validated for the adhesive in the 2<sup>nd</sup> Paper) are used. Since this stress space adaption leads to different equivalent stress ratios, the asymmetric Haigh diagram in the engineering stress space is transformed into a symmetric one in the equivalent stress space, which might lead to gaps in the Haigh diagram. A hybrid formulation of the Drucker-Prager criterion is proposed to alleviate this problem, so that the asymmetrical Drucker-Prager yield criterion can be used with a Haigh diagram in the engineering stress space again. The author contributions are described in the following:

**Michael Kuhn** manufactured the specimens and performed several biaxial S-N tests. He developed and implemented all proposed methods, wrote the paper and made the illustrations, which involved post-processing the  $\mu$ CT scans of the specimens.

**Nikolas Manousides** applied  $\mu$ CT scanning to assess the porosity of the specimens, pre-processed the scans and provided segmented data.

**Alexandros Antoniou** supervised Michael Kuhn at Fraunhofer IWES and provided scientific advice and support with executing the experiments.

**Claudio Balzani** supervised Michael Kuhn at Leibniz University Hannover and provided conceptual guidance/scientific supervision of all project phases.

All co-authors helped to review the paper before submission and participated in the journal review process. Changes to the manuscript during these revisions were implemented by Michael Kuhn.

A majority of the biaxial S-N tests and the programming of the biaxial testing machine was done by Martina Karalus and Henning Schnellen, who accompanied the tests as technicians at Fraunhofer IWES.





# Design and manufacturing optimization of epoxy-based adhesive specimens for multiaxial tests

1<sup>st</sup> Paper

With the overall objective to reliably identify influences of non-proportional loads, a precise material characterization is required to be able to separate non-proportional effects from others. A defect-free adhesive specimen suitable for multiaxial tests is hence essential. However, this has not been achieved so far since two-component and highly viscous fiber-reinforced adhesives demand a perfectly tuned manufacturing process to avoid mixing inhomogeneities and pores. In addition, the orientation of the reinforcement fibers needs to be the same for every specimen.

---

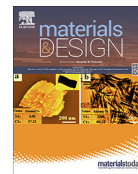
P1-1	Introduction .....	29
P1-2	Specimen design optimization .....	29
P1-3	Manufacturing optimization .....	32
P1-4	Quality assurance .....	35
P1-5	Uniaxial and biaxial static tests ....	36
P1-6	Porosity analysis of industrial dosing machines .....	38
P1-7	Conclusion .....	40





Contents lists available at ScienceDirect

## Materials &amp; Design

journal homepage: [www.elsevier.com/locate/matdes](http://www.elsevier.com/locate/matdes)

## Design and manufacturing optimization of epoxy-based adhesive specimens for multiaxial tests



Michael Wentingmann<sup>a,\*</sup>, Nikolas Manousides<sup>a</sup>, Alexandros Antoniou<sup>b</sup>, Claudio Balzani<sup>a</sup>

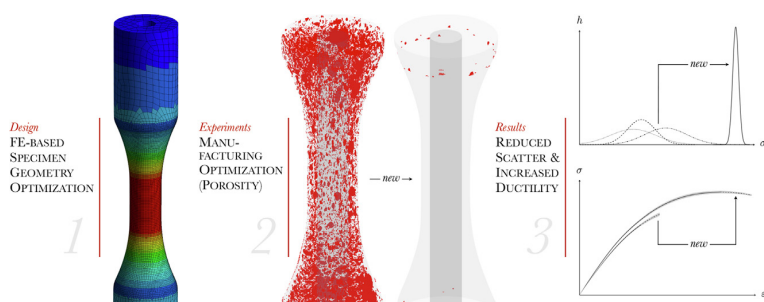
<sup>a</sup> Leibniz University Hannover, Institute for Wind Energy Systems, Appelstrasse 9A, 30167 Hannover, Germany

<sup>b</sup> Fraunhofer Institute for Wind Energy Systems IWES, Am Seedeich 45, 27572 Bremerhaven, Germany

### HIGHLIGHTS

- Finite Element based specimen geometry optimization resulted in smooth stress distributions and reduced measurement uncertainties of material properties.
- Combining vacuum speed mixing and 3D printed mold inserts led to low porosity specimens, which was verified with  $\mu$ CT scanning.
- Machine-mixed specimens showed ductile behavior while hand-mixed specimens were rather brittle.
- Applied optimizations significantly reduced scatter in all measured material properties and increased strength and strain to failure.

### GRAPHICAL ABSTRACT



### ARTICLE INFO

#### Article history:

Received 23 July 2021  
 Revised 11 October 2021  
 Accepted 31 October 2021  
 Available online 02 November 2021

#### Keywords:

Structural adhesives  
 Multiaxial testing  
 Porosity analysis  
 Wind turbine rotor blades

### ABSTRACT

Specimen design and manufacturing quality are decisive factors in the experimental determination of material properties, because they can only be reliably determined if all undesired influences have been minimized or are precisely known. The manufacture of specimens from highly viscous, two-component and fiber-reinforced structural adhesives presents a challenge from this point of view. Therefore, a design and manufacturing optimization procedure for fiber-reinforced structural adhesives and multiaxial testing was developed. It incorporated a finite element parametric study to minimize stress concentrations in the specimen geometry. Vacuum speed mixing was combined with 3D printed mold inserts to enable the manufacture of homogeneous specimens with negligible porosity. The method was demonstrated by means of a structural adhesive used to manufacture wind turbine rotor blades, while the manufacturing quality was verified with high-resolution X-ray microscopy ( $\mu$ CT scanning), enabling detailed detection of pores and geometrical imperfections. The results of uniaxial and biaxial static tests show maximized strength and stiffness properties, while the scatter was minimized in comparison to that stated in international literature. A comparison of the mechanical properties and associated manufacturing techniques is given. The comparison includes a porosity analysis of a specimen from an industrial dosing machine used for rotor blade manufacture.

© 2021 The Author(s). Published by Elsevier Ltd. This is an open access article under the CC BY license (<http://creativecommons.org/licenses/by/4.0/>).

\* Corresponding author.

E-mail address: [research@iwes.uni-hannover.de](mailto:research@iwes.uni-hannover.de) (M. Wentingmann).

## 1. Introduction

Complex multiaxial loads arise in a variety of engineering disciplines, most of which use structural adhesives in joining processes. To ensure the safe operation of these systems, it is therefore necessary to evaluate the performance of structural adhesives in multiaxial load scenarios.

### 1.1. Bond lines in wind turbine rotor blades

Among the fields of application of structural adhesives, the wind energy industry in particular is confronted with big challenges in the manufacture of rotor blades. In the manufacturing process of a typical rotor blade, the aerodynamic shells and shear webs are manufactured separately and adhesively joined. Owing to economic constraints and the size of the separate parts, the adhesive also serves as a compensation for manufacturing tolerances. Hence bond lines with a thickness of 10 to 15 mm are usual, depending on the radial and chordwise position [7,19,24,29].

In addition, rotor blades of wind turbines have to withstand high multiaxial loads within their expected lifetime of 20 years. The multiaxiality results from the stochastic wind load in the flapwise direction, which is superimposed with gravitational edgewise loads caused by the rotation of the rotor.

To take account of these loads and manufacturing conditions, adhesives have been developed especially to meet the requirements of the wind energy industry. These adhesives are usually two-component, epoxy-based adhesives with high viscosity. Some are short fiber-reinforced to improve the material properties, e.g., the fatigue performance and cohesive strength [13].

As large quantities need to be applied in a short period of time, the mixing and application process is performed using dosing and dispensing machines [29]. Subsequent to the adhesive application, the shear webs are installed with special positioning equipment and the aerodynamic shells are joined using hinged mold setups, for example. Previously applied surplus adhesive is pushed inward and outward of the targeted bonding location in these production steps.

### 1.2. State of the art specimen manufacture

In recent publications dealing with rotor blade adhesives, the mixing process used in the specimen manufacture has been simplified and done manually [24,25,35]. This leads to inhomogeneous mixing results and higher levels of porosity, which in turn diminish the mechanical properties of the cured adhesive.

This trend may be amplified during the mold injection process as the injection speed, injection position, mold geometry, vents, etc., can all contribute to the formation of air traps and therefore might increase the levels of porosity and the inhomogeneities. In [11], the presence of voids was attributed to manual pouring and casting, as voids also occurred in specimens, which were mixed in degassed conditions. The specimens in [9] also exhibited high levels of porosity, however, the manufacturing methods used for mixing and mold injection are not clearly specified, therefore hand-mixing seems likely.

This gives rise to the question of how the properties derived from these simplified specimens represent the industrial mixing quality of rotor blade manufacturing and also the associated mechanical properties. This is especially important for multiaxial bulk adhesive specimens, which are particularly challenging to manufacture. However, due to the multiaxiality of the loads of a rotor blade, cf. Section 1.1, multiaxial bulk specimens are required to analyze the cohesive properties in complex loading conditions.

### 1.3. Aims and outline

To identify material properties unaffected by porosities or inhomogeneities, this work focuses on the geometry and manufacturing optimization of specimens suitable for multiaxial tests. While the motivation for this work is based on wind energy applications, the developed methodology and results have multidisciplinary applicability.

Section 2 summarizes the finite element-based geometry optimization of the specimen. In Section 3, the manufacturing optimization steps are explained. The resulting specimen quality is discussed in Section 4, and the results of the uniaxial and biaxial static experiments are shown and compared to international literature in Section 5. In Section 6, the specimen quality in this work is compared to a specimen from an industrial dosing and dispensing machine used for rotor blade manufacture. The transferability of the laboratory material characterization to the rotorblade manufacturing process is discussed.

## 2. Specimen design optimization

Several specimen geometries and test configurations are available in the literature for multiaxial tests, e.g., plates [12,26], cruciform types [8,16,27], and tubes [9,30,35]. In general, tubular specimens are described as being most versatile, mainly because multiaxial loads can be applied via arbitrary combinations of normal forces and torsion. The load state can also be proportional or non-proportional depending on the phase shift of the normal and torsional loads. In addition, tubular specimens do not require special load frames, demonstrating enhanced compatibility with testing machinery.

Owing to the aforementioned reasons, the specimen design in this work was chosen to be tubular.

### 2.1. Optimization objectives

To reliably determine material properties, the following objectives should be met:

1. minimize stress concentrations and maximize the probability of failure within the test section (i.e. sufficient tapering required)
2. approximately constant shear stress in the cross section of the test section (i.e. limitation of the maximum wall thickness)
3. the clamping area must withstand the clamping loads (i.e. limitation of the maximum inner radius)
4. the resulting test loads must be reasonable for the testing machine chosen in both static and fatigue operation to avoid control issues at low load levels (i.e. limitations of the inner radius and the minimum wall thickness)
5. the specimen must not buckle (i.e. limitations of specimen height and wall thickness)

The first objective can be met in a finite element parametric study comparing the maximum equivalent stress in the tapered and clamping section  $\sigma_{outer}$  with that of the test section  $\sigma_{test}$ , leading to the definition of a stress ratio  $\alpha$  given by

$$\alpha = \frac{\sigma_{outer}}{\sigma_{test}}. \quad (1)$$

The stress ratio needs to be smaller than 1.

Objectives 2–4 can be fulfilled by setting proper boundary conditions. Objective 5 can only be realized by means of a linear buckling analysis, since a non-linear analysis requires too much computational time for several thousand design variations (design points). Fig. 1 visualizes the design parameters used for this study.

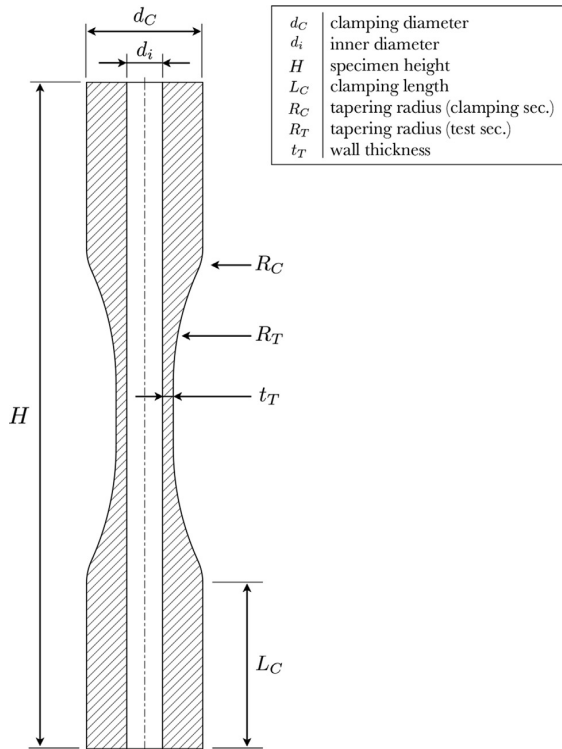


Fig. 1. Specimen design parameters for the finite element parametric study.

## 2.2. Boundary conditions

The clamping diameter  $d_C$  and clamping length  $L_C$  are specified by the testing machine. For this study, a servohydraulic Walter + Bai LFV 100-T2000 with cylindrical specimen grips was used. The machine has independent control circuits for axial and torsional loads and can therefore be used for multiaxial testing [34]. The cylindrical grips set the clamping diameter of the specimen to  $d_C = 30$  mm and the clamping length to  $L_C = 43$  mm.

The minimum wall thickness  $t_T$  was chosen to be 2 mm to ensure that the specimen would not be damaged in the demolding process and to meet objective 4. The maximum wall thickness was limited to 3 mm to account for optimization objective 2.

The maximum inner radius was set to  $r_{i,max} = 6.5$  mm to meet objective 3 with a sufficient safety factor and to allow for a wide range of  $R_T$  and  $R_C$ .

The overall height of the specimen  $H$  was restricted to 185 mm, because at this height the maximum capacity of the vacuum mixer is reached for all parameter combinations, see Section 3.1.

The test section height was fixed to a minimum of 16.5 mm in order to facilitate the application of strain gauges or other kinds of instrumentation.

Parameter combinations which violated any of the aforementioned boundary conditions were discarded. This limited the maximum values for  $R_C$  and  $R_T$  in order to keep to the specified minimum height of the test and clamping section.

## 2.3. Adhesive system

For the experimental campaign, the EPIKOTE™ Resin MGS™ BPR 135G3 adhesive system was used in combination with the EPIKURE™ Curing Agent MGS™ BPH 137G. The solvent free system is

epoxy-based, glass fiber-reinforced and very common in the wind energy industry. The adhesive shows shear thinning behavior for all available hardeners [13]. More detailed information on the resin/hardener combinations and related shear thinning, glass transition and mechanical behavior can be found in the technical data sheet of the adhesive [13].

The dimensions of the reinforcement fibers are not published. The fiber volume content was estimated at approximately 8–12 % by means of a preliminary  $\mu$ CT-analysis, but further verification is necessary.

## 2.4. Finite element modelling

The finite element parametric study was set up in Ansys® Mechanical [2] in combination with a parameterized geometry model in Ansys® SpaceClaim [3]. The parameterized geometries were meshed using solid elements with quadratic shape functions (SOLID186 and 187). The element length outside the test and tapering section was chosen to be 3.5 mm. Inside the tapering and test section the element length was reduced to 0.75 mm, resulting in roughly 250,000 nodes on average for the entire mesh. All design points were evaluated assuming isotropic linear elasticity in separate setups for tension, torsion, compression, and linear buckling.

The stiffness properties were adapted from [35]. The global failure criteria of Stassi-D'Alia [28] and Beltrami [4] were employed as both criteria have been used to evaluate rotor blade adhesives elsewhere [9,23,35,36]. In contrast to the maximum distortion criterion formulated by von Mises (Eq. 2 below, which predicts deviatoric failure), the Beltrami criterion (Eq. 3 below) also includes hydrostatic and therefore volumetric failure. This is considered to be valid for polymers in general [5,20] and also for reinforced polymers [14]. In Eqs. 2 and 3,  $\sigma_1, \sigma_2, \sigma_3$  denote the principal stresses, while  $\nu$  is the Poisson ratio. For incompressible materials with a Poisson ratio of 0.5 the Beltrami criterion converges to the von Mises criterion.

$$\sigma_{vM} = \sqrt{\frac{(\sigma_1 - \sigma_2)^2 + (\sigma_2 - \sigma_3)^2 + (\sigma_3 - \sigma_1)^2}{2}} \quad (2)$$

$$\sigma_B = \sqrt{\sigma_1^2 + \sigma_2^2 + \sigma_3^2 - 2\nu(\sigma_1\sigma_2 + \sigma_1\sigma_3 + \sigma_2\sigma_3)} \quad (3)$$

The Stassi-D'Alia criterion is suitable for adhesives since it takes into account the asymmetry of the static strengths in tension and compression. This is expressed by the factor  $\kappa$ , which is the ratio between the compressive and tensile strength, see Eq. 4.

$$\sigma_S = \frac{(\kappa - 1)I_1 + \sqrt{(\kappa - 1)^2 I_1^2 + 4\kappa \sigma_{vM}^2}}{2\kappa} \quad (4)$$

In Eq. 4,  $I_1$  denotes the first invariant of the stress tensor, and  $\sigma_{vM}$  the equivalent stress according to Eq. 2. When the tensile and compressive strengths are equal,  $\kappa$  is equal to 1 and Eq. 4 becomes Eq. 2. Therefore  $\sigma_{vM}$  can be seen as a special case of  $\sigma_S$ . Using the data published in [35] results in a strength ratio factor of  $\kappa = 2.03$ .

## 2.5. Sensitivity study

A sensitivity study was conducted to limit the design space. The design space of this study is shown in Table 1. A total of 2631 design points were evaluated, which is fewer than the combinatorics of all parameters predict, because not all parameter combinations result in valid geometry models in compliance with the boundary conditions specified in Section 2.2.

Although the wall thickness and the inner radius showed no clear trend regarding the stress ratio  $\alpha$ , the tapering radius  $R_T$

**Table 1**  
Design space for the sensitivity study of the finite element parametric study (2631 evaluable design points in total).

Parameter	min [mm]	incr [mm]	max [mm]
$H$	–	–	185
$t_T$	2	0.1	3
$r_i$	4	0.1	6.5
$R_T$	38	12	110
$R_C$	20	4	36

**Table 2**  
Design space for the final evaluation of the finite element parametric study (1430 evaluable design points in total).

Parameter	min [mm]	incr [mm]	max [mm]
$H$	165	5	185
$t_T$	2	0.1	3
$r_i$	4	0.1	6.5
$R_T$		max. possible value	
$R_C$		max. possible value	

showed distinct dependencies. With increasing  $R_T$  a significant decrease in  $\alpha$  was observed, which was within expectations. On the other hand,  $R_C$  had no systematic influences on the stress ratio, see Fig. 2.

Nevertheless,  $R_C$  is still important when it comes to the mold injection process, where a smooth transition from test to clamping section helps to prevent the formation of air traps, see Section 3.2. Therefore,  $R_T$  and  $R_C$  were limited to their respective maxima, which depend on the other variables  $r_i$ ,  $t$ , and  $H$ . Since a large specimen height  $H$  allows for larger values of  $R_T$  and  $R_C$ , the minimum height was set to 165 mm. The design space for the final evaluation is shown in Table 2.

## 2.6. Results

The final design and the resulting stress ratios are shown in Table 3. The ratios are just below or equal to the threshold of 1 for each equivalent stress criterion mentioned in Section 2.4.

To be able to compare the final configuration with previously published tubular geometries, those used in [9,35] were analyzed in the same way as the design points of this study. The comparison revealed that both of these specimens show significant stress concentrations at the end of the tapered section. For this comparison, the transition between tapering and test section was smoothed with a radius of 4 mm in both cases, which is big enough to avoid numerical singularities and still small enough to be an accurate geometry approximation.

The predictions of  $\alpha$  show different trends for the compression load case. While the Beltrami criterion predicted  $\alpha > 1$  for the geometries of [9,35] and therefore failure outside the test section, the Stassi-D'Alia criterion predicted failure within the test section ( $\alpha < 1$ ). This difference originates from the fact that only the latter accounts for the asymmetry of tensile and compressive strengths. Hence, for this linear elastic study, the results of the Beltrami criterion for tension and compression are the same.

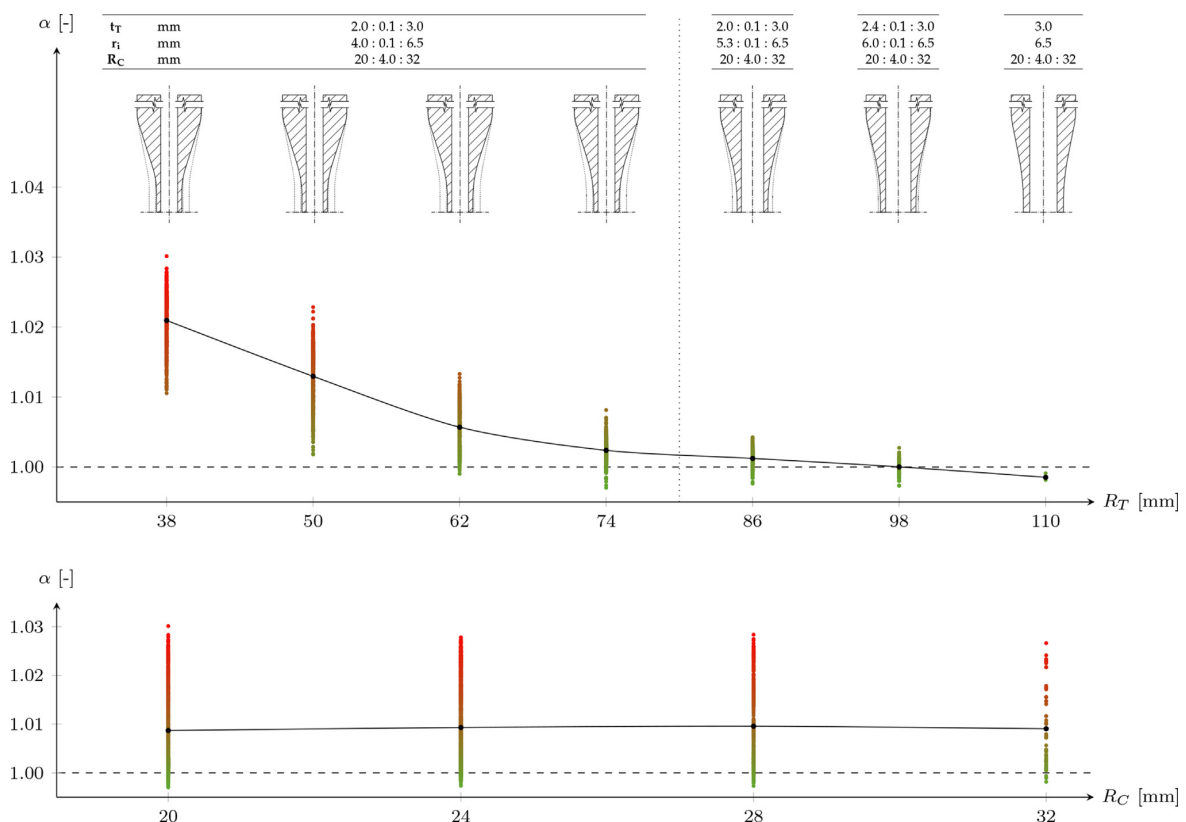


**Fig. 2.** Results of the sensitivity study for the tensile load case. Stress ratio  $\alpha$  versus the tapering radii  $R_T$  and  $R_C$ . While  $\alpha$  decreases for increasing test section tapering radii  $R_T$ , the tapering radius towards the clamping section  $R_C$  shows no distinct trend. The parameter ranges of  $t_T$ ,  $r_i$  and  $R_C$  are shown at the top with corresponding visualizations of the specimen geometry. The parameter ranges are indicated as minimum: increment: maximum.

**Table 3**

Comparison of the stress ratio  $\alpha$ , linear buckling load factor in compression  $\lambda$ , and geometry parameters of the final configuration in this work with previously published multiaxial adhesive specimen designs. The stress distribution for the tensile load case is shown as an example with regions of high stress in red and low stress in blue. \* Documented as 0 mm, but set to 4 mm in order to avoid numerical singularities.

Parameter			Zarouchas et al. [35]	Fernandez et al. [9]	This Work
$\alpha$	Tension	Beltrami	1.1189	1.0496	0.9880
		Stassi-D'Alia	1.2336	1.1155	0.9961
	Compression	Beltrami	1.1189	1.0496	0.9880
		Stassi-D'Alia	0.9696	0.9636	0.9776
	Torsion	Beltrami	1.0706	1.0433	0.9996
		Stassi-D'Alia	1.0707	1.0432	0.9995
$\lambda$	lin. buckling load factor (compr.)	–	8.5375	10.5420	8.8439
Geometry	$H$	mm	120.0	160.0	175.0
	$t_T$	mm	2.5	3.0	2.8
	$r_i$	mm	12.5	7.5	4.7
	$R_T$	mm	*4.0	*4.0	72.0
	$R_C$	mm	*4.0	*4.0	14.0

Considering the linear buckling load factors in compression, the geometries used in [35] and this work are approximately equal at  $\lambda = 8.54$  and  $\lambda = 8.84$ , respectively. The geometry used in [9] achieves  $\lambda = 10.54$ , which is related to a 60 mm distance between the clamping sections instead of 100 mm in the case of [35], and 89 mm in the case of the specimen proposed in this work.

The material properties derived from the optimized specimen in this study should be more reliable, considering that the stress concentrations and measurement uncertainties associated with it were successfully minimized. In terms of buckling, the specimen is expected to act in a comparable way to the specimen in [9,35].

### 3. Manufacturing optimization

The specimen geometry will only have a significant impact on the experimental campaign if the manufacturing quality is sufficiently high, since local imperfections such as pores also introduce stress concentrations. Therefore, a detailed examination of the manufacturing options and their optimization potential was carried out.

#### 3.1. Optimal mixing quality

To obtain a homogeneous, pore-free mixture, a planetary centrifugal vacuum mixer [32] was used. The operating principle of such a mixer is shown in Fig. 3. The resin and hardener are placed in a mixing container, which spins in an inclined position while at the same time rotating in the normal plane. This generates a whirling motion and mixes the resin with the hardener uniformly within a few minutes.

As the standard mixing containers do not have an outlet suitable for cartridge guns or pumps, the container was replaced with

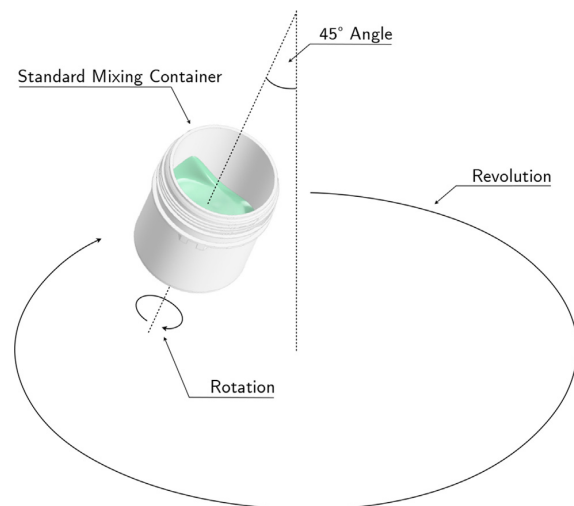


**Fig. 3.** Mixing procedure of a planetary centrifugal vacuum mixer. The mixture is rotated at an angle, while the container is forced into a revolution in the normal plane.

a dosing cartridge. The cartridge chosen was smooth on the inside, so that no stiffeners or other internal structures could disturb the mixing process [22]. It also had a large inner diameter, so that it could be used to mix reasonable amounts of adhesive with good mixing aspect ratios. The mixing aspect ratio is defined as the infill height of the material ( $H_{material}$ ) divided by the diameter of the mixing container ( $D_{container}$ ), Eq. 5.



$$\Lambda_{\text{mix}} = \frac{H_{\text{material}}}{D_{\text{container}}} \quad (5)$$

Incorporating tolerances of the resin and hardener densities and the inner cartridge diameter, the resulting aspect ratio for this study is about  $\Lambda_{\text{mix}} = 0.7$ , which is the upper limit of the recommended range of 0.2 to 0.7. To make the cartridge compatible with the container mount of the mixer, a 3D printed adapter was developed.

To find the optimal mixing parameters, the same mass of adhesive was mixed with nine different mixing parameter settings. The surface temperature was measured with an infrared thermometer (accuracy:  $\pm 1.5$  °C, resolution:  $-30$  to  $500$  °C) directly after the mixing process. The mixtures were cured at room temperature and cut along their longitudinal axis. The cured parts were photographed and the mixing quality was evaluated by analyzing the respective rgb-color histograms. Supplementary to the histograms, the multivariate coefficient of variation of the rgb-colors and the number of unique rgb-colors ( $C_{\text{unique}}$ ) were interpreted as a metric of homogeneity. The multivariate coefficient of variation was calculated according to [1], Eq. 6.

$$C_V = \sqrt{\frac{\mu^T \Sigma \mu}{(\mu^T \mu)^2}} \quad (6)$$

Therein  $\mu$  is the vector of the corresponding mean values and  $\Sigma$  is the covariance matrix.

A mixing time of 3 min in combination with a revolution speed of 1500 rpm led to a very homogenous mixture, which was pore-free and reliably reproducible. The surface temperature increased to 40 °C, which is 10 °C more than the recommended conditions stated in the adhesive data sheet [13], but since this rather mild temperature increase only affects the pot life, this was accepted in order to reduce the viscosity, which is expected to help with the mold injection process. Fig. 4 shows an exemplary excerpt of the mixing parameter analysis including the configuration chosen.

### 3.2. Mold design and injection process

The design of injection molds is an important factor for the overall quality of the specimen, as it impacts the probability that air traps will be created. Two major issues for this study were identified:

1. The tubular specimen design in combination with the chemical shrinkage of the adhesive requires the option to pull or push out the center rod after the curing process.
2. Owing to the high viscosity of the adhesive, it is not possible to pour it into the mold. Instead, it needs to be injected in a continuous motion.

To solve the injection problem, two possible solutions were considered, which are shown in Fig. 5. The first option is to use the center rod itself for the injection. This has the advantage that the flow front is likely to be homogeneous. On the other hand, the center rod cannot be supported at the bottom, so the wall thickness has to be large enough to maintain sufficient stiffness in order to hold the centered position during the injection process. A small inner diameter of the rod combined with large lengths and a high viscosity of the adhesive will lead to very high friction. The hollow rod is also difficult to clean, so that a disposable hose is required inside it, further decreasing the injection diameter and increasing the friction inside the rod.

The second option is to inject from the side, which solves the friction problem. This also allows the rod to be supported at the bottom of the mold, ensuring that it stays centered. It also makes it feasible to push the rod out rather than being limited to pulling it out. However, this option will make injection more difficult, because the adhesive will be pushed against the rod, pile up and leave voids at the opposite side.

In order to decide on one of the injection options, both were tested with 3D printed mold setups. As the overall friction of the rod injection option was too high to be overcome by available technical options, the main focus was shifted to disposable, 3D printed mold inserts to homogenize the flow front of the side injection option.

Three different insert design concepts were tested in several iterations. Table 4 shows the different insert designs and the resulting flow fronts of the last design iterations for different time steps. The overall last design iteration (No. 8) led to the formation of a very homogeneous flow front, ensuring the same mixing quality inside the mold as in the cartridge after the mixing process. The homogeneity of the flow front is expected to provide a homogeneous distribution and orientation of the reinforcement fibers of the adhesive. It should be noted that the insert design is directly related to the injection speed due to the shear thinning behavior of the adhesive.

To vent the cartridge in parallel to the injection process, the cartridge piston was perforated, and equipped with a semipermeable

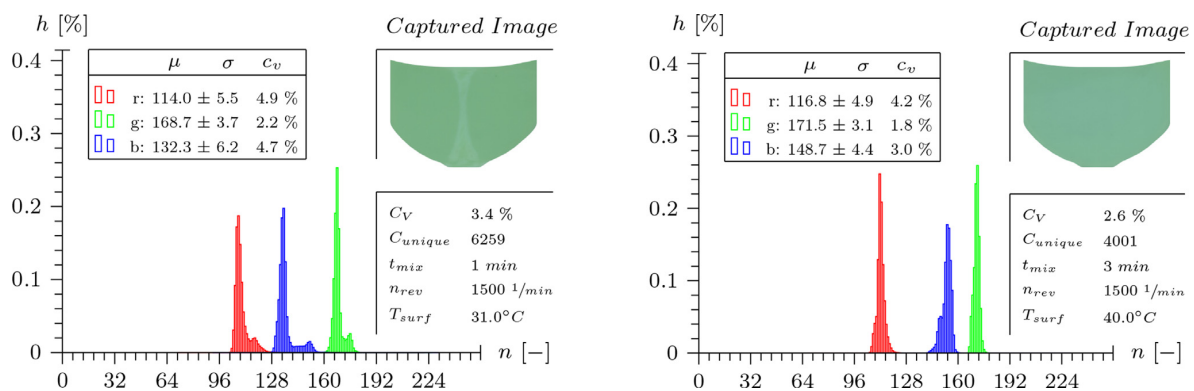


**Fig. 4.** Result excerpt of the experiments to find the optimal mixing parameters. On the left, the mixing time was too short, leading to an inhomogeneous mixture visualized by brighter colors in the middle of the cured part, as a result of the centrifugal mixing procedure. The final configuration is shown on the right. The rgb-color histograms were analyzed in terms of mean value  $\mu$ , standard deviation  $\sigma$ , coefficient of variation  $c_v$ , multivariate coefficient of variation  $C_V$  and unique number of colors  $C_{\text{unique}}$ . Mixing parameters: mixing time  $t_{\text{mix}}$ , revolutions per minute  $n_{\text{rev}}$  and surface temperature  $T_{\text{surf}}$ .

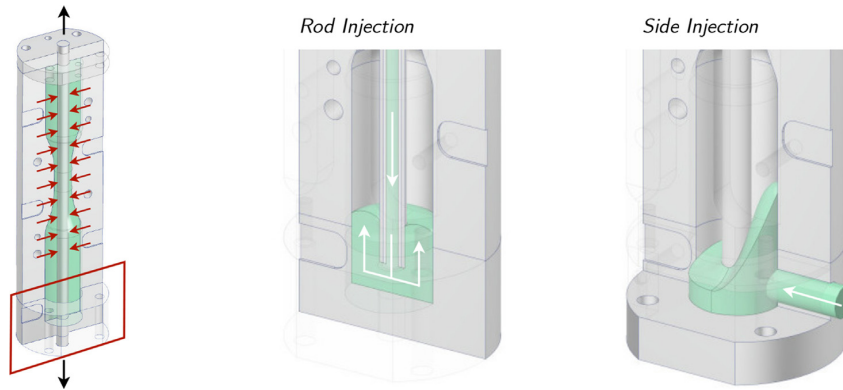


**Fig. 5.** Injection Options. Rod injection leads to very high friction, but the flow front is likely to be homogeneous. The side injection option introduces less friction, but the adhesive will pile up at the center rod. For both options, the center rod must be pushed or pulled out because of the chemical shrinkage of the adhesive.

**Table 4**

Mold inserts (3D printed) to homogenize the flow front of the side injection. The upper section shows the different design strategies, while the lower section depicts video snapshots of the injection process at different relative injection times. Insert 8 was chosen as the final design, as it led to a homogeneous flow front which could be reliably reproduced.

3D printed Test Mold	Flow	Design	Insert
	Unidirectional 	Static (PLA) 	1.  → 2.  → 3.
		Kinematic (TPU) 	4.  → 5.  → 6.
	Bidirectional 	Static (PLA) 	7.  → 8.

Final Design Iteration	Relative Injection Time				
	0 %	25 %	50 %	75 %	100 %
3.					
6.					
Chosen Design 8.					

membrane and a 3D printed adapter for an electric cartridge gun to ensure that the piston would not tilt, see Fig. 6. For the cartridge to mold connection, a straight 3D printed nozzle was used to prevent a bent hose causing the formation of air traps.

The final mold design is shown in Fig. 7. The bottom lid needed to be split to be able to demold the specimen including the injection nozzle. The vent was positioned below the top lid and made of four 3D printed polycarbonate parts, which were able to with-

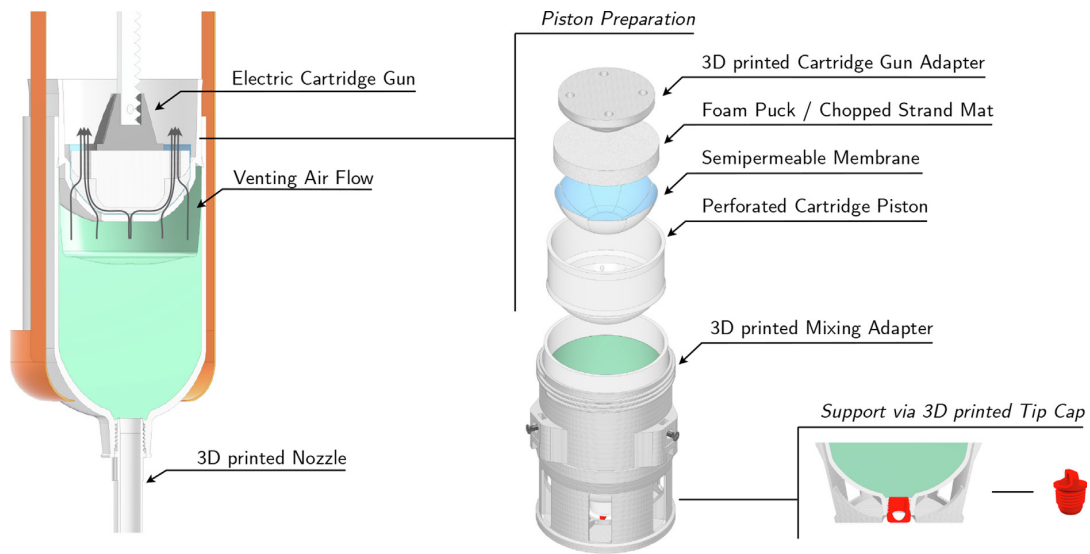


Fig. 6. Cartridge piston preparation to generate a venting airflow in order to prevent the transfer of voids into the mold.

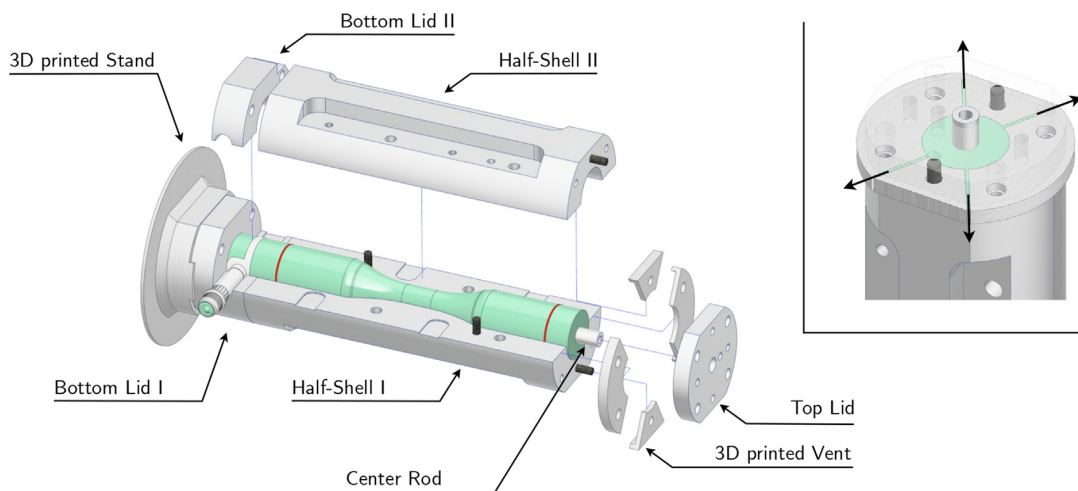


Fig. 7. Final mold configuration. The mold is filled in an upright position. Venting channels are provided by 3D printed parts. The center rod is pressed out of the closed mold with a hydraulic press. The cured specimens are cut at the indicated red lines after demolding.

stand the temperatures present in the tempering process. Similar to the bottom lid, the vent was split to ensure easy demolding, cleaning and reuse.

The upper and lower sections of the mold were extended to be able to cut the areas close to the injection and venting points, so that the final specimen would not be affected by race tracking effects due to a changing flow front in these areas.

#### 4. Quality assurance

To limit unknown influences on the material properties, the manufacturing was documented in detail and examined using high-resolution X-ray microscopy ( $\mu$ CT scanning). It is thus more likely that the scatter of the material properties can be linked to the material itself, rather than being interpreted as the effects of defects.

#### 4.1. Manufacturing performance

In respect of the mixing quality, see Section 3.1, it was possible to precisely adjust the mixing ratio of resin and hardener. The resin and hardener were weighed with a linearity of 50 mg [15], leading to an average mixing ratio (by weight) of 100: 44.99  $\pm$  0.04. Therefore, it is expected that the mixing ratio is eliminated as a source of uncertainty.

The tempering process was carried out with a programmable oven [18] and controlled with separate temperature sensors inside the molds. Fig. 8 shows the temperature profile of the first specimen production batch (nine specimens). At first, the oven stayed unheated for 6 h to slowly initiate the curing process. The profile defined in the data sheet [13] was set subsequently, and consisted of a 1 °C/min heat-up, 4 h at 75 °C and a 1 °C/min cool-down. The time delay of the adhesive temperature in relation to the oven tem-

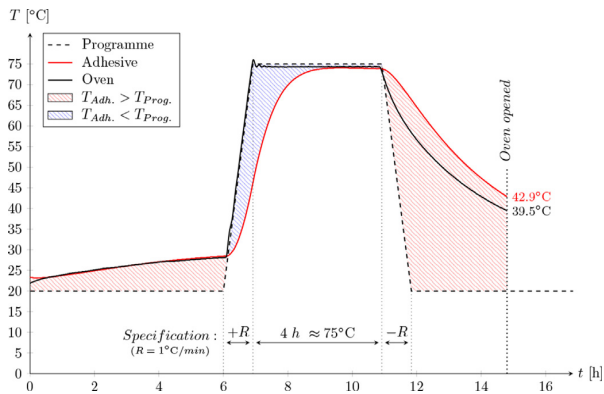


Fig. 8. Exemplary tempering profile for the specimen manufactured. Production batch 1 of 24.

perature led to the adhesive spending less time within the peak temperature regime, but since the oven was not actively cooled there was additional heat flow before the heat-up (exothermal) and during the cool-down (residual heat). The average oven temperature on opening was 34.4 °C.

Humidity and ambient temperature in the accredited laboratory were kept at  $50 \pm 10\%$  and  $23 \pm 2$  °C at all times. Influences of varying humidity or ambient temperature on the material properties during storage, manufacture or testing are therefore expected to be negligible.

#### 4.2. High-resolution X-ray evaluation

To check the porosity and geometrical imperfections of the specimens a Zeiss Xradia 410 Versa high-resolution X-ray microscope [6] was used. The scans were limited to the tapered and test section of the specimens to save time, since low levels of porosity in the clamping sections will most likely not affect the specimen performance. Avizo software [31] was used to export convex hull point clouds of the specimens' contour, the center rod and the pores. The post-processing was done in Matlab [17].

In most cases, small pore clusters were found at the end of the upper tapered section, which were generated by slight cross sectional injection speed differences and resulting race tracking effects. At the lower end of the specimens, small pores were detected, that are considered to be the result of race tracking effects within the cartridge at the end of the injection process. However, in both cases the pores were so small that it is very unlikely they have an effect on the material properties measured in the test section.

To verify the impact of the optimizations presented in this paper, three hand-mixed specimens were made in addition to the optimized ones. Table 5 shows the post processed scans of ten optimized specimens and the hand-mixed specimens. While the porosity of the optimized specimens is negligible, the hand-mixed specimens clearly show severe porosity.

The minimal cross sectional areas were extracted from the scan data, further increasing the determination accuracy of the engineering material properties.

## 5. Uniaxial and biaxial static tests

Uniaxial and biaxial static tests were performed to assess the impact of the optimizations on the material properties of the adhesive.

#### 5.1. Instrumentation

Two strain gauge rosettes were applied to every specimen in diametrically opposite positions to be able to detect and compensate load imbalances. The strain gauges chosen had a low stiffness and self-temperature compensation suitable for epoxy resins [33].

The servohydraulic testing machine [34] used in this study was equipped with a load cell calibrated for class 0.5 to ensure good data quality.

#### 5.2. Uniaxial tests

The tensile tests were performed using the optimized and hand-mixed specimens shown in Table 5. A displacement rate of 1 mm/min was used for both specimen types. Fig. 9 shows the estimated

Table 5

Qualitative porosity comparison of the machine-mixed and hand-mixed specimens from this study. Pores are shown in red. While the machine-mixed specimens have negligible overall porosity and none at all in the test section, hand-mixing results in high levels of porosity throughout the specimens. The specimen numbers are given below the respective depictions.

Optimized (Machine-Mixed) Specimens					Hand-Mixed Specimens		
024	041	048	067	073	204	205	206
075	124	132	144	150			

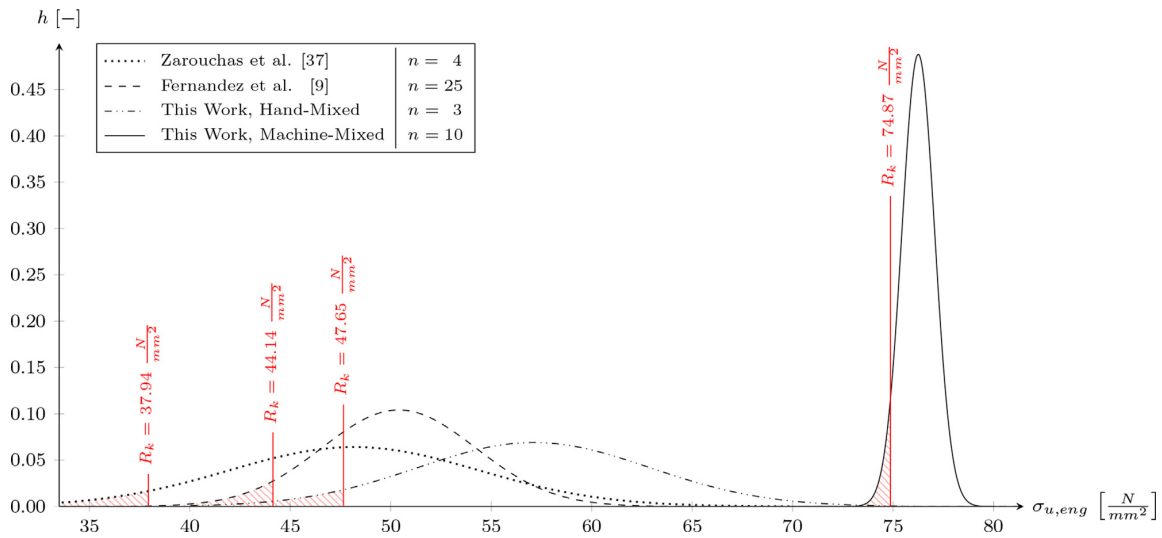


**Fig. 9.** Estimated frequency distributions of the ultimate engineering tensile strength of Zarouchas et al. [37], Fernandez et al. [9] and this work. Red lines indicate the characteristic strength calculated as the 5th percentile of the frequency distributions,  $n$  is the number of specimens.  $\sigma_u$  corresponds to  $\sigma_f$  for all hand-mixed specimens due to brittle behavior (high level of porosity).

frequency distributions of the ultimate engineering tensile stress and the corresponding characteristic strength. The characteristic strength is calculated as the 5th percentile of the estimated frequency distributions. Compared to the results of [9,37], the strength of the optimized specimen is much higher and in good agreement with the strength documented in the data sheet of the adhesive (75 MPa) [13]. In addition, the scatter and therefore the uncertainty is much lower. The same pattern was found for every other mechanical property measured, which is shown in Table 6. The scatter detected is most likely attributable to slight orientation and distribution variations of the reinforcement fibers. Different levels of microporosity, too small to be detected with the scan accuracy used, are also possible, but since the vacuum mixer is very efficient, this is not as likely.

It should be noted that the exact distribution and orientation of the reinforcement fibers is not known. This would require a much higher scan resolution than the one used, which was sufficient to determine porosities and geometrical imperfections. The low scat-

ter seen in the data could therefore be the result of homogeneously chaotic or homogeneously aligned fiber orientations. The latter, anisotropic case seems more likely since the relationship between the elasticity modulus and the shear modulus, Eq. 7, which is valid for isotropic materials, is not valid for the properties derived in this work, see Table 6. An anisotropy is also found for the results of [37]. In [9] the Poisson ratio was not measured, so that the potential degree of anisotropy is unknown.

$$G \neq \frac{E}{2(1+\nu)} \quad (7)$$

The hand-mixed specimens from this work also exhibit a higher strength than the specimens of [9,37], which indicates that the geometry optimization worked well. However, this difference could also arise from an even higher level of porosity in the specimen of [9,37] or may be related to the small number of specimens. Alternating fiber directions could also affect the comparability of the results. The modulus of elasticity of the hand-mixed specimen

**Table 6**

Comparison of material properties derived from uniaxial tests of bulk tubular specimens. Properties measured in this work were derived by averaging the measurements of the two strain gauge rosettes used to compensate minor load imbalances. Stiffness properties were determined within the strain range of 0.1–0.2 %. The mean value  $\mu$ , standard deviation  $\sigma$  and coefficient of variance  $c_v$  are shown for the tensile failure strength  $\sigma_f$ , tensile failure strain  $\varepsilon_f$ , modulus of elasticity  $E$ , Poisson ratio  $\nu$ , and shear modulus  $G$ .

Parameter	Property	Unit	Adhesive	This Work	This Work	Zarouchas	Fernandez
			Data Sheet [13]	optimized	hand-mixed	et al. [37]	et al. [10]
$\sigma_f$	$\mu$	$\frac{N}{mm^2}$	75	76.03	57.12	48.17	50.40
	$\sigma$		n/a	$\pm 0.92$	$\pm 5.78$	$\pm 6.22$	$\pm 3.83$
	$c_v$	%	n/a	1.21	10.12	12.92	7.60
$\varepsilon_f$	$\mu$	$\frac{\mu m}{m}$	29000	31399	14084	10228	17900
	$\sigma$		n/a	$\pm 2353$	$\pm 1585$	$\pm 1330$	$\pm 3025$
	$c_v$	%	n/a	7.49	11.25	13.00	16.90
$E$	$\mu$	$\frac{N}{mm^2}$	5500	5711	5315	5412	3928
	$\sigma$		n/a	$\pm 56$	$\pm 192$	$\pm 164$	$\pm 503$
	$c_v$	%	n/a	0.97	3.62	3.03	12.80
$\nu$	$\mu$	-	n/a	0.373	0.372	0.398	n/a
	$\sigma$		n/a	$\pm 0.005$	$\pm 0.016$	$\pm 0.013$	n/a
	$c_v$	%	n/a	1.44	4.34	3.28	n/a
$G$	$\mu$	$\frac{N}{mm^2}$	n/a	1597	n/a	1511	1477
	$\sigma$		n/a	$\pm 29$	n/a	$\pm 75$	$\pm 75$
	$c_v$	%	n/a	1.82	n/a	4.94	5.10

in this work is very close to the results of [37], however. It is thus possible to conclude that the difference in failure strength and strain is likely linked to the stress concentrations and the geometry optimization, respectively.

The averaged engineering stress strain curves of the optimized and hand-mixed specimens in this work are shown in Fig. 10. While the failure strength  $\sigma_f$  of the optimized specimen is 1.33 times higher than that of the hand-mixed ones, the total failure strain  $\epsilon_f$  is 2.23 times higher. The plastic strain  $\epsilon_{f,pl}$  increased more than 5-fold. Hence, the porosity difference leads to a brittle material in the hand-mixed case and a ductile material in the machine-mixed case. The stiffness difference was estimated as 7%. The typical tensile fracture pattern is shown in Fig. 11.

### 5.3. Biaxial tests

The biaxial tests in this work were performed with displacement control due to the large strains measured in the tensile tests. The displacement rates were adjusted for each axial to torsional load ratio in order to keep the principal strain approximately equal for each ratio at the beginning of the linear elastic section. The effects of different strain rates on ductility and strength were thus minimized. The typical fracture pattern with an initial strain rate ratio of  $\dot{\epsilon}_0/\dot{\gamma}_0 = 1/4$  is shown in Fig. 12.

The failure strengths derived from the biaxial tests are shown in Fig. 13. An ellipsis was fitted to the data set in a non-linear least squares optimization under the assumption that the major axis of the ellipsis coincides with the x-axis. The measurement scatter is indicated by the minimal distance to the ellipsis. As in the case with the tensile tests, it can be observed that the optimized specimens in this work show a higher strength and significantly reduced scatter.

Note that all shear related calculations in [9,35] are based on St. Venant theory. For the sake of comparison this is adopted in this work and shear stresses are calculated according to Eq. 8.

$$\tau = \frac{T \cdot r_o}{\frac{\pi}{2}(r_o^4 - r_i^4)} \quad (8)$$

Herein,  $T$  is the torque,  $r_o$  the outer radius and  $r_i$  the inner radius of the test section.

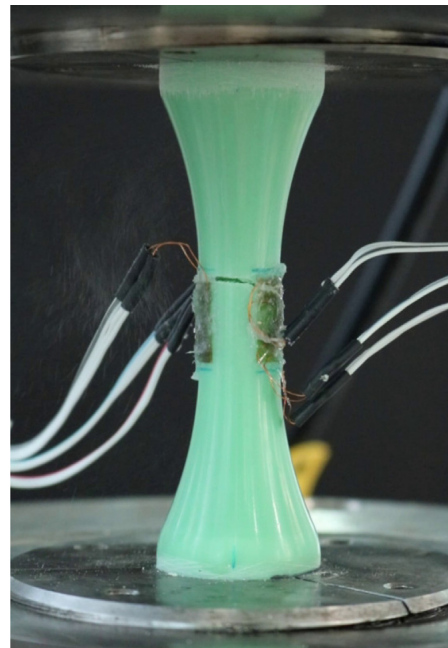


Fig. 11. Typical fracture observed in the tensile tests.

## 6. Porosity analysis of industrial dosing machines

To enable the comparison of the achievable pore density of the laboratory mixer and an industrial one, cured adhesive inside a conveyor hose of a typical industrial dosing and dispensing machine [21] was analyzed. The processed adhesive was the same system as in this work, see Section 2.3, while 137GF hardener was used instead of 137G. It was assumed that the difference in hardener does not affect the pore density. The cured adhesive inside the hose was  $\mu$ CT-scanned with an accuracy comparable to that used for the tubular specimens in this study.

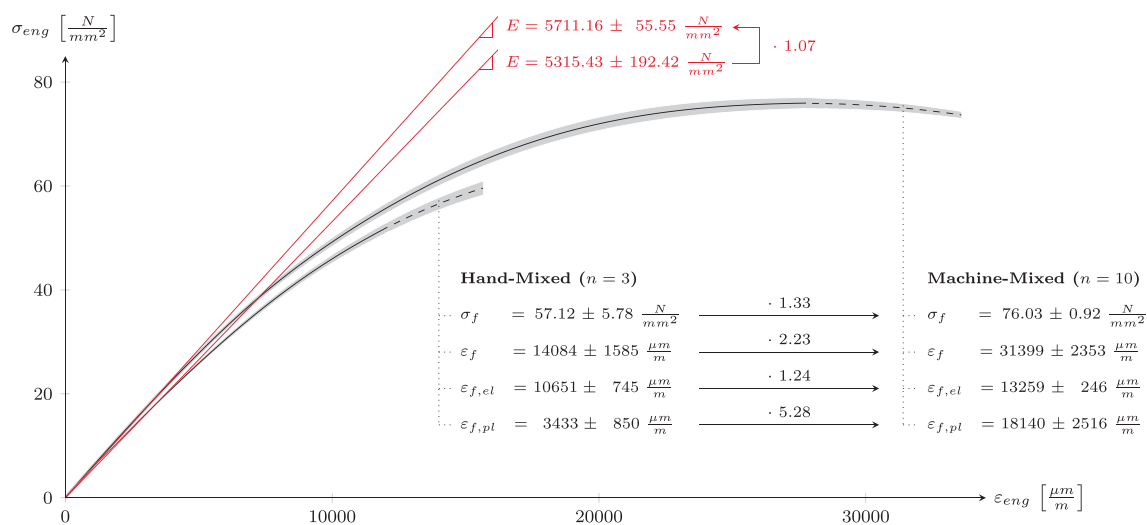
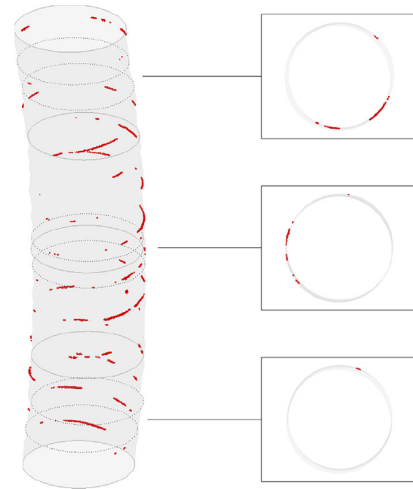


Fig. 10. Averaged engineering stress strain curves of the tensile tests for the machine-mixed and hand-mixed specimens in this work. Gray areas represent the standard deviation of the normal stresses. Dashed lines indicate the range from minimum to maximum failure strain,  $n$  is the number of specimens.



**Fig. 12.** Typical fracture observed in the biaxial tests with an initial strain rate ratio of  $\dot{\epsilon}_0/\dot{\gamma}_0 = 1/4$ .

Fig. 14 shows a 3D depiction and cross sectional views of the inner hose contour and the pores detected. Similar to the machine-mixed specimens in this work, only very small pores were identified, which are probably the result of race tracking effects caused by small ripples on the inner contour of the conveyor hose. The mixing quality in terms of porosity is therefore



**Fig. 14.** Qualitative porosity analysis of cured adhesive inside a conveyor hose of an industrial dosing and dispensing machine. The scanned part had a height of 83 mm and an inner diameter of 19 mm (3/4"). The inner contour is shown in gray, pores are highlighted in red. The adhesive is not shown to increase the visibility of the pores.

comparable to that of the manufacturing procedure presented in this work. However, it must be noted that only one specimen from a single dosing machine was analyzed, so that further experimental verification is necessary. It should also be mentioned that large voids can still be present inside the bond lines due to the application process or subsequent manufacturing steps, although the overall porosity might be low.

As shown in Section 5.2, the adhesive exhibits anisotropic behavior due to the reinforcement fibers. Since the orientation of the fibers is dependent on the flow front during the injection pro-

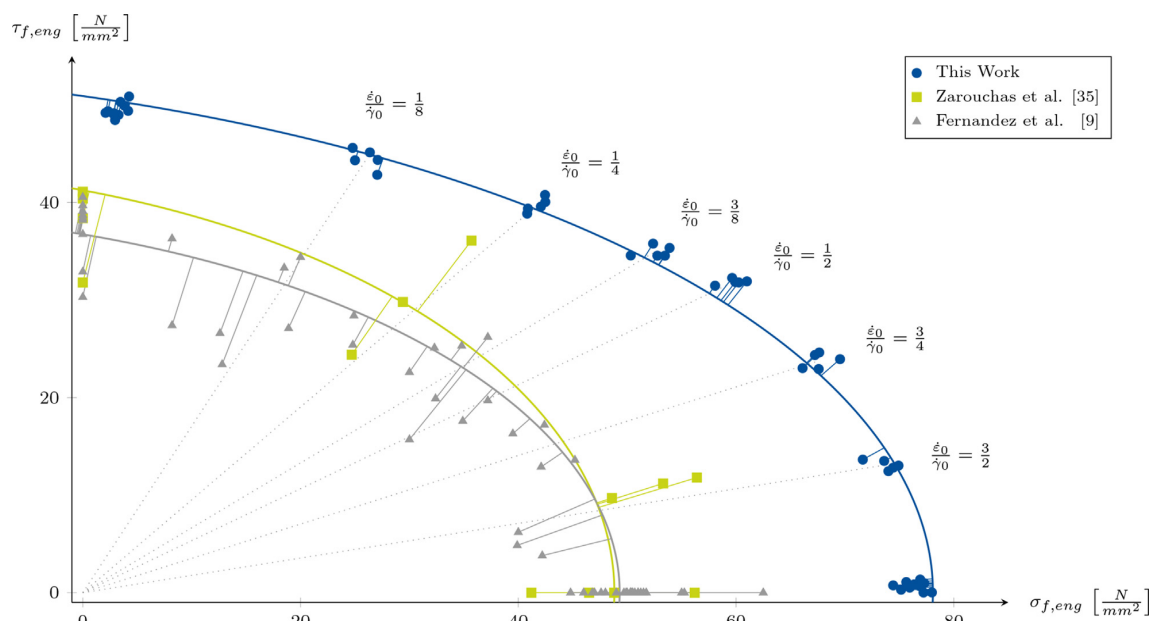


**Fig. 13.** Comparison of engineering failure stresses of bulk adhesive specimens from this study, Zarouchas et al. [35] and Fernandez et al. [9]. Owing to the high quality of the specimens used in this work, the failure strength is higher than that of the hand-mixed specimens in [9,35]. The initial strain rate ratios shown are only valid for the specimens in this study. Measurement scatter is indicated by the minimal distance to a best-fit ellipsis.

cess on the coupon level, the fiber orientation of rotor blade bond lines will likely also depend on the application process used for the adhesive. Squeezing effects caused by the blade mold closing process mean that the fiber orientation may diverge from the application direction set beforehand by the dosing machine operator. Therefore coupon test results are only generally transferable to rotor blade bond lines if the fiber distributions and orientations are known. Other influencing factors such as the tempering process also affect the transferability of coupon tests. The estimation of in-situ bond line properties therefore remains a challenging task.

## 7. Conclusion

Multiaxial testing provides the opportunity to test materials and structures in load cases that are close to real world loads of components. However, owing to the more complex test setup, the potential uncertainties associated with these tests are higher than in uniaxial tests. When the material quality is severely affected by the manufacturing processes, e.g., in the case of two-component, fiber-reinforced structural adhesives with high viscosity, the overall uncertainties might be too high to derive reliable material models if the manufacturing is simplified and done manually.

This study therefore focused on the design and manufacturing optimization of specimens made of a fiber-reinforced structural adhesive used for the manufacture of wind turbine rotor blades. The specimen geometry was optimized in a finite element parametric study to avoid stress concentrations. The mixing quality was subsequently optimized using a planetary centrifugal vacuum mixer. To ensure that the mixture was injected into the molds without generating additional porosity and to achieve a homogeneous flow front, 3D printed mold inserts were developed.

The presented optimization procedure is expected to be generally transferable to other types of materials if the mixing parameters and the injection speed are adjusted with respect to the viscosity of the respective material. The limiting factor with high viscosity materials is expected to be the mold injection process and the friction generated therein. The choice of the failure criteria in the finite element optimization might also differ with other materials, although the optimization strategy and objectives stay the same.

High-resolution X-ray tomography was used to check geometrical imperfections and the porosity of the specimens. The scans verified that the porosity of the specimens is negligible. Other effects such as the mixing ratio or the tempering cycle were precisely controlled as well. It is therefore concluded that the optimization presented in this paper enables the determination of material properties unimpeded by manufacturing simplifications.

Owing to the high quality of the specimens, the material properties measured showed significantly less scatter compared to those published in international literature. This is expressed by very low coefficients of variation for strength and stiffness properties of about 1 %. Furthermore, the optimized specimens showed increased failure strength (+33 %), stiffness (+7 %), and failure strain (+123 %) compared to hand-mixed specimens in tensile tests. The measured failure strain difference incorporates a more than 5-fold increase in the plastic strain, so that the machine-mixed specimens can be classified as ductile, while the hand-mixed specimens are more brittle due to their high porosity.

The  $\mu$ CT-analysis of cured adhesive inside a conveyor hose of an industrial dosing and dispensing machine revealed that the mixing quality in terms of the porosity is as low as that of the manufacturing procedure presented in this work. However, the transfer of coupon test results to rotor blade bond lines is only valid if the effects of the distribution and orientation of the reinforcement fibers, as

well as all other manufacturing effects on the in-situ characteristics, are known. The fiber orientation inside the specimens in this work is not yet known, but since the flow front within the injection process is very homogeneous, the fibers are likely distributed in the same manner in all the specimens. This is also reflected by the low scatter of the test results. The relationship of the stiffness moduli in tension and shear indicates anisotropic behavior, therefore a certain degree of alignment of the reinforcement fibers seems likely, but further experimental validation is required.

Apart from that, it is expected that the material properties derived from the specimens in this work represent a significantly more accurate material characterization than that obtained from hand-mixed specimens.

## CRedit authorship contribution statement

**Michael Wentingmann:** Implementation of the finite element parametric study, manufacturing optimization, manufacturing and instrumentation of the specimens, execution of the experiments,  $\mu$ CT-scan post-processing, illustrations and writing of the paper. **Nikolas Manousides:** High-resolution X-ray microscopy ( $\mu$ CT scanning) of the specimens and segmentation pre-processing. **Alexandros Antoniou:** Scientific advice and support with executing the experiments at Fraunhofer IWES. **Claudio Balzani:** Conceptual guidance and scientific supervision of all project phases.

## Data availability

The raw/processed data required to reproduce these findings cannot be shared at this time due to legal or ethical reasons.

## Declaration of Competing Interest

The authors declare that they have no known competing financial interests or personal relationships that could have appeared to influence the work reported in this paper.

## Acknowledgements

This work was supported by the German Federal Ministry for Economic Affairs and Energy (BMWi) in the ReliaBlade project (Grant Nos. 0324335A, 0324335B).

## References

- [1] A. Albert, L. Zhang, A novel definition of the multivariate coefficient of variation, *Biometr. J.* 52 (2010) 667–675, <https://doi.org/10.1002/bimj.201000030>.
- [2] Ansys®, Mechanical Enterprise, Release 19.2, 2021a.
- [3] Ansys®, SpaceClaim, Release 19.2, 2021b.
- [4] E. Beltrami, Sulle condizioni di resistenza dei corpi elastici, *Il Nuovo Cimento* 18 (1885) 145–155, <https://doi.org/10.1007/BF02824697>.
- [5] R.M. Caddell, R.S. Raghava, A.G. Atkins, Pressure dependent yield criteria for polymers, *Mater. Sci. Eng.* 13 (1974) 113–120, [https://doi.org/10.1016/0025-5416\(74\)90179-7](https://doi.org/10.1016/0025-5416(74)90179-7).
- [6] A.G. Carl Zeiss, Zeiss Xradia 410 Versa, 2021. <https://www.zeiss.com/microscopy/int/products/x-ray-microscopy/zeiss-xradia-410-versa.html>.
- [7] A.G. Cassano, S. Dev, M. Maiaru, C.J. Hansen, S.E. Stapleton, Cure simulations of thick adhesive bondlines for wind energy applications, *J. Appl. Polym. Sci.* 138 (2021) 49989, <https://doi.org/10.1002/app.49989>.
- [8] S. Demmerle, J.P. Boehler, Optimal design of biaxial tensile cruciform specimens, *J. Mech. Phys. Solids* 41 (1993) 143–181, [https://doi.org/10.1016/0022-5096\(93\)90067-P](https://doi.org/10.1016/0022-5096(93)90067-P).
- [9] G. Fernandez, D. Vandepitte, H. Usabiaga, S. Debruyne, Static and cyclic strength properties of brittle adhesives with porosity, *Int. J. Fatigue* 117 (2018) 340–351, <https://doi.org/10.1016/j.ijfatigue.2018.08.018>.
- [10] G. Fernandez, D. Vandepitte, H. Usabiaga, B. Van Hoorweder, S. Debruyne, Experimental identification of static and dynamic strength of epoxy based adhesives in high thickness joints, *Int. J. Solids Struct.* 120 (2017) 292–303, <https://doi.org/10.1016/j.ijsolstr.2017.05.012>.



- [11] A.I.M. Foletti, J.S. Cruz, A.P. Vassilopoulos, Fabrication and curing conditions effects on the fatigue behavior of a structural adhesive, *Int. J. Fatigue* 139 (2020) 105743, <https://doi.org/10.1016/j.ijfatigue.2020.105743>.
- [12] T.J. George, J. Seidt, M.H.H. Shen, T. Nicholas, C.J. Cross, Development of a novel vibration-based fatigue testing methodology, *Int. J. Fatigue* 26 (2004) 477–486, <https://doi.org/10.1016/j.ijfatigue.2003.10.012>.
- [13] Hexion™, Technical Data Sheet - EPIKOTE™ Resin MGS™ BPR 135G-Series and EPIKURE™ Curing Agent MGS™ BPH 134G-137GF, 2021.
- [14] C.P.R. Hoppel, T.A. Bogetti, J.W. Gillespie, Literature Review-Effects of Hydrostatic Pressure on the Mechanical Behavior of Composite Materials, *J. Thermoplast. Compos. Mater.* 8 (1995) 375–409, <https://doi.org/10.1177/089270579500800403>.
- [15] Kern & Sohn GmbH, EMB 2000-2, 2021. <https://www.kern-sohn.com/shop/en/basic-balances/school-balances/EMB/>.
- [16] A. Makinde, L. Thibodeau, K.W. Neale, Development of an apparatus for biaxial testing using cruciform specimens, *Exp. Mech.* 32 (1992) 138–144, <https://doi.org/10.1007/BF02324725>.
- [17] Matlab®, R2020b, 2021.
- [18] Memmert GmbH + Co. KG, Universal Oven, 2021. <https://www.memmert.com/products/heating-drying-ovens/universal-oven>.
- [19] P. Noever-Castelos, B. Haller, C. Balzani, Validation of a modelling methodology for wind turbine rotor blades based on a full scale blade test, *Wind Energy Sci. Discuss.* 2021 (2021) 1–32, <https://doi.org/10.5194/wes-2021-24>.
- [20] K.D. Pae, S.K. Bhatija, The Effects of Hydrostatic Pressure on the Mechanical Behavior of Polymers, *J. Macromol. Sci. Part C* 13 (1975) 1–75, <https://doi.org/10.1080/15321797508068145>.
- [21] ReliaBlade Project, Increased Reliability of Rotor Blades. Grant numbers 0324335A, 0324335B, 2021. <https://www.reliablade.com>.
- [22] Ritter GmbH, 610 ml Dosing Cartridge. <https://www.ritter-cartridges.de/en/products/dosing-cartridges-syringes>, 2021.
- [23] M. Rosemeier, A. Krimmer, A. Bardenhagen, A. Antoniou, Tunneling Crack Initiation in Trailing-Edge Bond Lines of Wind-Turbine Blades, *AIAA J.* 57 (2019) 5462–5474, <https://doi.org/10.2514/1.j058179>.
- [24] F. Sayer, A. Antoniou, A. van Wingerde, Investigation of structural bond lines in wind turbine blades by sub-component tests, *Int. J. Adhes. Adhes.* 37 (2012) 129–135, <https://doi.org/10.1016/j.ijadhadh.2012.01.021>.
- [25] A.T. Sears, D.D. Samborsky, P. Agastra, J.F. Mandell, Fatigue Results and Analysis for Thick Adhesive Notched Lap Shear Test, in: *Proc. AIAA SDM Wind Energy Session*, 2010. doi: <https://doi.org/10.2514/6.2010-2821>.
- [26] J. Shewchuk, S.Y. Zamrik, J. Marin, Low-cycle Fatigue of 7075-T651 Aluminum Alloy in Biaxial Bending, *Exp. Mech.* 8 (1968) 504–512, <https://doi.org/10.1007/BF02327127>.
- [27] A. Smits, D. Van Hemelrijck, T.P. Philippidis, A. Cardon, Design of a cruciform specimen for biaxial testing of fibre reinforced composite laminates, *Compos. Sci. Technol.* 66 (2006) 964–975, <https://doi.org/10.1016/j.compscitech.2005.08.011>.
- [28] F. Stassi-D'Alia, Flow and fracture of materials according to a new limiting condition of yielding, *Meccanica* 2 (1967) 178–195, <https://doi.org/10.1007/BF02128173>.
- [29] K.P. Subrahmanian, F. Dubouloz, Adhesives for bonding wind turbine blades, *Reinf. Plast.* 53 (2009) 26–29, [https://doi.org/10.1016/S0034-3617\(09\)70044-X](https://doi.org/10.1016/S0034-3617(09)70044-X).
- [30] G. Tao, Z. Xia, Fatigue behavior of an epoxy polymer subjected to cyclic shear loading, *Mater. Sci. Eng. A* 486 (2008) 38–44, <https://doi.org/10.1016/j.msea.2007.08.044>.
- [31] Thermo Fisher Scientific, Avizo 2020.2 User Guide, 2020.
- [32] Thinky Corporation, Thinky ARV-310 planetary centrifugal vacuum mixer, 2021. [https://www.thinkymixer.com/en-gl/products\\_category/thinkymixer](https://www.thinkymixer.com/en-gl/products_category/thinkymixer).
- [33] Tokyo Measuring Instruments Laboratory Co., Ltd., GFRAB-3-350-50, 2021. [https://tml.jp/e/product/strain\\_gauge/gf\\_list.html](https://tml.jp/e/product/strain_gauge/gf_list.html).
- [34] Walter + Bai AG, Axial/ Torsional Test Systems, 2021. [https://www.walterbai.com/page/products/Materials\\_Testing\\_Systems/Combined\\_Axial-Torsional\\_Testing\\_System/index.php](https://www.walterbai.com/page/products/Materials_Testing_Systems/Combined_Axial-Torsional_Testing_System/index.php).
- [35] D. Zarouchas, R. Nijssen, Mechanical behaviour of thick structural adhesives in wind turbine blades under multi-axial loading, *J. Adhes. Sci. Technol.* 30 (2016) 1413–1429, <https://doi.org/10.1080/01694243.2016.1146392>.
- [36] D.S. Zarouchas, A.A. Makris, F. Sayer, D. Van Hemelrijck, A.M. Van Wingerde, Investigations on the mechanical behavior of a wind rotor blade subcomponent, *Compos. Part B: Eng.* 43 (2012) 647–654, <https://doi.org/10.1016/j.compositesb.2011.10.009>.
- [37] D.S. Zarouchas, R.P.L. Nijssen, D.R.V. van Delft, Failure analysis of structural adhesives in wind turbine blades under multiaxial loading, in: *Proc. DURACOSYS Conference*, 2012b.



## 3

## Yield surface derivation for a structural adhesive based on multiaxial experiments

2<sup>nd</sup> Paper

Based on the optimized specimens, uni- and biaxial static tests are conducted to characterize the adhesive in terms of stiffness and strength properties. A yield surface analysis is conducted to find the most suitable yield criterion, i.e., equivalent stress formulation, which can later be used for fatigue life estimations. With the derivation of the yield surface, novel approaches regarding the elasto-plastic shear stress estimation and yield locus identification (elliptical scaling approach) are developed.

---

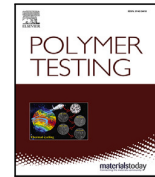
P2-1	Introduction .....	44
P2-2	Specimens and test setup .....	45
P2-3	Elasto-plastic shear stress correction	47
P2-4	Yield surface derivation.....	48
P2-5	Result discussion.....	52
P2-6	Conclusion .....	54





Contents lists available at ScienceDirect

## Polymer Testing

journal homepage: [www.elsevier.com/locate/polytest](http://www.elsevier.com/locate/polytest)

## Yield surface derivation for a structural adhesive based on multiaxial experiments

Michael Wentingmann<sup>a,\*</sup>, Nikolas Manousides<sup>a</sup>, Alexandros Antoniou<sup>b</sup>, Claudio Balzani<sup>a</sup><sup>a</sup> Leibniz University Hannover, Institute for Wind Energy Systems, Appelstraße 9A, 30167 Hannover, Germany<sup>b</sup> Fraunhofer Institute for Wind Energy Systems IWES, Am Seedeich 45, 27572 Bremerhaven, Germany

## ARTICLE INFO

## Keywords:

Structural adhesives  
Multiaxial testing  
Elasto-plastic shear stresses  
Yield surface  
Wind turbine rotor blades

## ABSTRACT

Yield surface determination is an essential part of a material characterization, enabling the qualification of a suitable yield criterion. In the case of two-component, fiber-reinforced structural adhesives the manufacturing quality of the specimens is directly linked to the determination accuracy of the yield surface. Therefore, this work was based on specimens that have been optimized in a previous study utilizing a structural, epoxy-based adhesive designed for the manufacture of wind turbine rotor blades. This allowed for a precise identification of a yield locus in combined tension–torsion and compression–torsion experiments. A practical elasto-plastic shear stress correction was developed to account for the transition between elastic and plastic states. In addition, a scaling method of an elliptical yield locus fitting function is proposed to calculate equivalent stresses and strains. The obtained results are discussed regarding influences of viscoelasticity and are compared to existing yield criteria.

## 1. Introduction

The yield surface determination of a material is an important experimental procedure for engineering purposes. Up to the yield point, arbitrary multiaxial stress–strain states can be converted to scalar equivalent stresses and strains using yield criteria. This allows for a simplified structural analysis for most engineering problems. The experimental verification of the yield surface is therefore an important step to qualify yield criteria.

## 1.1. Definition of yielding

Yielding is defined as the onset of plastic deformation. While some metals show a pronounced yield point, most other materials gradually work harden. For the latter kind of materials, the yield point is usually defined using an offset plastic strain in such a way that the level of plasticity is tolerable and the stress state can be approximated as linear elastic. The applicable plastic strain may vary depending on the intended use of the material and the required level of safety. Some engineering problems may lead to the definition of yield when the proportional limit is reached while others allow a plastic strain of up to 0.2 %.

As an alternative, it has been proposed in [1,2] to define the yield point as the absolute maximum of the second derivative of the stress–strain curve. This way, the yield point represents the point at which

the rate of change of the tangent modulus, i.e., the curvature of the stress–strain curve, is maximized [1,2].

Both yield point definitions are shown in Fig. 1.

## 1.2. Experimental yield point detection

Tubular specimens in combination with universal tension–torsion testing machines offer a versatile test setup for the yield locus determination, as arbitrary biaxial stress states ( $\sigma/\tau$ ) can be reached with different combinations of normal and torsional loads. These and similar setups have been used extensively to characterize the initial and post yield loci of metals [3–7] and polymers [8–10].

To identify a yield point experimentally based on the offset strain definition, the deviation from the linear elastic stress–strain relationship must be detected. This can be achieved by calculating the plastic strain either in-situ or in retrospect. Once the plastic strain has reached a level that can be associated with yielding, the yield point is identified. If the plastic strain can be calculated in-situ, it is possible to use the specimen again at another stress ratio in case the plastic strain has been sufficiently small [5].

The general problem associated with this approach is that the plastic strain offset must be an equivalent strain. Otherwise the discrepancy between normal and shear strains in the engineering stress–strain space

\* Corresponding author.

E-mail address: [research@iwes.uni-hannover.de](mailto:research@iwes.uni-hannover.de) (M. Wentingmann).

<https://doi.org/10.1016/j.polymeresting.2022.107648>

Received 16 February 2022; Received in revised form 8 April 2022; Accepted 23 May 2022

Available online 2 June 2022

0142-9418/© 2022 The Authors. Published by Elsevier Ltd. This is an open access article under the CC BY license (<http://creativecommons.org/licenses/by/4.0/>).

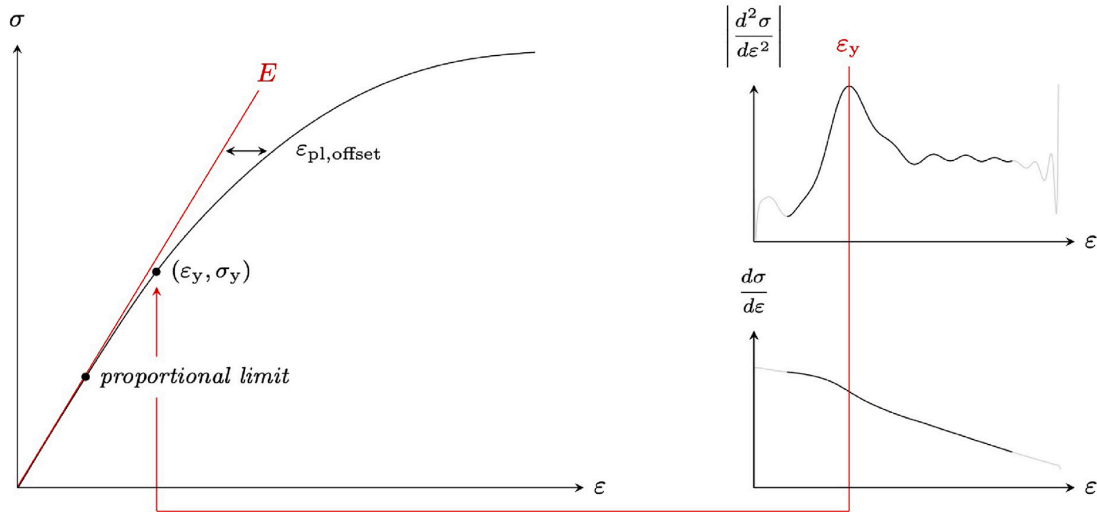


Fig. 1. Definition of yielding via an arbitrary plastic offset strain or the absolute maximum of the second derivative of the stress–strain curve as proposed in [1,2]. The curves depict the results for a tensile specimen from this work, see Section 4.1.

denoted by  $\varepsilon$  and  $\gamma$ , respectively, will lead to incorrect yield points. Consider for example the biaxial formulation of the plastic von Mises strain  $\varepsilon_{vM,pl}$  given by

$$\varepsilon_{vM,pl} = \sqrt{\varepsilon^2 + \frac{\gamma^2}{3}}. \quad (1)$$

If this formula is used to calculate plastic offset strains in the torsion test, the offset strain in shear  $\gamma$  must be  $\sqrt{3}$ -times bigger than the offset normal strain  $\varepsilon$  in the tension test to reach an equal equivalent offset strain in both tests.

This discrepancy also arises for normal strains if a material exhibits a strength asymmetry in tension and compression, which is observed for several kinds of polymers [11]. The offset strain discrepancy vanishes, if the proportional limit can be precisely identified, since the offset strain in this point is zero by definition. This allows for a yield point detection without an a priori knowledge of an appropriate yield criterion. However, this limit is very challenging to detect, as it requires a very sensitive strain measurement and a very fine tuned testing machine. Alternatively, the proportional limit can be estimated based on a backwards interpolation to the linear elastic region if the entire stress–strain curve was recorded [5,12].

In case an applicable yield criterion is known a priori, the yield point detection is easier, as the plastic strain offset can be calculated using the equivalent strain formulation in-situ or in retrospect. This may apply if the material of interest belongs to a well characterized class of materials. For instance if the yield point needs to be detected for a metal alloy [3].

Considering the derivative-based yield point definition given in [1, 2], yielding can be detected subsequent to the recording of the complete stress–strain curve. No arbitrarily chosen strain offsets are required in this approach, but since a recording of a stress–strain curve results in a discrete time series, a continuous function fit is necessary to calculate derivatives. This may result in a yield point, which is dependent on the fitting function used. A sensitivity analysis is therefore advisable.

### 1.3. Structural adhesives for wind turbine rotor blades

Although many yield criteria have been identified for different kinds of polymers, the validation of a yield criterion for structural adhesives used in the wind energy sector is not well described in literature.

Especially for the case of short fiber-reinforced adhesives, which are commonly used for the manufacture of rotor blades, information is limited to [8,10].

The stress–strain responses in [8,10] were characterized as brittle and therefore the failure stress–strain state was used to identify a yield criterion. The brittle material behavior was, however, attributed to non-representative specimen manufacturing methods (hand-mixing), which led to high levels of porosity. It has been shown recently that the used adhesive is not brittle if the manufacturing is done in a comparable way to rotor blade manufacture (machine-mixing) [13]. The results published in [8,10] are therefore not representative for the porosity level that is achieved with industrial dosing machines and modern rotor blades, respectively.

### 1.4. Aims and outline

In this paper, the yield surface is determined for a short fiber-reinforced structural adhesive, based on the optimized, machine-mixed specimens presented in [13]. This way, a yield criterion is identified which is unaffected by manufacturing induced defects of the underlying specimens.

In Section 2, the specimen manufacturing and the test setup are briefly summarized. A practical elasto-plastic shear stress correction is developed in Section 3 to account for the transition between the fully elastic and fully plastic shear stress regime. The yield surface determination is carried out in Section 4 and discussed in Section 5.

## 2. Specimens and test setup

The tapered, tubular specimens for the experimental campaign were made of EPIKOTE™ Resin MGS™ BPR 135G3 in combination with EPIKURE™ Curing Agent MGS™ BPH 137G [13]. The system is an epoxy-based, short glass fiber-reinforced structural adhesive and commonly used in the wind energy industry [14].

The manufacturing was based on machine-mixing and the manufacturing quality was verified via high-resolution X-ray microscopy ( $\mu$ CT scanning) using a Zeiss Xradia 410 Versa [15] in order to guarantee homogeneous specimens with negligible porosity. A qualitative porosity comparison of the specimens used for this study is given in Fig. 2.

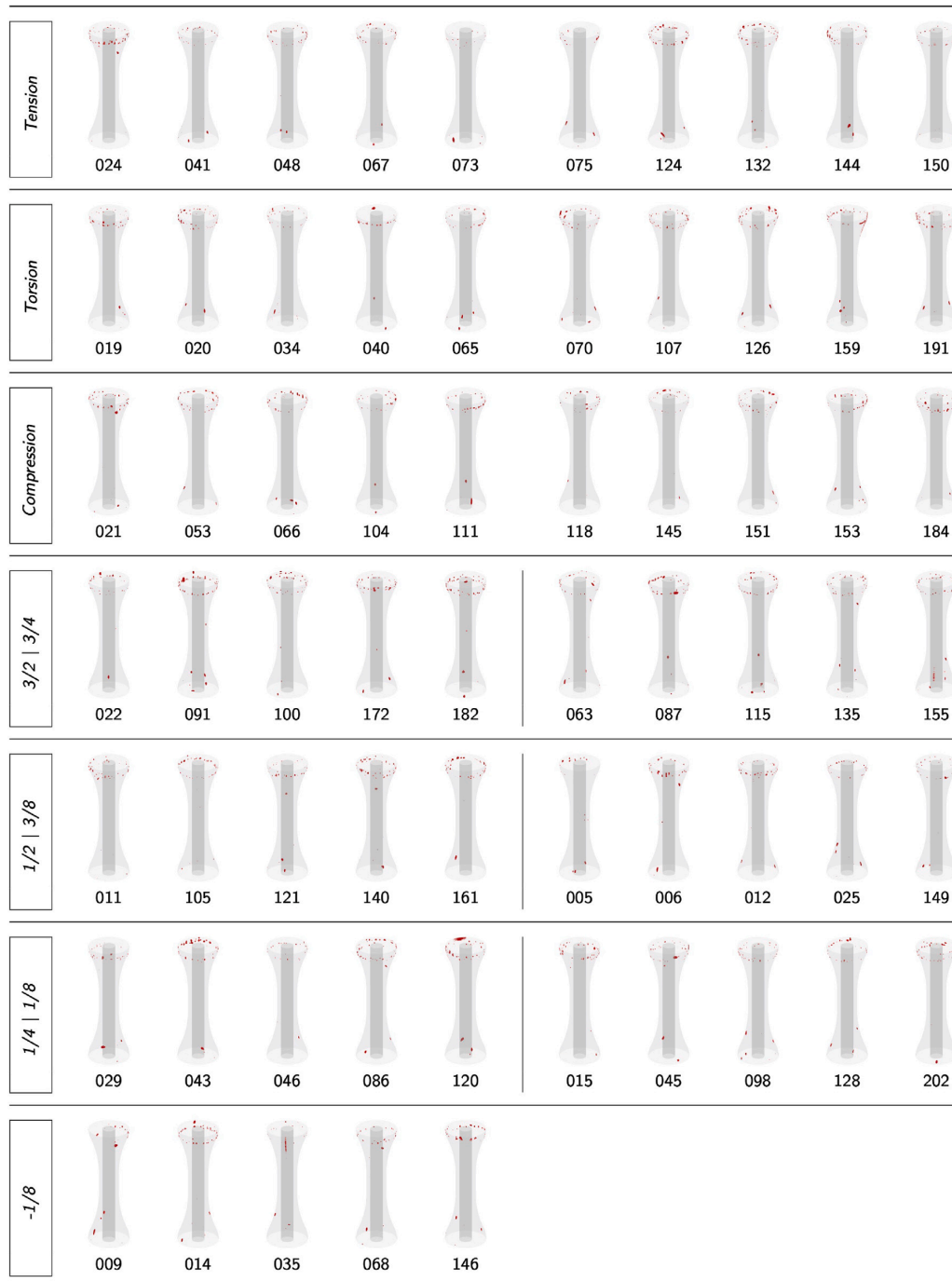


Fig. 2. Qualitative porosity comparison of the specimens manufactured in [13] and used for this study. Pores are indicated in red. Initial strain rate ratios of the biaxial tests are indicated as  $\dot{\epsilon}_0/\dot{\nu}_0$ . The specimen numbers are given below the respective depictions.

The fiber distribution and orientation within the specimens is not yet known, because the scan resolution was not high enough to resolve single fibers. However, the low scatter of the stiffness and strength properties in combination with a well controlled manufacturing procedure led to the conclusion that the fibers are either orientated homogeneously chaotic or homogeneously aligned. The latter was identified as more likely, since the isotropic relationship of the stiffness properties

is not valid, i.e.

$$G \neq \frac{E}{2(1+\nu)}. \quad (2)$$

Herein,  $G$ ,  $E$ , and  $\nu$  are the shear modulus, the Young's modulus, and the Poisson's ratio for an isotropic material. Therefore an anisotropy is likely present [13].

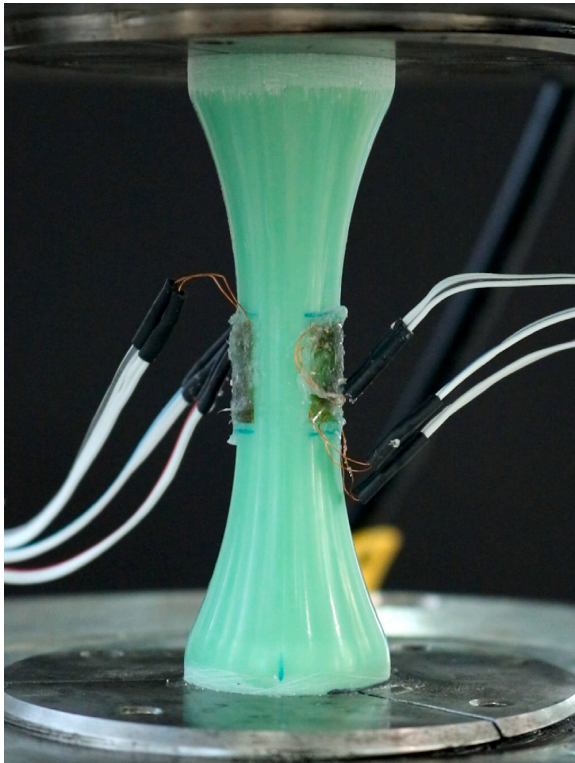


Fig. 3. Test setup for every static test conducted in [13].

The experiments were conducted in displacement control using a servohydraulic Walter + Bai LFV 100-T2000, which enables multiaxial coupon tests via independent control of axial and torsional loads [16]. Data quality was ensured with a class 0.5 calibrated load cell and two low stiffness strain gauge rosettes on each specimen, which were specifically designed for measurements on epoxy resins [17]. It was possible to account for minor load imbalances by installing the strain gauges diametrically opposite to each other. The test setup is shown in Fig. 3. More detailed information about the manufacturing and testing conditions can be found in [13].

### 3. Elasto-plastic shear stress correction

To be able to detect yield points in torsional load states, a smooth elasto-plastic shear stress transition is required and derived in the following.

#### 3.1. Shear stress formulae

The torque  $T$  applied to a tubular specimen is equal to the area integral of the radial shear stress distribution  $\tau(r, \gamma)$  multiplied by the radius  $r$  as given by the relationship

$$T = \int_A \tau(r, \gamma) \cdot r \, dA = 2\pi \int_{r_i}^{r_o} \tau(r, \gamma) \cdot r^2 \, dr. \quad (3)$$

Therein,  $r_o$  is the outer radius and  $r_i$  the inner radius. In the purely elastic case, the shear stress gradient within the wall thickness of a tube is linearly dependent on the radius. Replacing  $\tau(r, \gamma)$  in Eq. (3) with a linear relationship and subsequently solving the integral results in

$$\tau_{el} = \frac{T \cdot r}{\frac{\pi}{2} (r_o^4 - r_i^4)} = \frac{T \cdot r}{J}. \quad (4)$$

Eq. (4) can also be rewritten with the polar moment of inertia  $J$ . This formulation is also known as St. Venant torsion and should be used to determine elastic properties such as the tangent shear modulus  $G$ .

The other extreme case is the purely plastic stress state, where the radial shear stress distribution can be approximated as constant. Applying this relationship to Eq. (3) yields

$$\tau_{pl} = \frac{3T}{2\pi (r_o^3 - r_i^3)}. \quad (5)$$

In between the elastic and plastic case, the radial shear stress distribution can be characterized as elasto-plastic, referring to a plastic outer annulus combined with an elastic inner annulus. A simplified empirical approximation for this stress state and thin-walled tubular specimens is given in the ASTM Standard E2207-15 [18] by

$$\tau_{ASTM} = \frac{T}{\frac{\pi}{2} (r_o^2 - r_i^2) (r_o + r_i)}. \quad (6)$$

This approach provides similar results as Bredt's Equation [19], which is more common in European literature.

#### 3.2. A practical approach for the elasto-plastic transition

Since the transition between the elastic and elasto-plastic stress state formulated in Eqs. (4) and (6) is not continuous, the yield point estimation becomes difficult. Therefore, a practical approach for a smooth transition is proposed in the following.

Assuming that the initial stress state is fully linear elastic and the stress state close to failure is completely plastic, Eq. (4) and (5) were interpreted as boundary stress states. These boundaries were connected using a spline function, resulting in an estimated, but continuous shear stress-strain curve.

Since the radial shear strain distribution remains linear for the entire range from elastic to fully plastic, it can be calculated based on a shear strain measurement, e.g., on the outer annulus. Given the calculated radial shear strain distribution, the radial shear stress distribution was read from the estimated stress-strain curve. The resulting torque was computed numerically using Eq. (3). On the basis that the calculated torque could be compared to the measured one, the spline-transition function could be validated. As a result of that, the start- and end-points of the spline could be optimized iteratively. Additional spline nodes can be used to manipulate the slope if required. This procedure is visually summarized in Fig. 4.

In this work the spline was iteratively optimized using a genetic algorithm (Global Optimization Toolbox, Matlab [21]) and two additional spline nodes for both the uniaxial torsion tests (Section 4.2) and the biaxial experiments (Section 4.3). In case the failure state is not fully plastic, the spline nodes can be iteratively adapted in between  $\tau_{el}$  and  $\tau_{pl}$ .

It should be noted that the differences between the fully elastic and fully plastic formulations of Eqs. (4) and (5) depend on the ratio between the outer and the inner radius of the specimen (called radial ratio in the following). The same holds for Eqs. (4) and (6), see Fig. 5. The higher the radial ratio, the lower the differences of the predicted shear stresses. However, even for very thin-walled (high radial ratio) specimens, the proposed elasto-plastic transition is still relevant, because an ideal radial ratio close to 1 leads to an infinitely thin wall thickness, which is not manufacturable. In fact, the ASTM Standard E2207-15 [18] advises not to exceed a radial ratio of 0.89 to avoid buckling. At this ratio the difference between the elastic and plastic state is still 5% [20], which causes a significant discontinuity in the case of a yield point analysis.

Considering that the ratio  $\tau_{pl}/\tau_{el}$  is constant until failure and that the adhesive was proven to exhibit significant ductility [13], it is expected that the shear failure stresses given in [8,10] need to be corrected with the respective ratios shown in Fig. 5. This is because the values stated in [8,10] were the result of high porosity levels (effect of defects) rather

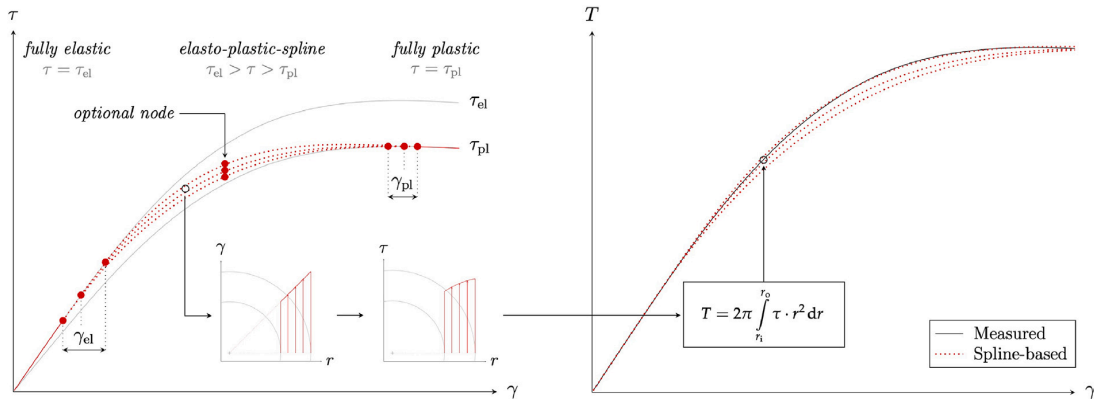


Fig. 4. Spline-based elasto-plastic shear stress approach. The fully elastic ( $\tau_{el}$ ) and fully plastic ( $\tau_{pl}$ ) formulations of Eqs. (4) and (5) are interpreted as boundaries. In between a continuous transition spline is used. Based on a shear strain measurement, the radial shear strain distribution can be calculated. The shear stresses are subsequently read from the estimated spline for the respective strain distribution. Using numerical integration, the radial shear stress distribution can be converted to torque with Eq. (3). Since the torque is also measured, an iteration is set up, which varies the start- ( $\gamma_{el}$ ) and the endpoint ( $\gamma_{pl}$ ) of the spline and optional additional nodes until the calculated torque converges to the measured one.

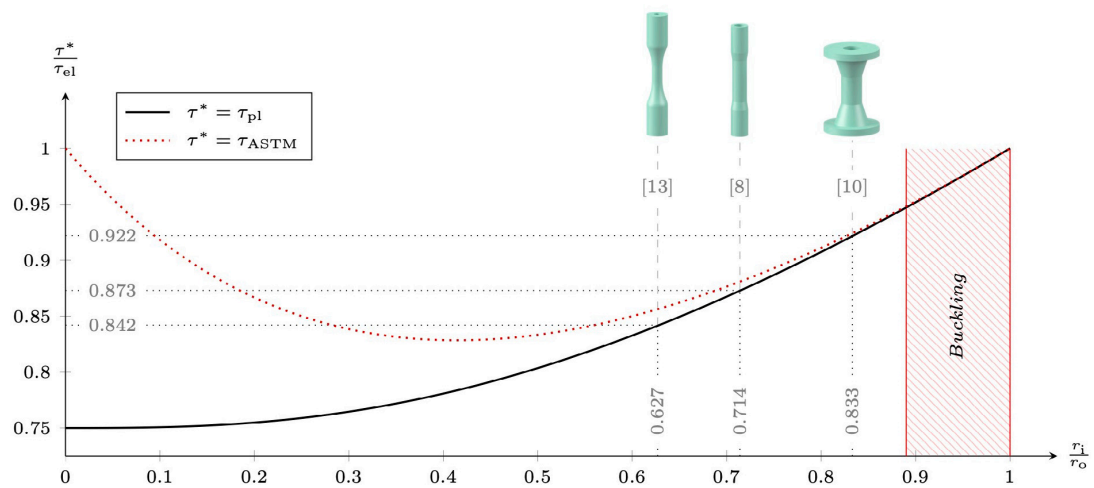


Fig. 5. Ratios of shear stress predictions from Eq. (4) to (6) plotted against the ratio of inner and outer specimen radius in the test section. Geometry examples from [8,10,13] are shown with their respective ratios of  $\tau_{pl}/\tau_{el}$  and  $r_i/r_o$ . Specimens with a radial ratio  $> 0.89$  are prone to buckling [18,20].

than a brittle behavior of the material itself. It is therefore likely that the material surrounding the pores plasticized significantly, but as the overall porosity level was very high, this was not perceived as global specimen behavior.

#### 4. Yield surface derivation

Due to changes of the specimen geometry during the static tests, the engineering stress–strain state does not represent the true stress–strain state. Therefore, the normal stresses and strains in the tension quadrant were estimated by the expressions

$$\epsilon = \ln(1 + \epsilon_{eng}), \quad (7)$$

$$\sigma = \sigma_{eng}(1 + \epsilon_{eng}), \quad (8)$$

while those in the compression quadrant were calculated by

$$\epsilon = -\ln(1 - |\epsilon_{eng}|), \quad (9)$$

$$\sigma = \sigma_{eng}(1 - |\epsilon_{eng}|). \quad (10)$$

The applied true strain correction can also be found in [22]. The true cross sectional area  $A^*$  can be calculated based on the constant volume assumption inherent to the true strain formulae:

$$A^* = \frac{A_0}{1 + \epsilon_{eng}}. \quad (11)$$

Therein  $A_0$  indicates the initial (engineering) cross section.

It was assumed that the cross-sectional properties do not change on account of torsional loads. Engineering shear stresses and strains were therefore interpreted as true stresses and strains. However, radial changes on account of normal loads were taken into account, so that the normal stress–strain correction did also affect the shear properties in the biaxial experiments. To apply this additional correction it was assumed that the ratio of the inner and outer radius is always constant:

$$\frac{r_o}{r_i} = \frac{r_o^*}{r_i^*} = C = const. \quad (12)$$



With Eq. (12) and the true cross section  $A^*$  from Eq. (11), the true inner and outer radii can be found by

$$r_i^* = \sqrt{\frac{A^*}{\pi(C^2 - 1)}}, \quad r_o^* = \sqrt{\frac{A^*}{\pi\left(1 - \frac{1}{C^2}\right)}}. \quad (13)$$

It should be noted that for most of the experiments, the failure strains exceeded the capabilities of the applied strain gauges. However, this did not affect the yield point derivation, since the failure of the strain gauges occurred significantly later than yielding and at the beginning of the fully plastic regime, which can be seen in the corresponding figures referred to in the following. It was assumed that the strain increment did not change after strain gauge failure, which corresponds to a linear extrapolation of the strain based on the last measured strain rate. Although this is expected to be a sufficient approximation, the strains subsequent to strain gauge failure should be treated with caution.

All tests were performed in displacement control on account of the ductility of the material. A displacement rate of 1 mm/min was used for the tensile tests, which corresponded to an initial strain rate of  $292 \pm 5$  ( $\mu\text{m}/\text{m})\text{s}^{-1}$ . Note that the strain rate was not constant due to displacement control. To minimize potential strain rate effects in the torsional and biaxial tests, the displacement rate was adjusted in such a way that the initial principal strain rate was similar to the tensile test. This way, the comparability of all tests is maximized for the given testing conditions.

#### 4.1. Yielding in tension

The yield point detection in tension was carried out for plastic offset strains within the range of 100 to 2000  $\mu\text{m}/\text{m}$  (0.01–0.2 %) and based on the derivative approach [1,2]. The true stress–strain diagram for tension is shown in Fig. 6 with values of the yield and ultimate stress–strain state.

It can be observed that the derivative-based yield point ( $\epsilon_y, \sigma_y$ ) is approximately centered between the yield points with plastic offset strains of 100  $\mu\text{m}/\text{m}$  ( $\epsilon_{y,0.01}, \sigma_{y,0.01}$ ) and 2000  $\mu\text{m}/\text{m}$  ( $\epsilon_{y,0.2}, \sigma_{y,0.2}$ ). For comparison purposes, the offset strain of the derivative-based yield point was calculated and found to be  $451 \pm 71$   $\mu\text{m}/\text{m}$ .

Since the derivative-based approach requires a continuous stress–strain function, the yield point is dependent on the fitting function of the discrete and noisy time series measured in the experiment. For this study, individual high order polynomial functions for each stress–strain curve were used subsequent to a Savitzky–Golay filter [23], which was applied to smoothen the measured stress–strain curve. These smoothened stress–strain curves were used as the basis for all calculations including the material property determination. However, as the filtering degree was carefully adjusted, the smoothening only eased the yield point evaluation and did not affect other material properties such as the respective modulus, e.g., the mean difference in Young's modulus was found to be 0.1 % if it was derived based on the unsmoothened stress–strain curves.

A sensitivity analysis was carried out to investigate the influence of the polynomial order of the fitting function on the yield point position. In the case of the tension test, convergence is reached at a polynomial degree larger than 20, see Fig. 6. In terms of a regular function fit, a polynomial degree of this magnitude is likely over-fitted and might lead to bad results if the function is used for predictions. In this case, however, each function fit is solely used for the yield point determination and not for extrapolation purposes. Therefore, even very high polynomial degrees are justified, which is why this fitting approach has also been used in other polymer yield point studies such as [24].

To find the absolute maximum of the second derivative, the start and end regions of the strain domain were excluded as indicated in Fig. 1 by gray lines. Within these excluded regions small stress fluctuations led to big disturbances of the derivatives. The limitation of

the start region was based on the lower limit of the employed stiffness evaluation range (1000–2000  $\mu\text{m}/\text{m}$  [13]). The excluded end region was determined via a relative strain offset to the ultimate strength position. Using the mentioned domain restriction, the maximum of the second derivative was distinctly identifiable for each recorded stress–strain curve in this work.

#### 4.2. Yielding in torsion and compression

It has been shown in [10] that the adhesive exhibits a significant strength asymmetry in tension and compression. The offset strains in shear and compression used for the yield point detection are therefore both affected by the aforementioned strain discrepancies to the tension test in the engineering stress–strain space  $\mathbb{R}^{\text{eng}}$ , see Section 1.2. Since the work hardening of the adhesive was not accounted for in [8,10], the reported equivalent stress formulation could not be used in this work.

The derivative-based yield point detection [1,2] is not affected by this problem in case of uniaxial loading, because it solely depends on the characteristic shape of the true stress–strain curve. Therefore it was used to determine the yield points in torsion and compression.

The true stress–strain curves for the torsion and compression test are shown in Fig. 6. The adhesive shows almost perfect plastic behavior in the torsion test, which justifies the transition assumption to the fully plastic regime in the spline-based shear stress determination explained in Section 3.2. For each estimated shear stress–strain (transition) curve, the remaining difference of the predicted torque and the measured one was negligible (0.49 % on average) until strain gauge failure.

In the compression tests, the specimens buckled after exceeding a critical plastic strain. This critical strain was significantly larger than the yield strain. Therefore, similar to strain gauge failures, this did not affect the yield point detection. The determination of buckling was based on a frame by frame video analysis of the experiments. The main reason for the compression buckling was attributed to the increased ductility of the specimens due to machine-mixing, which led to very low levels of porosity and a 5-fold increase of the plastic strain in the case of the tension test compared to hand-mixed specimens [13]. This increase in plastic strain was unexpected and was not accounted for in the geometry optimization of the specimens [13], that had to rely on the hand-mixed results of [8,10]. Therefore the buckling load factors associated with the geometries used in [8,10,13], which were found to be comparable in magnitude [13], are only valid for hand-mixed material parameters and do not apply for ductile, machine-mixed specimens.

#### 4.3. Yielding in biaxial stress states

The yield point detection requires a uniaxial stress–strain curve. For biaxial, axial-torsional load cases these curves must be calculated with an equivalent stress–strain formulation. This formulation is not yet known for the adhesive, but can be derived based on an elliptical function fit of the uniaxial yield points, which will be explained in the following.

Each yield criterion can be used as an equivalent stress–strain formulation if the criterion is scaled with the yield strength and yield strain, respectively. Consider the idealized, fictitious yield locus shown in Fig. 7, which is described by the expression

$$\sigma_{\text{VM}} = \frac{(\kappa_\sigma - 1)I_1 + \sqrt{(\kappa_\sigma - 1)^2 I_1^2 + 4\kappa_\sigma \sigma_{\text{VM}}^2}}{2\kappa_\sigma}. \quad (14)$$

Therein,  $\kappa_\sigma$  is the absolute ratio of the compressive and tensile yield strength,  $I_1$  denotes the first invariant of the stress tensor and  $\sigma_{\text{VM}}$  is the equivalent stress according to von Mises [25]. This expression is known as the Stassi-D'Alia criterion [26], while similar expressions were used by Raghava [27] and Christensen [28]. However, since it originated in a paper by Schleicher [29], which was based on von Mises work [25] and

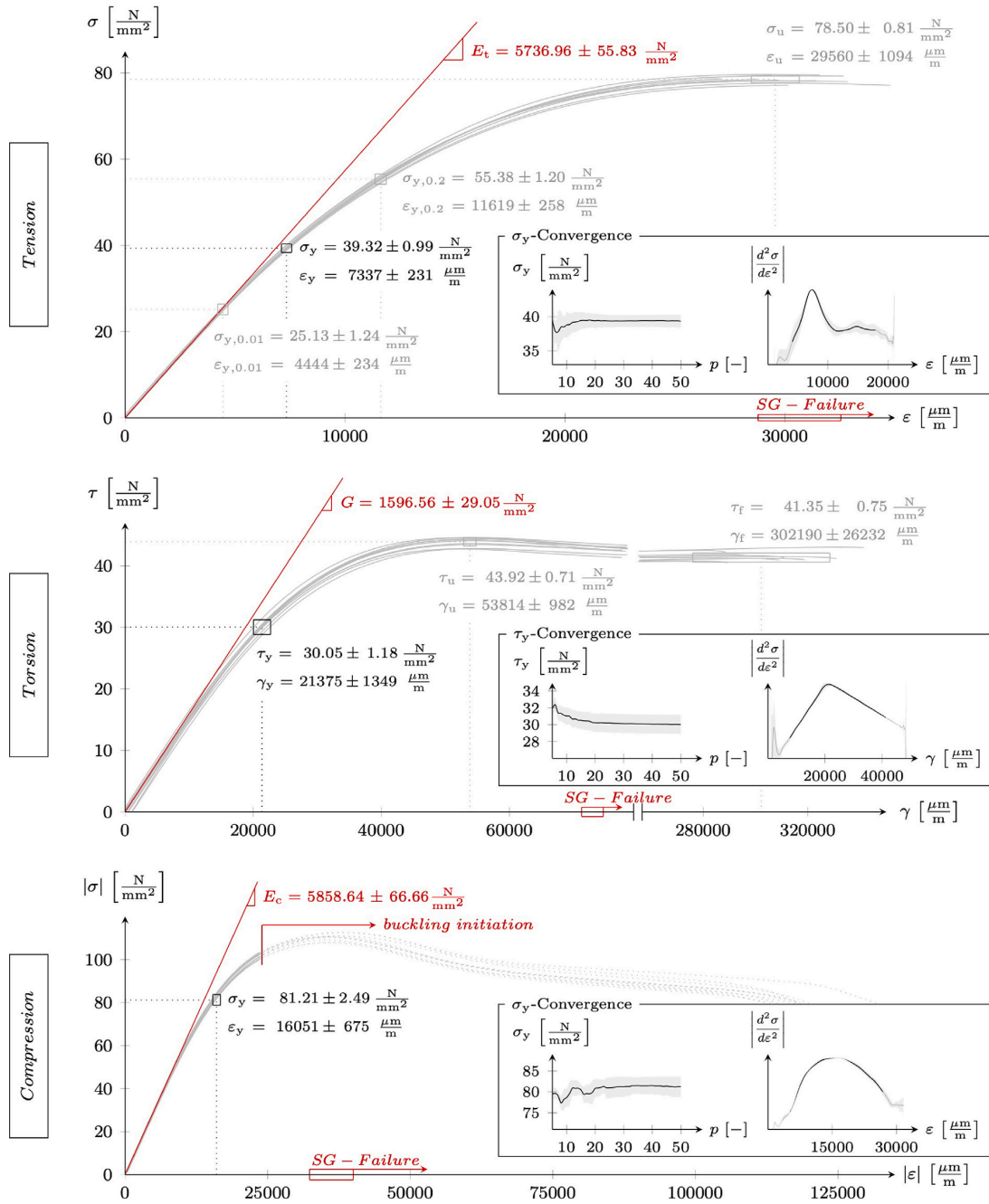


Fig. 6. Stress-strain diagram for uniaxial tension, torsion and compression with mechanical properties regarding the yield, ultimate and failure stress-strain state. The scatter of the respective points is depicted by the size of the boxes. The yield point ( $\epsilon_y, \sigma_y$ ) is based on the absolute maximum of the second derivative of the stress-strain curve. The dependency of  $\sigma_y$  on the polynomial degree  $p$  of the stress-strain curve fit is shown in the inserted figure, where the mean value of all specimens is shown in black and the standard deviation is indicated in gray. The other yield points were detected with the respective plastic offset strains indicated in the indices. Strain gauge (SG) failure is indicated at the x-axis. In case of the compression test the ends of the stress-strain curves mark the first crack, not the complete failure. Buckling initiation was estimated based on a video analysis.

was also commented by von Mises, it is referred to as the von Mises-Schleicher criterion in this work. Using Eq. (14) with the exemplary properties given in Fig. 7 results in 50 MPa for each point on the yield locus, which is equal to the yield strength in tension. Whether a certain point is on the yield locus can also be checked with the equation for

the (shifted) ellipsis itself, which is defined by

$$\frac{(\sigma - \sigma_0)^2}{a^2} + \frac{\tau^2}{b^2} = 1. \quad (15)$$

In case a point is not on the yield locus, the equivalent state can still be calculated by scaling the original yield ellipsis. Assume the point

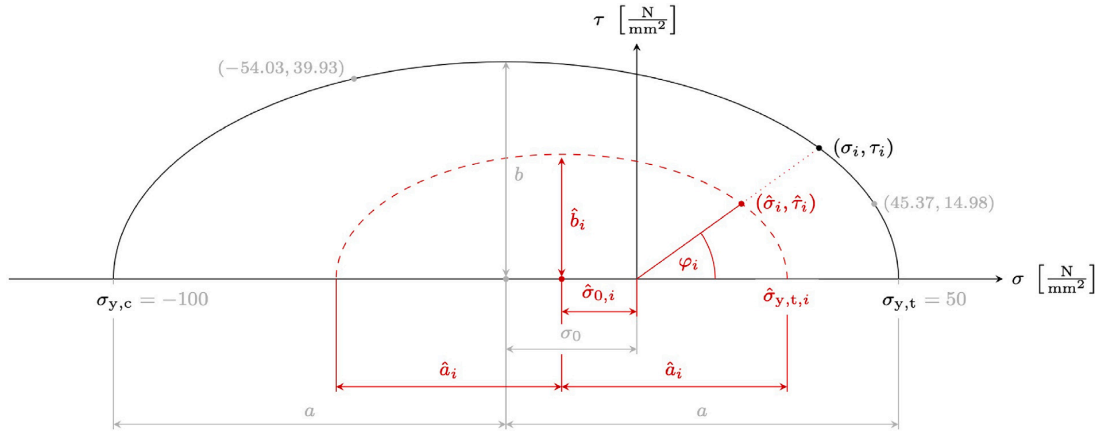


Fig. 7. Depiction of the ellipsis scaling approach based on an idealized, fictitious yield locus. Every point on a yield locus will lead to an equivalent stress, which is equal to the yield strength in tension. If a point  $(\hat{\sigma}_i, \hat{\tau}_i)$  is not on the original yield locus, the intersection point  $(\sigma_i, \tau_i)$  can be found. The relative ratios of these points can be used to calculate a scaled ellipsis (red) and therefore the scaled yield strength, which resembles the equivalent stress for  $(\hat{\sigma}_i, \hat{\tau}_i)$

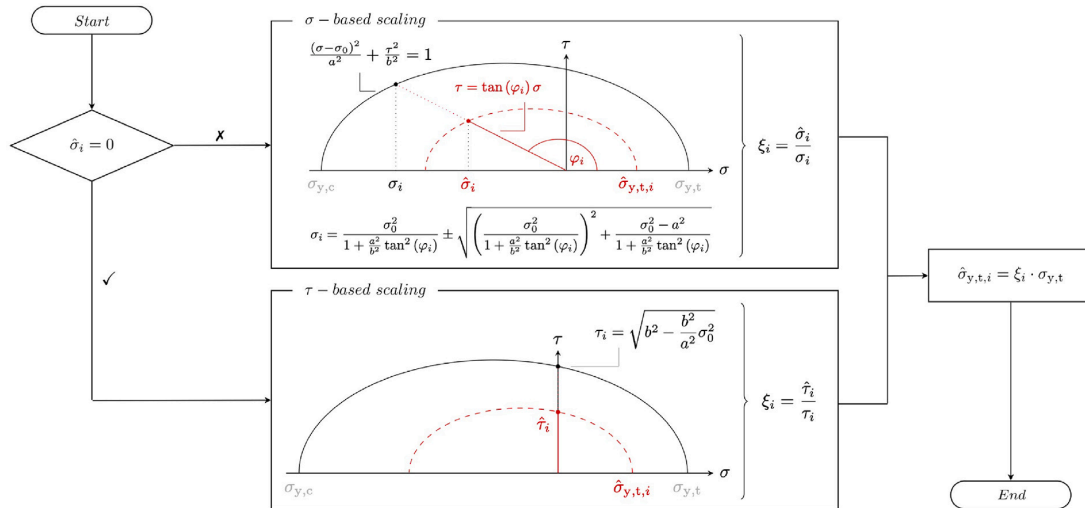


Fig. 8. Flow chart of the ellipsis scaling approach to calculate equivalent stresses based on an original ellipsis fit (yield locus) of experimental results.

$(\hat{\sigma}_i, \hat{\tau}_i)$  in Fig. 7 shall be converted to the equivalent stress–strain space  $\mathbb{R}^{eqV}$ . Based on the coordinates of the respective point, a linear equation can be computed, which passes the origin. This linear equation is given by

$$\tau = \tan(\varphi) \cdot \sigma \tag{16}$$

and can be inserted into Eq. (15) to find their intersection point  $(\sigma_i, \tau_i)$ . Once the intersection point is found, the scaled ellipsis parameters  $(\hat{\sigma}_0, \hat{a}, \hat{b})$  can be calculated, because the ratios of the scaled ellipsis parameter and the measured yield ellipsis remain constant:

$$\frac{\hat{\sigma}_i}{\sigma_i} = \frac{\hat{\tau}_i}{\tau_i} = \frac{\hat{b}_i}{b} = \frac{\hat{a}_i}{a} = \frac{\hat{\sigma}_{0,i}}{\sigma_0} = \frac{\hat{\sigma}_{y,t,i}}{\sigma_{y,t}} = \xi_i \tag{17}$$

Based on the scaling factor  $\xi_i$  the scaled yield strength  $\hat{\sigma}_{y,t,i}$  can be found, which reflects the equivalent stress for the given point  $(\hat{\sigma}_i, \hat{\tau}_i)$ . A flow chart of the required computations is given in Fig. 8. The yield strain can be found in a similar way when the  $\sigma - \tau$  coordinates are replaced with the corresponding  $\varepsilon - \gamma$  coordinates.

In case a time series needs to be converted to  $\mathbb{R}^{eqV}$ , this procedure must be repeated for each point within the series. The proposed scaling

process was compared to different yield criteria for randomized time histories, showing perfect agreement. Therefore, the conducted biaxial experiments were converted to  $\mathbb{R}^{eqV}$  using the proposed scaling method, followed by the yield point detection based on the second derivative of the equivalent stress–strain curve. The results of the biaxial experiments are summarized in Fig. 9 and Table 1.

The benefit of this scaling approach is that it only requires the original yield locus as an input, which can be an ellipsis fit of uniaxial experiments. An a priori knowledge of an appropriate yield criterion is therefore not necessary to calculate equivalent stresses and strains in terms of multiaxial experiments in combination with the derivative-based yield point detection. A potential bias of the results, due to an a priori chosen yield criterion is therefore minimized. The only assumption made, is that the initial yield locus is an ellipsis, which is valid for most engineering materials.

#### 4.4. Yield locus

The best fit ellipsis passing the yield points of the uniaxial tension, torsion and compression tests were found based on a non-linear

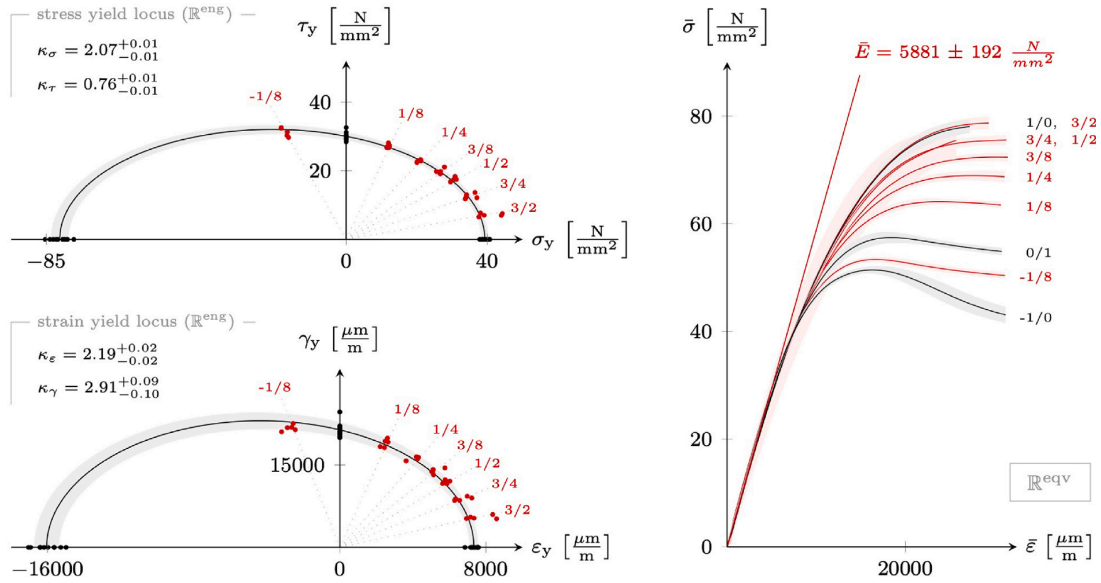


**Fig. 9.** Stress and strain yield locus of the analyzed adhesive with indications of the initial strain rate ratio  $\dot{\epsilon}_0/\dot{\gamma}_0$ . Both ellipses were fitted to the yield points of the uniaxial experiments. The yield points of biaxial ratios were determined based on the proposed ellipsis scaling approach and the resulting equivalent stress–strain curves ( $\mathbb{R}^{eqv}$ ) shown on the right. The equivalent stress–strain curves are clipped at  $\bar{\epsilon} = 31500 \mu\text{m}/\text{m}$  to improve the visibility of the linear elastic part.

**Table 1**

Summarized yield points for all static experiments conducted. For each initial strain rate ratio  $\dot{\epsilon}_0/\dot{\gamma}_0$  the amount of tested specimens is indicated by  $n$ . The derivative-based yield point ( $\bar{\epsilon}_y, \bar{\sigma}_y \in \mathbb{R}^{eqv}$ ) was determined using a polynomial fit to uniaxial stress–strain curves. In the case of the biaxial tests, these curves were estimated based on the ellipsis scaling approach presented in this work.  $\epsilon$  and  $\gamma$  as well as  $\sigma$  and  $\tau$  represent the stress–strain space coordinates ( $\mathbb{R}^{eng}$ ) of the respective yield points in the equivalent stress–strain space

$\dot{\epsilon}_0/\dot{\gamma}_0$ [-]	$n$ [-]	$\bar{\epsilon}_y$ [ $\mu\text{m}/\text{m}$ ]	$\epsilon$ [ $\mu\text{m}/\text{m}$ ]	$\gamma$ [ $\mu\text{m}/\text{m}$ ]	$\bar{\sigma}_y$ [ $\text{N}/\text{mm}^2$ ]	$\sigma$ [ $\text{N}/\text{mm}^2$ ]	$\tau$ [ $\text{N}/\text{mm}^2$ ]
1/0	10	7337 ± 231	7337 ± 231	0 ± 0	39.32 ± 0.99	39.32 ± 0.99	0.00 ± 0.00
3/2	5	7980 ± 733	7675 ± 748	5436 ± 315	42.05 ± 3.20	40.62 ± 3.26	7.16 ± 0.46
3/4	5	7545 ± 408	6674 ± 410	8842 ± 318	39.88 ± 1.65	35.09 ± 1.57	12.59 ± 0.76
1/2	5	7470 ± 153	5823 ± 144	11898 ± 308	40.25 ± 0.98	30.64 ± 0.64	17.58 ± 0.60
3/8	5	7512 ± 317	5220 ± 297	13873 ± 481	39.50 ± 1.26	26.71 ± 0.80	19.79 ± 0.80
1/4	5	7332 ± 306	4001 ± 344	16086 ± 343	38.99 ± 0.68	20.70 ± 0.55	22.88 ± 0.34
1/8	5	7430 ± 296	2475 ± 170	18973 ± 711	39.74 ± 0.76	11.91 ± 0.33	27.20 ± 0.55
0/1	10	7337 ± 463	0 ± 0	21375 ± 1349	39.32 ± 1.54	0.00 ± 0.00	30.05 ± 1.18
-1/8	5	6976 ± 200	-2739 ± 296	21715 ± 567	38.40 ± 1.56	-17.31 ± 1.02	31.25 ± 1.28
-1/0	10	7337 ± 309	-16051 ± 675	0 ± 0	39.32 ± 1.20	-81.21 ± 2.49	0.00 ± 0.00

least squares optimization assuming that the major axis of the ellipses coincide with the  $x$ -axis. The resulting ellipses equations are given by

$$\frac{(\sigma + 20.95)^2}{60.27^2} + \frac{\tau^2}{32.04^2} = 1, \quad (18)$$

$$\frac{(\epsilon + 4357)^2}{11694^2} + \frac{\gamma^2}{23034^2} = 1. \quad (19)$$

As explained in Section 4.3, these ellipses were subsequently used to calculate the equivalent stress–strain curves and the derivative-based yield points of the biaxial tests. These yield points were found to be very close to the mean ellipses. Only a few yield points were located outside the standard deviation of the ellipses. It is therefore concluded that the estimated ellipses in Fig. 9 accurately represent the yield locus for the investigated material.

The standard deviation of the ellipses is a result of the scatter of the uniaxial tests, cf. Table 1. It can be expressed by the ratio of the upper or lower limits (mean value ± standard deviation) of the identified yield strength or yield strain, leading to a set of yield strength and strain ratios given by

$$\kappa_\sigma = \frac{|\sigma_{y,c}|}{\sigma_{y,t}}, \quad \kappa_\tau = \frac{\tau_y}{\sigma_{y,t}}, \quad (20)$$

$$\kappa_\epsilon = \frac{|\epsilon_{y,c}|}{\epsilon_{y,t}}, \quad \kappa_\gamma = \frac{\gamma_y}{\epsilon_{y,t}}. \quad (21)$$

The respective standard deviations are shown in Fig. 9. Another way to verify the validity of the results is to check the equivalent Young's modulus  $\bar{E}$  of the equivalent stress–strain curves, which are shown on the right of Fig. 9. For all curves depicted  $\bar{E}$  is  $5881 \pm 192 \text{ N}/\text{mm}^2$ , which corresponds to a coefficient of variation of 3.3 % and represents a sufficiently small deviation from the ideal case of a unified modulus, confirming the applied methodology.

## 5. Result discussion

The results of the previous section are discussed below with respect to applied simplifications and accuracy.

### 5.1. Bi-modularity

The elastic modulus in compression was found to be 2.1 % higher than the modulus in tension. Assuming that the measurement data of the elastic moduli was normally distributed, this difference was verified to be significant by means of a t-test. In case of the Poisson's ratio the difference is 6.7 %. The material can therefore be classified as bi-modular, see Table 2. The bi-modularity of the adhesive is also reflected by different values of the yield strength ratio ( $\kappa_\sigma = 2.07$ ) and yield strain ratio ( $\kappa_\epsilon = 2.19$ ). Although all mentioned differences are rather small, it is expected that they will have a significant influence in a fatigue analysis.

**Table 2**  
Stiffness parameters and check for bi-modularity. Differences to [13] originate from the use of true stresses and strains.

$\dot{\epsilon}_0/\dot{\gamma}_0$	Parameter	Frequency Distributions
1/0	$E_t$	$5737 \pm 56 \frac{N}{mm^2}$
	$\nu_t$	$0.374 \pm 0.005$
-1/0	$E_c$	$5859 \pm 67 \frac{N}{mm^2}$
	$\nu_c$	$0.401 \pm 0.005$
0/1	$G$	$1597 \pm 29 \frac{N}{mm^2}$

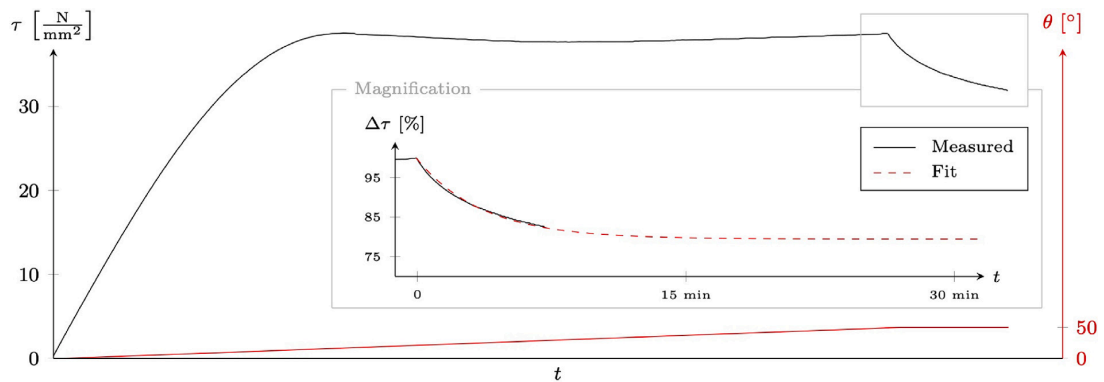


Fig. 10. Shear stress relaxation observed in a torsion setup test during a phase of constant angular displacement.

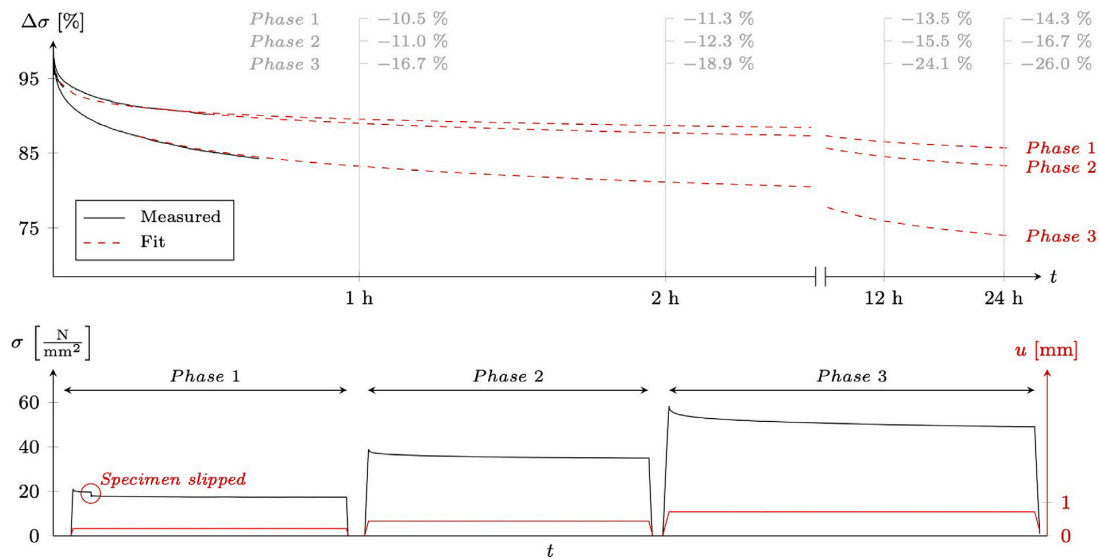


Fig. 11. Tensile stress relaxation in 3 consecutive phases with constant displacement.

5.2. Viscoelasticity

The yield locus was determined without viscoelasticity taken into account, although viscoelastic behavior, such as stress relaxation, was observed during preliminary tests.

The observed shear stress relaxation is shown in Fig. 10 and the tensile stress relaxation in Fig. 11. Note that in both cases the stress recovery was recorded with constant displacement, not with constant strain, since the specimens used for these preliminary tests were not

equipped with strain gauges. The specimens also did not fail at the end of the recording shown in Figs. 10 and 11.

The shear stresses were calculated based on the fully plastic formulation, Eq. (5), as the recovery was observed in the fully plastic regime. Moreover, it is emphasized that this observation was a by-product of the machine setup test and was not directly intended as a stress-relaxation test. Hence, e.g., the recorded relaxation time is quite short. Nevertheless the results are shown here as proof of the viscoelastic behavior.

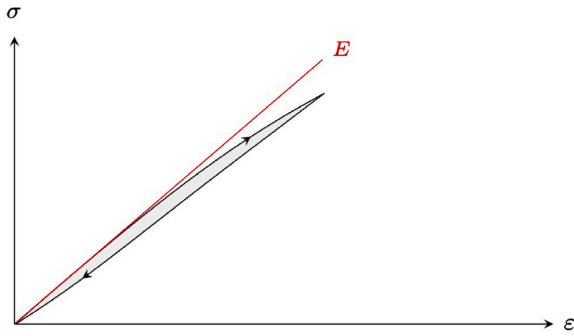


Fig. 12. Idealized viscoelastic hysteresis loop. Due to relaxation effects, the stress-strain state in this example is still completely elastic.

Power law functions were used to fit and extend the data of the torsion and tension relaxation phases. In the case of the torsion test it is predicted that about 20 % of the initial stress level is recovered after 15 min.

The tensile stress recovery was analyzed in three consecutive phases with an additional specimen to investigate the influence of the load level and plasticity on the stress recovery. The load level of phase 2 was chosen in such a way that it roughly corresponds to the tensile yield point identified in Section 4.1. The results show an increasing relaxation rate with increasing levels of plasticity. The tensile relaxation was also found to be slower than the shear stress relaxation, which is interpreted as another indication of the anisotropy of the material and the manufactured specimens, respectively.

It is expected that the viscoelastic behavior will postpone the yielding and therefore lead to higher yield strengths and strains. This is because recovery effects were mostly suppressed by the continuous loading (displacement control) within the yield locus experiments. Some amount of plastic strain in the stress-strain diagrams (Fig. 6) will therefore recover when the test is stopped. Fig. 12 visualizes this effect. As a result, the yield locus derived in this work is assumed to be a conservative estimation.

Apart from that, the stress recovery will influence the development of residual stresses within the adhesive, e.g., during the rotor blade manufacturing process.

### 5.3. Comparison to existing yield criteria

The derived stress yield locus was compared to several yield criteria that have been used to evaluate rotor blade adhesives elsewhere [30–32]. The comparison is shown in Fig. 13.

The von Mises–Schleicher criterion, Eq. (14), which was reported as a good fit in [8,10] (mentioned as the Stassi-D’Alia criterion, cf. Section 4.3) was found to be non-conservative leading to an overestimation of the yield strength in shear of about 7.9 %. This again underlines the importance of high quality specimens as well as proper consideration of elasto-plastic shear stresses, cf. Section 3.2.

The Drucker–Prager criterion [33] given by

$$\sigma_{DP} = \frac{(\kappa_\sigma - 1)J_1 + (\kappa_\sigma + 1)\sigma_{VM}}{2\kappa_\sigma} \quad (22)$$

is more conservative regarding shear stresses and led to a moderate overestimation of the yield strength in shear of about 1.8 %. This difference is within the range of the standard deviation of the yield strength in shear. In general the predictions of this criterion were very close to the ellipsis fit and the majority of the experimental results lies within the standard deviation of the criterion, which results from both the standard deviation of the yield strength in tension  $\sigma_{y,t}$  and that of the yield strength ratio  $\kappa_\sigma$ .

Criteria that do not account for the strength asymmetry in tension and compression, such as the von Mises [25] criterion, are expectedly very conservative in compression and shear. Since this kind of criteria can also be expressed as special cases of the asymmetric criteria with, e.g.,  $\kappa_\sigma = 1$ , the symmetric criteria seem obsolete. The asymmetric criteria can also be used for varying orientations of the reinforcement fibers by adjusting the yield strength ratio, bearing in mind that the yield locus derived in this work is only valid for the anisotropic specimen of this work, cf. Section 2. In terms of biaxial loading, the proposed ellipsis scaling approach represents a very flexible formulation of the yield locus as it is not limited to a specific material or theory.

The derived strain yield locus was compared to different formulations of the von Mises equivalent strain, see Fig. 13. Similar to the stress yield locus, the standard (symmetric) formulation provided the least accurate results. An adaptation of the Drucker–Prager stress formulation given by

$$\epsilon_{DP} = \frac{(\kappa_\epsilon - 1)J_1 + (\kappa_\epsilon + 1)(1 - 2\nu)\epsilon_{VM}}{2\kappa_\epsilon(1 - 2\nu)} \quad (23)$$

was a good improvement, but was still too conservative regarding shear. In Eq. (23)  $J_1$  is the first invariant of the strain tensor. The low accuracy in shear originates from the incorporation of the isotropic relationship of  $E$ ,  $G$  and  $\nu$ , see Eq. (2), in the standard von Mises formulation, which is not changed by scaling. Acceptable results can be achieved for the biaxial case by avoiding the aforementioned isotropic relation for the shear strains by using their anisotropic pendants  $E_{\parallel}$  and  $G_{\perp\parallel}$ , when the (biaxial) von Mises strain formulation is derived from the stress formulation:

$$\epsilon_{vM,iso} = \frac{\sigma_{VM}}{E} = \sqrt{\epsilon^2 + \frac{1}{4(1+\nu)^2} \cdot 3\gamma^2}, \quad (24)$$

$$\epsilon_{vM,aniso} = \frac{\sigma_{VM}}{E_{\parallel}} = \sqrt{\epsilon^2 + \frac{G_{\perp\parallel}^2}{E_{\parallel}^2} \cdot 3\gamma^2}. \quad (25)$$

This adaptation is, however, only valid for biaxial combinations of normal forces and torque and cannot be generalized, because that requires additional knowledge of the stiffness properties in all directions.

Based on the very good fit of the Drucker–Prager criterion to the experimental 2D stress and strain yield loci, it is expected that this criterion also approximates the 3D yield surface of the adhesive sufficiently in terms of common engineering applications. However, additional experimental verification is necessary to proof its validity in 3D stress states.

## 6. Conclusion

In this work, the yield surface of a structural adhesive was derived by means of multiaxial experiments. The utilized adhesive was short glass fiber-reinforced and is commonly used for the manufacture of wind turbine rotor blades. Yielding was identified when the absolute maximum of the second derivative of the stress-strain curve was reached.

To be able to detect yielding during elasto-plastic stress-strain states in torsional experiments, a practical spline-based transition approach was developed to connect the fully elastic and fully plastic regimes. In the approach the transition spline is iteratively updated until the resulting calculated torque matches the experimentally determined one.

Ellipses were fitted to the yield points in uniaxial tension, compression and torsion. Based on a proposed scaling approach of these ellipses, equivalent stresses and strains could be calculated, enabling the yield point detection in biaxial, axial-torsional load cases. The resulting yield points were very close to the initially fitted ellipses. In addition, the coefficient of variation of the Young’s modulus in the equivalent stress-strain space was very low. Both of these findings were interpreted as a verification of the applied methodology.

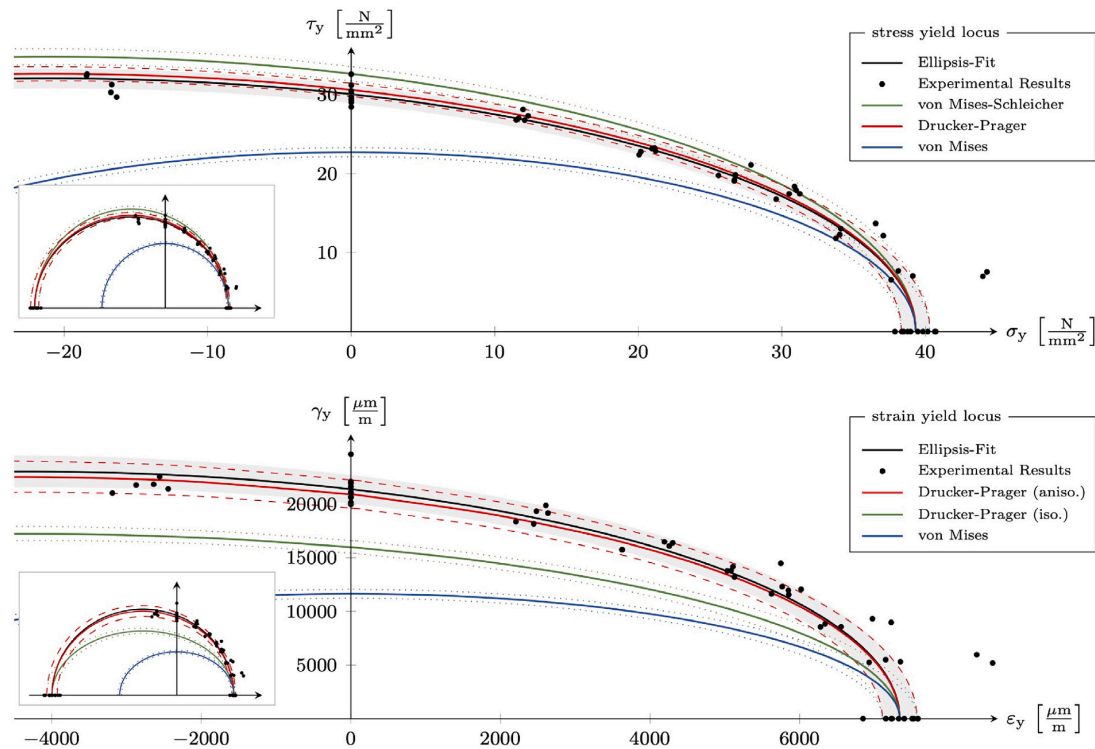


Fig. 13. Stress and strain yield locus comparison with different yield criteria. The main figures are zoomed in sections of the whole figures shown in the respective bottom left. The standard deviation of the respective criteria is indicated by dashed or dotted lines.

The experimentally identified stress yield locus is a very good match to the Drucker–Prager criterion. A reliable and safe usage of this criterion in biaxial ( $\sigma/\tau$ ) load cases is provided by the low overall scatter of the results and design-driving yield strengths. In case of the strain yield locus an anisotropic equivalent strain formulation is required for a sufficient fit. An adaption of the Drucker–Prager criterion to the 3D yield surface is expected to be a valid engineering approximation, given the excellent fit of the criterion to the 2D yield loci. However, further experimental verification is required to validate this hypothesis.

Although the material was proven to exhibit viscoelastic behavior, this was not accounted for in the yield surface determination. Stress relaxation effects were therefore mostly suppressed in the continuous, displacement-controlled experiments. Based on that, it was concluded that the derived yield surface is a conservative approximation. Nevertheless the results in this work are still expected to represent an accurate approximation for engineering purposes, given that the underlying specimens were virtually free of imperfections such as mixing inhomogeneities or porosities. However, given the anisotropic properties of the specimens, the identified yield surface is only valid for the fiber orientation present in the specimens of this work. The determination of the fiber orientation will be done in an upcoming publication. In addition, the validity of the Drucker–Prager criterion will be analyzed for specimens with different fiber orientations to verify its general applicability to the adhesive.

#### CRediT authorship contribution statement

**Michael Wentingmann:** Development and implementation of the proposed methods, yield surface analysis, post-processing of the  $\mu$ CT-scan-segmentation, illustrations and writing of the paper. **Nikolas Manousides:** High-resolution X-ray microscopy ( $\mu$ CT-scanning) of the specimens and segmentation pre-processing. **Alexandros Antoniou:**

Scientific advice and support with executing the experiments at Fraunhofer IWES. **Claudio Balzani:** Conceptual guidance and scientific supervision of all project phases.

#### Declaration of competing interest

The authors declare that they have no known competing financial interests or personal relationships that could have appeared to influence the work reported in this paper.

#### Data availability

The raw/processed data required to reproduce these findings cannot be shared at this time due to legal or ethical reasons.

#### Acknowledgments

This work was supported by the German Federal Ministry for Economic Affairs and Climate Action (BMWK) in the ReliaBlade project (grant numbers 0324335A, 0324335B).

#### References

- [1] R.M. Christensen, Observations on the definition of yield stress, *Acta Mech.* 196 (2008) 239–244, <http://dx.doi.org/10.1007/s00707-007-0478-0>.
- [2] R.M. Christensen, *The Theory of Materials Failure*, Oxford University Press, 2016, 978-0198794707.
- [3] G. Hu, K. Zhang, S. Huang, J.-W.W. Ju, Yield surfaces and plastic flow of 45 steel under tension-torsion loading paths, *Acta Mech. Solida Sin.* 25 (2012) 348–360, [http://dx.doi.org/10.1016/S0894-9166\(12\)60032-9](http://dx.doi.org/10.1016/S0894-9166(12)60032-9).
- [4] H.A. Lauer, N.K. Gupta, A study of yield surface upon reversal of loading under biaxial stress, *ZAMM - J. Appl. Math Mech / Zeitschrift für Angewandte Mathematik und Mechanik* 63 (1983) 497–504, <http://dx.doi.org/10.1002/zamm.19830631005>.

- [5] W.M. Mair, H.L.D. Pugh, Effect of pre-strain on yield surfaces in copper, *J. Mech. Eng Sci* 6 (1964) 150–163, [http://dx.doi.org/10.1243/JMES\\_JOUR\\_1964\\_006\\_025\\_02](http://dx.doi.org/10.1243/JMES_JOUR_1964_006_025_02).
- [6] P.M. Naghdi, F. Essenburg, W. Koff, An experimental study of initial and subsequent yield surfaces in plasticity, *J. Appl. Mech.* 25 (1958) 201–209, <http://dx.doi.org/10.1115/1.4011745>.
- [7] A. Phillips, H. Moon, An experimental investigation concerning yield surfaces and loading surfaces, *Acta Mech.* 27 (1977) 91–102, <http://dx.doi.org/10.1007/BF01180078>.
- [8] G. Fernandez, D. Vandepitte, H. Usabiaga, S. Debruyne, Static and cyclic strength properties of brittle adhesives with porosity, *Int. J. Fatigue* 117 (2018) 340–351, <http://dx.doi.org/10.1016/j.ijfatigue.2018.08.018>.
- [9] R.K. Mittal, I.P. Singh, Large deformation behavior of some thermoplastics, *Polymer Eng. Sci* 22 (1982) 358–364, <http://dx.doi.org/10.1002/pen.760220606>.
- [10] D. Zarouchas, R. Nijssen, Mechanical behaviour of thick structural adhesives in wind turbine blades under multi-axial loading, *J. Adhes. Sci. Technol.* 30 (2016) 1413–1429, <http://dx.doi.org/10.1080/01694243.2016.1146392>.
- [11] J. Zhang, H. Jiang, G. Kang, C. Jiang, F. Lu, A new form of equivalent stress for combined axial-torsional loading considering the tension-compression asymmetry of polymeric materials, *RSC Adv.* 5 (2015) 72780–72784, <http://dx.doi.org/10.1039/C5RA15230E>.
- [12] G.I. Taylor, H. Quinney, The plastic distortion of metals, *Philosoph. Trans R. Soc London. Ser A, Containing Papers of A Mathematical Or Physical Character* 230 (1931) 323–362, <http://dx.doi.org/10.1098/rsta.1932.0009>.
- [13] M. Wentingmann, N. Manousides, A. Antoniou, C. Balzani, Design and manufacturing optimization of epoxy-based adhesive specimens for multiaxial tests, *Mater. Des.* 212 (2021) 110213, <http://dx.doi.org/10.1016/j.matdes.2021.110213>.
- [14] Hexion™, Technical Data Sheet - EPIKOTE™ Resin MGS™ BPR 135G-Series and EPIKURE™ Curing Agent MGS™ BPH 134G-137GF, 2021.
- [15] A.G. Carl Zeiss, Zeiss Xradia 410 Versa, 2021, Accessed: June, 2022, <https://www.zeiss.com/microscopy/int/products/x-ray-microscopy/zeiss-xradia-410-versa.html>.
- [16] Walter + Bai AG, Axial / torsional test systems, 2021, Accessed: June, 2022, [https://www.walterbai.com/page/products/Materials\\_Testing\\_Systems/Axial-Torsional\\_Testing\\_System/index.php](https://www.walterbai.com/page/products/Materials_Testing_Systems/Axial-Torsional_Testing_System/index.php).
- [17] Tokyo Measuring Instruments Laboratory Co., Ltd., GFRAB-3-350-50, 2021, Accessed: June, 2022, [https://tml.jp/e/product/strain\\_gauge/gf\\_list.html](https://tml.jp/e/product/strain_gauge/gf_list.html).
- [18] ASTM E2207-15, Standard practice for strain-controlled axial-torsional fatigue testing with thin-walled tubular specimens, 2021.
- [19] R. Brecht, Kritische Bemerkungen zur Drehungselastizität, 1896, *ZVDI* 40, No. 28, S. 785–790 and No. 29, S. 813–817.
- [20] J.T.P. de Castro, M.A. Meggiolaro, *Fatigue Design Techniques under Real Service Loads. Volume II - Low-Cycle and Multiaxial Fatigue, 1.*, CreateSpace Independent Publishing Platform, 2016, 978-1530797042.
- [21] Matlab®, R2020b, 2021.
- [22] J. Chakrabarty, *Applied Plasticity, Second Edition*, Springer, 2010, 978-0387776736.
- [23] A. Savitzky, M.J.E. Golay, Smoothing and differentiation of data by simplified least squares procedures, *Anal. Chem.* 36 (1964) 1627–1639, <http://dx.doi.org/10.1021/ac60214a047>.
- [24] V.C. Beber, P.H.E. Fernandes, J.E. Fragato, B. Schneider, M. Brede, Influence of plasticity on the fatigue lifetime prediction of adhesively bonded joints using the stress-life approach, *Appl. Adhesion Sci* 4 (2016) 1–18, <http://dx.doi.org/10.1186/s40563-016-0062-8>.
- [25] R. von Mises, *Mechanik der festen Körper im plastisch-deformablen Zustand, Nachrichten von der Gesellschaft der Wissenschaften zu Göttingen, Mathematisch-Physikalische Klasse* 4 (1913) 582–592.
- [26] F. Stassi-D'Alia, Flow and fracture of materials according to a new limiting condition of yielding, *Meccanica* 2 (1967) 178–195, <http://dx.doi.org/10.1007/BF02128173>.
- [27] R. Raghava, R.M. Caddell, G.S.Y. Yeh, The macroscopic yield behaviour of polymers, *J. Mater Sci* 8 (1973) 225–232, <http://dx.doi.org/10.1007/BF00550671>.
- [28] R.M. Christensen, A two-property yield, failure (fracture) criterion for homogeneous, isotropic materials, *J. Eng. Mater Technol* 126 (2004) 45–52, <http://dx.doi.org/10.1115/1.1631024>.
- [29] F. Schleicher, Der Spannungszustand an der Fließgrenze (Plastizitätsbedingung), *ZAMM - J. Appl Math Mech / Zeitschrift für Angewandte Mathematik und Mechanik* 6 (3) (1926) 199–216, <http://dx.doi.org/10.1002/zamm.19260060303>.
- [30] A.E. Antoniou, M.M. Vespermann, F. Sayer, A. Krimmer, Life prediction analysis of thick adhesive bond lines under variable amplitude fatigue loading, in: 18th European Conference on Composite Materials (ECCM18), 2018, <http://dx.doi.org/10.5281/zenodo.3558781>.
- [31] P. Noever Castelos, C. Balzani, On the impact of multi-axial stress states on trailing edge bondlines in wind turbine rotor blades, *J. Phys. Conf. Ser.* 753 (2016) 062002, <http://dx.doi.org/10.1088/1742-6596/753/6/062002>.
- [32] D.S. Zarouchas, A.A. Makris, F. Sayer, D. Van Hemelrijck, A.M. Van Wingerde, Investigations on the mechanical behavior of a wind rotor blade subcomponent, *Composites B* 43 (2012) 647–654, <http://dx.doi.org/10.1016/j.compositesb.2011.10.009>.
- [33] D.C. Drucker, W. Prager, Soil mechanics and plastic analysis or limit design, *Quart. Appl. Math.* 10 (1952) 157–165, <http://dx.doi.org/10.1090/qam/48291>.



## 4

# Fatigue properties of a structural rotor blade adhesive under axial and torsional loading

3<sup>rd</sup> Paper

Subsequent to the static characterization, the material behavior of the adhesive is analyzed under uniaxial fatigue loading. The data from these experiments serves as the basis for intended (non-proportional) fatigue life predictions, as it enables the construction of a Haigh diagram and can be used to calibrate critical plane models. Different S-N models are compared to identify the best-fit and to derive an engineering approximation for gigacycle fatigue applications. Accompanying stiffness degradation measurements allow to derive a detailed load level-dependent model and a residual fatigue life prediction of run-out specimens.

---

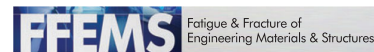
P3-1	Introduction .....	58
P3-2	Specimens and fatigue test setup ...	59
P3-3	Uniaxial S-N curves .....	62
P3-4	Stiffness degradation .....	70
P3-5	Conclusion .....	74



Received: 7 June 2022 | Revised: 17 October 2022 | Accepted: 4 December 2022

DOI: 10.1111/ffe.13925

## ORIGINAL ARTICLE



WILEY

# Fatigue properties of a structural rotor blade adhesive under axial and torsional loading

Michael Kuhn<sup>1</sup> | Nikolas Manousides<sup>1</sup> | Alexandros Antoniou<sup>2</sup> | Claudio Balzani<sup>1</sup>

<sup>1</sup>Institute for Wind Energy Systems, Leibniz University Hannover, Hannover, Germany

<sup>2</sup>Institute for Wind Energy Systems, Fraunhofer IWES, Bremerhaven, Germany

**Correspondence**

Michael Kuhn, Institute for Wind Energy Systems, Leibniz University Hannover, Appelstraße 9A, 30167 Hannover.  
Email: [research@iwes.uni-hannover.de](mailto:research@iwes.uni-hannover.de)

**Funding information**

BMWK; German Federal Ministry for Economic Affairs and Climate Action (BMWK), Grant/Award Numbers: 0324335A, 0324335B

**Abstract**

Axial and torsional fatigue tests at different stress ratios were performed on a structural adhesive designed for wind turbine rotor blades. By employing previously optimized specimens, fatigue properties were recorded without influences of manufacturing-induced defects such as pores. The Stüssi S–N model was an excellent fit to the data and was combined with a Haibach extension line to account for uncertainties in the gigacycle fatigue regime. A comparison of the results with hand-mixed specimens revealed significant and load level-dependent differences, indicating that manufacturing safety factors should be applied to the slope of the S–N curve. The experiments were accompanied by stiffness degradation measurements, which enabled an analysis of Young's and shear modulus degradation interactions. The degradation was modeled using power law fits, which incorporated load level-dependent fitting parameters to allow for a full description of the stiffness reduction and a prediction of the residual fatigue life of run-out specimens.

**KEYWORDS**

multiaxial fatigue, porosity, stiffness degradation, structural adhesives, wind turbine rotor blades

## 1 | INTRODUCTION

In order to assure the structural reliability of a material in cyclic loading conditions, experimental fatigue tests have to be conducted. This way, the dependence of the material properties on the load level and the cycles to failure can be established. In most cases, this is done with coupon specimens whose results are transferred to the analysis of more complex structures. Hence, coupon level fatigue tests are most representative for these structures if the manufacturing and general processing of the

respective material is done in a comparable way for the coupon specimens and the final structure.

### 1.1 | Fatigue in bond lines of wind turbine rotor blades

In the manufacture of wind turbine rotor blades, two aerodynamic half shells and multiple shear webs are joined using structural adhesives. On account of the size of the separate parts, the adhesive also serves as a mitigation for

This is an open access article under the terms of the [Creative Commons Attribution](https://creativecommons.org/licenses/by/4.0/) License, which permits use, distribution and reproduction in any medium, provided the original work is properly cited.

© 2022 The Authors. *Fatigue & Fracture of Engineering Materials & Structures* published by John Wiley & Sons Ltd.

manufacturing tolerances. Therefore, the bond line geometry varies along the length of the blade, with common thickness variations between 10 and 15 mm.<sup>1-3</sup>

In addition to challenges in the manufacturing process, wind turbine rotor blades are exposed to very high fatigue loads. The rotation of the rotor imposes a varying gravitational load, which is superimposed by a stochastic wind load leading to complex multiaxial loads over a lifetime of at least 20 years.<sup>4-6</sup>

Given the high fatigue loads of rotor blades, a reliable characterization of the fatigue properties of the employed materials is of utmost importance. As the reliability of fatigue data directly impacts the applicable safety margins in the blade design, this greatly impacts the optimization potential as well. In addition, the advent of digital twins of rotor blades requires well-known margins of the material properties.<sup>1,7,8</sup>

## 1.2 | Experimental investigations of bond line fatigue

Although the adhesive application in rotor blade manufacturing is done using dosing machines,<sup>3</sup> which generally involves a vacuum-based mixing process, most publications on the mechanical properties of rotor blade adhesives are based on hand-mixed specimens.<sup>2,9-11</sup>

Due to high porosity levels attributed to hand-mixing, the derived material properties are diminished and are not representative for modern rotor blade manufacture. In a recent publication,<sup>12</sup> the porosity level of hand-mixed coupon specimens was compared with machine-mixed ones utilizing  $\mu$ CT scans. In a comparison with a scan of cured adhesive inside a conveyor hose of an industrial dosing and dispensing machine, it was found that the machine-mixed specimens had a comparable porosity level, while the quality of the hand-mixed specimens was insufficient to represent the industrial standard. In terms of material properties, it was proven that the ultimate static strength in tension of hand-mixed specimens was 33% less than that of machine-mixed specimens with negligible porosity. The plastic strain increased by a factor of 5.28, so that hand-mixed specimens could be classified as brittle while machine-mixed specimens were rather ductile. At the same time, the scatter of the static material properties drastically decreased for machine-mixed specimens in comparison with the hand-mixed ones; for example, the coefficient of variation of the tensile failure strength was 1.21% for the machine-mixed specimens while it was up to 12.92% for the hand-mixed ones. Since the scatter of fatigue tests can be expected to be much larger than in static tests, fatigue tests with hand-mixed specimens will lead to much more conservative and unreliable data sets.

Additionally, data on the stiffness degradation are scarce. However, since these data enable more comprehensive material modeling, they are a valuable byproduct of fatigue tests. A reliable stiffness degradation model might also be useful to estimate the residual fatigue life of run-out specimens. If the degradation is non-linear, the modeling of sequence effects in the fatigue life prediction might also be possible.

Note that the transfer of mechanical properties of (bulk) adhesive specimen to the joint and interface scale is not trivial due to manufacturing related effects resulting from the application and curing process (degree of polymerization, exothermicity, and residual stresses).<sup>12-15</sup> However, testing virtually defect free coupon specimens allows for a pristine material characterization, which in turn enables the quantification of effects of defects such as pores with additional (lower quality) coupon specimens or joint scale tests. This way, safety factors can be adapted to different manufacturing techniques, for example, in rotor blade manufacture, where pores might still occur due to the application process of the adhesive and reinforcement fibers within the adhesive might be aligned differently.

## 1.3 | Aims and outline

Since most contributions to the analysis of rotor blade bond line fatigue were based on hand-mixed specimens, compare Section 1.2, the scatter of the results might be governed by manufacturing imperfections. Therefore, it is difficult to derive fatigue properties of the material itself. This might also render the validation of damage prediction models impossible, especially in case of more complex multiaxial loading scenarios.

In order to derive more reliable fatigue properties, the optimized specimens from a previous study<sup>12</sup> are used in this work. These specimens allow for a fatigue characterization in both axial and torsional loads, while being virtually free of imperfections such as porosities. Separate specimens for different load scenarios are also not required, and possible stress concentration issues with different specimen geometries are prevented.

Section 2 summarizes the specimen manufacturing and testing conditions. The results of uniaxial fatigue tests and corresponding curve fits are shown in Section 3 followed by stiffness degradation measurements in Section 4.

## 2 | SPECIMENS AND FATIGUE TEST SETUP

The manufacturing of the utilized specimens and fatigue testing conditions are briefly explained in the following.

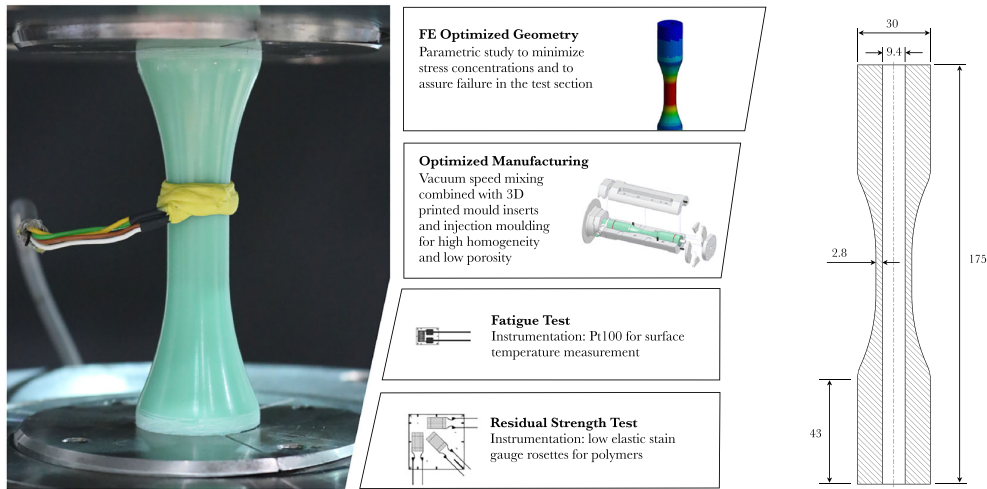


**FIGURE 1** Test setup for every fatigue test conducted. A Pt100 sensor is used to measure the surface temperature. In case a run-out is declared, a residual strength test is performed using strain gauge rosettes.<sup>16</sup> Optimization processes related to the specimen geometry and manufacturing were presented in a previous publication.<sup>12</sup> Dimensions in mm. [Colour figure can be viewed at [wileyonlinelibrary.com](http://wileyonlinelibrary.com)]



**FIGURE 2** Qualitative porosity comparison of the specimens used for this study. Pores are indicated in red. The specimen numbers are given left of the respective depictions. The specimens are sorted according to the respective cycles to failure shown in Table 1. [Colour figure can be viewed at [wileyonlinelibrary.com](http://wileyonlinelibrary.com)]

## 2.1 | Material system and manufacturing

The specimens used for the experiments in this work were made of EPIKOTE™ Resin MGS™ BPR 135G3 mixed with EPIKURE™ Curing Agent MGS™ BPH 137G.<sup>12</sup> The material is a structural adhesive and commonly used in the wind energy industry. It is epoxy-based and short glass fiber-reinforced.<sup>17</sup>

The tubular and tapered geometry of the specimens, compare Figure 1, was optimized in a parametric study based on finite element analyses, while the manufacturing employed vacuum speed mixing in combination with 3D printed mold inserts in an injection molding process. Details concerning the manufacturing process can be found in a dedicated paper.<sup>12</sup>

To verify the manufacturing quality regarding the porosity and mixing homogeneity, high-resolution X-ray microscopy ( $\mu$ CT scanning) was employed using a Zeiss Xradia 410 Versa.<sup>18</sup> The scans required for this work are depicted in Figure 2 and show that the porosity is negligible close to the test section. It should be noted that the scans did not allow for an analysis of the orientation of the reinforcement fibers as the voxel size was limited to approximately 32  $\mu\text{m}$ . This will be done in a future work. An anisotropy of the specimens was, however, confirmed by analogy of the stiffness in axial and torsional direction.<sup>12</sup> A primarily axial orientation of the reinforcement fibers is likely.

## 2.2 | Fatigue test setup

A servohydraulic Walter + Bai LFV 100-T2000 was used for the experiments, which has independent control of axial and torsional loads.<sup>19</sup> In combination with tubular specimens, the independency of the load application

allows for versatile tests, which are not feasible with, for example, arcan fixtures.

Since the measurement campaign of this work is based on a polymer, which was proven to show viscoelastic behavior,<sup>20</sup> in situ temperature measurements were conducted with Pt100 sensors attached to the surface of the specimens as shown in Figure 1. In order not to increase the specimens temperature too much (approximate limit: +5 K above ambient temperature), the test frequencies were adjusted at each load level. Simultaneously, the test frequency adaption lowers viscoelastic effects since the strain rate is more similar on the respective load levels than in tests with constant test frequencies.

The stiffness degradation measurements were inspired by Adden and Horst<sup>21</sup> and consisted of repeated displacement-controlled steps in axial and torsional direction. The amount of measurement repetitions resulted from a fixed number of cycles in between the degradation characterization steps. It was adjusted in such a way that the stiffness degradation could be modeled with at least 50 individual measurements for each specimen to assure a sufficient resolution of the data. Since the respective displacements were very small and approximately the same as in static stiffness measurements, for example, corresponding to 2000  $\mu\text{m}/\text{m}$  in axial direction, these additional measurements have negligible effect on the fatigue life. In addition, the load–displacement curve is approximately linearly proportional to the stress–strain curve at these displacement levels. Therefore, the stiffness degradation can be approximated without additional strain gauges or other measurement devices, reducing the experimental effort. A flow chart of the employed stiffness degradation measurement is shown in Figure 3.

All fatigue tests were intended as load-controlled tests. However, due to a problem with the inertia compensation of the torsional load cell, torque-control was

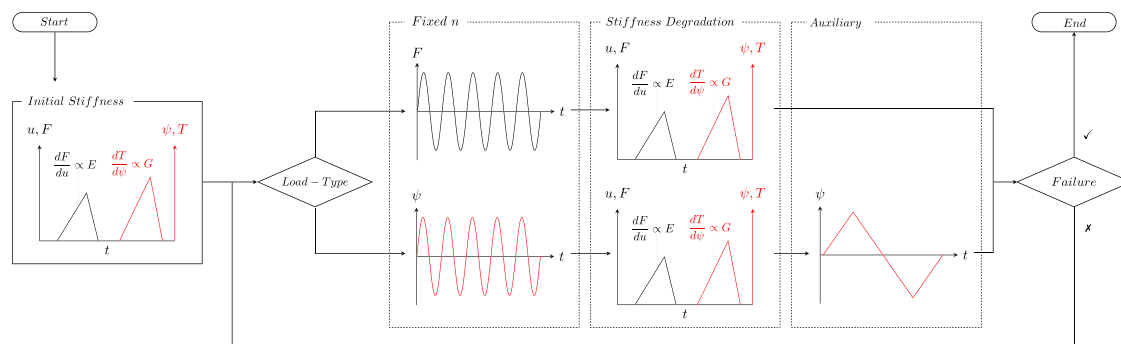


**FIGURE 3** Flow chart of the stiffness degradation measurement in both axial and torsional direction to identify  $E$  and  $G$  modulus degradation. Degradation measurements are implemented as displacement-controlled steps and repeated after a fixed number of cycles  $n$ . [Colour figure can be viewed at [wileyonlinelibrary.com](http://wileyonlinelibrary.com)]

not possible at the usual fatigue testing frequencies. Therefore, the torsional fatigue tests had to be performed in displacement control instead. To be able to convert the displacement-based results to stress-based results in a postprocessing step, a very slow auxiliary cycle was implemented after the stiffness degradation step; see Figure 3. Since the displacement rate of this cycle matched the one of the static tests, the torque measurement for this cycle was reliable. Details of the conversion will be discussed in Section 3.2.

### 3 | UNIAXIAL S-N CURVES

Fatigue data in this work were measured in both axial and torsional directions at a stress ratio  $R = -1$ , defined as the ratio of minimum and maximum stress:

$$R = \frac{\sigma_{\min}}{\sigma_{\max}}. \quad (1)$$

To investigate the effect of a mean stress on the fatigue life, an additional axial S-N curve was recorded at  $R = 0$ . In all cases, the stiffness degradation measurement was included as described in Section 2.2.

#### 3.1 | S-N models

Since the inception of fatigue tests by Wöhler,<sup>22</sup> many S-N curve descriptions have been proposed. The approach by Basquin<sup>23</sup> is among the most widely used models. It predicts an exponential relationship between the stress amplitude  $\sigma_a$  and the load cycles  $N$  and is given by

$$\sigma_a = \alpha N^\beta. \quad (2)$$

Therein,  $\alpha$  and  $\beta$  are curve fitting parameters. While the Basquin approach is popular due to its simplicity, it also tends to be non-conservative in the low cycle fatigue (LCF) regime and too conservative in the very high cycle fatigue (VHCF) regime.

The non-conservatism of the Basquin approach in the LCF regime was solved by Sendekyj<sup>24</sup> who proposed an asymptotic behavior of the S-N curve towards the ultimate static strength  $R_m$  expressed by

$$\sigma_a = \frac{R_m}{(1 - \alpha + \alpha N)^\beta}. \quad (3)$$

To account for both the LCF and the VHCF issues of the Basquin approach, different (inverse) sigmoidal-

shaped S-N curves have been proposed. One of them is the Stüssi<sup>25</sup> S-N formulation given by

$$\sigma_a = \frac{R_m + \alpha N^\beta \sigma}{1 + \alpha N^\beta}, \quad (4)$$

where  $\sigma$  is the fatigue limit amplitude, which is often also referred to as the endurance limit. A more recent approach was proposed by Kohout and Věchet,<sup>26</sup> which can be formulated as follows:

$$\sigma_a = \sigma \left( \frac{N + \alpha}{N + \gamma} \right)^\beta, \quad (5)$$

where  $\gamma$  is another curve fitting parameter.

The curve fitting parameters  $\alpha, \beta, \gamma$ , and  $\sigma$  of the S-N approaches can be obtained via a non-linear least squares optimization. The minimization function can utilize the stress-based formulations or the rearranged cycle-based formulations. As each of these minimization strategies can lead to different curve fitting parameters, the parameters from the best overall curve fit or the more conservative resulting S-N curve can be chosen.

Note that in this work the ultimate static strength  $R_m$  corresponds to  $N = 0.25$  for the S-N modeling, since a static tests can be interpreted as the first quarter of a full cycle.

#### 3.2 | Conversion from displacement to load control

On account of the displacement-controlled torsional fatigue tests, the applied torque is not constant but a collective. The approximation of this collective was done via auxiliary steps in the stiffness degradation routine, compare, Figure 3. The peak values of these auxiliary cycles matched the fatigue amplitude and allowed the construction of torque-collectives in a post-processing step; two of those are shown on the left of Figure 4.

The mean torque-collectives of all load levels were subsequently converted into shear stress collectives using the relationship of torque  $T$  and shear stress  $\tau$  measured in the static tests.<sup>20</sup> Strain rate effects in the fatigue tests might alter the  $T/\tau$ -relationship of the static tests, but since the displacement rate of the auxiliary cycle was the same as in the static tests, this is expected to be a valid engineering approximation. As an increase in strain rate usually coincides with higher peak stresses, this procedure is also expected to be conservative when it is based on the slow strain rates of static tests. However, strain

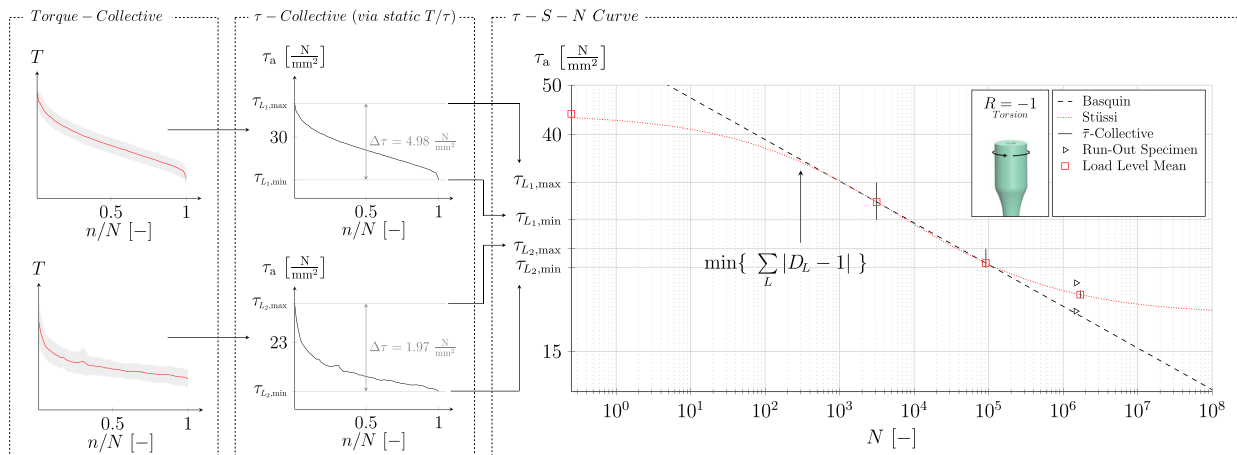


**FIGURE 4** Conversion steps from displacement (rotation angle) controlled data to a  $\tau$ -S-N curve. Torque collectives are generated via auxiliary measurements, compare Figure 3, and converted to shear stress collectives via the relationship of torque and shear stress measured in static tests.<sup>20</sup> The shear collectives form a vertical line in the S-N diagram, which is the basis for a damage-based optimization to find the best-fit S-N curves. [Colour figure can be viewed at [wileyonlinelibrary.com](http://wileyonlinelibrary.com)]

rate effects of the adhesive are yet to be validated in future experiments.

The mean  $\tau$ -collectives were subsequently transferred to the S-N diagram, leading to a vertical line for each investigated load level. The linear damage accumulation rule<sup>27</sup> was assumed to be valid in order to fit S-N curves to the data. Based on this assumption, an optimization was set up, which minimized the damage difference to the ideal value of  $D=1$  at each load level. The best-fit results of the S-N models according to Basquin and Stüssi are shown on the right of Figure 4. Given that the damage-equivalent amplitude of the first load level is approximately the mean value of the respective  $\tau$ -collective seems plausible as this collective is close to being linear. Likewise, it is reasonable that the damage-equivalent amplitude of the second load level is within the lower third of the respective collective, which decreases rapidly at first and transitions into a slow linear decline.

With respect to the assumptions explained above, the described conversion methodology is expected to be an accurate and conservative approximation for engineering purposes.

### 3.3 | Experimental results

The results of the fatigue tests are shown in Figure 5 and Table 1. It can be observed that the Basquin S-N curve is expectedly non-conservative in the LCF regime and too conservative in the VHCF regime for all stress ratios and load types. Deviations of the experimental data to the

Basquin S-N curve start from approximately 100,000 to 200,000 cycles in each case.

Both the Stüssi- and the Kohout-Věchet S-N curves fit the experimental data very well. A deviation of these approaches to one another is only visible in the LCF and VHCF regime, whereas the Stüssi approach is more conservative in both cases and is hence interpreted as the best-fit. The Sendekyj S-N curve matches the Kohout-Věchet approach in the LCF regime and is similar to the Basquin line afterwards.

The experimental results are also summarized in Table 1. The test frequency was varied in order to limit internal heating of the specimens and strain rate effects. In most cases, the temperature increase in comparison with the ambient temperature was below 3 K. However, some specimens reached 4–6.65 K, which was most probably caused by friction between the Pt100 and the specimen due to an insufficient fixture of the sensor, as other specimens did not heat up as much in the same testing conditions. Slight variations of the measured temperatures may have been caused by minor positioning differences of the Pt100 on the tapered specimens. Nevertheless, it is expected that the average temperature increase during the experiments has a negligible effect on the fatigue life. Minor variations of the stress amplitudes within each load level resulted from very small cross-sectional differences of the specimens in addition to minimal changes of the load amplitude on account of the testing machine controller.

The S-N fitting parameters can be found in Table 2. On account of the different S-N formulations, the

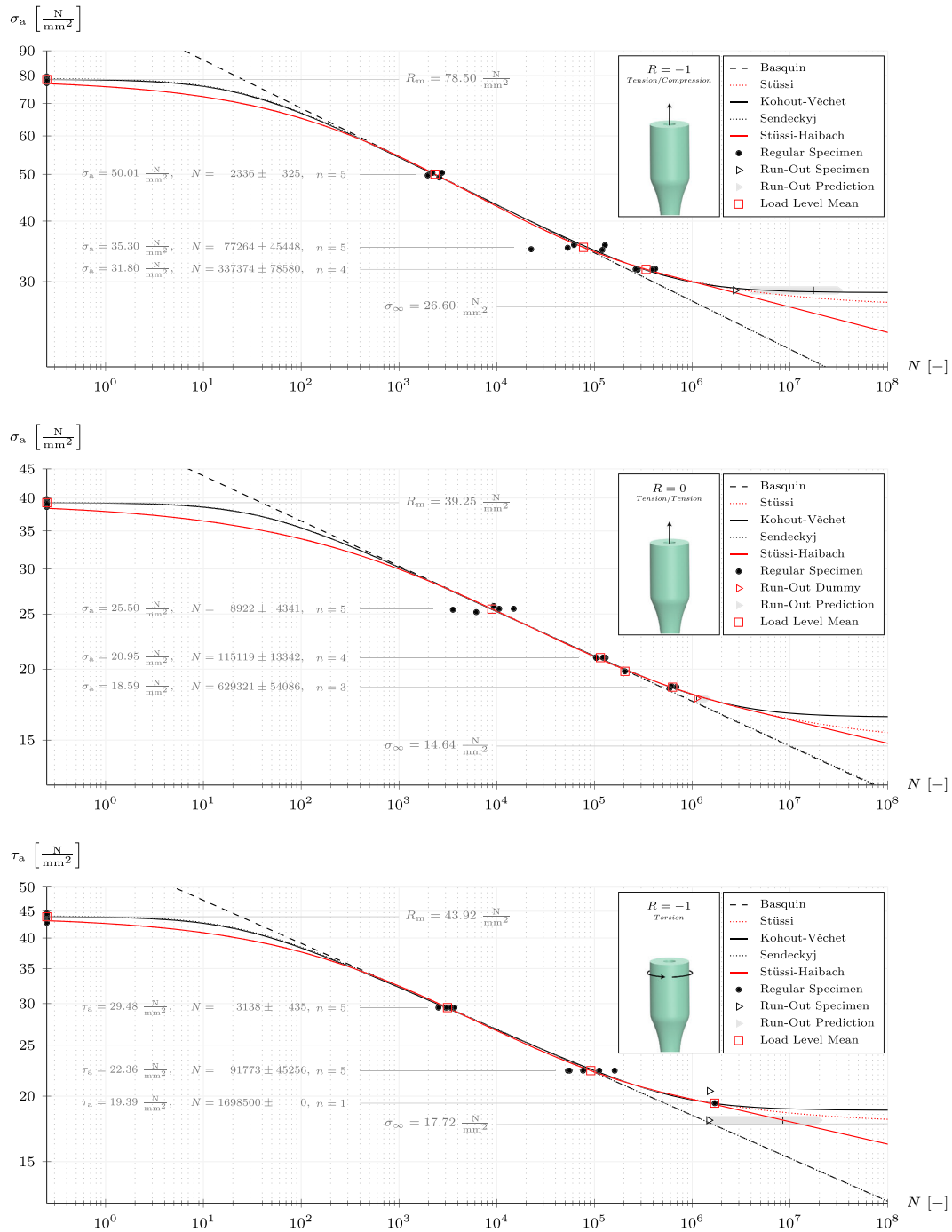


FIGURE 5 S-N curves for tension/compression, tension/tension and torsion with corresponding load level mean values and static strength  $R_m$ . The fatigue limit  $\sigma$  is based on the respective Stüssi S-N curve fit. The number of failed specimens of a load level is indicated by  $n$ . [Colour figure can be viewed at [wileyonlinelibrary.com](http://wileyonlinelibrary.com)]

parameters cannot be easily compared with each other. The applied Haibach extension will be discussed in Section 3.4.

In total, four specimens were excluded from the S-N fits. Specimen 042 was accidentally preloaded in tension during clamping due to very tight tolerances of the



TABLE 1 Summarized fatigue results for all experiments conducted.

Load type	Specimen no.	$\sigma_a$ [N/mm <sup>2</sup> ]	$\tau_a$ [N/mm <sup>2</sup> ]	$N$ [-]	$f$ [1/s]	$\Delta T_{\max}$ [K]	$\tilde{E}_f$ [%]	$\tilde{G}_f$ [%]
$\sigma_a^{R=-1}$	177	49.73	—	1970	1.0	2.72	88.5	95.9
	051	50.43	—	2164	1.0	2.79	88.1	96.1
	183	50.33	—	2202	1.0	3.07	86.4	93.1
	171	49.24	—	2587	1.0	4.22	85.3	93.3
	136	50.35	—	2759	1.0	3.71	88.1	95.5
	010	34.99	—	22531	3.0	0.58	91.2	96.9
	114	35.23	—	53261	3.0	4.15	87.0	95.0
	189	35.72	—	61858	3.0	1.00	85.4	93.6
	007	34.87	—	120433	3.0	3.87	91.4	97.3
	194	35.68	—	128148	3.0	4.07	85.5	95.5
	203	31.82	—	263633	3.0	2.47	88.4	95.6
	054	31.73	—	276747	3.0	2.61	91.9	96.9
	139	31.76	—	390704	3.0	3.32	91.4	96.7
	094	31.88	—	418412	3.0	3.32	91.1	98.0
	174	28.79	—	*2760000	3.0	1.94	93.7	99.5
	$\sigma_a^{R=0}$	154	25.43	—	3568	1.0	1.06	96.9
169		25.19	—	6179	1.0	0.63	95.2	97.9
207		25.82	—	9322	1.0	0.75	95.4	97.1
199		25.53	—	10606	1.0	0.93	96.5	97.4
026		25.54	—	14937	1.0	0.40	97.7	98.2
112		20.98	—	103500	3.0	1.63	98.2	100.9
193		20.92	—	104284	3.0	1.94	96.5	97.9
069		20.95	—	122507	3.0	1.52	96.1	100.0
198		20.94	—	130186	3.0	1.71	97.4	99.7
042		20.89	—	+346500	3.0	0.89	96.2	98.0
106		19.82	—	204793	4.0	1.53	98.7	98.6
167		18.50	—	e345000	4.0	—	—	—
110		18.49	—	585123	4.0	1.76	96.5	99.2
108		18.67	—	613208	4.0	2.00	97.5	—
099		18.60	—	689632	4.0	1.64	95.5	98.6
$\tau_a^{R=-1}$		089	—	29.48	2536	0.5	1.28	95.7
	186	—	29.48	3015	0.5	1.00	94.2	85.1
	123	—	29.48	3057	0.5	3.23	93.2	81.7
	197	—	29.48	3383	0.5	2.19	96.0	83.5
	077	—	29.48	3697	0.5	1.95	95.8	84.0
	083	—	22.36	53607	1.5	2.41	94.0	90.0
	179	—	22.36	55661	1.5	3.45	93.8	86.6
	192	—	22.36	76596	1.5	5.46	93.8	88.1
	173	—	22.36	112000	1.5	4.36	94.7	85.8
	072	—	22.36	161000	1.5	2.24	96.4	90.5
	084	—	20.37	f30000	3.0	—	—	—
	059	—	20.37	f134000	3.0	6.65	95.6	90.5
	057	—	20.44	*1500000	3.0	4.34	97.9	87.4

TABLE 1 (Continued)

Load type	Specimen no.	$\sigma_a$ [N/mm <sup>2</sup> ]	$\tau_a$ [N/mm <sup>2</sup> ]	$N$ [-]	$f$ [1/s]	$\Delta T_{\max}$ [K]	$\tilde{E}_f$ [%]	$\tilde{G}_f$ [%]
	119	—	19.39	1698500	3.0	4.18	100.1	91.9
	166	—	17.99	*1480000	3.0	2.96	96.5	91.9

Note: Therein,  $f$  is the test frequency,  $\Delta T_{\max}$  is the maximum temperature difference to the ambient temperature, and  $\tilde{E}_f$  and  $\tilde{G}_f$  correspond to the relative stiffness degradation before failure. Run-out specimens are indicated with superscript \*. Nontypical fracture surfaces are marked by a superscript <sup>f</sup>. Specimen 042, also marked with a superscript +, was accidentally preloaded during clamping. The superscript <sup>e</sup> marks a worst-case estimate due to a data recording error. All superscripts refer to the  $N$  column.

TABLE 2 Fitting parameters of all S-N models used in this work.

Load type	Model	$\alpha$ [-]	$\beta$ [-]	$\gamma$ [-]	$\sigma$ [N/mm <sup>2</sup> ]	$R_m$ [N/mm <sup>2</sup> ]	$N_{\text{ext}}$ [-]	$\sigma_{a,\text{ext}}$ [N/mm <sup>2</sup> ]	$\beta_{\text{ext}}$ [-]
$\sigma_a^{R=-1}$	Basquin	108.3051	-0.0996	—	—	—	—	—	—
	Sendeckyj	0.0392	0.0997	—	—	78.5026	—	—	—
	Stüssi	0.0538	0.4022	—	26.6030	78.5026	530,000	31.0088	-0.0524
$\sigma_a^{R=0}$	Kohout-Véchet	24.4363	-0.0996	651,716.72	28.4735	—	—	—	—
	Basquin	52.5354	-0.0793	—	—	—	—	—	—
	Sendeckyj	0.0263	0.0789	—	—	39.2513	—	—	—
	Stüssi	0.0590	0.3367	—	14.6433	39.2513	3,860,000	16.9343	-0.0413
$\tau_a^{R=-1}$	Kohout-Véchet	37.9438	-0.0793	2,174,478.52	16.4639	—	—	—	—
	Basquin	56.9826	-0.0819	—	—	—	—	—	—
	Sendeckyj	0.0412	0.0819	—	—	43.9170	—	—	—
	Stüssi	0.0515	0.3939	—	17.7151	43.9170	630,000	20.1167	-0.0427
	Kohout-Véchet	22.9564	-0.0819	735,298.70	18.8014	—	—	—	—

Note:  $R_m$  was determined in a previous publication.<sup>20</sup> Note that  $\alpha$  is in N/mm<sup>2</sup> for the Basquin model and dimensionless for the others. The intersection point of the Stüssi and Haibach line is given by  $(N_{\text{ext}}, \sigma_{a,\text{ext}})$ .

specimen and the clamping gear. The preload was estimated to 51 N/mm<sup>2</sup>, which is above the yield point of 39.32 N/mm<sup>2</sup> and therefore led to strain hardening,<sup>20</sup> causing the fatigue life to approximately triple compared with the other specimens at the same load level, compare Table 1. Specimen 059 and 084 had a significantly lower fatigue life while also showing a fragmented fracture pattern, which was very different from the usual case of a governing 45° crack in torsion, compare Figure 6. Handling errors during the manufacturing (e.g., during demolding or grinding) are suspected to have caused precracks in these specimens. A data recording error caused the exclusion of specimen 167. The cycle to failure of this specimen is a worst-case estimation based on the approximate machine run time.

In four cases, the fatigue test had to be aborted, and a run-out was declared as the total number of cycles of the whole testing campaign was limited. All of these specimens were destroyed in residual strength tests, which are

discussed in Section 4 alongside a residual fatigue life prediction based on the stiffness degradation measurements.

Note that the presented results may differ for other test frequencies than the applied ones due to the viscoelastic behavior of the adhesive<sup>20</sup> and associated strain rate effects.

### 3.4 | Engineering approach to gigacycle fatigue

As (very) high-frequency fatigue testing machines, for example, piezoelectric or rotary bending machines, made experimental fatigue tests beyond 10<sup>7</sup> cycles possible from an economical point of view, the existence of a fatigue limit  $\sigma$  was discussed by several researchers.<sup>28–31</sup>

It was found that multiple materials indeed show a plateau of fatigue strength in between 10<sup>6</sup> and 10<sup>7</sup> cycles,

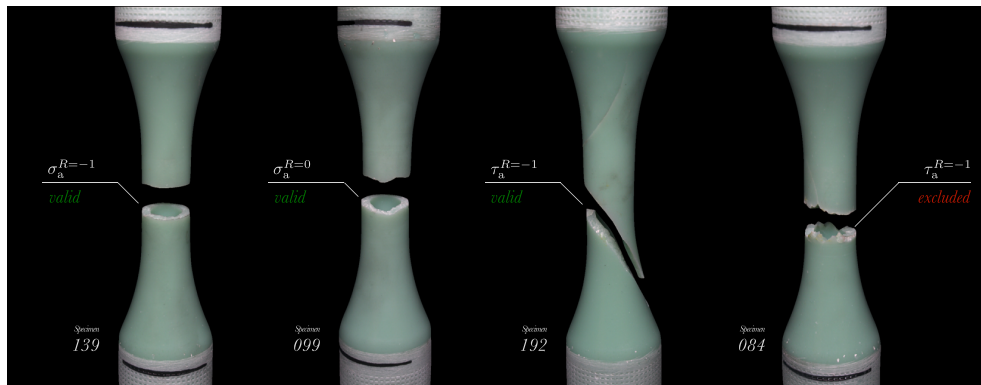


**FIGURE 6** Typical fracture patterns in the fatigue tests for all investigated load types. Specimen 084 was excluded from the analysis due to an atypical fracture pattern, which was probably caused by precracks on account of handling errors in the manufacturing process. [Colour figure can be viewed at [wileyonlinelibrary.com](http://wileyonlinelibrary.com)]

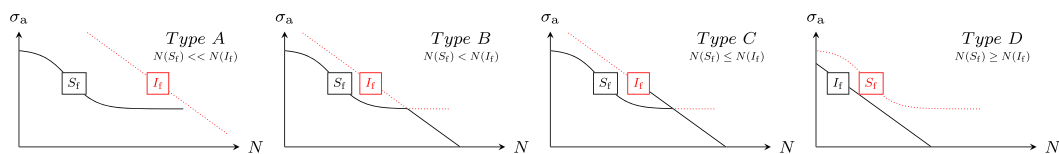


**FIGURE 7** Gigacycle fatigue types depicted in double logarithmic axes. Depending on the material, the fatigue life can be dominated by surface-induced failure  $S_f$ , internal damage initiation  $I_f$ , or mixtures of both phenomena. Adapted from Shiozawa et al.<sup>28</sup> [Colour figure can be viewed at [wileyonlinelibrary.com](http://wileyonlinelibrary.com)]

which previously led to the declaration of a fatigue limit, but beyond this regime, another significant decrease in fatigue strength was observed. This behavior was characterized by a duplex S–N approach, which incorporated a S–N curve for surface-induced failure  $S_f$  and another for internal failure initiation  $I_f$ .<sup>28</sup> Depending on the material, four different types can exist, which are shown in Figure 7. Therein, the Stüssi S–N curve was chosen to model the surface-induced failure, since it well represents the results in this work, while the internal damage initiation S–N curve is represented by a straight line (Basquin approach). According to Shiozawa et al.<sup>28</sup> the four types are as follows:

- A. surface failure dominated fatigue life
- B. surface failure up to the VHCF regime followed by a distinct change to internal damage initiation
- C. mixture of surface and internal damage initiation
- D. internal failure dominated fatigue life

Although this concept was derived from experiments with metal alloys, it is expected to be transferable to polymers, as the same holds for nearly all S–N models. However, the experimental results from this work are rather limited concerning (very) high cycle data, since there

were only five specimens in total with more than  $10^6$  cycles. Therefore, it is not known which gigacycle type is valid for the adhesive. Hence, the Haibach extension<sup>32</sup> to the VHCF regime was combined with the Stüssi S–N curve. The Haibach extension is based on an assumed continuation of the S–N curve in the VHCF regime with a slope

$$k_{\text{ext}} = 2k - 1, \quad (6)$$

where  $k$  is the slope within the high cycle fatigue regime and the slope of the Basquin line, respectively. Equation (6) can also be rewritten using the curve fitting parameter  $\beta$  of the Basquin model resulting in

$$\beta_{\text{ext}} = \left( \frac{2}{\beta} + 1 \right)^{-1}. \quad (7)$$

Using this extension in combination with the Stüssi approach, the very good fit of the Stüssi S–N curve can be utilized up to the high cycle fatigue regime and a rather conservative approach is made for VHCF. Since the transition point of the Stüssi S–N curve to the extension line is chosen in such a way that the slope of the Stüssi S–N

curve matches the one of the extension line, the transition is smooth and does not require a decision on where the extension should start in terms of a stress or cycle threshold. The derived Stüssi–Haibach S–N curves are included in Figure 5, and the additional parameter set is shown in Table 2.

Note that in case future experiments reveal that the adhesive is a type B material, there is a chance that the Haibach extension line crosses the  $I_f$ -line, which could lead to non-conservative fatigue life predictions. However, this would most probably be the case at very small stress amplitudes and very high cycle numbers. With the use of proper safety factors, this risk is expected to be tolerable, given the alternatives of trusting the fatigue limit theorem with limited data or using the very conservative Basquin approach. However, further tests in the VHCF regime are required to distinctly identify the best-fit S–N model in a probabilistic manner, as limited data and scatter at very high cycles to failure do not yet allow a final conclusion.

### 3.5 | Apparent yield strength separation points

Sigmoidal-shaped S–N models such as the ones from Stüssi<sup>25</sup> and Kohout and Věchet<sup>26</sup> incorporate the ultimate static strength. Motivated by the very good fit of both models to the data, a comparison of static and fatigue data was done for different yield strengths, which were determined in a previous publication.<sup>20</sup> These are the following:

1.  $\sigma_{y,0.2}$  - traditional yield strength at a plastic offset strain of 0.2% (2000  $\mu\text{m}/\text{m}$ )
2.  $\sigma_y$  - derivative-based yield strength according to Christensen<sup>33,34</sup>
3.  $\sigma_{y,0.01}$  - surrogate proportional limit at a plastic offset strain of 0.01% (100  $\mu\text{m}/\text{m}$ )

In case of the shear-based S–N curve, the respective plastic offset strains have to be converted to the equivalent stress-strain space, which was done using the experimental (strain) yield locus in combination with an elliptical scaling approach.<sup>20</sup>

The comparison of the static stress-strain curves (true stresses and strains) and the S–N results is shown in Figure 8. Note that the ordinate of the axial S–N curves in Figure 8 shows the maximum stress and not the amplitude; hence, the  $R = 0$  curve is above the  $R = -1$  curve. In addition, the strain rate in the static tests was different from the strain rate in the S–N tests. Thus, the comparison is affected by the viscoelasticity of the adhesive.

However, due to the low temperature increase in the experiments and the test frequency adaption on each load level, compare Table 1, this influence was minimized as much as possible.

It was found that  $\sigma_{y,0.2}$  can be approximated as the upper separation point of the Basquin- and Stüssi S–N curves. While this approximation is quite accurate for the axial S–N curves of this work, it is a rough estimation for torsion. The surrogate proportional limit  $\sigma_{y,0.01}$  is very close to the apparent fatigue limit  $\sigma$  predicted by the Stüssi S–N curve for both axial and torsional data at  $R = -1$ . However, at  $R = 0$ , this is not the case for the recorded data. The derivative-based yield strength  $\sigma_y$  might serve as a rough estimation for the lower separation point of the Basquin- and Stüssi S–N curves for axial fatigue tests; however, this does not apply for torsion.

While these findings are not decisive enough to derive general rules, they can still serve as useful first approximations. For instance, during the experimental determination of a S–N curve, only one load level is necessary for a Stüssi S–N curve fit if the ultimate strength and the surrogate proportional limit  $\sigma_{y,0.01}$  are used as asymptotes. This is expected to help with specimen allocation and planning of test machine occupancy.

### 3.6 | Comparison with literature

Publicly available information on the coupon level fatigue behavior of the rotor blade adhesive investigated in this work is limited to two publications<sup>9,10</sup> in terms of S–N data. For a fair comparison, the specimen geometry and stress ratio should be as similar as possible. Therefore, Fernandez et al<sup>9</sup> is used for a comparison, since Sears et al<sup>10</sup> relied on lap shear tests. To account for similar stress ratios, only the torsional fatigue data of this work can be compared with Fernandez et al<sup>9</sup> as both were recorded at  $R = -1$ . The fatigue data presented in Fernandez et al<sup>9</sup> were normalized using the measured static shear strength. However, as the shear strength was calculated based on the purely elastic torsional formulae, it needs to be corrected, because the material was proven to exhibit significant plasticity.<sup>20</sup> The apparent brittle behavior of the tests in Fernandez et al<sup>9</sup> is hence attributed to a high porosity level, whereas the material surrounding the pores exhibited significant plastic strains.<sup>20</sup> Therefore, the purely plastic formulae result in a more realistic estimation of the shear strength. A correction factor of  $\tau_{pl} = 0.873 \cdot \tau_{el}$  was identified to account for this issue in a previous publication.<sup>20</sup> A deduction of the correction factor and a detailed discussion on elasto-plastic shear stresses in torsion tests can be found therein.

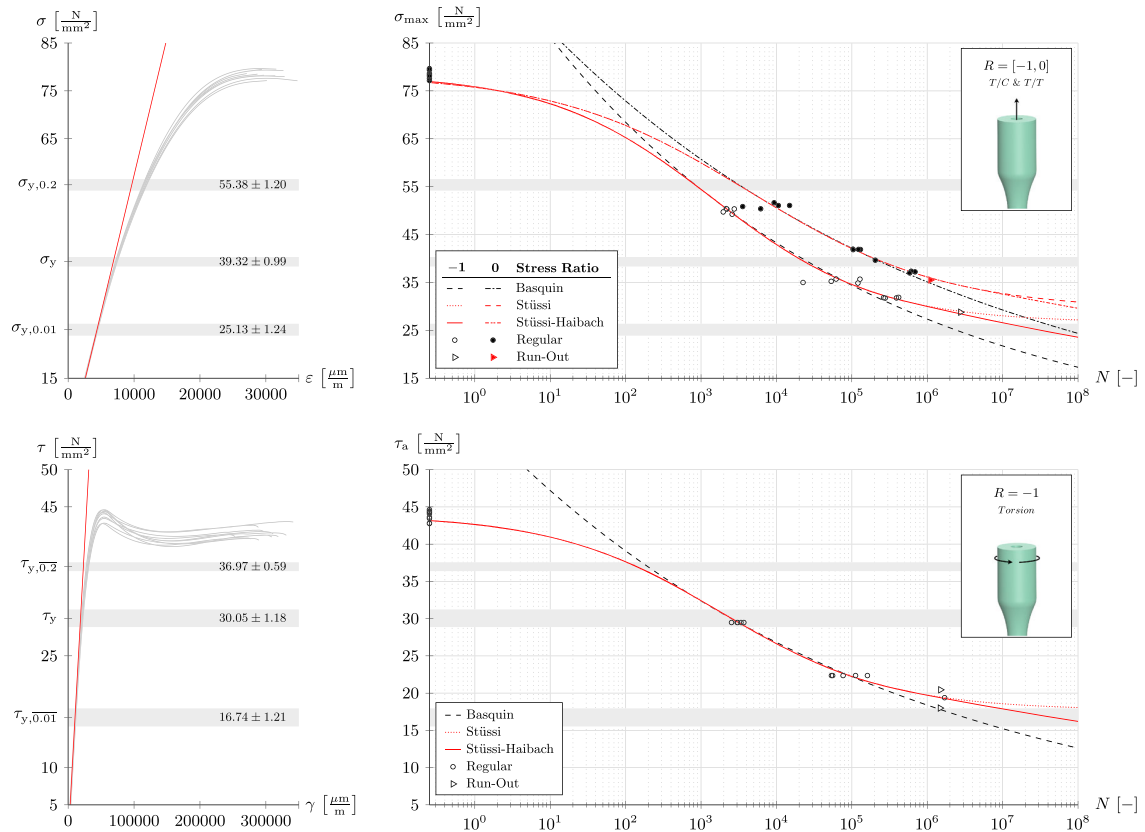


**FIGURE 8** Comparison of static (true) stress-strain curves with experimental fatigue results and corresponding S-N curve fits. Static results represent the tensile and torsion test carried out in a previous publication.<sup>20</sup> Gray horizontal bars represent different yield point definitions including their standard deviation. [Colour figure can be viewed at [wileyonlinelibrary.com](http://wileyonlinelibrary.com)]

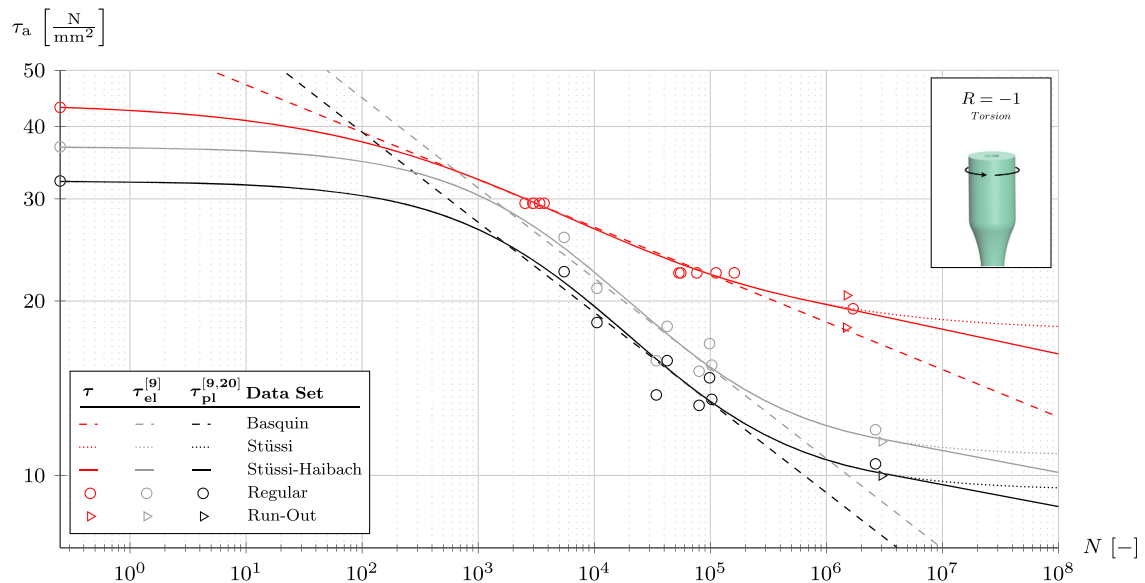


**FIGURE 9** Comparison of torsional S-N results. The data set of this work is labeled  $\tau$ , while data from Fernandez et al<sup>9</sup> are labeled  $\tau_{el}$  and  $\tau_{pl}$ . The latter was altered with a correction factor, which was derived in a previous publication.<sup>20</sup> A high porosity level in the specimens of Fernandez et al<sup>9</sup> is interpreted as the main reason for the reduced fatigue performance in comparison with this work. [Colour figure can be viewed at [wileyonlinelibrary.com](http://wileyonlinelibrary.com)]

The differences between the measurements presented in Fernandez et al<sup>9</sup> and this work are shown in Figure 9. The linear elastic results stated in Fernandez et al<sup>9</sup> are shown in gray, while the results including the mentioned correction are shown in black. Both versions show significantly reduced fatigue properties in comparison with the results of this work. Possible uncertainties related to the conversion of the displacement-controlled tests to load-controlled tests in this work, compare Section 3.2, are not expected to affect this, as the differences between the results are too large. In fact, neglected strain rate effects in the conversion, compare Section 3.2, are expected to result in a conservative estimation of this works' S–N curve. Therefore, it can be confirmed that the porosity level and the underlying manufacturing methods have a very significant impact.

The differences between both measurement campaigns are also load level-dependent. A constant safety factor to account for manufacturing defects in general is therefore not recommendable regarding the permissible amplitude or cycles to failure. However, a safety factor applied to the slope of the S–N curve seems to be a reasonable simplification. It must be noted that different tempering cycles and orientations of the reinforcement fibers can also contribute to the discussed differences in fatigue performance. Especially the orientation of the reinforcement fibers is likely to influence fatigue life since it can affect microscale and mesoscale crack orientations.<sup>35</sup> More detailed analyses are required to estimate the individual contribution of the porosity level, tempering, and fiber orientation in terms of material properties and safety factors. However, the porosity level is interpreted as the main reason for the differences in fatigue performance as similar load level-dependent observations have been made for various metallic alloys with different levels of porosity in literature.<sup>36–38</sup>

Despite the differences in fatigue performance shown in Figure 9, the Stüssi (or Stüssi–Haibach) S–N model fits the data very well. The same was found by Rosemeier and Antoniou<sup>39</sup> and Rosemeier et al<sup>40</sup> for other epoxy-based resins/adhesives. However, as the VHCF scatter remains unknown in the aforementioned publications, it is still required to verify S–N models in this regime on a statistical basis, compare Section 3.4.

## 4 | STIFFNESS DEGRADATION

The stiffness degradation measurements were done alongside the fatigue tests according to Figure 3. Since the degradation of the Young's and shear modulus was

measured independently of the active load type (axial or torsional), biaxial interactions could be analyzed.

### 4.1 | Cycle- and load-dependent modeling

The relative degradation is calculated as the ratio of the current modulus, which is a function of the cycle number  $n$ , and the initial modulus. The moduli are assumed to be linearly proportional to the measured load-displacement curves. This results in

$$E \propto \frac{dF}{du}, G \propto \frac{dT}{d\psi}, \quad (8)$$

$$\tilde{E}(n) = \frac{E(n)}{E_0} \cdot 100, \tilde{G}(n) = \frac{G(n)}{G_0} \cdot 100, \quad (9)$$

where  $E$  is the Young's modulus,  $G$  is the shear modulus,  $F$  and  $T$  are axial force and torque, and  $u$  and  $\psi$  are axial displacement and rotation.

The degradation model is set up with the normalized cycle count  $\tilde{N}$  and normalized load level  $\tilde{L}$  given by

$$\tilde{N} = \frac{n}{N}, \tilde{L} = \frac{\sigma_a}{R_m}. \quad (10)$$

In case of the torsional S–N tests,  $\tilde{L}$  is defined by the ratio between the shear stress amplitude  $\tau_a$  and the static shear strength, respectively.

Independent of the load type, it was found that the adhesive shows a rapid degradation of  $E$  and  $G$  during the first 5%–10% of fatigue life followed by a slower and approximately linear decline afterwards; see Figure 10 (black solid lines). A good fit of the recorded degradation is provided by a power law given by

$$\tilde{E} = 100 - A\tilde{N}^B, \quad (11)$$

where  $A$  and  $B$  are curve fitting parameters. The same model is also used for the  $G$  modulus degradation.

The overall degradation was found to be load level-dependent. However, an extrapolation of the data is difficult on account of the limited data set. Therefore, a conservative approach is chosen. Concerning a stress-based fatigue life analysis, a conservative approach represents the assumption of a low stiffness degradation in VHCF. This is because a stiffness degradation will lead to lower stresses and hence longer fatigue life. Therefore, it is

assumed that the stiffness degradation tends to zero at very small load amplitudes. Note, however, that in some engineering applications, an overestimation of the stiffness degradation might be a more conservative design approach than to neglect it. The tower clearance of wind turbine rotor blades could be such a case depending on the rotor blade design. Therefore, the extrapolation in

this work must be treated with caution, although the contribution of adhesive to the overall stiffness of a structure will most likely be small.

Given the assumption explained above, it is further assumed that the parameters  $A$  and  $B$  are load level-dependent and can be described by rational functions with a polynomial degree of 1 in the numerator and a

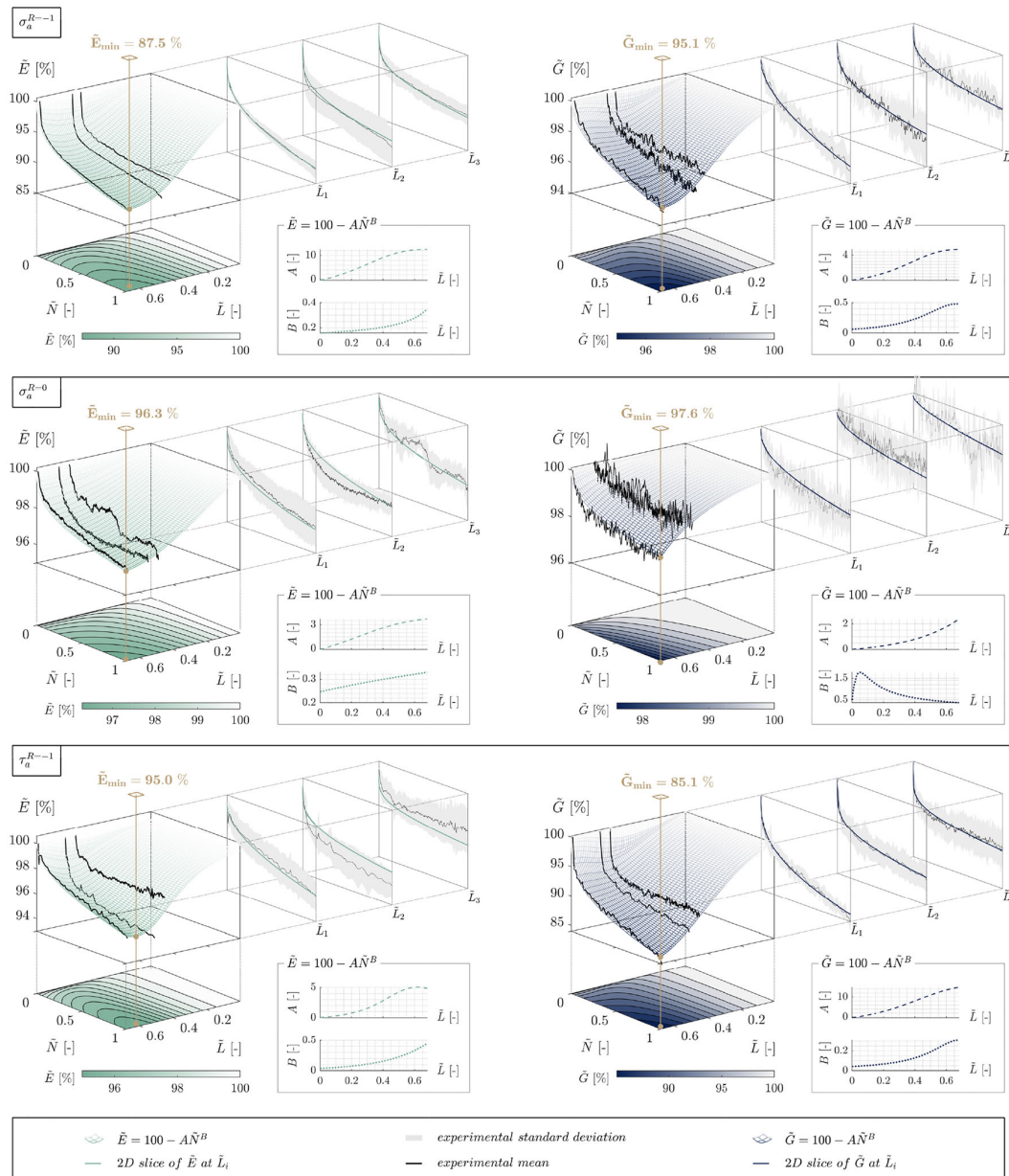


**FIGURE 10** Modeling of the relative stiffness degradation in tension/compression ( $\sigma_a^{R=-1}$ ), tension/tension ( $\sigma_a^{R=0}$ ) and torsion ( $\tau_a^{R=-1}$ ). A power law is used to model the data as a function of the normalized cycles to failure  $\tilde{N}$ . The fitting parameters of the power law ( $A$  and  $B$ ) were found to be rational functions of the normalized load level  $\tilde{L}$ . The respective functions of  $A(\tilde{L})$  and  $B(\tilde{L})$  are shown in inserted boxes. A comparison of the model prediction (colored) and the experimental mean (black) is given in 2D slices at each investigated load level ( $\tilde{L}_1, \tilde{L}_2, \tilde{L}_3$ ) showing good agreement. Fitting parameters are given in Table 3. [Colour figure can be viewed at [wileyonlinelibrary.com](http://wileyonlinelibrary.com)]

polynomial degree of 2 in the denominator such as the following:

$$A = \frac{p_1 \tilde{L} + p_2}{\tilde{L}^2 + q_1 \tilde{L} + q_2}, B = \frac{p_3 \tilde{L} + p_4}{\tilde{L}^2 + q_3 \tilde{L} + q_4}, \quad (12)$$

where  $p_1$  to  $p_4$  and  $q_1$  to  $q_4$  are curve fitting parameters. Based on this, the overall degradation functions depend on eight curve fitting parameters in addition to the respective ultimate static strength  $R_m$ .

To simplify the rational function fits of  $A$  and  $B$ , load-dependent smoothing splines were modeled in an intermediate step, which connected the recorded data points and the assumed zero degradation line at zero load. A complete degradation curve could thus be derived for each  $\tilde{L}$ , which was fitted with a power law according to Equation (11). This way, a smooth relationship between the power law fitting parameters  $A$  and  $B$  and the normalized load level  $\tilde{L}$  was generated. Therefore, enough data points were provided for the rational function fit of  $A$  and  $B$ , which are shown in Figure 10 (2D plots with grid) and Table 3. Given the adaptability of rational

function fits, the overall degradation model is very adaptable while the number of fitting parameters is still manageable.

The overall fit of the model to the measured data can be evaluated based on the 2D slices given in Figure 10. These depict the mean (black) and standard deviation (gray) of the experimental data in comparison with the model (colored). A good fit is provided for each load type. Since the experimental standard deviation is quite large, the upper and lower standard deviations were also modeled as offset-functions in the same way as the mean values. This way, the residual fatigue life prediction of run-out specimens, compare Section 4.3, includes the possibility of an uncertainty analysis. The additional fitting parameters are included in Table 3.

The degradation in the active load direction was found to be the largest in each test setup. For instance, if the adhesive is subjected to an axial  $R = -1$  load, the  $E$  modulus is reduced to 87.5%, while the  $G$  modulus is reduced to 95.1% on account of the axial load. This can be interpreted as a confirmation of the anisotropic behavior of the adhesive and an oriented crack growth during the experiments. Interestingly, the degradation at an

TABLE 3 Fitting parameters of the mean stiffness degradation functions ( $\mu$ ) with additional parameter sets for a positive ( $\mu^+$ ) and negative ( $\mu^-$ ) standard deviation offset, respectively.

Load type	Model	A [-]				B [-]			
		$p_1$ [-]	$p_2$ [-]	$q_1$ [-]	$q_2$ [-]	$p_3$ [-]	$p_4$ [-]	$q_3$ [-]	$q_4$ [-]
$\sigma_a^{R=-1}   \tilde{E}$	$\mu^+$	13.2392	-0.3163	-0.9134	0.9234	25.3665	-0.7556	100.0000	-1.2308
	$\mu$	6.2867	-0.1225	-0.8265	0.4323	-10.3208	13.7304	-99.9999	86.7407
	$\mu^-$	6.9112	-0.1613	-0.7964	0.3996	22.8418	-0.8368	100.0000	-1.2227
$\sigma_a^{R=-1}   \tilde{G}$	$\mu^+$	4.6684	-0.4116	-1.0753	0.9467	-11.1194	18.1751	-100.0000	84.7842
	$\mu$	1.6602	-0.0210	-1.0089	0.4498	0.0003	0.0309	-1.3263	0.5048
	$\mu^-$	2.5925	0.1159	-0.9686	0.5137	41.9786	6.6405	-26.8563	100.0000
$\sigma_a^{R=0}   \tilde{E}$	$\mu^+$	1.3670	-0.0586	-0.7755	0.3844	0.8300	-0.0236	1.5492	-0.0756
	$\mu$	3.5008	-0.0492	-0.6917	0.6369	23.4480	24.6517	33.6168	100.0000
	$\mu^-$	7.1944	-0.0094	-0.7435	1.0786	28.1620	0.3035	100.0000	6.1375
$\sigma_a^{R=0}   \tilde{G}$	$\mu^+$	0.2683	-0.0908	-1.4663	0.5899	0.0517	-0.0124	-0.7269	0.1330
	$\mu$	1.9030	-0.0193	-2.5075	1.7758	0.2650	0.0017	0.0496	0.0035
	$\mu^-$	100.0000	2.7864	-30.9189	43.1881	0.1571	0.0019	-0.1192	0.0445
$\tau_a^{R=-1}   \tilde{E}$	$\mu^+$	0.9033	-0.0849	-1.1623	0.4670	-0.0721	0.0093	-0.8627	0.0705
	$\mu$	0.7141	0.0132	-1.0914	0.3829	0.0769	0.0380	-1.9315	1.0528
	$\mu^-$	1.5705	-0.0010	-0.9956	0.3895	36.0028	6.5741	1.8603	100.0000
$\tau_a^{R=-1}   \tilde{G}$	$\mu^+$	7.8089	-0.4494	-1.5464	0.9363	-0.0390	0.0329	-1.4448	0.5381
	$\mu$	7.3408	-0.2099	-1.1399	0.6338	-0.0137	0.0225	-1.3975	0.5308
	$\mu^-$	7.0820	-0.1529	-0.9809	0.4960	20.2098	7.2870	-23.9835	100.0000

Note: To avoid replication errors, all digits should be used.



active torsional  $R = -1$  load approximately mirrors the degradation with an active axial load at the same stress ratio, resulting in a  $G$  modulus reduction to 85.1% and a  $E$  modulus reduction to 95.0% based on the active torsional load.

In comparison, the degradation at an active axial  $R = 0$  load is the smallest. Since this load type also has the smallest load amplitudes, it is concluded that the load amplitude is governing the stiffness degradation and not the maximum load resulting from the combination of mean load and amplitude. Hence, a mean load reduces the fatigue life of the adhesive but does not increase stiffness degradation.

As the stiffness degradation is non-linear in each case, these measurements might serve as a basis to include sequence effects in the fatigue life prediction. The validation of a possibly non-linear damage accumulation can, however, not be done with this work's uniaxial fatigue tests. Upcoming biaxial fatigue tests will provide more possibilities in this regard.

Further experiments are required to validate the stiffness degradation model in the VHCF regime. Strain rate-related differences of the respective load levels were minimized by an adaption of the test frequency in the S-N tests, compare Section 2.2.

## 4.2 | Comparison with residual strength tests

In case a run-out was declared, a residual strength test (RST) was performed. Strain gauge rosettes, identical to the ones used in the previously carried out static tests,<sup>20</sup> were applied to most of the run-out specimens for these tests. Hence, the employed force- and displacement-based stiffness degradation measurement could be validated by comparison of the accumulated degradation of the fatigue test and the stiffness measurement of the RST. The degradation identified by these methods was found to be different by approximately  $\tilde{E} - \tilde{E}_{\text{RST}} \approx 0.5\%$  and  $\tilde{G} - \tilde{G}_{\text{RST}} \approx 2\%$ . In all cases, the stiffness degradation measured in the RSTs was smaller than the last measurement in the fatigue test. Therefore, these deviations are expected to be influenced by viscoelastic recovery effects of the adhesive,<sup>20</sup> because the specimen instrumentation and preparation for the RSTs took time. This would also explain the larger difference in torsion, since the viscoelastic recovery was found to be faster in this case.<sup>20</sup> Independent of viscoelastic effects, the results of the employed fatigue stiffness degradation measurement method are close to the instrumented RSTs, confirming the validity of the method. An influence of testing machine compliance was not identified and therefore neglected.

In addition, the residual strength tests were compared with regular static tests. In Figure 11, a comparison between the static tensile test from a previous publication<sup>12,20</sup> and the RST of run-out specimen 174 is shown at the top. This specimen withstood  $2.76 \cdot 10^6$  cycles at a fully reversed axial load of  $28.79 \text{ N/mm}^2$ , and yet the ultimate strength is about 4.0% higher than the average of the static tensile test. At the same time, the Young's modulus decreased by 5.8%. Given the very low scatter of the static tests and the well-controlled manufacturing process in general,<sup>12</sup> the strength difference is more likely to be phenomenological than coincidence. While the stiffness degradation is attributed to cyclic matrix softening, the increase in strength is linked to strain hardening. Interestingly, the post-fatigue strain hardening was more significant than in the regular static tests. A potential reorientation of the polymer chains or the reinforcement fibers could contribute to this effect, although this is also expected to happen in the static tests. However, due to the matrix softening in fatigue, the reorientation could have been more significant than in the regular static tests. A more general interpretation is that accumulated (small scale) damage during fatigue alleviates stress

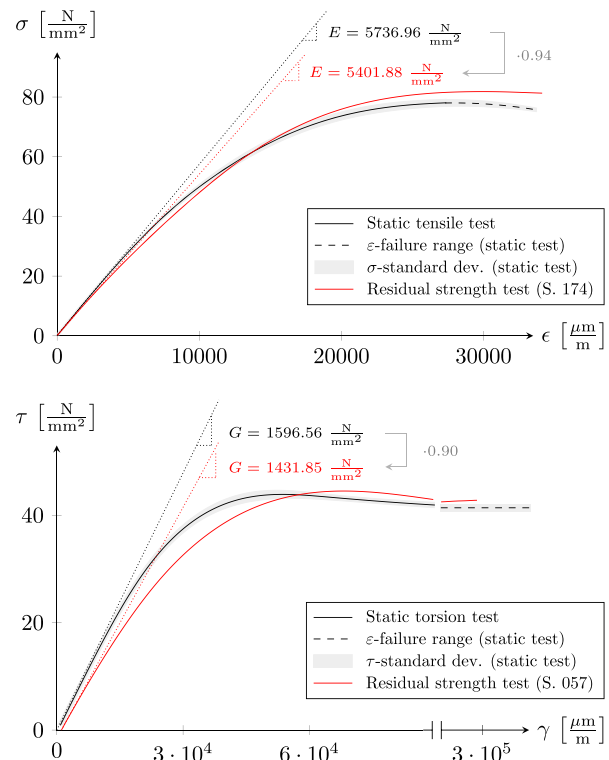


**FIGURE 11** Residual strength test for run-out specimen 174 (tested in tension/compression loading at  $R = -1$ ) and run-out specimen 057 (tested in torsional loading at  $R = -1$ ). Static test data were taken from previous publications.<sup>12,20</sup> [Colour figure can be viewed at [wileyonlinelibrary.com](http://wileyonlinelibrary.com)]

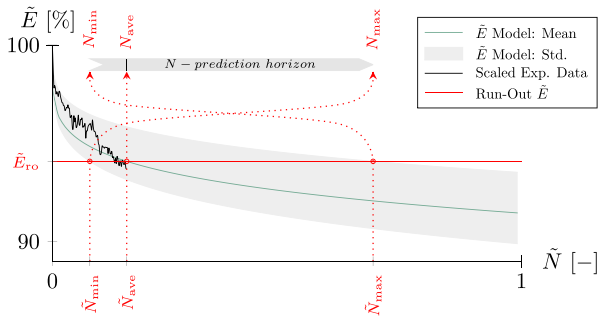


**FIGURE 12** Stiffness degradation-based fatigue life estimation of run-out specimen 174 using the  $\tilde{E}$  model and its standard deviation. Intersections of the last measured degradation  $\tilde{E}_{ro}$  with the  $\tilde{E}$  model lead to a predicted fatigue life horizon. [Colour figure can be viewed at [wileyonlinelibrary.com](http://wileyonlinelibrary.com)]

concentrations,<sup>41</sup> which in turn may allow for a higher ultimate strength in a post-fatigue test.

Figure 11 also shows the RST of specimen 057, which was tested in fully reversed torsion up to  $1.5 \cdot 10^6$  cycles. In this case, the ultimate strength difference is insignificant at about 1%, while the stiffness degraded by approximately 10%. The torsional RST appears as a delayed version of the regular static test, and a potential (additional) reorientation effect concerning the ultimate strength was not significant.

Further experimental validation of the fiber reorientation hypothesis is necessary.

### 4.3 | Run-out fatigue life estimation

Based on the load level and the accumulated stiffness degradation of the run-out specimens, a residual fatigue life estimation is possible. Given the limited data, their standard deviation, and the assumptions used to model the stiffness degradation, these predictions have to be understood as rough estimations.

The residual life estimation is schematically shown in Figure 12 for specimen 174. The degradation functions are evaluated at the respective load level of the run-out specimen. Subsequently, the intersection points of the model with the last recorded degradation value ( $\tilde{E}_{ro}$ ) are calculated. In case the measurement was noisy, a direct power law fit of the experimental data can also be used to extract a smoothed  $\tilde{E}_{ro}$  value. Note that the first intersection point  $\tilde{N}_{min}$  corresponds to the maximum of the fatigue life prediction  $N_{max}$ , because the potential minimum of used cycles implies a maximum of residual cycles to failure. The absolute cycles to failure can be found as the inverse of the intersection points multiplied by the run-out cycles of the specimen, for example,

**TABLE 4** Stiffness degradation-based fatigue life estimation of run-out specimens.

Specimen no.	$N_{min}$ [-]	$N_{ave}$ [-]	$N_{max}$ [-]
174	4,036,622	17,420,943	34,629,862
057	—	—	—
166	1,480,000	8,462,946	21,467,943

$$N_{ave} = \frac{*(N)}{\tilde{N}_{ave}}. \quad (13)$$

When this is done for all intersection points, a prediction horizon can be calculated, compare Figure 12. The resulting fatigue life horizons for all run-out specimens are shown in Figure 5 and Table 4. In case of specimen 057, no intersection point was found, as the degradation of this specimen was even below the lower standard deviation of the model. Therefore, the fatigue life prediction was not applicable for this specimen. However, in case of specimen 174 and 166, the predicted life span is in good agreement with the Stüssi–Haibach S–N curve with respect to the expected standard deviation of S–N tests. It is emphasized that the stiffness degradation model is independent of the S–N fits. Therefore, the agreement of the fatigue life prediction horizons with the, for example, Stüssi–Haibach S–N curve can be interpreted as indications of their validity.

A qualitative verification of the prediction is provided by a comparison of the stiffness degradation model and the scaled experimental time series. In Figure 12, this is shown based on the mean intersection point of the stiffness degradation model, so that the run-out cycles  $*(N)$  of this specimen were scaled to  $\tilde{N}_{ave}$ . A reasonable agreement between the scaled experimental results and the model was found. The mean intersection point was therefore highlighted by a vertical black line in the fatigue life prediction horizon as the most probable result, compare Figures 12 and 5.

Theoretically, this approach can be applied to both the  $E$  and  $G$  modulus degradation measurement to gain a broader picture of the uncertainties. However, in this work, the stiffness degradation-based fatigue life estimation is solely done using the measurement from the active load component, as these data were in better agreement with the respective models and the overall degradation was more significant.

## 5 | CONCLUSION

Axial and torsional fatigue tests were carried out for a structural rotor blade adhesive at different stress ratios.

The specimens utilized for the experiments were optimized in a previous study in such a way that manufacturing-induced defects are minimized. This resulted in significantly improved fatigue properties in comparison to hand-mixed specimens with high porosity. This highlights the significance of the manufacturing process in terms of the reliability of the material properties, as low-quality specimens will lead to (very) conservative estimates and potentially wrong conclusions concerning the material modeling.

The Stüssi S–N approach was found to be an excellent fit of the data for all investigated stress ratios and load types. On account of recent gigacycle fatigue studies and the lack of data for the adhesive in this regime, a conservative engineering approximation was derived including a smooth transition of the Stüssi S–N curve to the Haibach extension line.

Based on the good fit of the sigmoidal-shaped Stüssi S–N curve and the very significant and load level-dependent differences of the results to hand-mixed specimens, a constant safety factor for manufacturing-induced defects in terms of permissible amplitude or cycles to failure does not seem recommendable. Instead, a safety factor related to the slope of the S–N curve was identified as a more appropriate option.

A comparison of the static (true) stress–strain curves and the S–N data indicated that a surrogate proportional limit at a plastic offset strain of 100  $\mu\text{m}/\text{m}$  may serve as a first approximation of the fatigue limit prediction by the Stüssi S–N line. While this fatigue limit is not trustworthy for gigacycle fatigue applications without sufficient experimental data, this approximation can still be useful for the allocation of specimens and testing equipment in the high cycle fatigue regime.

The experiments were accompanied by stiffness degradation measurements. It was found that the degradation of the stiffness moduli is load level-dependent and in between 5% and 15%. A smooth function fit of the data was generated employing a power law fit with load level-dependent fitting parameters. The model was applied to predict the residual fatigue life of run-out specimens. In addition, the driving factor for stiffness degradation was identified to be the stress amplitude, as a mean stress did not accelerate the degradation process.

#### ACKNOWLEDGMENTS

This work was supported by the German Federal Ministry for Economic Affairs and Climate Action (BMWK) in the ReliaBlade project (grant numbers 0324335A, 0324335B). The authors would like to acknowledge the work of Martina Karalus and Henning Schnellen, who accompanied the fatigue experiments as technicians and implemented the machine code. Open Access funding enabled and organized by Projekt DEAL.

#### AUTHOR CONTRIBUTIONS

**Michael Kuhn:** Development and implementation of the proposed methods, post-processing of the  $\mu\text{CT}$  scan segmentation, and illustrations and writing of the paper. **Nikolas Manousides:** High-resolution X-ray microscopy ( $\mu\text{CT}$  scanning) of the specimens and segmentation pre-processing. **Alexandros Antoniou:** Scientific advice and support with executing the experiments at Fraunhofer IWES. **Claudio Balzani:** Conceptual guidance and scientific supervision of all project phases.

#### CONFLICT OF INTEREST

The authors declare no potential conflict of interests.

#### FINANCIAL DISCLOSURE

None reported.

#### DATA AVAILABILITY STATEMENT

The raw/processed data required to reproduce these findings cannot be shared at this time due to legal or ethical reasons.

#### ORCID

Michael Kuhn  <https://orcid.org/0000-0002-5859-5444>

#### REFERENCES

1. Noever-Castelos P, Haller B, Balzani C. Validation of a modeling methodology for wind turbine rotor blades based on a full-scale blade test. *Wind Energy Sci.* 2022;7:105-127.
2. Sayer F, Antoniou A, van Wingerde A. Investigation of structural bond lines in wind turbine blades by sub-component tests. *Int J Adhes Adhes.* 2012;37:129-135.
3. Subrahmanian KP, Dubouloz F. Adhesives for bonding wind turbine blades. *Reinf Plast.* 2009;53:26-29.
4. Caous D, Bois C, Wahl J-C, Palin-Luc T, Valette J. Analysis of multiaxial cyclic stress state in a wind turbine blade. 20th ICCM; 2015.
5. Rommel DP, Di Maio D, Tinga T. Calculating wind turbine component loads for improved life prediction. *Renew Energ.* 2020;146:223-241.
6. Rosemeier M, Krimmer A, Bardenhagen A, Antoniou A. Tunneling Crack Initiation in Trailing-Edge Bond Lines of Wind-Turbine Blades. *AIAA J.* 2019;57:5462-5474.
7. Noever-Castelos P, Ardizzone L, Balzani C. Model updating of wind turbine blade cross sections with invertible neural networks. *Wind Energy.* 2022;25:573-599.
8. Sayer F, Antoniou A, Goutianos S, Gebauer I, Branner K, Balzani C. ReliaBlade Project: A Material's Perspective towards the Digitalization of Wind Turbine Rotor Blades. *IOP Conf Ser: Mater Sci Eng.* 2020;942:12006.
9. Fernandez G, Vandepitte D, Usabiaga H, Debruyne S. Static and cyclic strength properties of brittle adhesives with porosity. *Int J Fatigue.* 2018;117:340-351.
10. Sears AT, Samborsky DD, Agastra P, Mandell JF. Fatigue Results and Analysis for Thick Adhesive Notched Lap Shear Test. In: Proc. AIAA; 2010.

11. Zarouchas D, Nijssen R. Mechanical behaviour of thick structural adhesives in wind turbine blades under multi-axial loading. *J Adhes Sci Technol*. 2016;30:1413-1429.
12. Wentingmann M, Manousides N, Antoniou A, Balzani C. Design and manufacturing optimization of epoxy-based adhesive specimens for multiaxial tests. *Mater Des*. 2021;212:110213.
13. Antoniou A, Rosemeier M, Tazefidan K, Krimmer A, Wolken-Möhlmann G. Impact of Site-Specific Thermal Residual Stress on the Fatigue of Wind-Turbine Blades. *AIAA J*. 2020;58:4781-4793.
14. Krogh L, Schawe JEK, Possart W. Dynamic mechanical properties of very thin adhesive joints. *J Appl Polym Sci*. 2015;132:42058.
15. Ries M, Possart G, Steinmann P, Pfaller S. A coupled md-fe methodology to characterize mechanical interphases in polymeric nanocomposites. *Int J Mech Sci*. 2021;204:106564.
16. Tokyo Measuring Instruments Laboratory Co., Ltd.. GFRAB-3-350-50. [https://tml.jp/e/product/strain\\_gauge/gf\\_list.html](https://tml.jp/e/product/strain_gauge/gf_list.html), Accessed: October, 2022; 2021.
17. Hexion™. Technical Data Sheet - EPIKOTE™ Resin MGS™ BPR 135G-Series and EPIKURE™ Curing Agent MGS™ BPH 134G-137GF; 2021.
18. Carl Zeiss AG. Zeiss Xradia 410 Versa. <https://www.zeiss.com/microscopy/int/products/x-ray-microscopy/zeiss-xradia-410-versa.html>, Accessed: October, 2022; 2021.
19. Walter + Bai AG. Axial / Torsional Test Systems. [https://www.walterbai.com/page/products/Materials\\_Testing\\_Systems/Axial-Torsional\\_Testing\\_System/index.php](https://www.walterbai.com/page/products/Materials_Testing_Systems/Axial-Torsional_Testing_System/index.php), Accessed: October, 2022; 2021.
20. Wentingmann M, Manousides N, Antoniou A, Balzani C. Yield surface derivation for a structural adhesive based on multiaxial experiments. *Polym Test*. 2022;113:107648.
21. Adden S, Horst P. Stiffness degradation under fatigue in multi-axially loaded non-crimped-fabrics. *Int J Fatigue*. 2010;32:108-122.
22. Wöhler A. Über die Versuche zur Ermittlung der Festigkeit von Achsen, welche in den Werkstätten der Niederschlesisch-Märkischen Eisenbahn zu Frankfurt a. d. O. angestellt sind. *Zeitschrift für Bauwesen*. 1863;13:233-258.
23. Basquin OH. The exponential law of endurance tests. *Am Soc Test Mater*. 1910;10:625-630.
24. Sendekyj GP. Fitting models to composite materials fatigue data. *ASTM STP*. 1981;734:245-260.
25. Stüssi F. Zur Theorie der Dauerfestigkeit. *LABSE Congress Report*. 1956;5:229-234.
26. Kohout J, Věchet S. A new function for fatigue curves characterization and its multiple merits. *Int J Fatigue*. 2001;23:175-183.
27. Miner MA. Cumulative Damage in Fatigue. *J Appl Mech*. 1945;12:159-164.
28. Shiozawa K, Lu L, Ishihara S. S-N curve characteristics and subsurface crack initiation behaviour in ultra-long life fatigue of a high carbon-chromium bearing steel. *Fatigue Fract Eng M*. 2001;24:781-790.
29. Hong Y, Zhao A, Qian G, Zhou C. Fatigue strength and crack initiation mechanism of very-high-cycle fatigue for low alloy steels. *Metall Mater Trans A*. 2012;43:2753-2762.
30. Marines I, Bin X, Bathias C. An understanding of very high cycle fatigue of metals. *Int J Fatigue*. 2003;25:1101-1107.
31. Newman JCJ. Fatigue and Crack-Growth Analyses under Giga-Cycle Loading on Aluminum Alloys. *Procedia Eng*. 2015;101:339-346.
32. Haibach E. *Betriebsfestigkeit*: Springer-Verlag; 2006.
33. Christensen RM. Observations on the definition of yield stress. *Acta Mech*. 2008;196:239-244.
34. Christensen RM. *The Theory of Materials Failure*. Oxford University Press; 2016.
35. Rolland H, Saintier N, Raphael I, Lenoir N, King A, Robert G. Fatigue damage mechanisms of short fiber reinforced pa66 as observed in-situ synchrotron x-ray microtomography. *Compos Part B Eng*. 2018;143:217-229.
36. Biswal R, Zhang X, Syed AK, Awd M, Ding J, Walther F, Williams S. Criticality of porosity defects on the fatigue performance of wire + arc additive manufactured titanium alloy. *Int J Fatigue*. 2019;122:208-217.
37. Heuler P, Grimm J, Fuhrmann K, Troßmann T, Eulitz K-G. Influence of porosity and environmental impact on fatigue life of magnesium alloys. *Materialwiss Werkst*. 2008;39:694-701.
38. Mayer H, Papakyriacou M, Zettl B, Stanzl-Tschegg SE. Influence of porosity on the fatigue limit of die cast magnesium and aluminum alloys. *Int J Fatigue*. 2003;25:245-256.
39. Rosemeier M, Antoniou A. Probabilistic approach for the fatigue strength prediction of polymers. *AIAA J*. 2022;60:951-961.
40. Rosemeier M, Melcher D, Krimmer A, Wroblewski W, Antoniou A. Validation of crack initiation model by means of cyclic full-scale blade test. *J Phys Conf Ser*. 2022;2265:32045.
41. Curtis PT. Durability testing of polymer composites. In: Kelly A, Zweben C, eds. *Comprehensive Composite Materials*. Pergamon; 2000:163-182.

**How to cite this article:** Kuhn M, Manousides N, Antoniou A, Balzani C. Fatigue properties of a structural rotor blade adhesive under axial and torsional loading. *Fatigue Fract Eng Mater Struct*. 2023;46(3):1121-1139. doi:10.1111/ffe.13925

## 5

# Effects of non-proportionality and tension-compression asymmetry on the fatigue life prediction of equivalent stress criteria

4<sup>th</sup> Paper


The influence of non-proportional loads on the cycles to failure of the adhesive is analyzed experimentally by subjecting the specimens to biaxial fatigue loads with different levels of non-proportionality. In addition, the effect of non-proportional loads on the fatigue life prediction is shown by example of equivalent stress criteria, e.g., the previously validated Drucker-Prager criterion. The necessity to account for a tension-compression asymmetry is discussed since the asymmetry results in different Haigh diagram (stress space) representations and fatigue life predictions, respectively.

---

P4-1	Introduction . . . . .	79
P4-2	Experimental setup . . . . .	79
P4-3	Influence of non-proportional loads . . . . .	81
P4-4	Tension-compression asymmetry . . . . .	84
P4-5	Haigh diagram . . . . .	85
P4-6	Multiaxial fatigue life predictions . . . . .	87
P4-7	Conclusion . . . . .	92



# Effects of non-proportionality and tension–compression asymmetry on the fatigue life prediction of equivalent stress criteria

Michael Kuhn<sup>1</sup>  | Nikolas Manousides<sup>1</sup> | Alexandros Antoniou<sup>2</sup> | Claudio Balzani<sup>1</sup>

<sup>1</sup>Institute for Wind Energy Systems, Leibniz University Hannover, Hannover, Germany

<sup>2</sup>Institute for Wind Energy Systems, Fraunhofer IWES, Bremerhaven, Germany

## Correspondence

Michael Kuhn, Institute for Wind Energy Systems, Leibniz University Hannover, Appelstraße 9A, 30167 Hannover, Germany.  
Email: [research@iwes.uni-hannover.de](mailto:research@iwes.uni-hannover.de)

## Funding information

German Federal Ministry for Economic Affairs and Climate Action (BMWK), Grant/Award Numbers: 0324335A, 0324335B

## Abstract

Biaxial tension/compression–torsion fatigue tests with varying levels of non-proportionality were performed employing a structural adhesive designed for wind turbine rotor blades. The cycles to failure were found to be independent of the level of non-proportionality. It is demonstrated that numerical fatigue life predictions via rainflow-counted equivalent stress histories are not able to replicate these experimental observations and overestimate the fatigue life up to a hundredfold. The tension–compression asymmetry of the adhesive resulted in significant damage prediction differences depending on the stress space representation of the Haigh diagram. If not properly taken care of, the asymmetry will also lead to non-conservative results. While demonstrated with a short fiber-reinforced adhesive, the results can be transferred to other materials.

## KEYWORDS

multiaxial fatigue, non-proportionality, structural adhesives, tension–compression asymmetry, wind turbine rotor blades

## Highlights

- Non-proportional fatigue tests employing a structural adhesive.
- The cycles to failure were found to be independent of the level of non-proportionality.
- A tension–compression asymmetry significantly influences the fatigue life prediction.
- Rainflow-counted equivalent stresses overestimate the non-proportional fatigue life.

This is an open access article under the terms of the [Creative Commons Attribution](https://creativecommons.org/licenses/by/4.0/) License, which permits use, distribution and reproduction in any medium, provided the original work is properly cited.

© 2023 The Authors. *Fatigue & Fracture of Engineering Materials & Structures* published by John Wiley & Sons Ltd.

## 1 | INTRODUCTION

Fatigue damage modeling is usually based on uniaxial experimental data. However, multiaxial fatigue loads are very common in engineering applications. To allow for a broader understanding of multiaxial fatigue phenomena, these also have to be replicated in experiments. This way, the reliability of (multiaxial) fatigue damage models can be validated.

Among multiaxially loaded components, different loads can be independent of each other, which can lead to varying principal stress–strain directions. This load state is classified as non-proportional and can cause additional uncertainties with fatigue life predictions.<sup>1,2</sup>

Depending on the material, the same load amplitude can lead to different cycles to failure in a non-proportional load state compared to a proportional one. Sonsino<sup>3</sup> showed that ductile materials tend to exhibit a decreased fatigue life in non-proportional loads, while brittle materials can show increased fatigue life.

Independent of the altered cycles to failure, fatigue analyses for non-proportional loads require additional care, because of the potentially lower damage prediction quality of standard methods, such as the evaluation of rainflow-counted equivalent stress histories.<sup>1,2</sup>

One way to recreate non-proportional loads in experiments is to use tension/compression–torsion testing machines with a phase shift in between the sinusoidal normal load and the sinusoidal torsional load. Due to the complexity of the test setup and challenging tubular specimen manufacture,<sup>4</sup> non-proportional experiments on polymers<sup>5,6</sup> and other materials<sup>7–10</sup> are rather scarce in literature and non-existent in terms of structural adhesives for wind turbine rotor blades, yet.

Rotor blades of wind turbines are among the largest and most heavily loaded components of any kind. Due to their vast size and the stochastic nature of the wind, each blade experiences a 3D wind field and thus a stochastically varying wind load with each rotation. This wind load is superimposed with a gravitational load based on the rotation of the rotor, which is approximately sinusoidal and smoothed by the large inertia of the complete rotor.

The combination of the stochastic wind load and approximately deterministic gravitational load leads to complex multiaxial fatigue stresses, which can exhibit significant levels of non-proportionality depending on the blade design and average wind speed.<sup>11,12</sup> While these stress states are dominated by normal stresses due to bending in case of a high blade stiffness, modern rotor blades tend to be more flexible to limit bending stresses. Passive load control features such as bend–twist coupling<sup>13,14</sup> also introduce higher torsional loads in order to

limit bending loads. These developments contribute to a more significant influence of multiaxial and non-proportional load states.

In order to simplify the manufacturing, rotor blades of wind turbines are typically made using two aerodynamic half shells and shear webs, which are joined employing structural adhesives. As pointed out in Eder et al,<sup>15,16</sup> the complex multiaxial fatigue loads in the adhesive joints proved to be a design driver for rotor blades.

Therefore, enhanced understanding of the influence of multiaxial and non-proportional loads on the fatigue life of rotor blade adhesives can help to optimize rotor blades. This applies to the experimentally observed fatigue life and equivalent stress-based predictions thereof, since this methodology is frequently used in wind energy contexts.<sup>16–21</sup>

In this work, the influences of multiaxial non-proportional loads and tension–compression asymmetry on the fatigue life (prediction) are demonstrated by combined tension/compression–torsion experiments. The material under investigation is a structural adhesive commonly used in wind turbine rotor blades. However, general findings and discussions on the fatigue life prediction are not limited to this particular material. Virtually defect-free specimens and a large number of tests maximize the reliability of the results.

Section 2 specifies the material system, specimen manufacturing and test setup. The influence of non-proportional loads on the experimental fatigue life is shown in Section 3 followed by a discussion on the implications of a tension–compression asymmetry on the fatigue life prediction in Section 4. A Haigh diagram is constructed in Section 5, which is subsequently used in the multiaxial and equivalent stress-based fatigue life prediction in Section 6.

## 2 | EXPERIMENTAL SETUP

The manufacturing of the utilized specimens and fatigue testing conditions are briefly explained in the following.

### 2.1 | Material system

In this work, an epoxy-based and short glass fiber-reinforced adhesive is analyzed. As in previous studies<sup>4,22,23</sup> of the authors, EPIKOTE™ Resin MGS™ BPR 135G3 and EPIKURE™ Curing Agent MGS™ BPH 137G are used. The two-component structural adhesive is commonly used in the wind energy industry. Detailed material properties can be found in the data sheet<sup>24</sup> and the aforementioned studies by the authors.

## 2.2 | Specimen design and manufacturing

The specimen design and manufacturing process were optimized in a previous study.<sup>4</sup> The specimen geometry is a tapered tube, which was optimized in a finite element-based parametric study in such a way that stress concentrations were minimized. Vacuum speed mixing was combined with 3D-printed mold inserts in an injection molding process to assure a high mixing homogeneity and low porosity level.

Subsequent to the manufacturing, the specimen quality was analyzed employing high-resolution X-ray microscopy ( $\mu$ CT scanning) using a Zeiss Xradia 410 Versa.<sup>25</sup> Qualitative porosity scans are shown in Figure 1 for all specimens in this work. Similar to previous studies,<sup>4,22,23</sup> the porosity level is negligible in the test section. Only a small amount of pores was found at the end and outer perimeter of the tapered section. These pores are a result of race tracking effects, that is, slight differences of the cross-sectional flow speed distribution during the injection process. However, these pores do not influence the load distribution in the test section on account of their small size and distance to the test section.

Based on the anisotropic stiffness properties derived in a previous publication<sup>4</sup> and additional (very) high-resolution  $\mu$ CT scans, the specimens can be classified as transversely isotropic with a large majority of fibers

aligned in axial direction. Cumulative frequency distributions of the fiber orientation are shown in Figure 2. Therein,  $\theta$  is the angle between the longitudinal axis of the specimen and the axial orientation of the individual fibers. On average 73.7% of all fibers within the scanned areas exhibit an axial orientation with less than 20° deviation to the longitudinal axis of the specimen. Within a distance of 0.25 mm from the inner and outer perimeter, the fiber orientation is closer to a quasi-isotropic distribution (linear dashed lines in Figure 2). Therefore, the fiber orientation is linked to the injection speed, which is lower in close proximity to the mold due to friction. Due to the excellent manufacturing quality of the specimens and the low standard deviation of the results observed in previous studies,<sup>4,22,23</sup> it is expected that the fiber orientation is approximately the same in all specimens.

## 2.3 | Biaxial fatigue testing campaign

The biaxial (tension/compression–torsion) fatigue tests were performed with a servohydraulic Walter + Bai LFW 100-T2000<sup>26</sup> equipped with a class 0.5 calibrated load cell. In situ surface temperature measurements were conducted using Pt100 sensors. In addition, the test frequency was adjusted at each load level to limit internal heating of the specimens and strain rate effects on the different load levels.

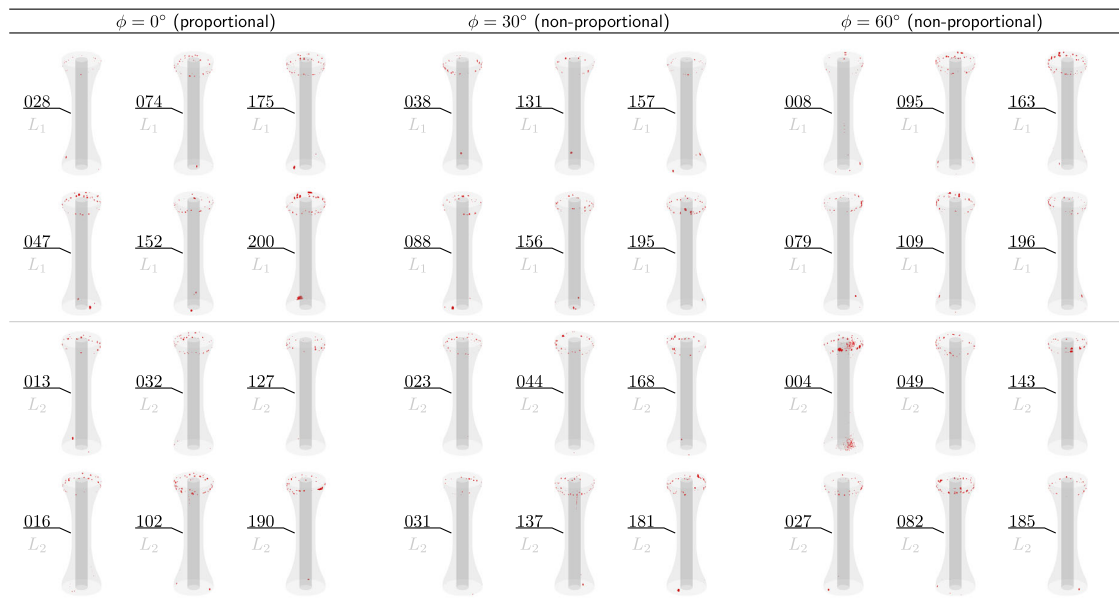


**FIGURE 1** Qualitative porosity comparison of the specimens used for this study. Pores are indicated in red. Specimen numbers and load level indications are given to the left of the respective depictions. The phase shift in between the axial and torsional load components is marked  $\phi$ . [Colour figure can be viewed at [wileyonlinelibrary.com](http://wileyonlinelibrary.com)]



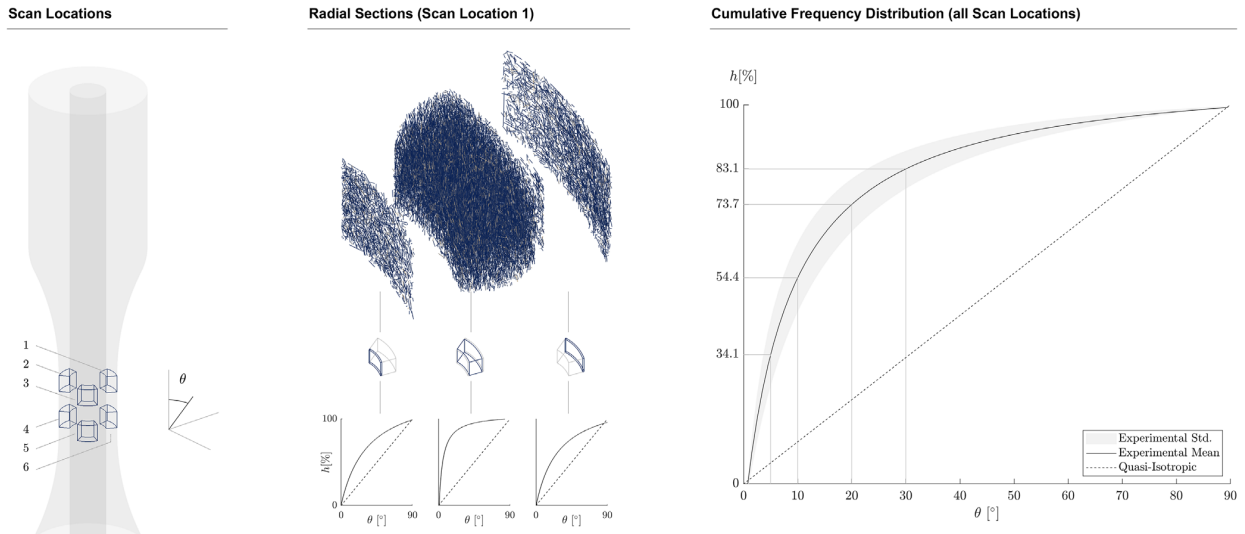


**FIGURE 2** Analysis of axial fiber orientation  $\theta$  within the test section of a specimen (wall thickness: 2.8 mm). Cumulative frequency distributions are provided for scan location 1 and for all scan locations combined (right). The radial slices (middle) have a width of 0.25, 2.3, and 0.25 mm, respectively. Blue color indicates a primarily axial fiber direction. The specimens can be classified as transversely isotropic with a large majority of the fibers aligned in axial direction. [Colour figure can be viewed at [wileyonlinelibrary.com](http://wileyonlinelibrary.com)]

Two load levels were chosen in such a way that the specimens fail in between  $10^4$  and  $10^5$  cycles. This way, the specimens fail close to the yield point of the material<sup>23</sup> in terms of an equivalent stress amplitude. The level of non-proportionality was adjusted using a phase shift  $\phi$  in between the axial and torsional load. A phase shift of  $\phi = 0^\circ$  represents a completely proportional load state and  $\phi = 90^\circ$  approximates a completely non-proportional load state in this work. Based on the results in Noever-Castelos et al,<sup>12</sup> it was decided to test intermediate states of  $\phi = 30^\circ$  and  $\phi = 60^\circ$  as these are very common in rotor blade bond lines in contrast to completely non-proportional states. Note that the level of non-proportionality is also related to the blade design, since the design decisions affect the multiaxial stress distribution.

To assure a reliable statistical evaluation of the results, each phase shift ( $0^\circ$ ,  $30^\circ$ ,  $60^\circ$ ) on each load level was tested with six specimens leading to 36 specimens in total.

The tests were intended to be load controlled. However, this was not possible in torsion on account of an issue with the inertia compensation of the torsional load cell, which was also apparent in the uniaxial tests of a previous study.<sup>22</sup> Therefore, only the axial component was load controlled, and the torsional component was displacement controlled. Both the axial and torsional components were applied as fully reversed loads. On account of the displacement control in torsion, the

applied shear stress is not constant, but a collective with roughly 5% degradation. However, this did not significantly change the level of non-proportionality as the phase shift  $\phi$  was still constant throughout the tests. The maximum change in non-proportionality was estimated at 2.96% (at Load Level 1 and  $\phi = 60^\circ$ ) according to the non-proportionality factor proposed by Meggiolaro and de Castro.<sup>27</sup>

### 3 | INFLUENCE OF NON-PROPORTIONAL LOADS

In this section, the experimental results and a classification of these with respect to literature are described.

#### 3.1 | Experimental results

The cycles to failure were found to be independent of the level of non-proportionality. This is true for the mean and the standard deviation as shown in Figure 3. This neutral behavior must, however, not be mistaken as a reason to neglect non-proportional effects, because these still have a significant effect on the numerical fatigue life prediction quality, which will be shown in Section 6.

The results are summarized in Table 1. On account of the low temperature increase during the experiments and

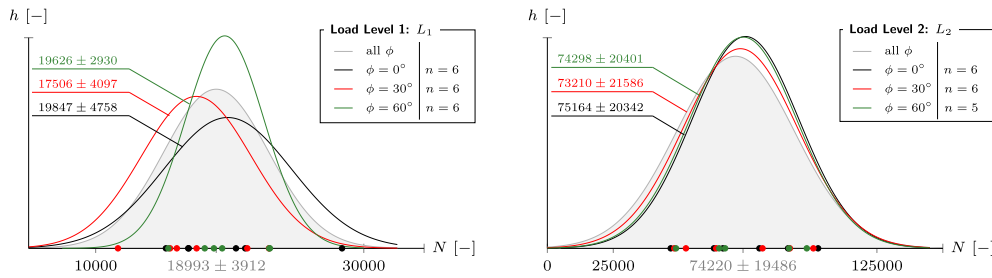


FIGURE 3 Frequency distributions of all biaxial fatigue tests with corresponding mean values and standard deviations. On both load levels, the cycles to failure  $N$  are independent of the phase shift  $\phi$  in between the axial and torsional load, that is, the level of non-proportionality. [Colour figure can be viewed at [wileyonlinelibrary.com](http://wileyonlinelibrary.com)]

TABLE 1 Summarized fatigue results.

Load Level 1 ( $L_1$ )				Load Level 2 ( $L_2$ )			
$\sigma_a = 25.50 \text{ N/mm}^2$ , $\tau_a = 21.72 \text{ N/mm}^2$ , $f = 1.0 \text{ Hz}$				$\sigma_a = 22.26 \text{ N/mm}^2$ , $\tau_a = 19.05 \text{ N/mm}^2$ , $f = 1.5 \text{ Hz}$			
Specimen No.	$\phi$ [°]	$N$ [-]	$\Delta T_{\max}$ [K]	Specimen No.	$\phi$ [°]	$N$ [-]	$\Delta T_{\max}$ [K]
028	0	15,238	2.12	190	0	46,790	4.22
200	0	16,905	2.57	102	0	63,182	4.15
152	0	16,941	2.88	016	0	66,571	6.95
047	0	20,467	2.88	127	0	80,437	4.01
074	0	21,154	2.37	013	0	91,302	3.20
175	0	28,378	3.37	032	0	102,700	4.52
195	30	11,665	1.63	137	30	48,134	5.04
156	30	15,550	1.99	181	30	52,560	4.46
088	30	16,053	—	168	30	64,048	4.54
038	30	17,529	1.81	044	30	81,620	2.68
131	30	21,312	2.56	031	30	92,000	2.84
157	30	22,927	1.92	023	30	100,900	3.35
109	60	15,425	2.28	185	60	48,795	2.54
008	60	18,134	2.34	143	60	65,153	2.98
095	60	18,820	2.15	082	60	67,440	0.90
196	60	19,437	2.87	049	60	91,699	3.25
163	60	22,943	3.70	004	60	98,402	3.75
079	60	22,996	2.15	027	60	208,500	2.18

Note: Therein,  $f$  is the test frequency,  $\Delta T_{\max}$  is the maximum temperature difference to the ambient temperature. A Pt100 sensor failed during the test of Specimen 088 and loosened in case of Specimen 016, increasing  $\Delta T_{\max}$  on account of friction.

the low overall standard deviation of the cycles to failure, it is expected that temperature-dependent effects can be neglected. The shear stress amplitudes given in Table 1 have to be understood as damage equivalent amplitudes of the shear stress collectives, which resulted from the displacement-controlled torsional load; compare Section 2.3.

Note that Specimen 027 was treated as an outlier due to a fatigue life of more than double the average.

However, this represents a conservative decision regarding the classification of a neutral material behavior in terms of cycles to failure.

### 3.2 | Influence of material ductility

The influence of non-proportional loads on the fatigue life was connected to the ductility of a material by

Sonsino.<sup>3</sup> It is stated there that the non-proportional fatigue life tends to decrease for ductile materials, while it tends to increase for brittle materials in comparison to the proportional fatigue life. A neutral behavior in terms of fatigue life was observed in case of moderate ductility and brittleness, respectively. The level of ductility can be estimated by the yield strength ratio  $\kappa_\tau$  given by

$$\kappa_\tau = \frac{\tau_y}{\sigma_{y,t}} \quad (1)$$

where  $\tau_y$  and  $\sigma_{y,t}$  are the yield strengths in shear and tension. According to Wächter et al.,<sup>28</sup> a fully brittle material is characterized by  $\kappa_\tau = 1$ , while either  $\kappa_\tau = 0.5$  or  $\kappa_\tau = 1/\sqrt{3}$  classifies a fully ductile material. These ratios also reflect different equivalent stress hypotheses, that is, Rankine<sup>29</sup> ( $\kappa_\tau = 1$ ), Tresca<sup>30</sup> ( $\kappa_\tau = 0.5$ ), and von Mises<sup>31</sup> ( $\kappa_\tau = 1/\sqrt{3}$ ).

The adoption of the yield strength ratio as a metric for ductility is supported by a discussion on the yield locus of the adhesive presented in a previous publication.<sup>23</sup> Therein, the Drucker–Prager<sup>32</sup> criterion was identified as a significantly better fit for rather ductile (machine-mixed) specimens in comparison to the von Mises–Schleicher<sup>33</sup> criterion, which was proposed for rather brittle (hand-mixed) specimens by other authors.<sup>34,35</sup> Since the Drucker–Prager criterion is more conservative in shear, its yield strength ratio ( $\kappa_\tau = 0.76$ ) is lower than that of the von Mises–Schleicher criterion ( $\kappa_\tau = 0.83$ ). The applicability of the yield strength ratio as a measure of ductility for the adhesive was thus validated by experiments. Figure 4 visually summarizes the influence of non-proportional loads in combination with the ductility definition explained above. Due to the

multi-axiality of the respective  $S$ – $N$  curves, an equivalent amplitude  $\bar{\sigma}_a$  is required. The yield strength ratio of the adhesive ( $\kappa_\tau = 0.76$ ) puts it in a neutral category. Given the fatigue results of this study, the observations by Sonsino<sup>3</sup> can be confirmed. Since material properties of polymers, for example, the ductility, typically exhibit a strong temperature dependence,<sup>36</sup> the influence of non-proportional loads will also be temperature dependent. High temperatures will increase ductility and therefore lead to a reduction of the non-proportional fatigue life observed at room temperature. This effect was also shown by Sonsino.<sup>3</sup> Therefore, a temperature related safety factor regarding the permissible cycles to failure seems appropriate to account for different operational temperatures in the field. The magnitude of this safety factor is still to be determined by experiments.

Concerning two-component, fiber-reinforced (rotor blade) adhesives or polymers, the non-proportional effects on the fatigue life will generally be coupled to the fiber distribution and orientation that is achieved in the manufacturing process; compare Section 2.2, because these parameters affect the ductility of the material. This also holds for the curing cycle.

### 3.3 | Fracture surface analysis

The ratio of normal and shear stresses in the experiments was estimated in such a way that their damage contribution is approximately equal in the proportional load case. This is reflected by the main crack orientation of the biaxial tests shown in Figure 5, which was found to be the approximate mean of uniaxial fatigue tests<sup>22</sup> in fully reversed axial and torsional loading, respectively.

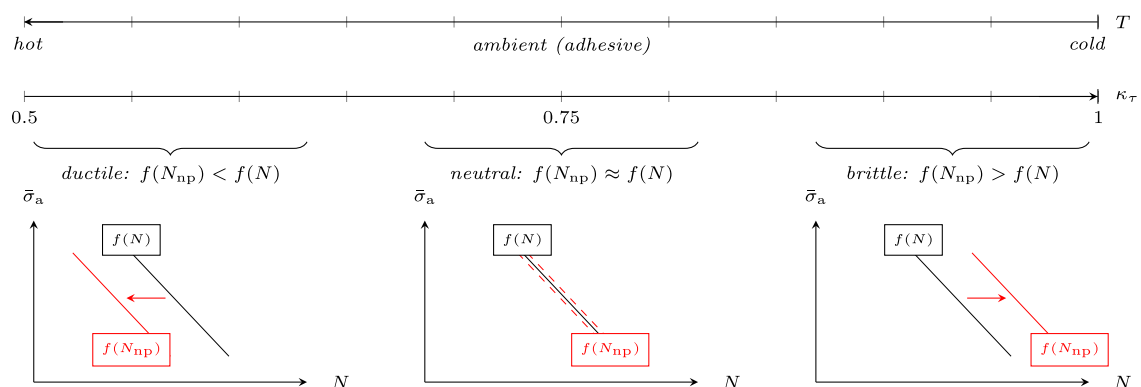


**FIGURE 4** Idealized influence of ductility on the  $S$ – $N$  behavior (equivalent amplitude vs. cycles to failure) with respect to the level of non-proportionality. High ductility is associated with decreased fatigue life under non-proportional loads, while brittle materials tend to show increased fatigue life in the same conditions. A measure of ductility is given by  $\kappa_\tau$ , the ratio of the yield strength in shear and tension. Since ductility is usually a function of temperature  $T$ , different behavior can be provoked. Fiber-reinforced adhesive was observed to be neutral at ambient temperature. [Colour figure can be viewed at [wileyonlinelibrary.com](http://wileyonlinelibrary.com)]

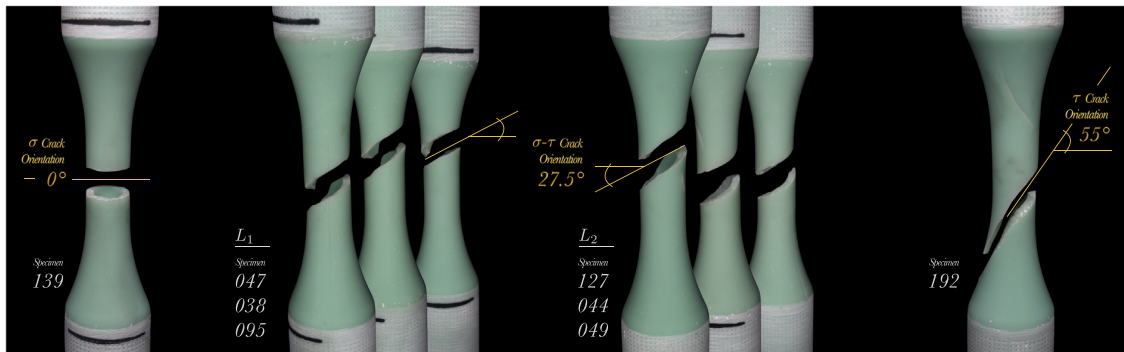


**FIGURE 5** Approximate orientation of fracture surfaces. The main crack orientation in the biaxial fatigue tests ( $\sigma$ - $\tau$ ) is approximately the mean of the uniaxial fatigue tests<sup>22</sup> in tension/compression ( $\sigma$ ) and torsion ( $\tau$ ). This observation is independent of the phase shift and level of non-proportionality, respectively, shown by three specimens from each load level with 0°, 30°, and 60° phase shifts; compare Table 1. [Colour figure can be viewed at [wileyonlinelibrary.com](http://wileyonlinelibrary.com)]

The main crack orientation was also independent of the level of non-proportionality, that is, the phase shift. This supports the findings regarding the neutral behavior of the adhesive with respect to the cycles to failure, because an altered main crack orientation could indicate a change in the damage mechanism. Simultaneously this highlights the reliability of the manufacturing process,<sup>4</sup> as different fiber orientations can introduce different micro- and meso-scale crack orientations.<sup>37</sup>

#### 4 | TENSION-COMPRESSION ASYMMETRY

The adhesive investigated in this work exhibits a strong tension-compression asymmetry, which can be expressed in terms of an axial yield strength ratio given by

$$\kappa_{\sigma} = \frac{|\sigma_{y,c}|}{\sigma_{y,t}}, \quad (2)$$

where  $\sigma_{y,c}$  is the yield strength in compression and  $\sigma_{y,t}$  is the yield strength in tension. The ratio was found to be 2.07 in a previous study.<sup>23</sup> As a result of this asymmetry, compression stresses are significantly reduced in the equivalent stress space  $\mathbb{R}^{\text{eqv}}$ , that is, the equivalent value of a compression stress is divided by 2.07 in this case. Therefore, the stress ratio  $R$  (ratio between minimum and maximum stress) in the engineering stress space  $\mathbb{R}^{\text{eng}}$  is different from the stress ratio  $\bar{R}$  in the equivalent stress space  $\mathbb{R}^{\text{eqv}}$ . This effect is visualized in Figure 6 (top).

Applying the strength asymmetry of the adhesive to a fully reversed, sinusoidal unit load in  $\mathbb{R}^{\text{eng}}$  results in a 0.26 N/mm<sup>2</sup> mean load (peak to peak mean) and a reduction of the stress ratio to  $\bar{R} = -0.48$  in  $\mathbb{R}^{\text{eqv}}$ . A fully

reversed stress ratio in  $\mathbb{R}^{\text{eqv}}$  can be achieved if the stress ratio in  $\mathbb{R}^{\text{eng}}$  resembles the tension-compression asymmetry, that is,  $R = \sigma_c/\sigma_t = -2.07$ . Less complicated conversions are found for pulsating stress ratios. In case of a pulsating load in compression (C-C, e.g.,  $R = -\infty$ ), the entire load history is compressed leading to smaller amplitudes and mean values in  $\mathbb{R}^{\text{eqv}}$ . However, in this case the stress ratio remains constant. A pulsating load in tension (T-T, e.g.,  $R = 0$ ) is not altered at all after the conversion to  $\mathbb{R}^{\text{eqv}}$ , since tension stresses already resemble equivalent stresses.

The scaling rules explained above were also transferred to a Haigh diagram at the bottom of Figure 6. Pulsating loads in tension are not scaled, leaving the positions of the respective  $S$ - $N$  lines in the Haigh diagram unchanged. In case of alternating loads, the stress ratio is changed and hence also the position of the respective  $S$ - $N$  lines. For pulsating compressive loads, the stress ratio remains constant. However, as the stress values get scaled, the position in the Haigh diagram also changes, transforming a shifted Haigh diagram in  $\mathbb{R}^{\text{eng}}$  into a symmetric one in  $\mathbb{R}^{\text{eqv}}$ .

An experimental verification of the tension-compression asymmetry in fatigue is also shown in Figure 7. Therein, the force displacement hysteresis of a uniaxial  $R = -1$  tension-compression test<sup>22</sup> is shown for different ratios between the actual cycles  $n$  and the cycles to failure  $N$ . A stiffness degradation is found in the tension quadrant, while virtually no change is observed in the compression quadrant. Thus, a tension stress is proven to exhibit more damage, that is, material degradation, than a compression stress of the same magnitude.

Given that the biaxial (tension/compression-torsion) experiments in this work were done at  $R = -1$  in  $\mathbb{R}^{\text{eng}}$ , the aforementioned scaling problem in  $\mathbb{R}^{\text{eqv}}$  affects the

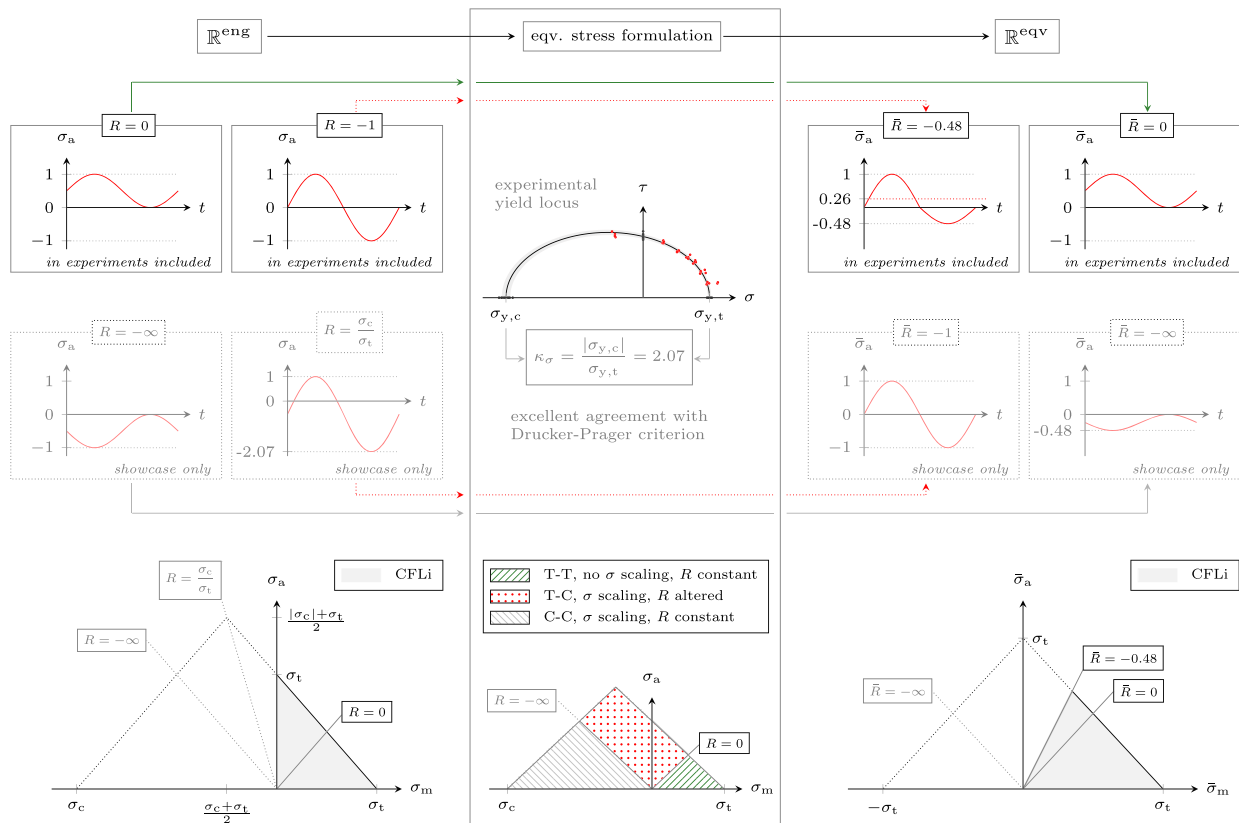


**FIGURE 6** Implications of a tension–compression asymmetry for fatigue. Negative stresses will be compressed after using an equivalent stress formulation in case  $|\sigma_{y,c}| > \sigma_{y,t}$ . This leads to a shift of the mean value, scaled amplitude, and a different stress ratio in the equivalent stress space  $\mathbb{R}^{eqv}$  depending on the stress ratio in the engineering stress space  $\mathbb{R}^{eng}$  and also affects the constant fatigue life interpolation (CFLi). The depicted yield locus was found to be representative for the adhesive in a previous study<sup>23</sup> and is excellently represented by the Drucker–Prager criterion. [Colour figure can be viewed at [wileyonlinelibrary.com](http://wileyonlinelibrary.com)]

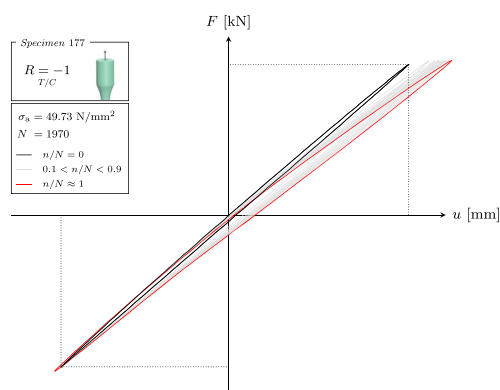


**FIGURE 7** Force displacement hysteresis of specimen 177 tested in fully reversed (uniaxial) tension–compression loading demonstrating a tension–compression asymmetry. Test conducted in Kuhn et al.<sup>22</sup> [Colour figure can be viewed at [wileyonlinelibrary.com](http://wileyonlinelibrary.com)]

re-calculation of the tests. Hence, a Haigh diagram is required and will be derived in the following.

It should be noted that a tension–compression asymmetry is found for a large variety of polymers<sup>38–42</sup> and other materials.<sup>43,44</sup> Therefore, this effect is not unique to the adhesive investigated in this work. In literature, however, implications of the asymmetry on the (equivalent) stress-based fatigue life prediction are hardly considered. This might lead to non-conservative fatigue life predictions, because stresses in  $\mathbb{R}^{eqv}$  are compared to  $S$ – $N$  lines, which are represented in the wrong stress space ( $\mathbb{R}^{eng}$ ).

## 5 | HAIGH DIAGRAM

Based on the uniaxial fatigue results recorded in a previous study,<sup>22</sup> a Haigh diagram is constructed in the following including a recently proposed  $S$ – $N$  formulation.

## 5.1 | Stüssi–Haibach $S$ – $N$ approach

The Stüssi–Haibach  $S$ – $N$  approach is a combination of the sigmoidal-shaped Stüssi<sup>45</sup>  $S$ – $N$  curve and the Haibach extension line<sup>46,47</sup> in the very high cycle fatigue (VHCF) regime and was proposed in a previous publication.<sup>22</sup> Regarding the adhesive, this approach represents an excellent fit of the  $S$ – $N$  data with an engineering approximation for VHCF, as there is not enough data to verify a fatigue limit. Since the Haibach extension line is modeled as a tangent of the Stüssi  $S$ – $N$  curve, a smooth transition between the models is established avoiding the necessity of an arbitrary transition point to be specified by the user. The model is thus easy to use and leads to consistent results. In case VHCF data are available, the slope of the extension line can also be adapted to provide the best overall fit. The approach is visualized in Figure 8.

In mathematical form, the Stüssi–Haibach  $S$ – $N$  approach is given by

$$\sigma_a = \begin{cases} \frac{R_m + \alpha N^\beta \sigma_\infty}{1 + \alpha N^\beta} & N < N_{\text{ext}}, \\ \alpha_{\text{ext}} N^{\beta_{\text{ext}}} & N \geq N_{\text{ext}}. \end{cases} \quad (3)$$

Therein,  $N_{\text{ext}}$  is the transition cycle number. In case  $N < N_{\text{ext}}$ , the Stüssi equation is used, where  $R_m$  is the ultimate (tensile) strength,  $\alpha$  and  $\beta$  are curve fitting parameters, and  $\sigma_\infty$  represents the (presumed) fatigue limit. If  $N \geq N_{\text{ext}}$ , a linear extension line is used according to the Basquin<sup>48</sup>  $S$ – $N$  model, where  $\alpha_{\text{ext}}$  and  $\beta_{\text{ext}}$  are curve fitting parameters. In the original proposal of the Stüssi–Haibach approach,<sup>22</sup> the slope of the extension line is found according to Haibach<sup>46,47</sup> via

$$\beta_{\text{ext}} = \left( \frac{2}{\beta} + 1 \right)^{-1}, \quad (4)$$

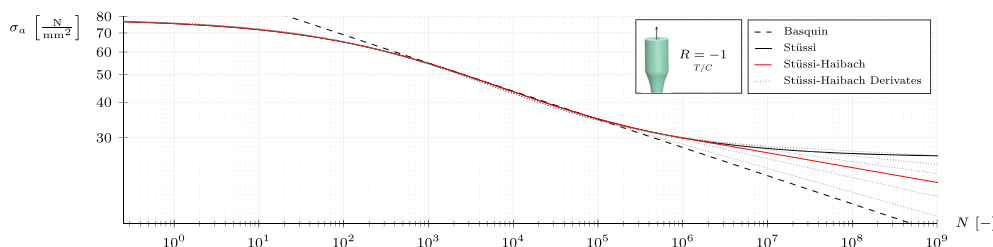


**FIGURE 8** Stüssi–Haibach approach and derivatives thereof. Depending on the availability of data in the VHCF regime, different (tangential) extension line slopes can be chosen. The depiction is based on uniaxial tension/compression data from a previous study.<sup>22</sup> [Colour figure can be viewed at [wileyonlinelibrary.com](http://wileyonlinelibrary.com)]

where  $\beta$  is the slope of the Basquin line fitted to the data in between the low cycle fatigue (LCF) and VHCF regime; compare Figure 8 (dashed line).

Afterwards, the extension line is modeled as a tangent to the Stüssi  $S$ – $N$  curve, which was previously fitted to all available data up to the VHCF regime. This way, the remaining variables  $\alpha_{\text{ext}}$  and  $N_{\text{ext}}$  can be found. However, if VHCF data is available, the extension line should be fitted to these data instead of using Equation (4) to allow for a better overall fit of the data; compare Figure 8 (Stüssi–Haibach derivatives).

In case the  $S$ – $N$  curve has a distinct plateau in the VHCF regime and a drop in fatigue strength beyond that, a combination of the Stüssi  $S$ – $N$  curve with the Sendekyj<sup>49</sup>  $S$ – $N$  curve might also provide a good approximation of the overall fatigue behavior. Shiozawa et al<sup>50</sup> among others<sup>51,52</sup> found evidence of such behavior, highlighting the importance of gigacycle fatigue tests.

## 5.2 | Constant fatigue life (CFL) model

Mean stress effects on the fatigue life of a material can be visualized in a Haigh diagram by connecting the available  $S$ – $N$  curves with respect to points of CFL. Depending on the material or the quantity of  $S$ – $N$  curves, different connection line models were proposed.

The linear Goodman<sup>53</sup> line is among the most widely used CFL models and can be expressed by

$$\frac{\sigma_a}{\sigma_a^{R=-1}} + \frac{\sigma_m}{R_m} = 1. \quad (5)$$

Therein,  $\sigma_a$  and  $\sigma_m$  represent an arbitrary stress amplitude and mean stress, while  $\sigma_a^{R=-1}$  is the stress amplitude of a fully reversed load with zero mean and  $R_m$  is the ultimate tensile strength. In case  $S$ – $N$  data for a stress ratio  $R \neq -1$  is available, the

Goodman approach can be adapted to a piecewise linear interpolation. For simplicity, the piecewise linear approach is chosen for all comparisons and analyses in this work. In addition, the measured  $S$ - $N$  curves are used without any statistical modification. The Haigh diagrams are therefore based on  $P_{50}$  Stüssi–Haibach  $S$ - $N$  curves.

### 5.3 | Model generation and discussion

In Kuhn et al,<sup>22</sup> two axial  $S$ - $N$  curves were recorded at  $R = -1$  and  $R = 0$ . Wentingmann et al<sup>23</sup> determined the tensile strength  $R_m$ , which corresponds to  $R = 1$ .

The resulting Haigh diagram in  $\mathbb{R}^{\text{eng}}$  is shown at the top of Figure 9. It was assumed that maximum amplitudes are found at  $R = \sigma_c/\sigma_t$  and that the yield strength ratio  $\kappa_\sigma = 2.07$  is still valid for the ultimate strength ratio. By converting the diagram to  $\mathbb{R}^{\text{eqv}}$ , the tension-based results  $\mathbf{R} = [0,1]$  remain unchanged, whereas the  $S$ - $N$  curve at  $R = -1$  is transformed according to the tension-compression asymmetry; compare Section 4. Therefore, the experimental  $R$  range in  $\mathbb{R}^{\text{eqv}}$  is limited to  $\bar{R} = [-0.48, 0, 1]$ . As a result, a gap in between  $\bar{R} = -0.48$  and  $\bar{R} = -1$  in  $\mathbb{R}^{\text{eqv}}$  exists, since experimental data for  $\bar{R} = -1$  are not available. Two possibilities were considered to circumvent the  $\bar{R}$ -gap, which are shown at the bottom of Figure 9.

In the first approach, the connection lines in between  $\bar{R} = -0.48$  and  $\bar{R} = 0$  are linearly extrapolated. This assumption is based on the overall linearization of the CFL lines in  $\mathbb{R}^{\text{eqv}}$  in between the measured (and transformed)  $S$ - $N$  curves. On account of that, the difference of the piecewise linear connection lines to global linear connection lines (traditional Goodman approach) is small for the recorded data in  $\mathbb{R}^{\text{eqv}}$ . Therefore, a piecewise linear extrapolation seems to be a reasonable engineering approximation. The linearization effect is also visualized in the mid of Figure 9, where the Haigh diagrams in  $\mathbb{R}^{\text{eng}}$  and  $\mathbb{R}^{\text{eqv}}$  are compared. In  $\mathbb{R}^{\text{eqv}}$ , the connection lines in between  $\bar{R} = -0.48$  and  $\bar{R} = 0$  (in red) are almost a perfect linear continuation of the connection lines between  $\bar{R} = 0$  and  $\bar{R} = 1$ .

The second approach is based on a conversion of a shear  $S$ - $N$  curve, which was also recorded at  $R = -1$  in Kuhn et al,<sup>22</sup> to  $\mathbb{R}^{\text{eqv}}$  using the Drucker–Prager criterion. By employing Drucker–Prager, shear stresses are transformed to equivalent tension values. This conversion is independent of the sign of the respective shear stress, because there is no strength asymmetry in shear. Assuming that the Drucker–Prager criterion can be used in fatigue, the transformation of the shear  $S$ - $N$  curve to  $\mathbb{R}^{\text{eqv}}$  will therefore result in an

equivalent  $\bar{R} = -1$  curve. This approach is called  $\tau_{\text{eqv}}$ -method in the following.

In comparison, the  $\tau_{\text{eqv}}$ -method leads to more conservative results than the linear extrapolation in the LCF regime up to approximately  $10^4$  cycles. With cycles above  $10^5$ , the  $\tau_{\text{eqv}}$ -method leads to more optimistic predictions than the linear extrapolation. However, as the Drucker–Prager equivalent stress formulation is strictly speaking only valid until the yield point and does not account for any plasticity effects, the large LCF differences are not representative. A clear conclusion on which approach is superior can only be drawn if additional data at  $R = \sigma_c/\sigma_t$  becomes available, as these data will be scaled to  $\bar{R} = -1$  in the same manner as the axial  $S$ - $N$  lines in this work.

The differences of the CFL connection lines in  $\mathbb{R}^{\text{eng}}$  and  $\mathbb{R}^{\text{eqv}}$  are shown in the mid section of Figure 9. Regardless of the extrapolation approach, the differences are significant with respect to alternating load cases ( $R < 0$ ). In addition, the  $\mathbb{R}^{\text{eqv}}$  CFL lines are found below the  $\mathbb{R}^{\text{eng}}$  CFL lines. This indicates that stress-based fatigue analyses of materials that exhibit a tension-compression asymmetry require a Haigh diagram in  $\mathbb{R}^{\text{eqv}}$  to avoid non-conservative fatigue life predictions in combination with asymmetric yield criteria such as the Drucker–Prager criterion.

## 6 | MULTIAXIAL FATIGUE LIFE PREDICTIONS

In this section, different invariant-based fatigue life predictions are compared with the experimental results. The procedure consists of the following steps in each case:

1. Calculation of an equivalent stress history  $\sigma_{\text{eqv}}(t)$
2. Rainflow count of the equivalent stress history to identify amplitudes and associated mean values for each cycle  $n_i$
3. Evaluation of permissible cycles  $N_i$  via a Haigh diagram
4. Linear damage accumulation<sup>54</sup>

The damage of each cycle is calculated as the ratio of the identified cycles and the permissible cycles to failure for the respective amplitude and mean value, that is,

$$D = \sum_i \frac{n_i}{N_i}. \quad (6)$$

This and similar procedures have been used extensively in literature<sup>16–21,55</sup> for multiaxial fatigue life

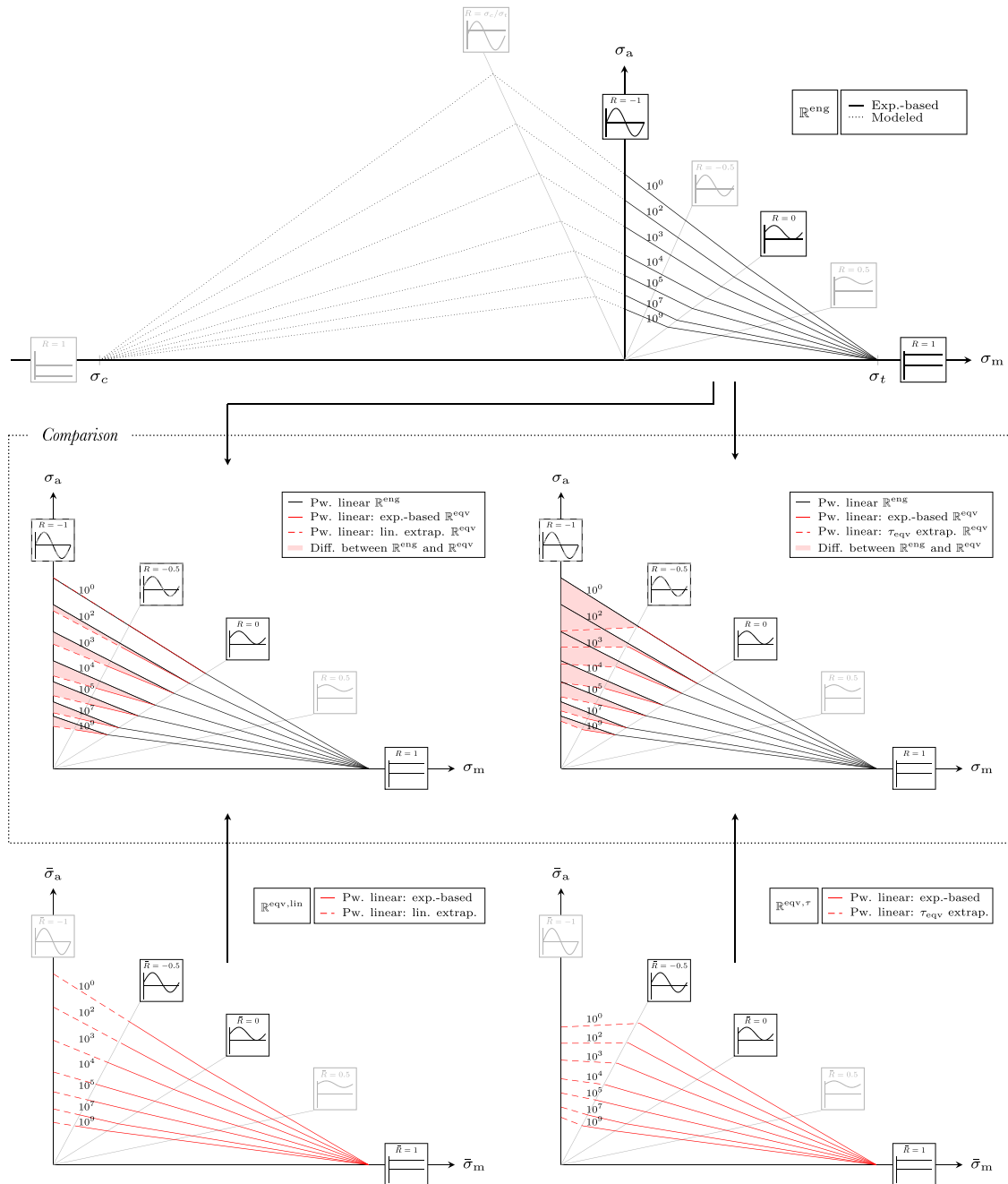


**FIGURE 9** Haigh diagram in  $R^{\text{eng}}$  (top) in comparison to Haigh diagrams in  $R^{\text{eqv}}$  (bottom). On the bottom left, linear extrapolations of the piecewise (pw) connection lines are modeled to overcome the gap in between  $\bar{R} = -0.48$  and  $\bar{R} = -1$  in  $R^{\text{eqv}}$ . On the bottom right this is done employing a shear  $S-N$  curve, which was converted to  $R^{\text{eqv}}$  using the Drucker-Prager criterion. The mid section shows a comparison of the  $R^{\text{eng}}$  and  $R^{\text{eqv}}$  diagrams, revealing significant differences regardless of the extrapolation approach in  $R^{\text{eqv}}$ . Experimentally measured (exp.-based)  $S-N$  curves are indicated by black  $R$ -markers; gray  $R$ -markers are for visualization purposes.  $\bar{R} = -0.48$  is depicted as  $\bar{R} = -0.5$ . [Colour figure can be viewed at [wileyonlinelibrary.com](http://wileyonlinelibrary.com)]

predictions. However, influences of non-proportional loads, tension-compression asymmetry, and the sign of the equivalent stress are often neglected.<sup>17,20,21</sup> Therefore,

these influences will be analyzed in the following to demonstrate their effects on the fatigue life prediction based on different equivalent stress approaches.



## 6.1 | Equivalent stress formulations

Wentingmann et al<sup>23</sup> found that the yield locus of the investigated adhesive can be described with the Drucker-Prager criterion, which is expressed by

$$\sigma_{DP} = \frac{(\kappa_\sigma - 1)I_1 + (\kappa_\sigma + 1)\sigma_{vM}}{2\kappa_\sigma}. \quad (7)$$

Therein,  $I_1$  is the first invariant of the stress tensor,  $\kappa_\sigma$  is the strength ratio given in Equation (2), and  $\sigma_{vM}$  is the well known von Mises<sup>31</sup> stress.

For the fatigue life prediction, the Drucker-Prager yield criterion will be used as an example for an equivalent stress formulation, which accounts for a tension-compression asymmetry, that is, an asymmetric yield locus. The von Mises yield criterion is used to evaluate the fatigue life when the tension-compression asymmetry is neglected and a symmetric yield locus is relied on. In both cases, the sign of the equivalent stress is determined via the sign of the largest absolute principle stress:

$$\sigma_{eqv,s} = \begin{cases} \text{sign}(\sigma_1) \cdot \sigma_{eqv} & |\sigma_1| \geq |\sigma_3|, \\ \text{sign}(\sigma_3) \cdot \sigma_{eqv} & |\sigma_1| < |\sigma_3|. \end{cases} \quad (8)$$

Signed criteria are indicated with a subscript  $s$  in the following. Note that the aforementioned sign correction does not work in case of pure torsion.

All equivalent stresses are a function of time  $t$  in this work. The phase shift  $\phi$ , used to provoke a non-proportional stress state in the biaxial ( $\sigma$ - $\tau$ ) experiments, is therefore recreated mathematically by

$$\sigma_z(t) = \sigma_a \sin(2\pi ft + \phi), \quad (9)$$

$$\tau_{z\eta}(t) = \tau_a \sin(2\pi ft), \quad (10)$$

where subscript  $a$  indicates the respective stress amplitudes and  $f$  represents the (test) frequency, which are both noted in Table 1,  $\sigma_z$  is the axial stress and  $\tau_{z\eta}$  is the shear stress from torsion (at the outer perimeter of the specimen).

## 6.2 | Hybrid equivalent stress

As shown in Section 5.3, the stress space of the Haigh diagram should be adapted to the equivalent stress formulation used, that is, asymmetric criteria require a

Haigh diagram in  $\mathbb{R}^{eqv}$  and symmetric criteria can be related to a Haigh diagram in  $\mathbb{R}^{eng}$ .

However, a hybrid formulation of asymmetric equivalent stress criteria allows for the use of the Haigh diagram in  $\mathbb{R}^{eng}$  again. This hybrid formulation is generated when the conversion of compressive normal stresses is suppressed. This way, asymmetric criteria work in a similar way as their symmetric counterparts, that is, the shear stresses are converted to  $\mathbb{R}^{eqv}$  and all normal stresses are treated as tensile stresses, which do not need to be converted separately. The only difference between a hybrid formulation of an asymmetric yield criterion and a standard symmetric one is thus the shear stress sensitivity, that is, the respective yield strength ratio  $\kappa_\tau$ ; compare Section 3.2. Therefore, the tension-compression asymmetry is shifted from the equivalent stress criterion to the  $\mathbb{R}^{eng}$  Haigh diagram. This is visually summarized in Figure 10.

In a biaxial tension/compression-torsion context, the hybrid formulation is achieved by allowing only positive normal stresses as input parameters to the equivalent stress formulation. For the Drucker-Prager criterion, this yields

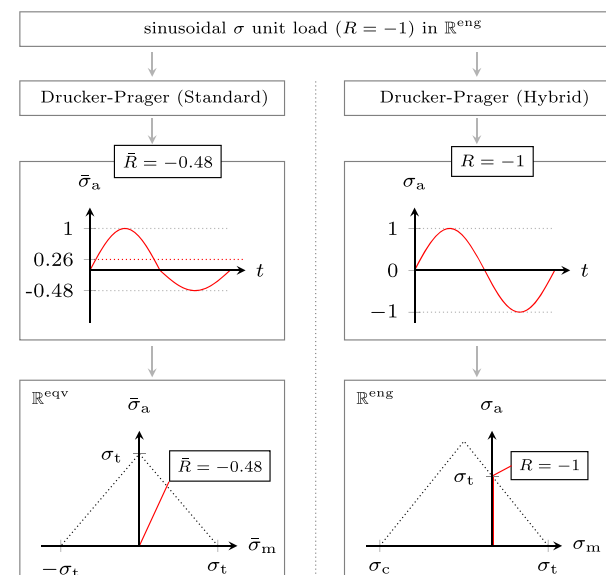


**FIGURE 10** Conversion of a sinusoidal  $\sigma$  unit load with the standard and hybrid formulation of the Drucker-Prager criterion. The standard version leads to a compressed negative half wave, a mean stress and requires an equivalent (symmetric) Haigh diagram. The hybrid version allows to use a conventional (but asymmetric) Haigh diagram in  $\mathbb{R}^{eng}$  as the negative half wave is not compressed. Both versions account for a tension-compression asymmetry,  $S$ - $N$  data availability is thus decisive. [Colour figure can be viewed at [wileyonlinelibrary.com](http://wileyonlinelibrary.com)]

$$\sigma_{\text{DP,hyb}} = \frac{(\kappa_{\sigma} - 1)|\sigma_z| + (\kappa_{\sigma} + 1)\sqrt{\sigma_z^2 + 3\tau_{z\eta}^2}}{2\kappa_{\sigma}} \quad (11)$$

The sign of the hybrid equivalent stress is restored as the sign of the absolute largest principle stress; compare Section 6.1.

The benefit of the hybrid formulation is that it offers the choice of using the Haigh diagram in  $\mathbb{R}^{\text{eng}}$  or  $\mathbb{R}^{\text{eqv}}$ . This is especially useful in cases where the load state is precisely known, so that interpolations and extrapolations within the respective Haigh diagram can be minimized. In this work, for instance, the  $\mathbb{R}^{\text{eng}}$  Haigh diagram is more useful as this version includes data at  $R = -1$ , which is equal to the  $\mathbb{R}^{\text{eng}}$  stress ratio of the biaxial tests, thus enabling a direct comparison with a single  $S$ - $N$  curve.

### 6.3 | Influences of non-proportional loads

Considering that the level of non-proportionality was found not to alter the cycles to failure for the investigated adhesive, an ideal damage prediction model will result in CFL independent of the level of non-proportionality. In this regard, the consistency of the damage prediction is more important than values close to the ideal of  $D = 1$  as a constant value might be adaptable to  $D = 1$  via calibration factors.

As mentioned in the previous section, the (signed) hybrid formulation of the Drucker–Prager criterion enables a direct comparison of the biaxial data (resulting equivalent stresses) with a single  $S$ - $N$  curve (tension–compression at  $R = -1$  in  $\mathbb{R}^{\text{eng}}$ ). This comparison is

shown in Figure 11. Using the proposed hybrid formulation of the Drucker–Prager criterion, the resulting equivalent stress amplitude matches very well with the uniaxial  $S$ - $N$  curve for the proportional load case ( $\phi = 0^\circ$ ). This can be interpreted as a confirmation that equivalent stress hypotheses can be used for multiaxial fatigue analyses. However, this solely applies to the proportional load case as the predicted amplitudes do not match the  $S$ - $N$  curve for the non-proportional (out-of-phase) load cases. Since the amplitude predictions of the signed hybrid Drucker–Prager criterion for the out-of-phase configurations ( $\phi = 30^\circ$ ,  $\phi = 60^\circ$ ) are found below the  $S$ - $N$  curve in Figure 11, the horizontal distance to the  $S$ - $N$  curve indicates a longer fatigue life than observed by experiments as the specimens failed within the gray scatter bands.

The equivalent amplitude decline results from the phase shift in between the normal and shear stress history, because the maxima of the stress components do not overlap anymore. The decline of the equivalent amplitude with increasing phase shift is also illustrated in Figure 12 (bottom) for the signed and unsigned versions of the hybrid Drucker–Prager criterion. While the principal stress-based sign correction works fine for the proportional load case, it leads to a discontinuous time series if a phase shift and therefore a non-proportional load case is present; compare Figure 12 (black lines, bottom). Even though this discontinuous time series is not physical, it leads to significantly larger amplitudes compared to the unsigned version shown in red. In fact, the unsigned formulation rapidly gets to a level that can be considered as insignificant in terms of fatigue damage. In addition, the mean value seems to increase for the unsigned equivalent stress, which is wrong as there is no mean value in the applied axial or torsional load in the experiments.

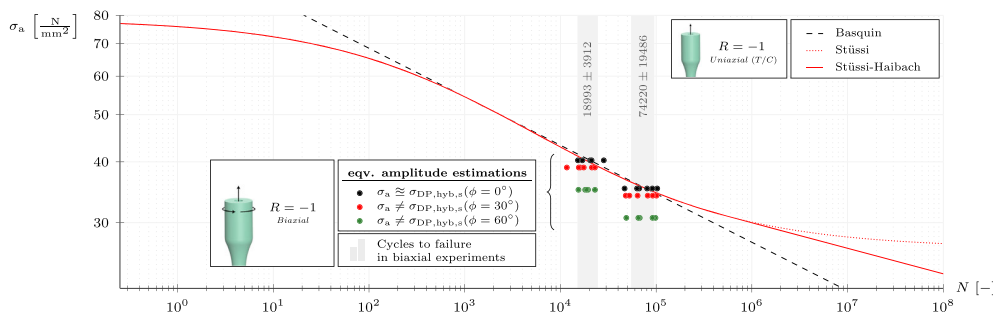


**FIGURE 11** Comparison of uniaxial tension–compression  $S$ - $N$  curves ( $\mathbb{R}^{\text{eng}}$ ) from a previous publication<sup>22</sup> with equivalent amplitude estimations for the biaxial fatigue data using the signed hybrid formulation of the Drucker–Prager criterion, Equation (11). Good agreement of the amplitude estimations with the  $S$ - $N$  curves is found for proportional load cases ( $\phi = 0^\circ$ ), while non-proportional load cases do not match. Thus, the (horizontal) distance to the  $S$ - $N$  curves indicates a longer fatigue life than experimentally observed (gray scatter band). [Colour figure can be viewed at [wileyonlinelibrary.com](http://wileyonlinelibrary.com)]

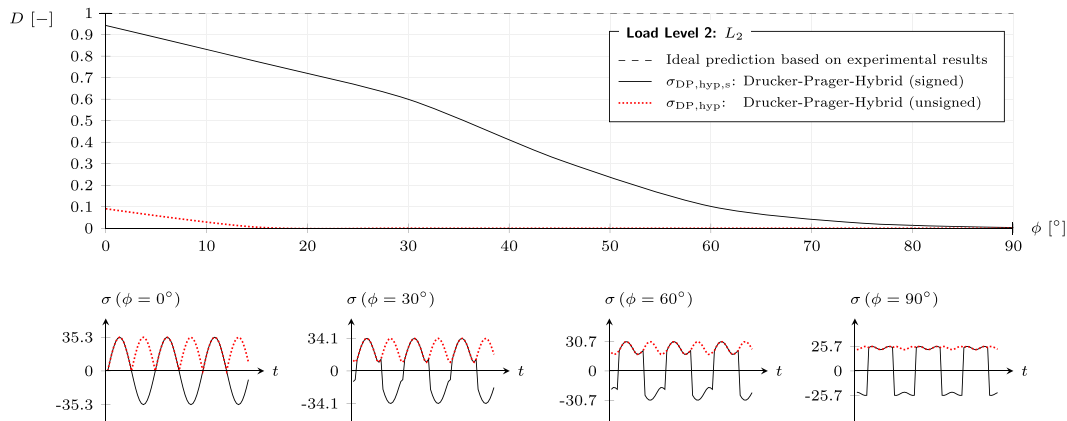


**FIGURE 12** Predicted damage of the signed and unsigned versions of the hybrid Drucker–Prager criterion in relation to the level of non-proportionality, that is, the phase shift  $\phi$  in between the axial and torsional load (top). High levels of non-proportionality lead to large differences of the damage predictions and the experimental results (top, dashed line). Exemplary equivalent stress histories demonstrate the influence of a phase shift on amplitude and mean value (bottom). The declining amplitude is the root cause for bad damage predictions in this case. [Colour figure can be viewed at [wileyonlinelibrary.com](http://wileyonlinelibrary.com)]

**TABLE 2** Linearly accumulated damage ( $D$ ) predictions for both load levels including different Haigh diagram types (cf. Figure 9) and equivalent stress criteria at different levels of non-proportionality and phase shift, respectively.

Haigh diagram	Eqv. stress	$L_1$				$L_2$			
		$\phi = 0^\circ$	$\phi = 30^\circ$	$\phi = 60^\circ$	$\phi = 90^\circ$	$\phi = 0^\circ$	$\phi = 30^\circ$	$\phi = 60^\circ$	$\phi = 90^\circ$
$\mathbb{R}^{eng}$	$\sigma_{DP,hyb}$	0.210	0.005	0.000	0.000	0.091	0.000	0.000	0.000
	$\sigma_{DP,hyb,s}$	1.023	0.723	0.212	0.011	0.942	0.599	0.102	0.003
	$\sigma_{DP}$	0.105	0.014	0.000	0.000	0.045	0.002	0.000	0.000
	$\sigma_{DP,s}$	0.563	0.391	0.116	0.008	0.429	0.262	0.044	0.002
	$\sigma_{vM}$	1.009	0.081	0.000	0.000	0.677	0.012	0.000	0.000
	$\sigma_{vM,s}$	3.283	2.338	1.094	0.491	3.508	2.471	1.012	0.366
$\mathbb{R}^{eqv,lin}$	$\sigma_{DP}$	0.105	0.014	0.000	0.000	0.045	0.002	0.000	0.000
	$\sigma_{DP,s}$	1.804	1.365	0.592	0.125	1.985	1.422	0.494	0.066
	$\sigma_{vM}$	1.009	0.081	0.000	0.000	0.677	0.012	0.000	0.000
	$\sigma_{vM,s}$	9.582	7.311	3.979	2.124	13.289	10.163	5.389	2.658
$\mathbb{R}^{eqv,\tau}$	$\sigma_{DP}$	0.105	0.014	0.000	0.000	0.045	0.002	0.000	0.000
	$\sigma_{DP,s}$	2.470	1.830	0.764	0.143	2.348	1.651	0.541	0.041
	$\sigma_{vM}$	1.009	0.081	0.000	0.000	0.677	0.012	0.000	0.000
	$\sigma_{vM,s}$	65.905	38.923	13.682	5.122	41.758	27.699	11.285	4.394

The differences in damage prediction quality of the signed and unsigned hybrid Drucker–Prager criterion are shown at the top of Figure 12. The decrease in accumulated damage  $D$  is clearly visible for an increasing phase shift for both versions and mirrors the mentioned amplitude decline. However, the signed version generates good results for (very) low phase shifts, whereas the unsigned version is significantly non-conservative at all times.

## 6.4 | Comparison of modeling approaches

The accumulated damage of all analyzed equivalent stress formulations, Haigh diagram types, and phase shifts is shown in Table 2. Regardless of the equivalent stress formulation, Haigh diagram type, or load level, increasing levels of non-proportionality led to (rapidly)

decreasing damage predictions. In a fully non-proportional case, the damage can be two orders of magnitude lower, even in case a good match was found for a proportional load case; compare  $\sigma_{DP,hyb,s}$  in Table 2. Therefore, applications and validations of this and similar fatigue damage prediction procedures for, for example, rotor blade adhesive joints<sup>17,20,21</sup> should be interpreted as solutions, which are limited to proportional load states. Hence, a more robust method such as the critical plane approach<sup>1,2,56-58</sup> is required for accurate multiaxial fatigue damage predictions given that the level of non-proportionality is not zero in rotor blades of wind turbines<sup>12</sup> and other structures. Although demonstrated with a structural adhesive, these findings can also be transferred to other materials since the root cause for the decreasing damage prediction quality is the amplitude underestimation in non-proportional cases, which is linked to equivalent stress criteria in general.

It is worth noting that all unsigned criteria predict the same damage for all Haigh diagram types in case of proportional loading ( $\phi = 0^\circ$ ), for example, the von Mises criterion predicts  $D0.677$  at  $L_2$  in each case. This is because unsigned criteria lead to a stress ratio of  $R = 0$  at  $\phi = 0^\circ$ , that is, a minimum value of exactly zero; compare Figure 12 (bottom, left). This stress ratio is not affected by a tension–compression asymmetry as shown in Figures 6 and 9. Therefore, the High diagram type is not affecting the damage prediction in this case. Apart from that, even small levels of non-proportionality will lead to a drastic decrease in damage prediction quality, resulting in a very unreliable behavior of these criteria.

Based on the differences of the Haigh diagram in  $\mathbb{R}^{eng}$  and  $\mathbb{R}^{eqv}$  shown in Figure 9, the predicted damage of signed criteria is larger when the  $\mathbb{R}^{eqv}$  types are used. The influences of non-proportional loads are also less pronounced in case of the  $\mathbb{R}^{eqv}$  Haigh diagram. For instance, the factor in between the fully proportional and fully non-proportional case using the signed Drucker-Prager criterion is 74 for the  $\mathbb{R}^{eng}$  variant at  $L_1$  and 14 for the  $\mathbb{R}^{eqv,lin}$  variant.

As pointed out in Section 6.2, the difference of a hybrid version of an asymmetric yield criterion and a symmetric one is solely the shear stress sensitivity. The influence of this sensitivity can be observed by comparing the results of the signed hybrid Drucker-Prager and signed von Mises criterion in Table 2, where the latter predicts a damage that is significantly larger.

Note that the experiments did not include data at  $\phi = 90^\circ$ . Therefore, the results presented above are extrapolated in this regard. However, it is expected that this represents a valid engineering approximation given the validated neutral  $S-N$  behavior up to  $\phi = 60^\circ$ .

## 6.5 | Discussion of modeling influences

CFL connection line types different from the piecewise linear approach will lead to different results for each equivalent stress hypothesis and phase shift. However, the general trend of a decreasing damage prediction quality with increasing levels of non-proportionality is independent of the connection line type and therefore persists.

The influence of non-proportional loads is dependent on a variety of parameters such as the load level, the ratio of normal to shear stresses and their individual stress ratio. The load level dependence is related to the decrease in equivalent amplitude with increasing non-proportionality, compare Figure 12 (bottom), and the use of the Stüssi-Haibach  $S-N$  approach, which introduces non-linear sections in the  $S-N$  diagram, compare Figure 8. The ratio of normal and shear stresses in conjunction with their individual stress ratio affects the maximum level of non-proportionality. High mean loads in combination with small amplitudes usually lead to smaller levels of maximum non-proportionality and therefore also reduce influences on the damage prediction quality. Nevertheless, non-proportional loads need to be accounted for in any case for a safe structural design.

## 7 | CONCLUSION

Biaxial (tension/compression–torsion) fatigue tests with varying levels of non-proportionality were conducted employing a structural adhesive. It was found that non-proportional loads did not change the cycles to failure, categorizing the adhesive as a neutral material. This categorization matches recent findings where the non-proportional  $S-N$  behavior was connected to the ductility of a material.

An excellent specimen quality and a high number of tests increased the reliability of the results in this work, as effects of defects (pores, etc.) were negligible and the overall scatter was small.

Due to a strong tension–compression asymmetry of the investigated adhesive, implications thereof on the fatigue life prediction were analyzed. Significant differences were found comparing a Haigh diagram in the engineering and the equivalent stress space, whereat the CFL connection lines in the equivalent stress space were found below the ones from the engineering stress space. Therefore, a Haigh diagram in the equivalent stress space should be used in conjunction with equivalent stress criteria that account for a tension–compression asymmetry, for example, the Drucker-Prager criterion,

to avoid non-conservative fatigue life predictions. Alternatively, a hybrid formulation of an asymmetric yield criterion allows the usage of a Haigh diagram in the engineering stress space again. This formulation was derived for the Drucker–Prager criterion in this work. As both proposals account for a tension–compression asymmetry, uncertainties with interpolations and extrapolations in the respective Haigh diagram can be minimized by choosing one of the aforementioned approaches.

An analysis of several equivalent stress criteria and Haigh diagram types was carried out concerning effects of non-proportional loads on the fatigue life prediction. The stress-based fatigue life prediction methodology resembled the state of the art in wind energy contexts. However, even in cases where a good match of the numerical prediction and experimental observation was achieved for a proportional load state, the prediction quality rapidly decreased for increasing levels of non-proportionality. As a result, fatigue life over-predictions by two orders of magnitude were found to be common for the test setup of this work. Thus, more robust methods are required to assure a reliable fatigue life prediction under non-proportional loads, which will be addressed in an upcoming publication.

#### AUTHOR CONTRIBUTIONS

**Michael Kuhn:** Conceptualization; formal analysis; methodology; software; visualization; writing—original draft preparation (lead); writing—review and editing (lead). **Nikolas Manousides:** Resources ( $\mu$ CT Scans); writing—original draft preparation (supporting); writing—review and editing (supporting). **Alexandros Antoniou:** Project administration; supervision; writing—original draft preparation (supporting); writing—review and editing (supporting). **Claudio Balzani:** Project administration; supervision; writing—original draft preparation (supporting); writing—review and editing (supporting); funding acquisition.

#### ACKNOWLEDGMENTS

This work was supported by the German Federal Ministry for Economic Affairs and Climate Action (BMWK) in the ReliaBlade project (Grants 0324335A and 0324335B). The authors would like to acknowledge the work of Martina Karalus and Henning Schnellen, who accompanied the fatigue experiments as technicians and implemented the machine code. Open Access funding enabled and organized by Projekt DEAL.

#### CONFLICT OF INTEREST STATEMENT

The authors declare no potential conflict of interests.

#### DATA AVAILABILITY STATEMENT

The data that support the findings of this study are available from the corresponding author upon reasonable request.

#### ORCID

Michael Kuhn  <https://orcid.org/0000-0002-5859-5444>

#### REFERENCES

- de Castro JTP, Meggiolaro MA. *Fatigue Design Techniques Under Real Service Loads. Volume II—Low-Cycle and Multiaxial Fatigue*. 1st ed.: CreateSpace Independent Publishing Platform; 2016.
- Socie DF, Marquis GB. *Multiaxial Fatigue*. Society of Automotive Engineers, Inc.; 2000.
- Sonsino CM. Multiaxial fatigue life response depending on proportionality grade between normal and shear strains/stresses and material ductility. *Int J Fatigue*. 2020;135:105468.
- Wentingmann M, Manousides N, Antoniou A, Balzani C. Design and manufacturing optimization of epoxy-based adhesive specimens for multiaxial tests. *Mater Des*. 2021;212:110213.
- De Monte M, Moosbrugger E, Jaschek K, Quaresimin M. Multiaxial fatigue of a short glass fibre reinforced polyamide 6.6 - Fatigue and fracture behaviour. *Int J Fatigue*. 2010;32:17-28.
- Hecht M, Baumgartner J, Tews K, Çavdar S, Meschut G. Fatigue strength of adhesively butt-bonded hollow cylinders under multiaxial loading with constant and variable amplitudes. *Procedia Struct Integr*. 2022;38:251-259.
- Jin S, Sun J, Yuan H. Anisotropic cyclic plasticity modeling for additively manufactured nickel-based superalloys. *Fatigue Fract Eng M*. 2022;45:2371-2387.
- Qu WL, Zhao EN, Zhou Q, Pi Y-L. Multiaxial low-cycle fatigue life evaluation under different non-proportional loading paths. *Fatigue Fract Eng M*. 2018;41:1064-1076.
- Wiebesiek J, Störzel K, Bruder T, Kaufmann H. Multiaxial fatigue behaviour of laserbeam-welded thin steel and aluminium sheets under proportional and non-proportional combined loading. *Int J Fatigue*. 2011;33:992-1005.
- Wu Z-R, Hu X-T, Song Y-D. Multiaxial fatigue life prediction for titanium alloy TC4 under proportional and nonproportional loading. *Int J Fatigue*. 2014;59:170-175.
- Chen X, Eder MA. A critical review of damage and failure of composite wind turbine blade structures. In: IOP Conference Series: Materials Science and Engineering, Vol. 942. IOP Publishing; 2020:012001.
- Noever-Castelos P, Wentingmann M, Balzani C. *Comparative study of finite-element-based fatigue analysis concepts for adhesive joints in wind turbine rotor blades*. In: von Scheven M, Keip M-A, Karajan N, eds. 7th GACM. Institute for Structural Mechanics, University of Stuttgart; 2017:300-304.
- Montano Z, Kühn M, Daniele E, Stüve J. Bend-twist coupling on rotor blades for wind turbines. *Lightweight Des Worldwide*. 2018;11:42-47.
- Wiens M, Meyer T, Wenske J. Exploiting bend-twist coupling in wind turbine control for load reduction. *IFAC-PapersOnLine*. 2020;53:12319-12144.

15. Eder MA, Bitsche RD, Belloni F. Effects of geometric non-linearity on energy release rates in a realistic wind turbine cross section. *Compos Struct.* 2015;132:1075-1084.
16. Eder MA, Semenov S, Sala M. Multiaxial stress based high cycle fatigue model for adhesive joint interfaces. In: *Computational and Experimental Simulations in Engineering: Proceedings of ICCES2019*. Vol. 75. Springer, Cham; 2020: 621-632.
17. Antoniou AE, Vespermann MM, Sayer F, Krimmer A. Life prediction analysis of thick adhesive bond lines under variable amplitude fatigue loading. In: *18th European Conference on Composite Materials (ECCM18)*. Applied Mechanics Laboratory; 2018:1-8. ISBN: 9781510896932.
18. Jin KK, Ghulam M, Kim JH, Ha SK, López BM, Gorostidi A. Life prediction of wind turbine blades. In: *ICCM*; 2017.
19. Nijssen RPL, Van Delft DRV. Alternative fatigue formulations for variable amplitude loading of fibre composites for wind turbine rotor blades. *ESIS PUBL*, Vol. 32: Elsevier; 2003: 563-574.
20. Noever Castelos P, Balzani C. On the impact of multi-axial stress states on trailing edge bondlines in wind turbine rotor blades. *J Phys Conf Ser.* 2016;753:062002.
21. Rosemeier M, Melcher D, Krimmer A, Wroblewski W, Antoniou A. Validation of crack initiation model by means of cyclic full-scale blade test. *J Phys Conf Ser.* 2022;2265: 032045.
22. Kuhn M, Manousides N, Antoniou A, Balzani C. Fatigue properties of a structural rotor blade adhesive under axial and torsional loading. *Fatigue Fract Eng M.* 2023;46: 1121-1139.
23. Wentingmann M, Manousides N, Antoniou A, Balzani C. Yield surface derivation for a structural adhesive based on multiaxial experiments. *Polym Test.* 2022;113:107648.
24. Hexion™. Technical Data Sheet—EPIKOTE™ Resin MGS™ BPR 135G-Series and EPIKURE™ Curing Agent MGS™ BPH 134G-137GF; 2021.
25. Carl Zeiss AG. Zeiss Xradia 410 Versa. Accessed May 2023; 2021. <https://www.zeiss.com/microscopy/int/products/x-ray-microscopy/zeiss-xradia-410-versa.html>
26. Walter + Bai AG. Axial/Torsional Test Systems. Accessed May 2023; 2021. [https://www.walterbai.com/page/products/Materials\\_Testing\\_Systems/Axial-Torsional\\_Testing\\_System/index.php](https://www.walterbai.com/page/products/Materials_Testing_Systems/Axial-Torsional_Testing_System/index.php)
27. Meggiolaro MA, de Castro JTP. An improved multiaxial rain-flow algorithm for non-proportional stress or strain histories—Part I: enclosing surface methods. *Int J Fatigue.* 2012;42: 217-226.
28. Wächter M, Linn A, Wuthenow R, et al. On scaled normal stresses in multiaxial fatigue and their exemplary application to ductile cast iron. *Appl Mech.* 2022;3:259-295.
29. Rankine WJM. *A Manual on Applied Mechanics*. Richard Griffin and Company; 1858.
30. Tresca HE. *Sur l'écoulement des corps solides soumis a de fortes pressions*. Gauthier-Villars; 1864.
31. von Mises R. Mechanik der festen Körper im plastisch- deformablen Zustand. *Nachr Ges Wiss Göttingen, Math-Phys Kl.* 1913;4:582-592.
32. Drucker DC, Prager W. Soil mechanics and plastic analysis or limit design. *Quart Appl Math.* 1952;10:157-165.
33. Schleicher F. Der Spannungszustand an der Fließgrenze (Plastizitätsbedingung). *J Appl Math Mech.* 1926;6(3):199-216.
34. Fernandez G, Vandepitte D, Usabiaga H, Debruyne S. Static and cyclic strength properties of brittle adhesives with porosity. *Int J Fatigue.* 2018;117:340-351.
35. Zarouchas D, Nijssen R. Mechanical behaviour of thick structural adhesives in wind turbine blades under multi-axial loading. *J Adhes Sci Technol.* 2016;30:1413-1429.
36. Mallick PK, Zhou Y. Yield and fatigue behavior of polypropylene and polyamide-6 nanocomposites. *J Mater Sci.* 2003;38: 3183-3190.
37. Rolland H, Saintier N, Raphael I, Lenoir N, King A, Robert G. Fatigue damage mechanisms of short fiber reinforced PA66 as observed by in-situ synchrotron X-ray microtomography. *Compos Part B: Eng.* 2018;143:217-229.
38. Meneghetti G, Ricotta M, Lucchetta G, Carmignato S. An hysteresis energy-based synthesis of fully reversed axial fatigue behaviour of different polypropylene composites. *Compos Part B: Eng.* 2014;65:17-25.
39. Raghava R, Caddell RM, Yeh GSY. The macroscopic yield behaviour of polymers. *J Mater Sci.* 1973;8:225-232.
40. Siviour CR, Jordan JL. High strain rate mechanics of polymers: a review. *J Dyn Behav Mater.* 2016;2:15-32.
41. Tao G, Xia Z. Biaxial fatigue behavior of an epoxy polymer with mean stress effect. *Int J Fatigue.* 2009;31:678-685.
42. Zhang J, Jiang H, Kang G, Jiang C, Lu F. A new form of equivalent stress for combined axial-torsional loading considering the tension-compression asymmetry of polymeric materials. *RSC Adv.* 2015;5:72780-72784.
43. Chen J, Yao W, Gao D. Fatigue life evaluation of tension-compression asymmetric material using local stress-strain method. *Fatigue Fract Eng M.* 2020;43:1994-2005.
44. Wang X, Chen W, Yang M, et al. Improving tension/compression asymmetry of a hot-extruded Mg-Zn-Y-Zr alloy via yttrium addition. *Adv Eng Mater.* 2021;23: 2100087.
45. Stüssi F. Zur Theorie der Dauerfestigkeit. *IABSE Congress Report.* 1956;5:229-234.
46. Haibach E. The influence of cyclic material properties on fatigue life prediction by amplitude transformation. *Int J Fatigue.* 1979;1:7-16.
47. Haibach E. *Betriebsfestigkeit*. Springer; 2006.
48. Basquin OH. The exponential law of endurance tests. *Proc Am Soc Testing Mater.* 1910;10:625-630.
49. Sendeckyj GP. *Fitting Models to Composite Materials Fatigue Data*: ASTM International; 1981;245-260.
50. Shiozawa K, Lu L, Ishihara S. S-N curve characteristics and subsurface crack initiation behaviour in ultra-long life fatigue of a high carbon-chromium bearing steel. *Fatigue Fract Eng M.* 2001;24:781-790.
51. Hong Y, Zhao A, Qian G, Zhou C. Fatigue strength and crack initiation mechanism of very-high-cycle fatigue for low alloy steels. *Metall Mater Trans A.* 2012;43:2753-2762.
52. Newman JCJ. Fatigue and crack-growth analyses under gigacycle loading on aluminum alloys. *Procedia Eng.* 2015;101: 339-346.
53. Goodman J. *Mechanics Applied to Engineering*: Longmans, Green and Co.; 1914.

54. Miner MA. Cumulative damage in fatigue. *J Appl Mech.* 1945; 12:159-164.
55. Nieslony A. Determination of fragments of multiaxial service loading strongly influencing the fatigue of machine components. *Mech Syst Signal Pr.* 2009;23:2712-2721.
56. Deng Q-Y, Zhu S-P, He J-C, Li X-K, Carpinteri A. Multiaxial fatigue under variable amplitude loadings: review and solutions. *Int J Struct Integr.* 2022;13:349-393.
57. Deng Q-Y, Zhu S-P, Niu X, Lesiuk G, Macek W, Wang Q. Load path sensitivity and multiaxial fatigue life prediction of metals under non-proportional loadings. *Int J Fatigue.* 2023; 166:107281.
58. Wentingmann M, Noever-Castelos P, Balzani C. An adaptive algorithm to accelerate the critical plane identification for multiaxial fatigue criteria. In: Owen R, de Borst R, Reese J, Pearce C, eds. Proceedings of 6th European Conference on Computational Mechanics (ECCM 6)/7th European Conference on Computational Fluid Dynamics (ECFD 7). International Center for Numerical Methods in Engineering (CIMNE); 2018:1-10.

**How to cite this article:** Kuhn M, Manousides N, Antoniou A, Balzani C. Effects of non-proportionality and tension-compression asymmetry on the fatigue life prediction of equivalent stress criteria. *Fatigue Fract Eng Mater Struct.* 2023;46(9):3161-3178. doi:[10.1111/ffe.14065](https://doi.org/10.1111/ffe.14065)





## 6

## Non-proportional fatigue life prediction without critical plane analysis – The forced proportional interference approach

The gained knowledge of all previous analyses is combined into a final comparison of non-proportional fatigue life prediction models. A detailed analysis of the critical plane methodology is carried out and its robustness is found to be based on its asynchronous behavior. Based on that, a new approach for the non-proportional fatigue life prediction is proposed and validated for the experimental results.

---

6.1	Introduction . . . . .	98
6.2	Multiaxial fatigue analyses . . . . .	98
6.3	A new approach to non-proportional fatigue analyses . . . . .	103
6.4	Implementation of methods . . . . .	105
6.5	Comparison to experiments . . . . .	107
6.6	Concluding Remarks . . . . .	112

## 6.1 Introduction

In this Chapter, common CP algorithms are used for fatigue life predictions of the short fiber-reinforced structural adhesive to showcase their damage prediction quality for different levels of non-proportionality based on recent biaxial fatigue experiments [198]. In addition, the experimental results gave rise to the idea of a re-proportionalization of a stress history to make use of the good fatigue life predictions of invariant-based approaches in proportional load cases [198] and the neutral behavior of the adhesive under non-proportional loads. This way, a computationally efficient and easy-to-use fatigue life estimation for non-proportional load cases could be achievable, which is why this idea is explored in the following.

## 6.2 Multiaxial fatigue analyses

The state of the art of equivalent stress-based multiaxial fatigue analyses is described in the following with an emphasis on limitations and drawbacks of the respective approaches.

### 6.2.1 Level of non-proportionality

The level of non-proportionality  $f_{np}$  is a decisive factor to identify an appropriate method for the fatigue life estimation, i.e., global equivalent stresses in case of approximately proportional load cases and the CP approach for non-proportional load cases.

Several authors [24, 60, 90, 199, 200] have proposed  $f_{np}$  versions to categorize the level of non-proportionality based on the stress history. While the methodologies to calculate  $f_{np}$  vary, the interpretation of the factor is usually the same, i.e., a fully proportional load state is found for  $f_{np} = 0$  and a fully non-proportional case is characterized by  $f_{np} = 1$ . In this work, the factor proposed by Meggiolaro and de Castro [200] is relied on.

Figure 6.1 illustrates the dependency of  $f_{np}$  of several variables. In case of a fully reversed load, the level of non-proportionality can also be assessed in terms of a phase shift  $\phi$  in between the normal and shear stress time series, cf. Figure 6.1 (upper left), when the normal stress and the shear stress have the same frequency. A fully proportional load case is found for  $\phi = 0^\circ$  and a fully non-proportional case is declared at  $\phi = 90^\circ$ . However,  $f_{np}$  is a more general way to indicate the level of non-proportionality, because at stress ratios different from  $R = -1$ , a phase shift of  $\phi = 90^\circ$  does not necessarily indicate a fully non-proportional load state anymore. In fact, a fully non-proportional load case ( $f_{np} = 1$ ) is found only for alternating loads and the tension-compression (T-C) regime in the Haigh diagram, respectively, cf. Figure 6.1 (lower left). However,  $f_{np}$  can still reach 0.58 in pulsating load conditions (T-T, C-C), which is enough to significantly distort the damage prediction quality in fatigue analyses [198]. Note that Figure 6.1 was limited to equal stress ratios for normal stresses ( $R_\sigma$ ) and shear stresses ( $R_\tau$ ) for illustration purposes, i.e.,  $R_\sigma = R_\tau = R$ . In addition, the ratio between normal and shear stress amplitudes, i.e.,  $\sigma_a/\tau_a$ , also affects the (maximum) level of non-proportionality, cf. Figure 6.1 (right). A fully non-proportional load case is found only in case  $\sigma_a/\tau_a = \sqrt{3}$  for the employed  $f_{np}$  factor (Meggiolaro and de Castro [200]). However,  $f_{np}$  is still significant at other amplitude ratios.

While a non-proportionality factor is a good option to choose an appropriate fatigue life estimation method, it is not able to distinguish between high or low load levels. Therefore, its screening use case in fatigue analyses is limited with respect to computational efficiency, because it will advise to use the computationally intense CP approach in locations with high  $f_{np}$  even though the damage potential is low.

In terms of wind turbine rotor blades, Noever et al [72] found that  $f_{np}$  can reach very high values ( $> 0.85$ ) for the adhesive joints. However, the mean is generally lower ( $\approx 0.4$ ) and dependent on the blade design and wind speed, since the multiaxial stress state is dependent on these variables.

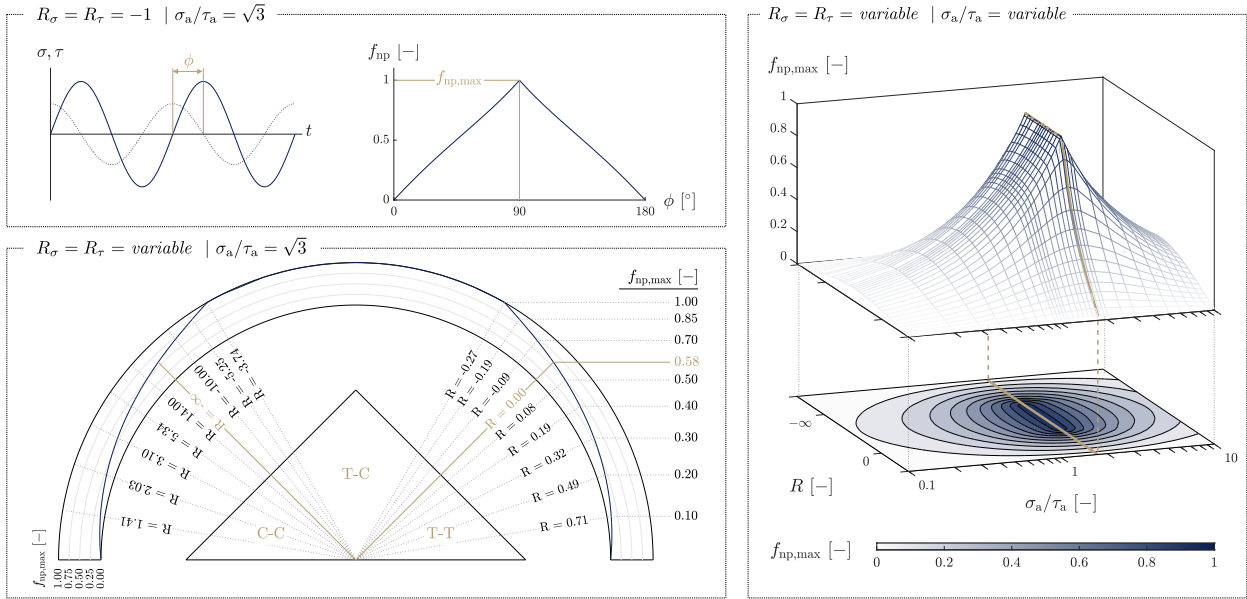


**Figure 6.1:** Level of non-proportionality  $f_{np}$  as a function of the phase shift  $\phi$  (upper left), the stress ratio between normal and shear stresses denoted by  $R_\sigma$  and  $R_\tau$  (lower left) and the amplitude ratio between normal and shear stresses  $\sigma_a/\tau_a$  (right). Equal frequencies used in all cases ( $f_\sigma = f_\tau$ ).

### 6.2.2 Overview: proportional loading

A proportional load case allows for a simplified analysis via a global equivalent stress, i.e., an invariant-based approach, which is indicated in Figure 6.2 by gray circular markers.

In the beginning, the entire stress history can (optionally) be filtered, e.g., using the multiaxial racetrack filter [78, 201] (MRF) to increase the computational efficiency of subsequent algorithms. A global equivalent stress criterion such as Drucker-Prager [202] or von Mises [203] is employed to reduce the 6D history to an equivalent 1D stress history. This equivalent history is used to identify load cycles via a uniaxial rainflow count [204]. A Haigh Diagram comprising, e.g., piecewise linear CFL interpolation lines is required to account for mean stress effects. The damage of each load cycle  $i$  can be estimated as the ratio of the identified cycles in the rainflow count  $n_i$  and permissible cycles to failure  $N_i$  from the Haigh diagram. The combined damage of all cycles  $D$  is calculated using the linear damage accumulation hypothesis [119], i.e.,

$$D = \sum_i \frac{n_i}{N_i}. \quad (6.1)$$

This methodology is limited to proportional load cases as shown, e.g., in a previous publication [198]. However, each sub-algorithm is well understood and optimized for computational efficiency.

### 6.2.3 Overview: non-proportional loading

In the more general case of non-proportional loading, the CP approach represents a physically meaningful way to estimate the fatigue life. The required algorithms are indicated in Figure 6.2 by blue circular markers.

In the CP approach, a material point is dissected into a large number of planes, whereat the most damaged plane is generally referred to as the critical plane [9]. Therefore, all algorithms listed in the following have to be evaluated on each potential critical plane. Hence, adaptive algorithms for the critical plane identification were proposed by several authors [121–123] to reduce the computational effort.

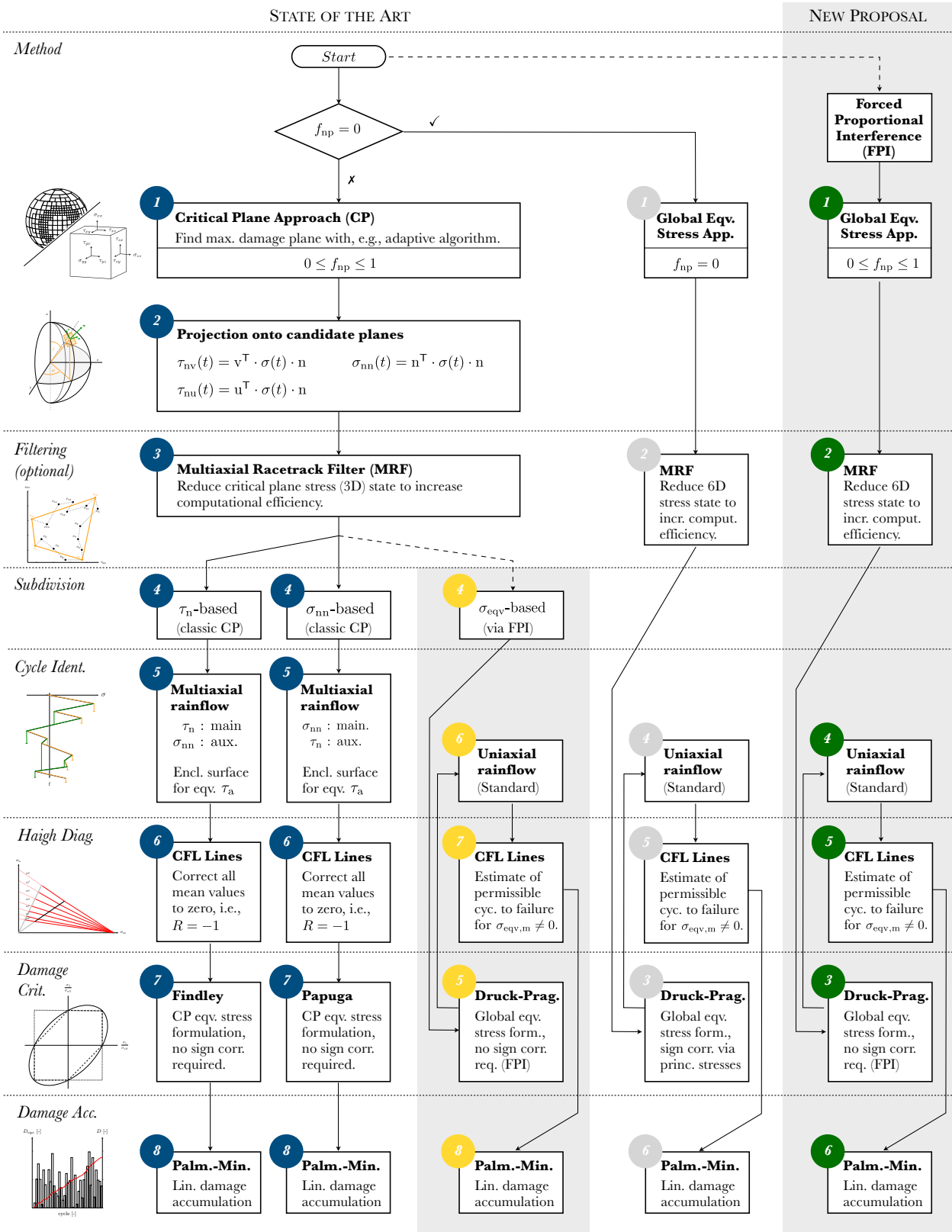


Figure 6.2: Synopsis of stress-based multiaxial fatigue approaches. Depicted methods and icons are exemplary.

In the first step, the global stress tensor is projected onto a candidate plane, resulting in two shear stresses ( $\tau_{nu}$ ,  $\tau_{nv}$ ) and one normal stress ( $\sigma_{nn}$ ) after multiplication of the stress tensor with the normal vector  $\mathbf{n}$  and the respective in-plane vectors  $\mathbf{u}$  and  $\mathbf{v}$ . Analog to the global equivalent stress approach, the CP stress history can optionally be filtered using, e.g., the MRF. Subsequently, it must be decided if the fatigue evaluation should be based on shear or normal stresses. Since this is mainly a decision driven by experience, the properties of the investigated material and the load case, it is certainly a complication in comparison to the global equivalent stress approach where no such distinction is required.

Depending on the chosen approach, a multiaxial rainflow count is employed, whereat the chosen stress component is counted actively in a main channel and the other one is processed in parallel in an auxiliary channel. In case of a shear stress-based approach, this means that, e.g., the modified Wang-Brown algorithm [83] (CP version) is used to identify cycles in the 2D shear stress history and the normal stress history is indexed according to the shear stress cycles. Since the shear stress cycles are still 2D, they need to be converted to an equivalent amplitude (and mean) in both the shear- and normal stress-based approach. Multiple enclosing surface methods to calculate the equivalent shear stress amplitude have been proposed [87–91, 205–208], whereat the polar moment of inertia method [91] (PMOI) is one of the more recent proposals, which accounts for the entire shape of the shear stress path without generalizing its shape by a simplified geometry (minimum ball [87], rectangle [88], minimum ellipsis [89], etc.).

Subsequent to the multiaxial rainflow count, a CP equivalent stress criterion is employed. Although the adoption of most CP criteria to fatigue life estimations do not explicitly include a mean stress correction via a Haigh diagram, its inclusion to the analysis routine is expected to result in more reliable fatigue life predictions. Therefore, this correction is applied for the identified shear and normal stress cycles to convert them to a corresponding zero mean value. This way, mean stresses are accounted for and the conventional fatigue formulations of the CP criteria do not have to be changed. Similar to the global equivalent stress approach, the damage is accumulated linearly [119], cf. Eq. 6.1. Thereafter, the most damaged plane is declared as the critical plane and used for the fatigue life prediction.

Although the methods within the CP approach are based on solid engineering approximations and physics, their validation is more difficult than in the global equivalent stress approach. Even in case sufficient experimental data is available, the interaction of the multiaxial rainflow count, equivalent shear stress criteria (PMOI, etc.) and CP damage criteria (including their calibration - Findley [92], Papuga [96], etc.) will lead to a complicated validation process.

#### 6.2.4 Signed equivalent stresses

Global equivalent stress criteria conventionally include quadratic terms, so that additional methods are required to restore the correct sign. Most commonly this is done employing the sign of the first invariant of the stress tensor or the sign of the absolute largest principal stress. While this yields good results for proportional load cases, it leads to discontinuous stress histories in case of non-proportional loads [198]. These discontinuities also alter the frequency content of the equivalent signal in comparison to the input signals. Moreover, the aforementioned methods do not work in case of pure shear. Nevertheless, the sign correction of global equivalent stress criteria is based on the sign of the absolute largest principal stress in this work for comparison purposes. More elaborate sign correction approaches were proposed in literature [74, 209], but are not considered here. Since the cycle identification in the CP approach happens before the equivalent stress criteria are used, a sign correction is not necessary. Instead, the resulting equivalent CP stresses already resemble equivalent amplitudes, which can be used in S-N diagrams to estimate their damage contributions. Therefore, CP criteria also do not result in a continuous time series as their global equivalent stress counterparts, but rather in a series of damaging events with time steps that are different from the original stress history, i.e., the original sampling rate.

### 6.2.5 Time dependencies

In case of global equivalent stress criteria, the components of the global stress tensor are converted to an equivalent stress in each time step. This translates to a synchronous conversion, which is afterwards evaluated in a uniaxial rainflow count.

On the other hand, CP criteria operate asynchronously, which can be derived from Figure 6.3. When the biaxial stress state taken from a previous publication [198] is projected onto a potential critical plane, this consequently results in a CP stress history that consists of two shear stress histories and a normal stress history. Assuming that a shear-based approach is chosen, a half cycle is identified as the time frame including the two most distant points on the 2D shear stress history. As indicated in Figure 6.3, the maximum of the normal stress, occurring in the same time frame as the entire shear stress (half) cycle, is not at the same position (in time) as the  $\tau_{nu}$  shear stress maximum. In fact, the normal stress maximum is closer to the minimum of the 2D shear stress history (in this case: point with the smallest distance to the origin).

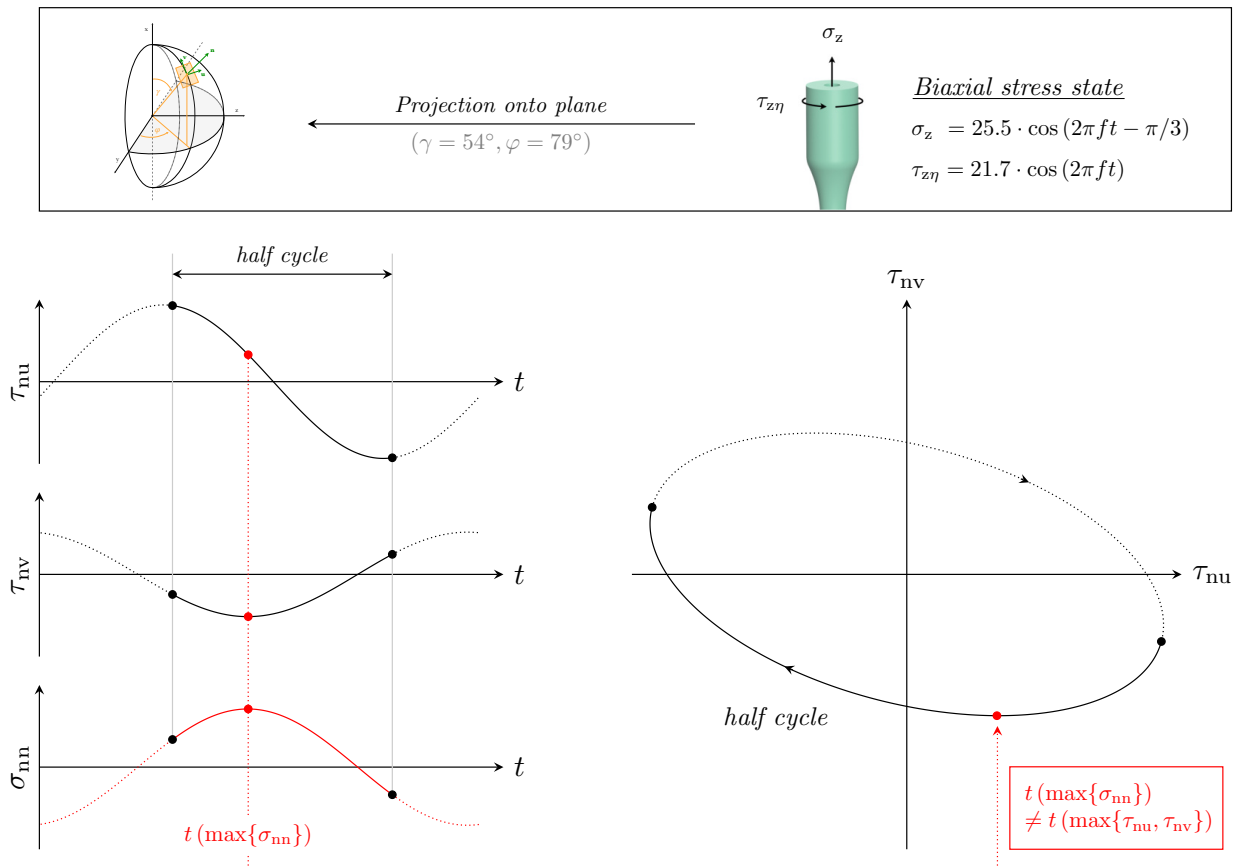


**Figure 6.3:** Time shift in between shear stress and normal stress maxima after projecting a biaxial stress state from experiments [198] onto a plane. By combining the shear and normal stress maxima/amplitudes of the identified cycle, critical plane criteria predict an asynchronous equivalent stress.

Despite of this, CP criteria such as the Findley criterion demand a direct superposition of the (combined) shear stress amplitude and the maximum normal stress, cf. Eq. 6.6. This corresponds to an asynchronous worst case approach, which is a reason why this approach leads to more consistent results with respect to the level of non-proportionality. In contrast, the global approach fails to do so, because it is a synchronous method, which leads to a distorted equivalent stress signal [198].

### 6.3 A new approach to non-proportional fatigue analyses

Based on the asynchronous behavior of CP criteria, cf. Section 6.2.5, and the recorded experimental results, cf. Section P4-3.1, a new way to mimic the asynchronous (worst case) approach of the CP method on a global stress level (invariant-based) is explored in the following for phase shift-induced non-proportional load cases.

#### 6.3.1 Basis: The LiWI approach

The linear wave interference equivalent stress hypothesis (LiWI) [209] is based on a fast Fourier transform (FFT) of the input stress components. It is able to generate an equivalent signal with the same frequency content as the original signal components and retains the correct sign without further corrections. The included FFT results in an estimation of the amplitude  $\hat{\sigma}(f_n)$  and phase shift  $\hat{\phi}(f_n)$  of every frequency  $f_n$  contained in the original signal, i.e., the stress components.

The LiWI approach is summarized in Figure 6.4 by the example of a von Mises equivalent stress and a plane stress state. With the FFT-decomposition of the input stress components, the equivalent stress is calculated for each identified frequency independently, e.g.,  $\hat{\sigma}_{vM}(f_3)$ . The resulting mono-frequent equivalent signals are subsequently summed up to a resulting signal, which corresponds to an inverse FFT (iFFT):

$$\sigma_{vM, LiWI}(t) = \sum_n \hat{\sigma}_{vM}(f_n) \cdot \cos(2\pi f_n t + \hat{\phi}_{vM}(f_n)) . \quad (6.2)$$

While the calculation of the respective amplitude of each mono-frequent equivalent signal  $\hat{\sigma}_{vM}(f_n)$  is done by employing the equivalent stress formulation (von Mises) with the respective stress amplitudes, e.g.,  $\hat{\sigma}_{vM}(f_1) = f(\hat{\sigma}_x(f_1), \hat{\sigma}_y(f_1), \hat{\tau}_{xy}(f_1))$ , the determination of the equivalent phase shift  $\hat{\phi}_{vM}(f_n)$  is not trivial [209]. In fact, the phase shift estimation is currently limiting the LiWI approach to a plane stress application due to its complexity. However, for this stress state the method results in a continuous signal, which is clearly more physically meaningful than the discontinuous signal resulting from a common (principal stress-based) sign correction, cf. Figure 6.4.

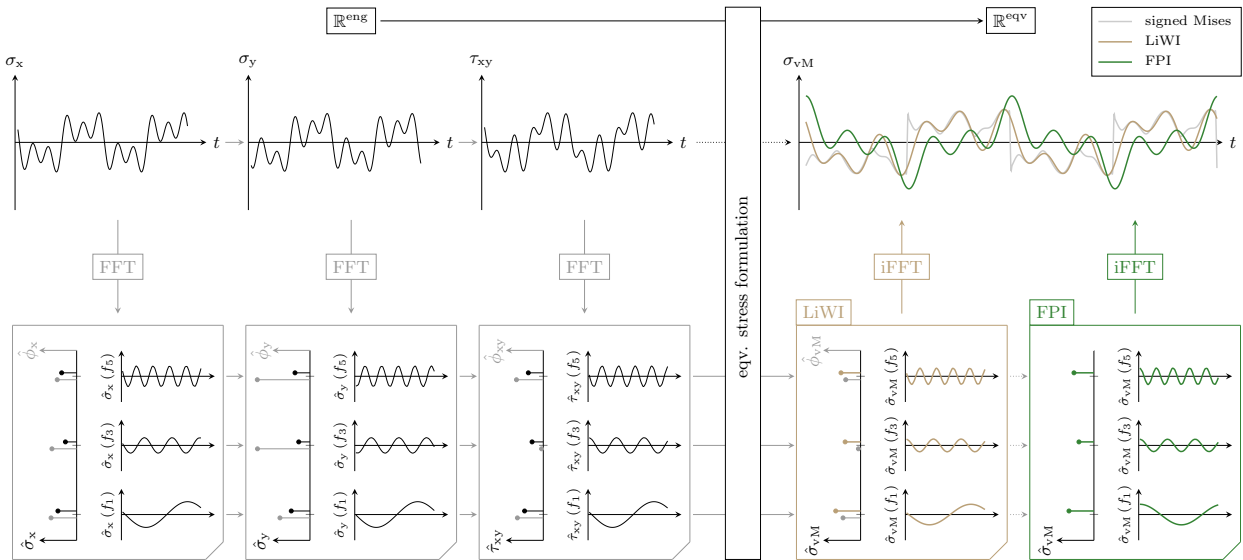


**Figure 6.4:** Flow chart of the LiWI and FPI approaches in comparison to the signed von Mises stress. Both the LiWI and FPI approaches maintain the frequency content of the original signals, do not require a separate sign correction and lead to continuous signals. These properties are not incorporated by state of the art equivalent stress theories, cf. the discontinuous signed von Mises stress history (upper right, gray).

The correct sign of the LiWI signal is a byproduct of the FFT-based analysis, wherein only the amplitudes and phase shifts are processed. The sign is therefore added in the iFFT step via multiplication with the corresponding cosine term.

### 6.3.2 Forced proportional interference

As explained in Section 6.2.5, the asynchronous behavior of the CP criteria is interpreted as a main reason for their robust fatigue life prediction quality. This behavior can be replicated for phase shift-induced non-proportional load cases by simplifying the LiWI approach in such a way that the phase shift estimation is neglected completely, cf. Figure 6.4. By neglecting the phase shift of each mono-frequent equivalent signal, a proportional load case is emulated leading to forced proportional interference (FPI), which is independent of the level of non-proportionality. Therefore, the resulting signal mimics critical plane criteria in this regard and the iFFT in context of a von Mises equivalent stress becomes:

$$\sigma_{\text{vM,FPI}}(t) = \hat{\sigma}_{\text{vM}}(f_0) + \sum_i \hat{\sigma}_{\text{vM}}(f_i) \cdot \cos(2\pi f_i t) . \quad (6.3)$$

Note that the sign of a potential mean stress will be contained in the phase at  $f = 0$  for each stress component, i.e.,  $\hat{\phi}(f_0) = 0$  for a positive mean stress and  $\hat{\phi}(f_0) = \pi$  for a negative mean stress. Therefore, the equivalent mean stress  $\hat{\sigma}_{\text{vM}}(f_0)$  marks the only exception to the procedure and the sign of  $\hat{\sigma}_{\text{vM}}(f_0)$  is calculated based on the sign of the absolute largest principal stress resulting from all existent mean stress components.

While the LiWI approach is currently limited to the plane stress application due to the rather complex determination of the phase angle, the FPI approach can be applied to any stress state and independently of the phase shift-induced level of non-proportionality. It is therefore represented as a new branch in Figure 6.2 (gray-shaded areas).

The FPI approach can also be used in a CP analysis to include an estimation of the fracture initiation plane. While this comes at a high computational cost on account of the iterative CP identification, the involved algorithms (uniaxial rainflow count, etc.) are easier to validate and most likely execute significantly faster than their multiaxial counterparts.

In addition, both the LiWI and the FPI approach are not limited to the von Mises equivalent stress. Adaptions of the LiWI approach to, e.g., the Tresca [210] and Rankine [211] criterion can be found in Schmidt and Pandiyya [209]. In case of the FPI method, the (mono-frequent) evaluation can be done with any equivalent stress criterion, since it is not limited by any phase shift estimations, demonstrating its versatility.

Note that the shear and normal stress amplitudes (and mean values) of mixed frequency signals, such as those depicted in Figure 6.4, have to incorporate equal ratios for all contained frequencies in order not to cause additional non-proportionalities, i.e.,  $\hat{\sigma}_x(f_i)/\hat{\tau}_{xy}(f_i) = \text{const.}$  A straightforward way to check the applicability of the FPI approach in its current form is thus a check of the non-proportionality factor  $f_{\text{np}}$  of the resulting stress history (6D) with zero phase shift. In case  $f_{\text{np}} \approx 0$ , the FPI approach can be applied. Otherwise additional sources of non-proportionality are present in the original stress history. Possible enhancements of the FPI approach for other sources of non-proportionality will be discussed in Section 6.5.4.

### 6.3.3 Fatigue life prediction concept

The FPI approach will lead to a re-proportionalization of a phase-shifted stress history. The predicted fatigue life will therefore stay constant if the level of non-proportionality is altered by changing phase shifts. This characteristic resembles a neutral material behavior regarding the cycles to failure at different levels of non-proportionality, cf. Figure P4-4, and therefore matches the experimentally observed behavior of the adhesive.



In case the fatigue life needs to be predicted for such a neutral material, the FPI flow chart in Figure 6.2 can be followed without any adaptation. However, if ductile ( $\tau_y/\sigma_y = 0.5$ ) or brittle ( $\tau_y/\sigma_y = 1$ ) materials are analyzed, the cycles to failure at high levels of non-proportionality will be different from the cycles to failure in proportional load states. In general, it can be expected that a high ductility tends to reduce the cycles to failure and brittle behavior tends to increase the cycles to failure in a non-proportional load state in comparison to a proportional load state [23], cf. Figure P4-4. Therefore, this shift of the cycles to failure must be captured experimentally to derive a correction factor  $\xi_{np}$  for the fatigue life estimation. This factor can be incorporated in the fatigue analysis routine in the damage accumulation step:

$$D = \sum_i \frac{n_i}{N_i} \cdot \xi_{np,i}(f_{np}, \kappa_\tau, T) . \quad (6.4)$$

Herein,  $n_i$  and  $N_i$  are (still) the identified cycles from a cycle counting algorithm and the permissible cycles to failure from a uniaxial S-N curve (or Haigh diagram), respectively. To include complex interrelations,  $\xi_{np}$  should be modeled as a function of the level of non-proportionality (cf. Figure 6.1), the ductility of the respective material, and the temperature.

To replicate the S-N behavior shown in Figure P4-4, the correction factor will generally exhibit the following magnitudes:

$$\xi_{np} \begin{cases} > 1 & , \text{ ductile} \\ = 1 & , \text{ neutral} \\ < 1 & , \text{ brittle} . \end{cases} \quad (6.5)$$

This way, the FPI approach shifts the dependency of the cycles to failure of the level of non-proportionality to a rather simple and experimentally determined correction factor. This simplifies comprehension and interpretation of the results, as this behavior is not (indirectly) hidden in the CP subroutines anymore, which will be discussed further in Section 6.5.

## 6.4 Implementation of methods

Brief summaries of the implementation of the methods shown in Figure 6.2 are given in the following as a basis for the fatigue life predictions in Section 6.5.

### 6.4.1 Global equivalent stress criteria

The Drucker-Prager [202] equivalent stress criterion was identified as the best option for the adhesive in Section P2-5.3. Hereafter, the Drucker-Prager criterion was extended to a hybrid version in Section P4-6.2, which allows to use a Haigh Diagram in the engineering stress space  $\mathbb{R}^{\text{eng}}$  without discarding effects of the strong tension-compression asymmetry of the adhesive.

Due to the good results achieved with the hybrid formulation for proportional load cases, the hybrid formulation is also used here for the global equivalent stress approach, cf. Figure 6.2. As stated in Section 6.2.4, the sign of equivalent stress criteria is corrected using the sign of the absolute largest principal stress.

To use the hybrid Drucker-Prager criterion in the FPI approach,  $I_1$  is calculated in a similar way as shown in Figure 6.4. First, the normal stress components are dissected via a FFT analysis. Subsequently, the mono-frequent parts of  $I_1$  are calculated as the sum of the respective stress components. The iFFT leads to the final result of  $I_1$ . The phase shift is neglected along the way (with the exception of potential mean values) according to the FPI approach. Finally, the re-proportionalized histories of  $\sigma_{vM}$  and  $I_1$  are combined, cf. Section P4-6.2. Note that the FPI approach will automatically result in the hybrid version of the Drucker-Prager criterion as the

amplitudes in the FFT are always positive (with the exception of a potentially negative mean stress at  $f = 0$ ). A sign correction is also unnecessary in this case, because of the cosine terms in the iFFT, cf. Section 6.3.1.

### 6.4.2 Critical plane equivalent stress criteria

In terms of the critical plane approach, the Findley [92] and Papuga PCr [96] criteria are used as representatives for an equivalent shear stress-based and an equivalent normal stress-based analysis, respectively.

The equivalent stress according to the Findley criterion [92, 97] can be expressed as

$$\sigma_F = a_F \cdot \tau_a + b_F \cdot \sigma_{nn,max} . \quad (6.6)$$

Therein,  $\tau_a$  is the shear stress amplitude resulting from an enclosing surface conversion of a full (or half) cycle, which was identified in the multiaxial rainflow count. The maximum normal stress occurring during that particular cycle is called  $\sigma_{nn,max}$ , while  $a_F$  and  $b_F$  are material parameters. The calibration of  $a_F$  and  $b_F$  is done using the following expressions [97]

$$a_F = 2\sqrt{\kappa_\infty - 1} , \quad b_F = 2 - \kappa_\infty , \quad (6.7)$$

where  $\kappa_\infty$  is the ratio between the fatigue limit for a fully reversed axial load ( $\sigma_\infty^{R=-1}$ ) and the fatigue limit for fully reversed torsion ( $\tau_\infty^{R=-1}$ ).

The Papuga PCr [96] criterion is given by

$$\sigma_{PCr} = \sqrt{a_c \tau_a^2 + b_c \left( \sigma_a + \frac{\tau_\infty^{R=-1}}{\sigma_\infty^{R=0}} \cdot \sigma_m \right)} . \quad (6.8)$$

Similar to the Findley criterion, the shear stress amplitude  $\tau_a$  is calculated using an enclosing surface method. Normal stress amplitude and mean value are denoted by  $\sigma_a$  and  $\sigma_m$ . The material parameters  $a_c$  and  $b_c$  are calibrated using the following formulae

$$a_c = \begin{cases} \frac{\kappa_\infty^2}{2} + \frac{\sqrt{\kappa_\infty^4 - \kappa_\infty^2}}{2} , & \kappa_\infty < \sqrt{\frac{4}{3}} \\ \left( \frac{4\kappa_\infty^2}{4 + \kappa_\infty^2} \right)^2 , & \kappa_\infty \geq \sqrt{\frac{4}{3}} \end{cases} \quad b_c = \begin{cases} \sigma_\infty^{R=-1} , & \kappa_\infty < \sqrt{\frac{4}{3}} \\ \frac{8\sigma_\infty^{R=-1}\kappa_\infty^2(4 - \kappa_\infty^2)}{(4 + \kappa_\infty^2)^2} , & \kappa_\infty \geq \sqrt{\frac{4}{3}} . \end{cases} \quad (6.9)$$

The fatigue limits necessary for the calibration of the Findley and Papuga PCr criterion were estimated in Section P3-3.3. However, since the recorded S-N data were limited in the very high cycle fatigue (VHCF) regime, the critical plane evaluation will include a sensitivity analysis regarding the calibration parameters.

As mentioned, the FPI approach can also be utilized within a CP analysis. In this case, the critical plane stress history is treated in the same way as the stress components of the global stress tensor, cf. Figure 6.4. Therefore, only the stress inputs are changed to  $\sigma_{nn}$ ,  $\tau_{nu}$  and  $\tau_{nv}$  in comparison to the global FPI version and no additional enclosing surface algorithms or other auxiliary methods are required.

### 6.4.3 Enclosing surface methods

To showcase the influence of different enclosing surface methods on the fatigue life prediction, three concepts are utilized in this work. The PMOI [91] is chosen as a physically-based method that accounts for the actual shape of the 2D shear stress path. In contrast, the minimum ball (MB) method [87] is used as a representative for simplified geometry projections. Additionally, the root mean square (RMS) approach [205] is implemented. The latter accounts for the outer shape of the 2D shear stress path, but neglects inner path segments. Therefore, the RMS method can be interpreted as a compromise between the PMOI and MB. Details concerning the implementation of the methods can be found in the aforementioned publications and in de Castro and Meggiolaro [9].

Note that the results of enclosing surface methods are usually different for half- or full cycles. While full cycles can be hard to detect for CP projections of random stress histories, their detection is trivial for constant amplitude stress histories. Since the experimental campaign, that this work is based on, employed constant amplitude stress histories, all enclosing surface methods will be evaluated based on full cycles.

### 6.4.4 Haigh diagram & S-N curves

Although a Haigh diagram is necessary for general multiaxial fatigue life predictions, it is not required here since the comparison of the fatigue methodologies is based on a constant amplitude experimental campaign at  $R = -1$  for both the axial and torsional load.

In case of the critical plane approach, the projection of the stress tensor to a candidate plane is a linear transformation. Therefore, a mean-free stress history remains as such on any investigated plane. Hence, a uniaxial S-N curve at  $R = -1$  is sufficient for the stress-based CP approach. The hybrid formulation of the Drucker-Prager criterion also simplifies the S-N requirements for the global approaches, as only the uniaxial tension-compression S-N curve at  $R = -1$  is required [198].

All required S-N curves were determined in Section P3-3.3 and were modeled using the Stüssi-Haibach S-N model [197, 198], which consists of a combination of the sigmoidal-shaped Stüssi [212] S-N curve and a Haibach [10, 213] extension line. No statistical manipulation of the S-N curves was carried out. Therefore, the analyses are based on  $P_{50}$  Stüssi-Haibach S-N curves.

### 6.4.5 Filtering & damage sphere discretization

As pointed out in Section 6.2, the MRF filter can be used to increase the computational efficiency. In this work, however, the filter is not used in order to focus on the comparison of the fatigue life prediction methods with as little bias as possible from supporting algorithms. For the same reason, an adaptive algorithm for the critical plane identification is not used. Instead, the damage (half-) sphere is discretized using equal area increments with a width of  $1^\circ$  according to Weber et al [77] leading to 20630 planes in total. Thus, each critical plane criterion is evaluated in the same way and based on a very fine discretization to avoid any distortions of the fatigue life prediction on account of a too coarse critical plane search.

## 6.5 Comparison to experiments

In the following, state of the art CP methods and the FPI approach, cf. Figure 6.2, are compared to the experimental results from Section P4-3.1.

### 6.5.1 Damage prediction quality

A comparison of the aforementioned multiaxial fatigue approaches is shown in Figure 6.5 based on load level 1 of the experimental campaign, cf. Section P4-3.1. The accumulated damage  $D$  of the respective methods is illustrated as a function of the phase shift  $\phi$ , i.e., the level of non-proportionality. Note that a logarithmic scale was used on the y-axis to enhance visibility. The depicted damage ratio is given by

$$\Lambda_D = \frac{D(\phi = 0^\circ)}{D(\phi = 90^\circ)}. \quad (6.10)$$

A ratio  $\Lambda_D < 1$  represents a conservative fatigue life prediction, while  $\Lambda_D > 1$  marks a non-conservative prediction and  $\Lambda_D = 1$  corresponds to a neutral behavior.

The influence of different enclosing surface methods (PMOI, RMS, MB) in the critical plane approach is illustrated in Figure 6.5 among different calibrations of the material parameters of the Findley and Papuga PCr criterion. The respective literature calibrations according to Eq. 6.7 and Eq. 6.9 are shown as dotted lines. An additional calibration was carried out, aiming at an ideal damage of  $D \approx 1$  at failure in a proportional load case ( $\phi = 0^\circ$ ). Although, the resulting damage is significantly different for these calibrations, the fatigue limits only had to be adjusted by  $\pm 12\%$  and  $\pm 1\%$  for the Findley and Papuga PCr criteria, respectively. Given the general uncertainty of experimental fatigue limit estimations, this is considered to be a (very) small deviation and can also be interpreted as a confirmation of the Stüssi S-N model, which was used to predict the (presumed) fatigue limits in Section P3-3.3. However, it also showcases the sensitivity of the criteria as small deviations of the calibration inputs can lead to significant differences in the damage prediction. An overview of the calibration parameters is provided in Table 6.1. Due to the constant amplitude fatigue tests with fully reversed loads, the mean value in Eq. 6.8 is zero. Therefore, the fatigue limit in tension at  $R = 0$  ( $\sigma_\infty^{R=0}$ ) is irrelevant in this work and was not part of the sensitivity study. Note, however, that  $\sigma_\infty^{R=0}$  can also be extracted from Section P3-3.3.

It is emphasized that the comparison is based on the observed neutral S-N behavior of the adhesive, cf. Figure P4-4. Assumptions on the damaging behavior of certain levels of non-proportionality inherent to the used methods will therefore be visible in the  $D(\phi)$  functions. For instance, the PMOI tends to result in increasing equivalent shear amplitudes with increasing levels of non-proportionality for the biaxial constant amplitude load case replicated in this work, which translated into an increase of damage in most cases. This increase overestimates the damage for a neutral material and is therefore found to be conservative. In case ductile materials are analyzed, which generally exhibit a shorter fatigue life in non-proportional load cases in comparison to proportional ones, cf. Figure P4-4, the predictions of the PMOI may

**Table 6.1:** Calibration of material parameters for the critical plane models. The fatigue limits were extracted from a previous publication [198].

Parameter	Unit	Literature calibration	$D(\phi = 0^\circ) \approx 1$	
			Findley	Papuga PCr
$\sigma_\infty^{R=-1}$	N/mm <sup>2</sup>	26.60	23.41	26.44
$\tau_\infty^{R=-1}$	N/mm <sup>2</sup>	17.72	19.85	17.83
$a_F$	–	1.416	0.847	–
$b_F$	–	0.499	0.821	–
$a_c$	–	2.078	–	2.004
$b_c$	N/mm <sup>2</sup>	14.268	–	21.850

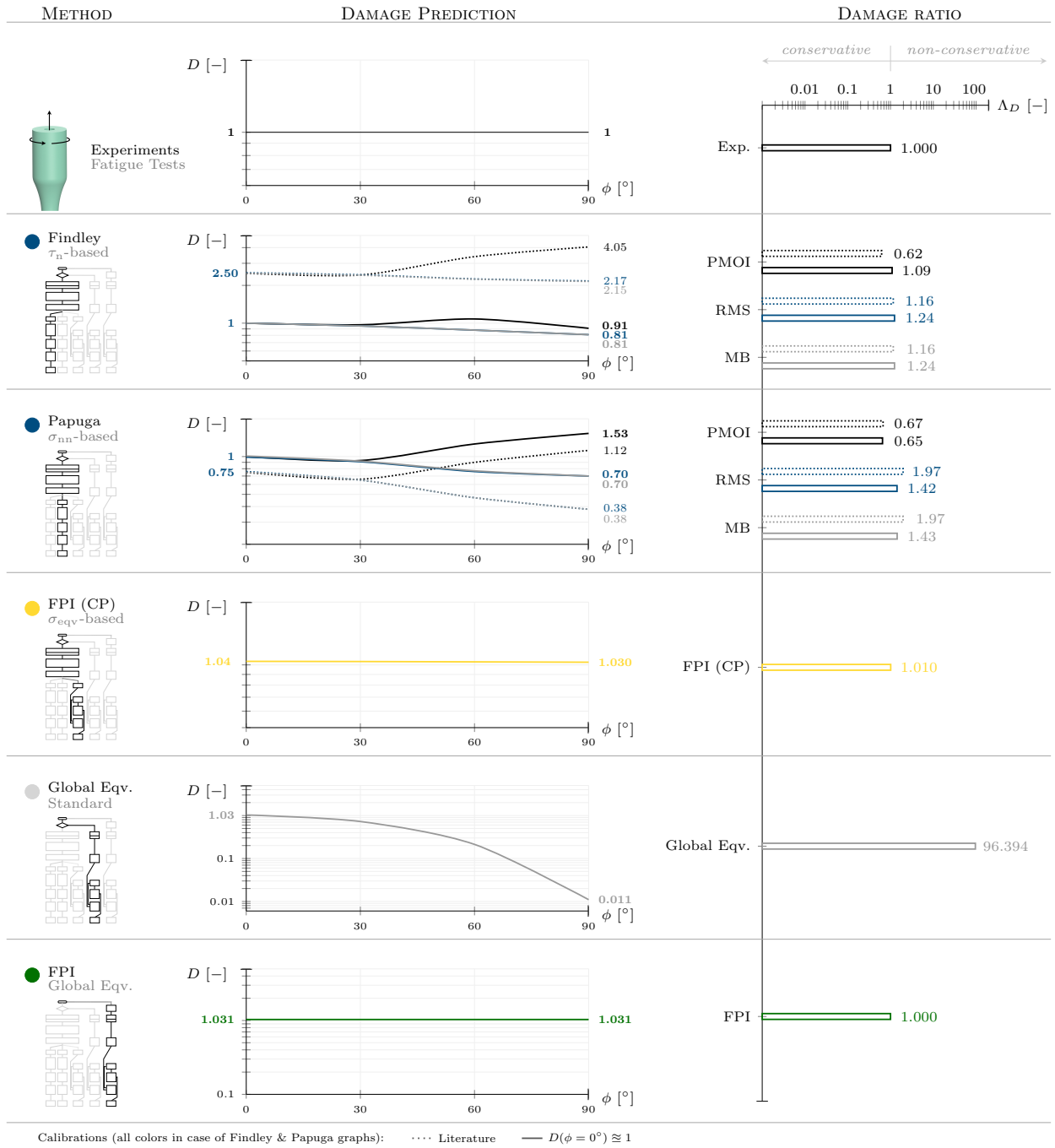


**Figure 6.5:** Accumulated damage  $D$  (logarithmic y-axis scale) as a function of phase shift  $\phi$ , i.e., the level of non-proportionality, for all multiaxial fatigue approaches in Figure 6.2 and based on load level 1 of the experimental campaign. An ideal prediction leads to a constant damage of  $D = 1$  according to the experimental results (top). In case of the critical plane analyses (Findley, Papuga), the influence of the chosen enclosing surface method (PMOI, RMS, MB) is depicted. Similarly, the influence of the material parameter calibrations are shown, where dotted lines mark the literature calibration and solid lines mark a calibration that leads to an ideal damage for a proportional load, i.e.,  $D(\phi = 0^\circ) \approx 1$ . The signed, hybrid Drucker-Prager criterion is used for the critical plane-based FPI approach, the global equivalent stress method and the global FPI approach. The damage ratio  $\Lambda_D$  (Eq. 6.10) separates conservative from non-conservative methods.

lead to more accurate results. In contrast, both the RMS and MB method led to decreasing equivalent shear amplitudes and therefore also to a decrease in damage with increasing levels of non-proportionality. Therefore, these methods can be interpreted to (partly) rely on brittle material behavior, which tends to show increased fatigue life in non-proportional load cases, cf. Figure P4-4. The differences of the MB- and RMS-based damage predictions were negligible for this work's load case.

Overall, the damage prediction quality of all investigated CP criteria is excellent in direct comparison to the global equivalent stress approach. This is reflected by a substantially improved damage ratio  $\Lambda_D$  of the CP criteria. While  $\Lambda_D$  is 96.39 for the global equivalent stress approach, it ranges between 0.62 and 1.97 for the CP approaches with the literature-based calibration and between 0.65 and 1.43 with the  $D(\phi = 0^\circ) \approx 1$  calibration. Therefore, the capability of the CP approach to generate reliable fatigue life predictions in non-proportional load cases for the investigated adhesive was proven in this work.

Regarding the FPI approach, the results are even better than the CP results for the analyzed load case. Its ideal damage ratio  $\Lambda_D = 1$  corresponds to a neutral behavior of the subroutines (eqv. stress criteria etc.) with respect to the level of non-proportionality. This is because the non-proportional damage dependence is entirely shifted to different sets of (biaxial) S-N curves and the corresponding correction factor  $\xi_{np}$ , cf. Eqs. 6.4-6.5. On that basis, the FPI approach represents an easy-to-use alternative to the traditional critical plane approach for phase shift-induced non-proportional loads.

Note that the damage prediction quality of the FPI approach is connected to the choice of the equivalent stress criterion. Therefore, deviations of the predictions to the ideal of  $D = 1$  at failure reflect the capability of the chosen criterion to model equivalent stresses for the respective material and its applicability to multiaxial fatigue analyses. In this work, the hybrid Drucker-Prager criterion led to very good results for both the global FPI approach and its CP variant. In addition, idealizations such as the linear damage accumulation affect the fatigue life prediction of all analyzed methods.

### 6.5.2 Fracture surface prediction

An often mentioned benefit of the critical plane approach is the prediction of the fracture initiation plane alongside the fatigue life analysis. Since the fracture initiation plane could not be experimentally detected, the observed fracture surfaces have to be used as an approximation.

In Section P4-3.3, the fracture surfaces were found to be approximately equal for all levels of non-proportionality for the investigated adhesive. This was interpreted as a validation of the neutral S-N behavior, because the damage mechanism did not change.

Figure 6.6 shows a photograph of the fracture surface of specimen 095 as a representative for all other tested specimens. The fracture surface of this specimen is approximately  $27.5^\circ$  in the yz-plane (z-axis represents axial direction). This observation was compared to the predictions of the Findley and Papuga PCr criteria (RMS-based  $D(\phi = 0) \approx 1$  calibrations) and the CP-version of the FPI approach. The failure plane angle  $\psi_f$  is found as the minimum angle of the critical plane projected to the xz- and yz-plane, respectively.

None of the investigated criteria is able to predict the experimentally observed fracture surface at all levels of non-proportionality, even though the Findley and Papuga PCr criterion were calibrated to an ideal damage of  $D \approx 1$  for a proportional load case. The damage spheres also appear qualitatively similar, despite of the different approaches. Only for the proportional load case, the estimation of the fracture initiation plane was rather close to the observed fracture surface orientation. Therefore, the information loss of the global FPI approach, which does not include a prediction of the fracture initiation plane, is rather small for this work's load case.

Note that the transversely isotropic behavior of the specimens might have influenced the prediction of the fracture initiation plane.

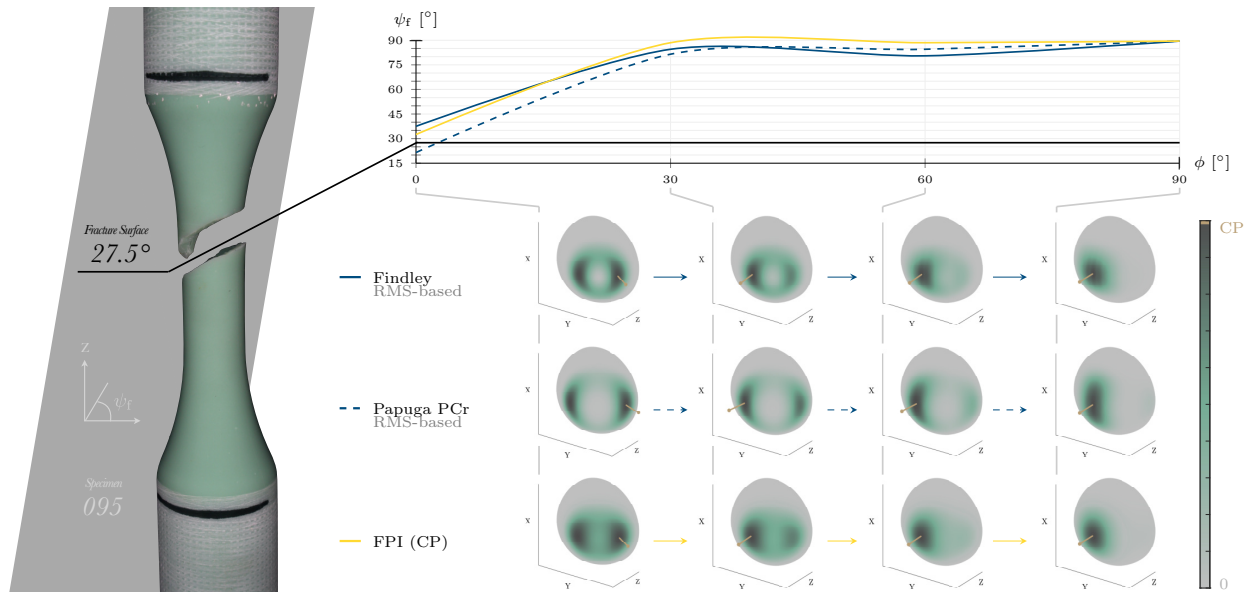


**Figure 6.6:** Experimental fracture surface of specimen 095 in comparison to critical plane predictions of the RMS-based and  $D(\phi = 0^\circ) \approx 1$  calibrated Findley and Papuga PCr criteria in addition to the CP-based FPI approach.

### 6.5.3 FPI: Computational efficiency & ease of use

Computational efficiency is a term, which is rarely connected with non-proportional fatigue analyses. However, in addition to the good damage predictions of the global FPI approach, it executes significantly faster than CP analyses. Differences in computation times will of course always depend on the code implementation and hardware. However, in most cases the FPI approach will be just as fast as a state of the art global equivalent stress analysis, since the time required for the FFT is comparable to a principal stress-based sign correction, which is not needed in the FPI approach.

With the current hardware and code implementation, the computation time to evaluate a single plane in the CP approach was 60 times higher than the complete evaluation of the FPI approach. The time for a complete CP analysis is approximately scaled by the computation time for a single plane and is therefore several orders of magnitude higher than that of the FPI approach. Note that the main reason for the slow performance of the CP analysis is the usage of the multiaxial rainflow count, cf. Section 1.2.1 and 6.2.3. However, to achieve equal speed levels for the entire analysis, the evaluation of a single plane will need to be orders of magnitude faster. The feasibility of this is extremely unlikely, because of the similarities in the damage evaluation of the approaches, cf. Figure 6.2. For instance, a multiaxial rainflow count on a plane has to follow the same engineering principles as the uniaxial one in the FPI approach. Therefore, it can be expected that the computation time of the FPI approach will always be substantially lower than that of CP applications.

Due to its computational efficiency, the FPI approach can also be used as a screening method in conjunction with an analysis of a non-proportionality factor  $f_{np}$ . This way, users of validated CP tool chains can limit the analysis to regions of high non-proportionality, which simultaneously exhibit a high damage potential, e.g., to estimate the fracture initiation plane alongside the fatigue life prediction. This distinction is not possible using solely a non-proportionality factor, because  $f_{np}$  does not differentiate between high or low load levels, cf. Section 6.2.1.

Given the complicated dependencies of the level of non-proportionality, the same  $f_{np}$  can be found for shear- or normal stress-dominated conditions, cf. Figure 6.1. The decision whether to use a shear- or normal stress-based CP approach therefore requires an additional algorithm. The CP version of the FPI approach alleviates this problem as such a distinction is not necessary. Additionally, the global FPI approach can be used for any phase shift-induced level of non-proportionality, cf. Figure 6.2, so that the aforementioned choices become irrelevant.

In case an asymmetric yield criterion such as the Drucker-Prager criterion is used, the FPI approach also leads to a hybrid version of the particular criterion, meaning that an asymmetric yield criterion can be used in conjunction with Haigh diagrams in the engineering stress space  $\mathbb{R}^{eng}$ . Since the use of Haigh diagrams in the equivalent stress space  $\mathbb{R}^{eqv}$  would normally be required for asymmetric yield criteria and the fact that  $\mathbb{R}^{eqv}$  Haigh diagrams are hardly considered in literature [198], this is a great benefit of the FPI approach and minimizes the risk of non-conservative fatigue life predictions.

Due to the fact that the FFT is a widely used and optimized algorithm in many software packages, the implementation and usage of the FPI approach is rather simple.

#### 6.5.4 FPI: Limitations & Possibilities

It has to be noted that the current version of the FPI approach is limited to phase shift-induced non-proportional stress histories. Other sources of non-proportionality such as different frequencies or stress ratios of normal and shear stresses were not considered in this work. However, the included FFT dissection of the stress components leads to a versatile setup, which can be enhanced for other load cases. An adaption to frequency-induced non-proportional stress histories might, for instance, be possible with a damage equivalent transformation of certain frequencies, which than (again) results in a worst case estimation. Analogously, different stress ratios might be incorporated into the FPI approach via a damage equivalent adaption using a Haigh diagram. Since these hypotheses can not be validated with the current experimental data, this will be addressed in the future.

As mentioned, the FPI approach can also be used as a screening method in conjunction with a non-proportionality factor in order to limit necessary evaluations of the critical plane approach to locations with both a high damage potential and a high level of non-proportionality. Therefore, future enhancements of the FPI approach do not necessarily need to include accurate fatigue life predictions, since an efficient estimation of the worst case damage potential will already provide a great benefit for screening purposes. This screening capability can also be applied to accelerate the identification of the critical plane, as the evaluation of candidate planes can be limited to those with a high damage potential.

In its current form, the FPI approach can only replace the critical plane approach for a rather limited set of load cases, i.e., phase-shifted stress histories. However, in these cases the approach provides a variety of benefits. It is thus shared with the research community in this early stage to foster and accelerate further developments.

## 6.6 Concluding Remarks

Different sets of fatigue life prediction algorithms were compared to the biaxial (tension/compression-torsion) fatigue experiments with different levels of non-proportionality on a structural adhesive. Critical plane-based algorithms were found to provide good fatigue life predictions for different levels of non-proportionality, while the traditional global equivalent stress approach (invariant-based approach) led to very non-conservative predictions.

Even though the critical plane approach led to reliable fatigue life predictions, the computation time is substantial and limits widespread application. Since the cycles to failure of the investigated



adhesive were found to be independent of the phase shift-induced level of non-proportionality, a new computationally efficient way for non-proportional fatigue life predictions was explored. Based on an FFT of a given stress history, this approach leads to a re-proportionalized equivalent stress history as the phase shift of the stress components is set to zero in the equivalent stress calculation. In comparison to the traditional critical plane approach, this forced proportional interference (FPI) approach leads to a variety of benefits:

1. The re-proportionalized equivalent stress history results in constant fatigue life predictions independent of the (phase shift-induced) level of non-proportionality. Thus, the fatigue life dependence on the level of non-proportionality is shifted to an S-N-based correction factor, which enables easier comprehension and interpretation of the results, as this dependence is not hidden in subroutines, e.g., enclosing surface methods in the critical plane analysis.
2. The computational efficiency is comparable to a state of the art equivalent stress analysis that is confined to proportional load cases. However, due to the FPI's applicability to any (phase shift-induced) level of non-proportionality, it is orders of magnitude faster than the otherwise required critical plane approach.
3. The usage of the FFT within the FPI approach directly leads to a signed equivalent stress without further corrections and contains the same frequency content as the original stress history.
4. The FPI approach can be used for any material when the equivalent stress criterion is chosen accordingly (von Mises, Drucker-Prager, etc.). This choice simultaneously is the only input parameter required, aside from S-N curves, which are essential for any stress-based fatigue analysis.
5. The FPI approach is easier to validate than critical plane methods, since it is coupled with well known uniaxial algorithms for fatigue analyses, e.g., the uniaxial rainflow count.
6. In case asymmetric yield criteria (Drucker-Prager, etc.) are chosen, the FPI approach will lead to a hybrid version of the respective criterion. This means that asymmetric criteria can be used with Haigh diagrams in the engineering stress space without loss of information or non-conservative results due to a tension-compression asymmetry.
7. Coupled with an estimation of the level of non-proportionality, the FPI approach can be utilized as an efficient screening method to decide where a critical plane analysis might be necessary. In addition, this screening capability can also be utilized to accelerate the critical plane identification. Hence, the FPI approach is also a useful tool for users with validated critical plane tool chains.

Given the excellent results of the FPI approach in this work, the critical plane approach seems obsolete for the investigated load case, where a phase shift was used to provoke a non-proportional load state. Nevertheless, further experimental validation of the new approach in more complex load cases is necessary, which also include sources of non-proportionality that are different from phase-shifted loads, i.e., different frequencies of normal and shear stresses, which were not accounted for, yet. However, in every case where an equivalent stress criterion was successfully validated for a proportional load state and where a phase shift is the main reason for a non-proportional load state, a reasonable engineering approximation of the fatigue life including all the aforementioned benefits can be expected employing the FPI approach.



# 7

## Conclusion and Outlook

In this final chapter, the achievements of this thesis are summarized and evaluated with respect to the overall objective. New research questions that result from these new insights are presented as an outlook for future projects.

---

7.1	Conclusion .....	116
7.2	Outlook .....	121

## 7.1 Conclusion

With the overall objective of this thesis defined as:

**Accurate and computationally efficient fatigue life prediction under multiaxial, non-proportional loads by example of a fiber-reinforced rotor blade adhesive,**

the state of the art had to be improved in different areas of research. Therefore, five work packages were defined to achieve this goal as the succession of multiple milestones, which are discussed in the following with respect to their contribution to the overall objective.

**1) Specimen Optimization.** A high manufacturing quality is difficult to achieve with two-component and highly viscous rotor blade adhesives, as every manufacturing step can introduce defects such as mixing inhomogeneities and pores or may lead to a randomization of the orientation of the reinforcement fibers. This is especially true for the manufacture of specimens that are intended for multiaxial tests, since these tests require a more complex specimen geometry and thus increase the potential for manufacturing-induced defects. Therefore, the ideal of a virtually defect-free adhesive specimen which is suitable for multiaxial tests was not achieved before. However, this kind of idealized specimen is required to be able to reliably distinguish the effects of non-proportional loads from other influences, such as defects or stress concentrations.

In an effort to create an ideal multiaxial specimen, a finite element (FE)-based parametric study was carried out to minimize stress concentrations that are induced by the tapered and tubular specimen geometry. Subsequently, a detailed manufacturing optimization was employed. As a first step of that, the mixing quality was optimized using a planetary centrifugal vacuum mixer. The ideal setup was found via a maximization of the color homogeneity of the mixtures. Secondly, the injection process was significantly improved by means of 3D printing. A customized mixing adapter allowed to mix the adhesive directly in the cartridge that was used for the mold injection process. A (manual) transfer of the mixture from a mixing cup to the injection device was thus unnecessary and the high quality of the mixture was maintained. Additional 3D printed injection nozzles and mold inserts allowed to transfer of the mixture into the molds. The resulting virtually defect-free specimen quality was verified by means of  $\mu$ CT scans and enabled the first (publicly available) characterization of the neat material.

The specimen manufacturing quality was compared to simplified (hand-mixed) specimen and revealed substantial differences in strength, stiffness and ductility on account of different porosity levels. In fact, the adhesive was previously characterized as brittle, while the neat behavior is rather ductile. An additional sample from an industrial dosing and dispensing machine for rotor blade manufacture also showed that the porosity level of the optimized specimens is comparable to the industrial mixing quality. At the same time, the coefficient of variation of all measured material properties was approximately an order of magnitude smaller compared to hand-mixed specimens. This is also referred to a very similar and predominantly axial orientation of the reinforcement fibers in each specimen.

In essence, the applied optimization techniques were based on established technologies, i.e., FE-based structural optimization, vacuum mixing, 3D printing and  $\mu$ CT scanning. However, it is the combination of these technologies that was unique, enabled virtually defect-free specimens and a precise material modeling in the following.

**2) Yield Locus Determination.** Yield criteria are typically used to calculate equivalent stresses and strains for multiaxial load states and therefore represent an important step in the material characterization. On account of high porosity levels in specimens used in yield locus determinations of the adhesive in literature, the proposed yield criteria do not represent the

neat behavior of the material. Additional modeling simplifications such as the assumption of a brittle behavior and the associated usage of purely elastic shear stress formulae introduced further inaccuracies. In fact, fracture stresses were used to model the equivalent stress-strain formulations and yield stresses were not stated at all. Given the overall objective of this thesis to accurately predict the fatigue life under non-proportional loads, these inaccuracies were unacceptable, so that the yield locus was derived based on the previously optimized specimens.

The identification of the yield point of a material is traditionally associated with an arbitrary plastic offset strain, i.e., 0.2 %. While this definition works fine for simple tension tests, it fails for the torsion test since the offset strain needs to be an equivalent strain ( $\varepsilon_t \neq \gamma$ ). This leads to the paradox situation that the yield criterion needs to be known to determine the yield criterion itself. The same applies for the compression test if the investigated material exhibits a tension-compression asymmetry, which is common for polymers and a variety of other materials ( $\varepsilon_t \neq \varepsilon_c$ ). In addition, the shear stress-strain curve, required for this kind of evaluation, needs to be modeled in such a way that the elasto-plastic transition is accurately described.

In order to solve these modeling problems, a new elasto-plastic shear stress estimation was proposed that iteratively adapts the stress-strain curve to minimize the difference of the resulting numerical torque to the measured one of the experiment. Thus, wall-thickness effects are also covered by this approach as the outer perimeter of the tubular specimens can plasticize while the inner perimeter can still exhibit elastic strains. Additionally, the yield point was determined via a derivative-based approach, so that the yield point could be estimated for uniaxial tests without an a priori knowledge of the yield criterion. However, its application to biaxial tests required a new method that is capable to predict equivalent stresses and strains based solely on the previously found uniaxial yield points. A scaling approach of an initial ellipsis fit to the experimental results was thus developed. Based on these new developments, the yield locus of the adhesive was found without bias of an a priori chosen equivalent stress-strain formulation while correctly accounting for the plasticity of the material.

The Drucker-Prager criterion was identified to be the best-fit model to the experimental yield locus. This criterion is significantly more conservative in shear (7.9 %) than previously suggested yield criteria and hence reduces the risk to over-predict the capacity of the material to withstand shear stresses. At the same time, the Drucker-Prager criterion accounts for the strong tension-compression asymmetry of the material. A situation previously found unacceptable (accuracy of yield locus) for the overall objective of this thesis was thus significantly improved and lead to new modeling approaches (elasto-plastic shear stresses & ellipsis scaling for equivalent stresses and strains), which are applicable for any kind of material. Hence, the basis to continue with (uniaxial) fatigue experiments was established.

**3) Uniaxial Fatigue Tests.** In order to conduct stress-based and non-proportional fatigue life predictions, S-N curves are required to construct a Haigh diagram and to calibrate critical plane models. While some S-N curves of the adhesive were published by other authors, these were (again) associated with large uncertainties due to a high porosity level in the specimens. In general, it can be expected that the standard deviation in fatigue tests is larger than in static tests, because even small-scale defects of the specimens can significantly alter the cycles to failure. Similar to the static material characterization, the corresponding fatigue characterization of the adhesive was thus not accurate enough for this work's overall objective, because a large scatter of the S-N curves might render the influence of non-proportional loads inconclusive.

Two axial S-N curves at  $R = -1$  and  $R = 0$  were recorded in addition to a torsional S-N curve at  $R = -1$ . The sigmoidal-shaped Stüssi S-N model was found to provide the best-fit of the experimental data for all S-N curves. However, as the tests were limited to a maximum of  $\approx 10^6$  cycles for each specimen at the lowest load level, an engineering approach for gigacycle fatigue was necessary, since rotor blades of wind turbines are typically subjected to  $> 10^8$  cycles.

Therefore, the Stüssi model was combined with a Haibach extension line ( $\approx$  double the slope of the Basquin S-N approach) in such a way that the extension line is tangential to the Stüssi S-N curve. This way, the new Stüssi-Haibach S-N model provides a very good fit of the experimental data and transitions into a reasonable engineering approximation for the gigacycle fatigue regime without the need to specify an arbitrary transition point of the Haibach extension line.

The Stüssi and Stüssi-Haibach S-N models were also found to provide a good fit of fatigue data of the adhesive in literature. A direct comparison of this work's results to literature revealed substantial differences of the cycles to failure and demonstrated a significant load level-dependent influence of pores. In addition, a surrogate proportional limit at a plastic offset of 0.01 % was found to be a reasonable indication of the fatigue limit that is predicted by the Stüssi S-N model. While this finding needs further validation, it provides useful information for the allocation of specimens and testing equipment in S-N tests.

All conducted S-N tests were accompanied by stiffness degradation measurements. The stiffness degradation was found to be load level-dependent and was modeled accordingly with load level-dependent power law functions. The model was applied to predict the residual fatigue life of run-out specimens. These predictions indicated the validity of the Stüssi S-N model.

Similar to the static material characterization, the uniaxial fatigue characterization was conducted based on the necessity of high accuracy data to fulfill the overall objective of this thesis. While the comparison of the new data to literature demonstrated that the data quality was significantly improved, a new S-N and stiffness degradation model were proposed. Based on the achieved results, the chance to identify the influence of non-proportional loads was substantially improved and thus targeted in the next step.

**4) Non-Proportional Fatigue Tests.** Non-proportional loads are able to alter the cycles to failure of a material in comparison to a corresponding proportional load. In addition, non-proportional load states can distort the numerical fatigue life prediction as, e.g., the implicitly assumed consistency of the principal stress/strain orientation in (rainflow-counted) equivalent stress-based approaches is not guaranteed anymore. On account of the required high-quality data from virtually defect-free specimens and the more complex test setup, non-proportional loads were not experimentally analyzed for rotor blade adhesives, yet.

By subjecting the adhesive to biaxial (tension/compression-torsion) loads with different phase shifts in between the axial and torsional load, the influence of non-proportional loads on the cycles to failure were investigated experimentally. It was found that the adhesive can be characterized as a neutral material, meaning that the cycles to failure or the fracture surface orientation were independent of the level of non-proportionality. This observation is in-line with recently published results in literature, that linked the ductility of a material to the change of fatigue life under non-proportional loads. This finding is, however, not a reason to neglect non-proportional loads in the fatigue life prediction. On the contrary, it is demonstrated that the usage of rainflow-counted equivalent stresses in non-proportional conditions can lead to an over-prediction of the fatigue life by up to two orders of magnitude, even though a good prediction is found for a proportional load state. Therefore, the current state of the art of multiaxial fatigue life predictions for rotor blade bond lines (rainflow-counted equivalent stresses) was proven to be significantly non-conservative for the non-proportional conditions present during operation of a wind turbine. The main reason for the bad prediction quality of this methodology in this case is that the stress amplitude decreases with increasing level of non-proportionality. The signal shape is also altered, so that an equivalent (signed) sinusoidal signal translates into a down-scaled rectangular signal when the level of non-proportionality is increased via a phase shift.

In addition, the effects of a tension-compression asymmetry on the fatigue life prediction were studied, because these were hardly considered in literature so far. In case such an asymmetry is present, the Haigh diagram needs to be adopted to the equivalent stress space to avoid non-conservative predictions. This is because the S-N curves in the Haigh diagram get scaled and re-positioned as the stress ratio changes in the equivalent stress space in the presence of a tension-compression asymmetry. If this is not accounted for and an asymmetric yield criterion is used in the fatigue life prediction (e.g. Drucker-Prager), the stress space of the equivalent stress formulation does not match the Haigh diagram, which in turn leads to false fatigue life predictions. To circumvent this source of error, a hybrid version of the asymmetric Drucker-Prager criterion was developed, which can be used with the traditional engineering stress space representation of the Haigh diagram again. Depending on the available S-N data, this hybrid version allows the choice of the Haigh diagram representation and thus helps to minimize the number of necessary interpolations. Although these findings were derived from experiments on the adhesive, they are not confined to this material, since a tension-compression asymmetry is found for a large variety of materials.

This non-proportional experimental campaign was the first ever conducted for a rotor blade adhesive and established new insights to its multiaxial fatigue behavior. Likewise, these results represented the last experimental milestone required for a detailed comparison of non-proportional fatigue life prediction methods.

**5) Multiaxial Fatigue Life Prediction.** With the proof that non-proportional loads significantly distort the fatigue analyses of rotor blade adhesives for the current state of the art methodology (rainflow-counted, global equivalent stresses), a detailed comparison with more sophisticated methods is necessary. Therefore, the critical plane (CP) approach was applied and calibrated with the experimental data. It was found to result in substantially better fatigue life predictions for the analyzed fiber-reinforced adhesive. Although the applied calibration and algorithms could be used for fatigue analyses of rotor blade bond lines, the vast computational effort of the CP approach makes it impractical for structural optimization processes despite its accuracy. Hence, a new method was explored based on the experimental insight that the adhesive exhibited a neutral behavior regarding the level of non-proportionality.

The robustness of the CP approach in non-proportional load cases was linked to its asynchronous prediction of equivalent stresses. For instance, the widely adopted Findley criterion demands a superposition of the shear stress amplitude with the maximum of the normal stress for each identified multiaxial cycle. These stresses, however, do not necessarily appear at the same time, so that the superposition of them leads to a worst-case analogy. Different levels of non-proportionality, that may lead to an increased time shift in between the shear stress amplitude and the normal stress maximum during a particular cycle, are therefore hardly relevant concerning the magnitude of the equivalent stress and might only lead to a different CP orientation. Interestingly, this worst case analogy of the CP approach can be emulated for the global equivalent stress approach for phase shift-induced non-proportional loads using a FFT. In this case, a re-proportionalized equivalent stress can be calculated based on the amplitude, frequency and phase content of each stress component. A forced proportional interference (FPI) of the stress component signals is generated. With that, the equivalent stress is independent of the phase shift-induced level of non-proportionality and therefore mimics the CP approach in this regard. Due to the neutral behavior of the investigated adhesive in non-proportional loads, the FPI approach is in excellent agreement with experimental observations, while the CP results were less accurate. In case a ductile or brittle material is analyzed, a correction factor is required that accounts for the change of the cycles to failure in non-proportional conditions.

A major benefit of the FPI approach is that it is just as computationally efficient as a global equivalent stress approach without being confined to proportional load states. In contrast to the CP approach this means *several* orders of magnitude less in computation time. In addition, the FPI approach does not incorporate any assumptions on the material behavior other than the S-N correction factor or the chosen equivalent stress formulation (e.g. Drucker-Prager). This greatly eases the interpretation of the results and the FPI's applicability to other materials in comparison to the CP approach, where, e.g., the enclosing surface methods indirectly assume brittle or ductile material behavior. Other issues such as a sign correction of the equivalent stresses are solved by incorporation of the FFT in the FPI approach automatically. Despite the promising results, the FPI approach needs further validation in more complex loading conditions, which also introduce other sources of non-proportionality than phase-shifted loads, cf. Figure 1.1. However, every time an equivalent stress formulation was successfully validated for a proportional load state, the FPI approach will lead to a reasonable engineering approximation of the fatigue life in (predominantly phase shift-induced) non-proportional conditions. Moreover, the FPI approach can be utilized as a fast screening method, so that users of already validated CP approaches can still save computational time, as only high-interest regions with a high level of non-proportionality and a high damage potential need to be analyzed. This distinction was previously not possible, as low damage areas can still exhibit a high level of non-proportionality. In addition, the screening capability can also accelerate the critical plane identification.

It is emphasized that the FPI approach represents a versatile concept for multiaxial and non-proportional fatigue analyses and is not simply a new failure criterion. In fact, the FPI approach can be used with any equivalent stress formulation and is hence also applicable for any material. The overall objective of this thesis to accurately *and* efficiently predict the fatigue life under multiaxial non-proportional loads was thus achieved without confinement to a specific material. The key achievements of the thesis are summarized in the following.

### Achievements

- Calibrated critical plane algorithms for non-proportional fatigue life predictions of rotor blade bond lines
- Proposal of an accurate, efficient, versatile and easy-to-use concept for non-proportional fatigue analyses (FPI approach)
- Derivation of several material-independent methods such as an elasto-plastic shear stress estimation, an elliptical yield locus scaling approach, a new S-N model (Stüssi-Haibach) for gigacycle fatigue, a novel load-dependent stiffness-degradation model and a hybrid formulation of the Drucker-Prager yield criterion to account for scaling issues of the Haigh diagram related to a tension-compression asymmetry
- Blueprint for the manufacture of virtually defect-free specimens from a two-component material (resin + hardener) suitable for multiaxial experiments
- First characterization of neat fiber-reinforced rotor blade adhesive in static and fatigue loading conditions including different levels of non-proportionality



## 7.2 Outlook

As with every research, improvements in a particular research area lead to a different perspective and new questions that build upon the gained insights. Therefore, new questions and research opportunities, which are based on this work, are discussed in the following.

### Further evaluation of this work's experiments

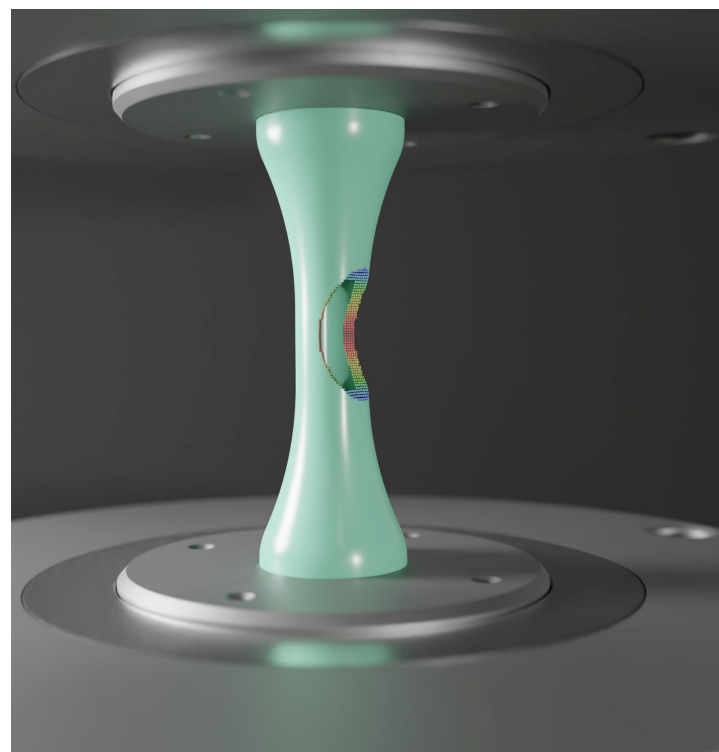
On account of the extensive experimental work, not all data have been evaluated, yet. Among potential other future uses of the data, three opportunities for further research were identified:

**1) Multiaxial Stiffness Degradation Model.** As with the uniaxial fatigue tests, the biaxial fatigue tests were accompanied by stiffness degradation measurements. Therefore, the influence of non-proportional loads on the stiffness degradation can be investigated. In addition, it can be checked if a superposition of the uniaxial degradation behavior is sufficient to approximate the more complex biaxial degradation. Potentially, a multiaxial stiffness degradation model can be derived and used for more accurate fatigue modeling in the future. This way, sequence effects could be modeled, which were not covered so far.

**2) Analysis of Pores using Digital Twins.** Aside from the defect-free specimens, a small number of specimens with slight imperfections, i.e., a single pore close to the test section, were tested. These dummy-specimens were predominantly used for machine setup tests. Therefore, the data acquisition was on the same level as with the regular tests. In addition, these specimens were also  $\mu$ CT scanned, so that it is possible to generate digital twin models of the specimens including the exact geometry of the pores, cf. Figure 7.1. The same applies for the high porosity level of the hand-mixed reference specimens. If such digital twin models can be validated with experimental data, any stochastic variation of pores can be modeled. With that, the impact of the level of porosity on the material properties can be approximated. Such a model would be of great value for the evaluation of manufacturing-induced defects and the transfer of coupon level data to more complex components.

**Figure 7.1:** Digital representation, i.e., digital twin, of a test in this work.

*What is the exact impact of pores on the material properties? The implementation of measured pore geometries from dummy- and hand-mixed specimens into FE-models might allow to answer this question.*



**3) Hardening Rule.** With the yield locus determination, the Drucker-Prager criterion was identified as the best-fit yield criterion. However, the experiments also allow for a more detailed analysis concerning the development of the (initial) yield surface with increasing plastic strains, i.e., a (biaxial) hardening rule.

### Open questions for new research projects

In addition to the opportunity to further evaluate the already recorded data, there are additional questions and applications that arise from this work. Some of these may require new research projects due to their complexity.

**1) Fatigue Life Prediction of Rotor Blade Bond Lines.** To demonstrate the influence of non-proportional loads, e.g., for the bond lines of wind turbine rotor blades, the calibrated CP approach should be compared to the standard global equivalent stress approach using normal operation loads from an aeroelastic simulation.

**2) Gigacycle Fatigue & Probabilistics.** Due to the extreme number of fatigue load cycles of rotor blades, gigacycle fatigue tests [214–218] need to be conducted on a coupon level to maximize the structural optimization potential and to validate S-N models, such as the Stüssi-Haibach approach proposed in this work. Based on these additional tests, probabilistic models should be applied to derive probabilistic S-N curves, i.e., P-S-N curves [219–224]. The neutral behavior of the adhesive under non-proportional loads also provides additional information on the scatter of the S-N curves, since 18 specimens on each biaxial load level led to a very good statistical basis.

**3) Level of Non-Proportionality in Blade Tests.** As mentioned in Section 1.2.3, biaxial fatigue tests of rotor blades have already been developed, cf. Figure 7.2, and provide a significant improvement in comparison to standard uniaxial tests. However, the level of non-proportionality of these tests was not quantified. Therefore, it is not yet clear how realistic the load states in these tests are compared to real (non-proportional) operational loads.



**Figure 7.2:** Biaxial Blade Testing at Fraunhofer IWES with a controlled elliptical tip displacement. ©#16

*What kind of level of non-proportionality can be achieved with this or similar setups?*

This problem also leads to the question how the chosen load introduction method and the associated finite element modeling affects the level of non-proportionality in wind turbine (rotor blade) simulations. A detailed analysis in this regard is necessary. However, a conclusion might only be possible by comparison to in-field strain measurements of true operational loads when these are combined with detailed wind-field measurements.

**4) More Complex Load Scenarios.** Although the tests in this work already incorporated a rather complex and non-proportional biaxial (tension/compression-torsion) load, the FPI approach needs further validation in even more complex load scenarios. Multiaxial (non-proportional) block or even randomized tests could establish a final conclusion on the validity of the approach. In addition, other ways to provoke a non-proportional stress state, cf. Figure 1.1, should be tested. A hexapod test setup can provide additional degrees of freedom in this regard, as it can transfer virtually any multiaxial and also non-proportional load to a specimen. This applies to both the coupon and the sub-component level. For instance, a vertical hexapod load introduction would enable multiaxial and non-proportional tests of beam structures, cf. Figure 7.3.

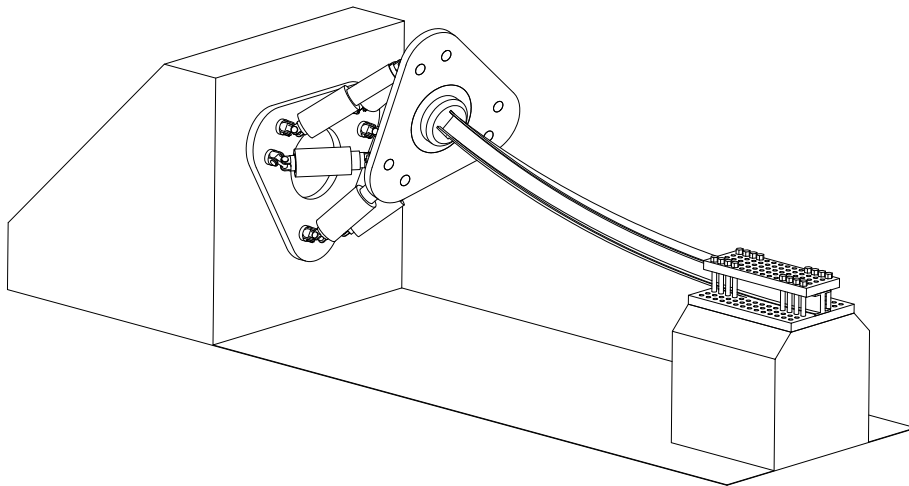


**Figure 7.3:** Proposal for a hexapod beam test.

*Realistic multiaxial non-proportional fatigue loads could be tested with this setup. What are the design requirements for such a test?*

**5) Influence of Reinforcement Fiber Orientation.** The manufactured adhesive specimens were confirmed to be transversely isotropic with a large majority of the fibers aligned in axial direction. Therefore, the derived material properties are confined to this fiber orientation. Different specimen geometries or an altered specimen manufacturing process will enable to quantify the influence of the orientation of the reinforcement fibers on the material properties. Semi-automated adhesive application devices such as the Variable Glue Applicator, cf. Figure 1.14, may also enable to adjust the orientation of the reinforcement fibers during rotor blade manufacture. A thorough investigation on this matter may improve the prediction of the material properties of rotor blade bond lines significantly.

**6) Viscoelastic Material Model.** The adhesive was identified to exhibit viscoelastic behavior, cf. Section P2-5.2. However, detailed experiments necessary to model these effects [225–230] were out of scope for this work. Therefore, the fatigue life prediction in this work did not account for viscoelastic effects. Strain rate changes, which might be apparent in, e.g., the bond lines of rotor blades during operation, are thus not accounted for with the current modeling approach. Additionally, temperature effects [228, 230, 231] were not analyzed, which also contribute to a change of the non-proportional material behavior due to a change of the ductility, cf. Figure P4-4.

**7) Characterization of Adhesion Properties.** The bulk adhesive specimen of this work enabled a detailed characterization of the cohesive material behavior. However, the adhesion properties were not analyzed, which might be necessary to accurately model fatigue degradation of more complex components. Test on butt-joints, which, e.g., connect two glass-fiber tubes, could provide a suitable test setup for biaxial (tension/compression-torsion) tests in static and (non-proportional) fatigue loads.

**8) Coupling of Modeling Approaches.** In this thesis, fatigue damage was calculated based on stress-based continuum mechanics approaches. Fracture mechanics-based approaches have not been considered although they are commonly used, e.g., for the trailing edge bond line [172, 232, 233]. A coupling of (non-proportional) continuum damage mechanics and fracture mechanics, as suggested in [20], might enable a more sophisticated fatigue modeling in case a damage tolerant (blade) design is targeted.

**9) Material Data Base.** Because rotor blades are composed of many different materials, ideally each material should be investigated concerning effects of non-proportional loads. A classification of wind energy-related materials according to Figure P4-4 would provide a great benefit for the structural optimization of the blades. Of course this also holds for the respective classification of other engineering materials for other industries, cf. Figure 1.2. Once such a data base is set up, the confidence level of a ductility-based sorting of materials (regarding non-proportional effects on the cycles to failure) might be high enough to reduce the experimental effort for new materials.

# List of Figures

1.1	Sources of non-proportional loads . . . . .	3
1.2	Examples of multiaxial, non-proportional fatigue across industries . . . . .	4
1.3	Multiaxial, non-proportional loads on rotor blades . . . . .	5
1.4	Aerodynamic loads at a blade cross section . . . . .	7
1.5	Projection of the stress tensor onto a plane . . . . .	10
1.6	Multiaxial Racetrack Filter . . . . .	10
1.7	Multiaxial rainflow count . . . . .	11
1.8	Convex hull algorithm for MWB rainflow count . . . . .	11
1.9	Enclosing surface methods . . . . .	12
1.10	Damage half sphere discretization . . . . .	13
1.11	Critical plane flowchart . . . . .	13
1.12	Rotor blade manufacturing - part 1/2 . . . . .	14
1.13	Rotor blade manufacturing - part 2/2 . . . . .	15
1.14	Adhesive application . . . . .	16
1.15	Mixing quality comparison . . . . .	17
1.16	Structural verification pyramid . . . . .	18
1.17	Cumulative thesis outline . . . . .	21
P1-1	Specimen design parameters . . . . .	30
P1-2	Results of the sensitivity study . . . . .	31
P1-3	Mixing procedure of a planetary centrifugal vacuum mixer . . . . .	32
P1-4	Optimal mixing parameters . . . . .	33
P1-5	Injection Options . . . . .	34
P1-6	Cartridge piston preparation . . . . .	35
P1-7	Final mold configuration . . . . .	35
P1-8	Tempering profile . . . . .	36
P1-9	Frequency distributions of the ultimate engineering tensile strength . . . . .	37
P1-10	Typical fracture observed in the tensile tests . . . . .	38
P1-11	Stress strain curves of the tensile tests . . . . .	38
P1-12	Typical fracture observed in the biaxial tests . . . . .	39
P1-13	Comparison of (biaxial) failure stresses . . . . .	39
P1-14	Qualitative porosity analysis of an industrial dosing machine . . . . .	39
P2-1	Definition of yielding . . . . .	45
P2-2	Qualitative porosity comparison . . . . .	46
P2-3	Test setup for every static test . . . . .	47
P2-4	Spline-based elasto-plastic shear stress approach . . . . .	48
P2-5	Ratios of shear stress predictions . . . . .	48
P2-6	Stress-strain diagram for uniaxial tension, torsion and compression . . . . .	50
P2-7	Ellipsis scaling approach based on an idealized, fictitious yield locus . . . . .	51

P2-8	Flow chart of the ellipsis scaling approach . . . . .	51
P2-9	Stress and strain yield locus . . . . .	52
P2-10	Shear stress relaxation . . . . .	53
P2-11	Tensile stress relaxation . . . . .	53
P2-12	Idealized viscoelastic hysteresis loop . . . . .	54
P2-13	Stress and strain yield locus comparison with different yield criteria . . . . .	55
P3-1	Test setup for every fatigue test . . . . .	60
P3-2	Qualitative porosity comparison . . . . .	60
P3-3	Flow chart of the stiffness degradation measurement . . . . .	61
P3-4	Conversion from displacement to load control . . . . .	63
P3-5	S-N curves for tension/compression, tension/tension and torsion . . . . .	64
P3-6	Typical fracture patterns in the fatigue tests for all investigated load types . .	67
P3-7	Gigacycle fatigue types . . . . .	67
P3-8	Comparison of static stress-strain curves with experimental fatigue results . .	69
P3-9	Comparison of torsional S-N results . . . . .	69
P3-10	Modeling of the relative stiffness degradation . . . . .	71
P3-11	Residual strength tests . . . . .	73
P3-12	Stiffness degradation-based fatigue life estimation . . . . .	74
P4-1	Qualitative porosity comparison . . . . .	80
P4-2	Analysis of fiber orientation . . . . .	81
P4-3	Frequency distributions of all biaxial fatigue tests . . . . .	82
P4-4	Idealized influence of ductility on the S-N behavior . . . . .	83
P4-5	Approximate orientation of fracture surfaces . . . . .	84
P4-6	Implications of a tension-compression asymmetry for fatigue . . . . .	85
P4-7	Force displacement hysteresis of specimen 177 . . . . .	85
P4-8	Stüssi-Haibach approach and derivatives thereof . . . . .	86
P4-9	Haigh diagram comparison (tension-compression asymmetry) . . . . .	88
P4-10	Hybrid Drucker-Prager criterion . . . . .	89
P4-11	S-N comparison with eqv. amplitude predictions . . . . .	90
P4-12	Damage prediction of the hybrid Drucker-Prager criterion . . . . .	91
6.1	Exemplary dependencies of the level of non-proportionality . . . . .	99
6.2	Synopsis of stress-based multiaxial fatigue approaches . . . . .	100
6.3	Asynchronous behavior of critical plane criteria . . . . .	102
6.4	Flow chart of the LiWI and FPI approaches . . . . .	103
6.5	Comparison of multiaxial fatigue criteria (predicted damages) . . . . .	109
6.6	Experimental fracture surface vs. critical plane predictions . . . . .	111
7.1	Digital twin specimen . . . . .	121
7.2	Biaxial blade testing . . . . .	122
7.3	Proposal for a hexapod beam test . . . . .	123

## Copyrights of included Pictures

This list contains the copyrights of Pictures that were included in Figures in non-paper sections. A bibliography reference with more detailed information can be found in the last column.

Context	ID	Copyright	Ref.
Figure 1.2	#1	© Siemens	[234]
	#2	© MSC	[235]
	#3	© Vlad Tchompalov / unsplash	[236]
	#4	© Philip Platzer / Red Bull Content Pool	[237]
Figure 1.12	#5	© Siemens	[238]
	#6	© Fraunhofer IWES	[239]
	#7	© Hawart	[240]
Figure 1.13	#8	© LM	[241]
	#9	© Motofil	[242]
	#10	© ABB	[139]
Figure 1.14	#11	© Fraunhofer IWES	[239]
Figure 1.16	#12	© Fraunhofer IWES	[243]
	#13	© Fraunhofer IWES	[244]
	#14	© Fraunhofer IWES	[245]
	#15	© Sander Weeteling / unsplash	[246]
Figure 7.2	#16	© Fraunhofer IWES	[247]

# List of Tables

P1-1	Sensitivity study: design space . . . . .	31
P1-2	Final evaluation: design space . . . . .	31
P1-3	Comparison with literature . . . . .	32
P1-4	Mold inserts (3D printed) . . . . .	34
P1-5	Qualitative porosity comparison . . . . .	36
P1-6	Comparison of material properties . . . . .	37
P2-1	Summarized yield points for all static experiments conducted . . . . .	52
P2-2	Stiffness parameters and check for bi-modularity . . . . .	53
P3-1	Summarized fatigue results for all experiments conducted . . . . .	65
P3-2	Fitting parameters of all S-N models . . . . .	66
P3-3	Fitting parameters of the stiffness degradation . . . . .	72
P3-4	Stiffness degradation-based fatigue life estimation . . . . .	74
P4-1	Summarized fatigue results . . . . .	82
P4-2	Damage comparison . . . . .	91
6.1	Calibration parameters of critical plane models . . . . .	108



# List of Abbreviations

<b>CFL</b>	constant fatigue life
<b>CFLi</b>	constant fatigue life interpolation
<b>CP</b>	critical plane
<b>CPU</b>	central processing unit
<b>CT</b>	computer tomography
<b>FE</b>	finite element
<b>FEA</b>	finite element analysis
<b>FFT</b>	fast Fourier transform
<b>FPI</b>	forced proportional interference
<b>iFFT</b>	inverse fast Fourier transform
<b>IWES</b>	Institute for Wind Energy Systems
<b>LCF</b>	low cycle fatigue
<b>LiWI</b>	linear wave interference equivalent stress hypothesis
<b>MB</b>	minimum ball
<b>MRF</b>	multiaxial racetrack filter
<b>MWB</b>	modified Wang-Brown algorithm
<b>PMOI</b>	polar moment of inertia
<b>RMS</b>	root mean square
<b>RST</b>	residual strength test
<b>TIB</b>	German National Library of Science and Technology
<b>UV</b>	ultraviolet (radiation)
<b>VHCF</b>	very high cycle fatigue

# List of Symbols

## Roman Symbols

Symbol	Description	Unit
$a$	Ellipsis fitting parameter	N/mm <sup>2</sup>
$a_c$	Material parameter for $\sigma_{PCr}$	–
$a_F$	Material parameter for $\sigma_F$	–
$A$	Cross sectional area	mm <sup>2</sup>
$A$	Rational function (stiff. deg. model)	–
$A_0$	Initial cross sectional area	mm <sup>2</sup>
$b$	Ellipsis fitting parameter	N/mm <sup>2</sup>
$b_c$	Material parameter for $\sigma_{PCr}$	N/mm <sup>2</sup>
$b_F$	Material parameter for $\sigma_F$	–
$B$	Rational function (stiff. deg. model)	–
$c$	Number of calculations	–
$c_V$	Coefficient of variation	%
$C$	Ratio of inner and outer specimen radius	–
$C_V$	Multivariate coefficient of variation	–
$C_{unique}$	Number of unique colors (within a mixture)	–
$d_C$	Clamping diameter of specimen	mm
$d_i$	Inner diameter of specimen	mm
$d_{ij}$	Euclidean distance in between the points $P_i$ and $P_j$	–
$D$	Damage	–
$D_{container}$	Diameter of mixing container	mm
$E$	Young's modulus	N/mm <sup>2</sup>
$\tilde{E}_{ro}$	Normalized Young's modulus of run-out specimen	%
$E_{\parallel}$	Young's modulus in axial, i.e., fiber direction	N/mm <sup>2</sup>
$f$	Frequency	Hz
$f_{np}$	Level of non-proportionality	–
$F$	Force	N
$G$	Shear modulus	N/mm <sup>2</sup>
$G_{\perp\parallel}$	Shear modulus perpendicular to axial / fiber direction	N/mm <sup>2</sup>
$h$	Frequency distribution	%
$H$	Height of specimen	mm
$H_{material}$	Infill height of material (mixing process)	mm
$I_1$	First invariant of stress tensor	N/mm <sup>2</sup>
$I_f$	Internal damage initiation	–
$J$	Polar moment of inertia	mm <sup>4</sup>
$J_1$	First invariant of strain tensor	$\mu\text{m}/\text{m}$
$k$	Slope of Basquin S-N model	–
$l$	Length of stress history	–

Symbol	Description	Unit
$L_1, L_2, L_3$	Load level in S-N tests	—
$L_C$	Clamping length of specimen	mm
$n$	Number of specimens	—
$n$	Number of cycles	—
$\mathbf{n}$	Normal vector (critical plane approach)	—
$n_{rev}$	Revolutions per minute (mixing process)	1/min
$N$	Cycles to failure	—
$N_{np}$	Cycles to failure in non-proportional load state	—
$p_1, p_2, p_3, p_4$	Fitting parameters (stiff. deg. model)	—
$P$	Point ( $\tau_{nu}, \tau_{nv}$ ) in shear-based multiaxial rainflow count	N/mm <sup>2</sup>
$q_1, q_2, q_3, q_4$	Fitting parameters (stiff. deg. model)	—
$r$	Radius	mm
$r_i$	Inner specimen radius	mm
$r_o$	Outer specimen radius	mm
$R$	Stress ratio: ratio of min. and max. stress	—
$\mathbf{R}$	Vector of stress ratios	—
$R_C$	Tapering radius towards clamping section of specimen	mm
$R_m$	Ultimate tensile strength	N/mm <sup>2</sup>
$R_T$	Tapering radius towards test section of specimen	mm
$\mathbb{R}^{eng}$	Engineering stress space	—
$\mathbb{R}^{eqv}$	Equivalent stress space	—
$S_f$	Surface induced failure	—
$t$	Time	s
$t_{mix}$	Mixing time	min
$t_T$	Wall thickness of specimen	mm
$T$	Torque	Nm
$T$	Temperature	°C
$T_{surf}$	Surface temperature	°C
$T_{Adh.}$	Adhesive temperature (during curing process)	°C
$T_{Prog.}$	Programmed oven temperature (during curing process)	°C
$u$	Axial displacement (specimen testing machine)	mm
$\mathbf{u}$	In-plane vector (critical plane approach)	—
$\mathbf{v}$	In-plane vector (critical plane approach)	—

## Greek Symbols

Symbol	Description	Unit
$\alpha$	Angle of attack	deg
$\alpha$	Stress ratio	—
$\alpha$	S-N fitting parameter	—
$\beta$	S-N fitting parameter	—
$\Delta\sigma$	Tensile stress relaxation	%
$\Delta\tau$	Shear stress relaxation	%
$\Delta T$	Temperature difference (specimen vs. ambient)	°C

Symbol	Description	Unit
$\varepsilon$	(True) normal strain	$\mu\text{m}/\text{m}$
$\dot{\varepsilon}_0$	Initial normal strain rate	$(\mu\text{m}/\text{m})\text{s}^{-1}$
$\varepsilon_{\text{vM,ansio}}$	von Mises equivalent strain (anisotropic modification)	$\mu\text{m}/\text{m}$
$\varepsilon_{\text{vM,iso}}$	von Mises equivalent strain (isotropic standard)	$\mu\text{m}/\text{m}$
$\gamma$	Latitude	deg
$\gamma$	S-N fitting parameter	–
$\gamma$	Shear strain	$\mu\text{m}/\text{m}$
$\dot{\gamma}_0$	Initial shear strain rate	$(\mu\text{m}/\text{m})\text{s}^{-1}$
$\kappa$	Yield strength ratio or yield strain ratio	–
$\kappa_\infty$	Fatigue limit ratio (critical plane approach)	–
$\lambda$	Buckling load factor (in compression)	–
$\Lambda_D$	Damage ratio (in fatigue life prediction)	–
$\Lambda_{\text{mix}}$	Mixing aspect ratio	–
$\nu$	Poisson ratio	–
$\mu$	Mean value	–
$\mu^-$	Mean value with negative standard deviation offset	–
$\mu^+$	Mean value with positive standard deviation offset	–
$\boldsymbol{\mu}$	Vector of mean values	–
$\varphi$	Longitude	deg
$\varphi_i$	Angle in ellipsis fitting	deg
$\phi$	Phase shift	deg
$\psi$	Rotational angle (specimen testing machine)	deg
$\psi_f$	Angle of fracture surface	deg
$\sigma$	Standard deviation	–
$\sigma$	(True) normal stress	$\text{N}/\text{mm}^2$
$\sigma_0$	Center normal stress of fitting ellipsis	$\text{N}/\text{mm}^2$
$\sigma_1, \sigma_2, \sigma_3$	Principle stresses ( $\sigma_1 > \sigma_2 > \sigma_3$ )	$\text{N}/\text{mm}^2$
$\sigma_F$	Findley equivalent stress (critical plane approach)	$\text{N}/\text{mm}^2$
$\sigma_\infty$	(Supposed) fatigue limit amplitude, i.e., endurance limit	$\text{N}/\text{mm}^2$
$\sigma_m$	Mean stress	$\text{N}/\text{mm}^2$
$\sigma_{\text{mn}}$	Normal stress component of critical plane stress history	$\text{N}/\text{mm}^2$
$\boldsymbol{\sigma}_{\text{outer}}$	Equivalent stress outside the specimen test section	$\text{N}/\text{mm}^2$
$\sigma_{\text{PCr}}$	Papuga equivalent stress (critical plane approach)	$\text{N}/\text{mm}^2$
$\boldsymbol{\sigma}_{\text{test}}$	Equivalent stress inside the specimen test section	$\text{N}/\text{mm}^2$
$\sigma_z$	Axial stress	$\text{N}/\text{mm}^2$
$\boldsymbol{\Sigma}$	Covariance matrix	–
$\tau$	Shear stress	$\text{N}/\text{mm}^2$
$\tau_{\text{ASTM}}$	Shear stress acc. ASTM E2207-15 (identical to Breddt)	$\text{N}/\text{mm}^2$
$\tau_n$	Shear stress history (2D) in critical plane approach	$\text{N}/\text{mm}^2$
$\tau_{\text{nu}}$	Shear stress component of critical plane stress history	$\text{N}/\text{mm}^2$
$\tau_{\text{nv}}$	Shear stress component of critical plane stress history	$\text{N}/\text{mm}^2$
$\tau_{z\eta}$	Shear stress from torsion	$\text{N}/\text{mm}^2$
$\theta$	Rotational angle (specimen testing machine)	deg
$\theta$	Angle between axial direction of specimen and fiber	deg
$\theta_t$	Twist angle	deg
$\xi_i$	Scaling factor (ellipsis fitting)	–
$\xi_{\text{np},i}$	S-N-based correction factor (FPI approach)	–

## Indices

Single-use indices or special cases are noted in the list of Roman and Greek symbols.

Symbol	Description
$\square^*$	Including true stress-strain correction
$\square$	Equivalent value, i.e., transformed to $\mathbb{R}^{\text{eqv}}$
$\hat{\square}$	Estimated property via FFT (or scaled ellipsis parameter)
$\tilde{\square}$	Normalized value (stiffness degradation model)
$\square^{R=0}$	Reference to a stress ratio of $R = 0$
$\square^{R=-1}$	Reference to a stress ratio of $R = -1$
$\square_{0.01}$	0.01 % plastic offset strain (surrogate proportional limit)
$\square_{0.2}$	0.2 % plastic offset strain
$\square_a$	Amplitude
$\square_{\text{ave}}$	Averaged
$\square_B$	Beltrami (equivalent stress or strain)
$\square_c$	Related to compressive material properties
$\square_{\text{DP}}$	Drucker-Prager (equivalent stress or strain)
$\square_{\text{el}}$	Elastic
$\square_{\text{eng}}$	Engineering
$\square_{\text{eqv}}$	Equivalent
$\square_{\text{ext}}$	Extension (Stüssi-Haibach S-N approach)
$\square_f$	Failure
$\square_{\text{hyp}}$	Hybrid formulation
$\square_L$	Load Level
$\square_{\text{max}}$	Maximum
$\square_{\text{min}}$	Minimum
$\square_{\text{pl}}$	Plastic
$\square_s$	Signed
$\square_S$	Stassi d'Alia (equivalent stress or strain)
$\square_t$	Related to tensile material properties
$\square_u$	Ultimate
$\square_{\text{vM}}$	von Mises (equivalent stress or strain)
$\square_{\text{vMS}}$	von Mises-Schleicher (equivalent stress or strain)
$\square_y$	Yield (stress or strain)
$\square_\varepsilon$	Related to normal strain
$\square_\gamma$	Related to shear strain
$\square_\sigma$	Related to normal stress
$\square_\tau$	Related to shear stress

# Bibliography

This bibliography list contains only those publications cited in non-paper sections.

- [1] United Nations General Assembly. Transforming our world: The 2030 Agenda for Sustainable Development. (A/RES/70/1), 2015.
- [2] United Nations. The Paris Agreement. *Framework Convention on Climate Change*, 2016.
- [3] I. J. J. van Straalen, J. Wardenier, L. B. Voegesang, and F. Soetens. Structural adhesive bonded joints in engineering - drafting design rules. *Int J Adhes Adhes*, 18:41–49, 1998.
- [4] J. B. Jørgensen, B. Sørensen, and C. Kildegaard. *Adhesive Joints in Wind Turbine Blades: PhD Thesis*. 2017.
- [5] P. Noever-Castelos. *Updating structural wind turbine blade models via invertible neural networks: Dissertation*. 2023.
- [6] F. Sayer, A. Antoniou, S. Goutianos, I. Gebauer, K. Branner, and C. Balzani. ReliaBlade Project: A Material's Perspective towards the Digitalization of Wind Turbine Rotor Blades. *IOP Conf Ser Mat Sci*, 942:012006, 2020.
- [7] M. Fahim, V. Sharma, T.-V. Cao, B. Canberk, and T. Q. Duong. Machine Learning-Based Digital Twin for Predictive Modeling in Wind Turbines. *IEEE Access*, 10:14184–14194, 2022.
- [8] D. F. Socie and G. B. Marquis. *Multiaxial Fatigue*. Society of Automotive Engineers, Inc., 2000. 978-0768004533.
- [9] J. T. P. de Castro and M. A. Meggiolaro. *Fatigue Design Techniques Under Real Service Loads. Volume II - Low-Cycle and Multiaxial Fatigue*. CreateSpace Independent Publishing Platform, 1. edition, 2016. 978-1530797042.
- [10] E. Haibach. *Betriebsfestigkeit*. Springer, 2006. 978-3540293637.
- [11] D. Radaaj and M. Vormwald. *Ermüdungsfestigkeit*. Springer, 2007. 978-3-540-71458-3.
- [12] A. Fatemi and D. F. Socie. A critical plane approach to multiaxial fatigue damage including out-of-phase loading. *Fatigue Fract Eng M*, 11: 149–165, 1988.
- [13] C. M. Sonsino. Multiaxial fatigue of welded joints under in-phase and out-of-phase local strains and stresses. *Int J Fatigue*, 17:55–70, 1995.
- [14] C. Riess, W. Hiese, M. Obermayr, and M. Vormwald. Engineering approaches to multiaxial and non-proportional fatigue of notched components. *Mater Sci Eng Technol*, 49:381–391, 2018.
- [15] M. Einolghozati, M. K. Farahani, H. R. Lari, and A. Bahri. A Novel Approach for Numerical Calculation and Optimization of High-Cycle Fatigue Life under Multi-Axial Loads. *SAE Technical Paper*, 1:0968, 2014.
- [16] N. Gates and A. Fatemi. Multiaxial variable amplitude fatigue life analysis including notch effects. *Int J Fatigue*, 91:337–351, 2016.
- [17] Hexion™. Technical Data Sheet - EPIKOTE™ Resin MGS™ BPR 135G-Series and EPIKURE™ Curing Agent MGS™ BPH 134G-137GF, 2022.
- [18] M. A. Eder, R. D. Bitsche, and F. Belloni. Effects of geometric non-linearity on energy release rates in a realistic wind turbine cross section. *Compos Struct*, 132:1075–1084, 2015.
- [19] M. A. Eder, S. Semenov, and M. Sala. Multiaxial Stress Based High Cycle Fatigue Model for Adhesive Joint Interfaces. Okada, H., Atluri, S. (eds) Computational and Experimental Simulations in Engineering. ICCES 2019. Mechanisms and Machine Science, pages 612–632, 2020.
- [20] Xiao Chen and Martin A. Eder. A Critical Review of Damage and Failure of Composite Wind Turbine Blade Structures. volume 942 of *IOP Conf Ser Mat Sci*, page 012001, 2020.
- [21] P. Zuo and A. P. Vassilopoulos. Review of fatigue of bulk structural adhesives and thick adhesive joints. *Int Mater Rev*, 66:313–338, 2021.
- [22] L. Mishnaevsky Jr. Root Causes and Mechanisms of Failure of Wind Turbine Blades: Overview. *Materials*, 15:2959, 2022.
- [23] C. M. Sonsino. Multiaxial fatigue life response depending on proportionality grade between normal and shear strains/stresses and material ductility. *Int J Fatigue*, 135:105468, 2020.
- [24] M. L. Larsen, J. Baumgartner, H. B. Clausen, and V. Arora. A new constant amplitude equivalent principal component analysis-based method for non-proportionality quantification of variable amplitude loaded welded joints in large-scale structures. *Int J Fatigue*, 163:107008, 2022.
- [25] S. Márquez-Domínguez and J. D. Sørensen. Fatigue Reliability and Calibration of Fatigue Design Factors for Offshore Wind Turbines. *Energies*, 5:1816–1834, 2012.

- [26] Y. Dong and D. M. Frangopol. Risk-informed life-cycle optimum inspection and maintenance of ship structures considering corrosion and fatigue. *Ocean Eng*, 101:161–171, 2015.
- [27] M.M. Derriso, C.D. McCurry, and C.M. Schubert Kabban. A novel approach for implementing structural health monitoring systems for aerospace structures. In Fuh-Gwo Yuan, editor, *Structural Health Monitoring (SHM) in Aerospace Structures*, pages 33–56. Woodhead Publishing, 2016. ISBN 978-0-08-100148-6.
- [28] S. M. O. Tavares and P. M. S. T. de Castro. An overview of fatigue in aircraft structures. *Fatigue Fract Eng M*, 40:1510–1529, 2017.
- [29] D. Caous, C. Bois, J.-C. Wahl, T. Palin-Luc, and J. Valette. Analysis of multiaxial cyclic stress state in a wind turbine blade. ICCM20, 2015.
- [30] D.P. Rommel, D. Di Maio, and T. Tinga. Calculating wind turbine component loads for improved life prediction. *Renew Energy*, 146:223–241, 2020.
- [31] M. Rosemeier, A. Krimmer, A. Bardenhagen, and A. Antoniou. Tunneling Crack Initiation in Trailing-Edge Bond Lines of Wind-Turbine Blades. *AIAA J*, 57:5462–5474, 2019.
- [32] M. Li. An iteration method to adjusting random loading for a laboratory fatigue test. *Int J Fatigue*, 27:783–789, 2005.
- [33] Z. Li and J. W. Ringsberg. Fatigue routing of container ships—assessment of contributions to fatigue damage from wave-induced torsion and horizontal and vertical bending. *Ships Offshore Struct*, 7:119–131, 2012.
- [34] Z. Li, J. W. Ringsberg, and G. Storhaug. Time-domain fatigue assessment of ship side-shell structures. *Int J Fatigue*, 55:276–290, 2013.
- [35] P. S. van Lieshout. *On the assessment of multi-axial fatigue resistance of welded steel joints in marine structures when exposed to non-proportional constant amplitude loading: Dissertation*. 2020.
- [36] H. den Besten. Fatigue damage criteria classification, modelling developments and trends for welded joints in marine structures. *Ships Offshore Struct*, 13:787–808, 2018.
- [37] P. S. van Lieshout, J. H. den Besten, and M. L. Kaminski. Validation of the corrected Dang Van multiaxial fatigue criterion applied to turret bearings of FPSO offloading buoys. *Ships Offshore Struct*, 12:521–529, 2017.
- [38] Y. Dong, Y. Garbatov, and C. Guedes Soares. Review on uncertainties in fatigue loads and fatigue life of ships and offshore structures. *Ocean Eng*, 264:112514, 2022.
- [39] W. Popko. *Impact of Sea Ice Loads on Global Dynamics of Offshore Wind Turbines: Dissertation*. 2020.
- [40] R. H. Leggatt. Residual stresses in welded structures. *Int J Pres Ves Pip*, 85:144–151, 2008.
- [41] A. Ince and G. Glinka. Innovative computational modeling of multiaxial fatigue analysis for notched components. *Int J Fatigue*, 82:134–145, 2016.
- [42] Y. S. Kong, S. Abdullah, D. Schramm, M. Z. Omar, and S. M. Haris. Correlation of Uniaxial and Multiaxial Fatigue Models for Automobile Spring Life Assessment. *Exp Techniques*, 44:197–215, 2020.
- [43] A.-S. Béranger, J.-Y. Bérard, and J.-F. Vittori. A Fatigue Life Assessment Methodology For Automotive Components. In G. Marquis and J. Solin, editors, *Fatigue Design of Components*, volume 22 of *European Structural Integrity Society*, pages 17–25. Elsevier, 1997.
- [44] K. Reza Kashyzadeh. Effects of Axial and Multiaxial Variable Amplitude Loading Conditions on the Fatigue Life Assessment of Automotive Steering Knuckle. *J Fail Anal Prev*, 20:455–463, 2020.
- [45] C. M. Sonsino and R. Franz. Multiaxial fatigue assessment for automotive safety components of cast aluminium EN AC-42000 T6 (G-ALSi7Mg0.3 T6) under constant and variable amplitude loading. *Int J Fatigue*, 100:489–501, 2017.
- [46] K. Reza Kashyzadeh, G. H. Farrahi, M. Shariyat, and M. T. Ahmadian. Experimental accuracy assessment of various high-cycle fatigue criteria for a critical component with a complicated geometry and multi-input random non-proportional 3D stress components. *Eng Fail Anal*, 90:534–553, 2018.
- [47] P. Heuler, T. Bruder, and H. Klätschke. Standardised load-time histories - a contribution to durability issues under spectrum loading. *Mater Sci Eng Technol*, 36:669–677, 2005.
- [48] X. Yu. On the fatigue crack growth analysis of spliced aircraft wing panels under sequential axial and shear loads. *Eng Fract Mech*, 123:116–125, 2014.
- [49] Z. Kapidžić, S. B. Lindström, and J. Lundgren. Incremental fatigue damage model: application to plane problems with non-proportional loading. ICAS, 2022.
- [50] K. Koski, J. Tikka, M. Bäckström, A. Siljander, S. Liukkonen, and G. Marquis. An aging aircraft’s wing under complex multiaxial spectrum loading: Fatigue assessment and repairing. *Int J Fatigue*, 28:652–656, 2006.
- [51] M. Erickson, A. R. Kallmeyer, R. H. Van Stone, and P. Kurath. Development of a Multiaxial Fatigue Damage Model for High Strength Alloys Using a Critical Plane Methodology. *J Eng Mater Technol*, 130:041008, 2008.

- [52] F. Esmaeili, T. N. Chakherlou, and M. Zehsaz. Prediction of fatigue life in aircraft double lap bolted joints using several multiaxial fatigue criteria. *Mater Design*, 59:430–438, 2014.
- [53] D. C. Lombardo. Helicopter Structures - A Review of Loads, Fatigue Design Techniques and Usage Monitoring. Technical report, Department of Defence Canberra (Australia), 1993. ADA267115.
- [54] M. Garcia, C. A. Pereira Baptista, and A. Nussbaumer. Multiaxial fatigue study on steel transversal attachments under constant amplitude proportional and non-proportional loadings. MATEC Web Conf 165, page 16007, 2018.
- [55] Z. Fu, Y. Wang, B. Ji, and F. Jiang. Effects of multiaxial fatigue on typical details of orthotropic steel bridge deck. *Thin Wall Struct*, 135:137–146, 2019.
- [56] S. Puerto Tchemodanova, M. Mashayekhi, M. Sanayei, and E. Santini Bell. Multiaxial fatigue assessment of complex steel connections: A case study of a vertical-lift gussetless truss bridge. *Eng Struct*, 235:111996, 2021.
- [57] A. Bernasconi, M. Filippini, S. Foletti, and D. Vaudo. Multiaxial fatigue of a railway wheel steel under non-proportional loading. *Int J Fatigue*, 28:663–672, 2006.
- [58] E. Leidich, J. Vidner, and B. Brůžek. Integral Approach for Endurance Limit Evaluation on Shrink-Fitted Assemblies. *Bulletin Appl Mech*, 5:44–49, 2009.
- [59] L. Reis, B. Li, and M. de Freitas. A multiaxial fatigue approach to Rolling Contact Fatigue in railways. *Int J Fatigue*, 67:191–202, 2014.
- [60] T. Itoh, M. Sakane, M. Ohnami, and D. F. Socie. Nonproportional Low Cycle Fatigue Criterion for Type 304 Stainless Steel. *J Eng Mater Technol*, 117:285–292, 1995.
- [61] W. Maktouf, K. Ammar, I. Ben Naceur, and K. Saï. Multiaxial high-cycle fatigue criteria and life prediction: Application to gas turbine blade. *Int J Fatigue*, 92:25–35, 2016.
- [62] F. Berti, P.-J. Wang, A. Spagnoli, C. Guala, F. Migliavacca, G. Pennati, E. R. Edelman, and L. Petrini. Fatigue behavior of Nitinol medical devices under multi-axial non-proportional loads. volume 300 of *ICMFF12*, page 12001, 2019.
- [63] M. V. S. Pereira, F. A. Darwish, A. Feiferis, and T. Lima Castro. Multiaxial fatigue criteria applied to motor crankshaft in thermoelectric power plants. volume 300 of *ICMFF12*, page 04003, 2019.
- [64] Y. Wang, J. Liu, W. Duan, Z. Pan, and Y. Qiao. Fatigue of vulcanized natural rubber under proportional and non-proportional loading. *Fatigue Fract Eng M*, 43:2232–2246, 2020.
- [65] Z. Montano, M. Kühn, E. Daniele, and J. Stüve. Bend-twist Coupling on Rotor Blades for Wind Turbines. *Lightweight Design Worldwide*, 11: 42–47, 2018.
- [66] M. Wiens, T. Meyer, and J. Wenske. Exploiting Bend-Twist Coupling in Wind Turbine Control for Load Reduction. volume 53 of *IFAC PapersOnLine*, pages 12139–12144, 2020.
- [67] F. M. Jensen, P. M. Weaver, L. S. Cecchini, H. Stang, and R. F. Nielsen. The Brazier effect in wind turbine blades and its influence on design. *Wind Energy*, 15:319–333, 2012.
- [68] M. A. Eder and R. D. Bitsche. A qualitative analytical investigation of geometrically nonlinear effects in wind turbine blade cross sections. *Thin Wall Struct*, 93:1–9, 2015.
- [69] P. U. Haselbach, M. A. Eder, and F. Belloni. A comprehensive investigation of trailing edge damage in a wind turbine rotor blade. *Wind Energy*, 19:1871–1888, 2016.
- [70] W. Hu. *Reliability-based design optimization of composite wind turbine blades for fatigue life under wind load uncertainty: PhD Thesis*. 2015.
- [71] W. Hu, K. K. Choi, O. Zhupanska, and J. H. J. Buchholz. Integrating variable wind load, aerodynamic, and structural analyses towards accurate fatigue life prediction in composite wind turbine blades. *Struct Multidiscip O*, 53:375–394, 2016.
- [72] P. Noever Castelos, M. Wentingmann, and C. Balzani. Comparative study of finite-element-based fatigue analysis concepts for adhesive joints in wind turbine rotor blades. *GACM*, pages 1–5, 2017.
- [73] W. Hu, W. Zhao, Y. Wang, Z. Liu, J. Cheng, and J. Tan. Design optimization of composite wind turbine blades considering tortuous lightning strike and non-proportional multi-axial fatigue damage. *Eng Optimiz*, 52:1868–1886, 2020.
- [74] H. Mertens, R. Kamieth, and R. Liebich. Fatigue calculation for transient proportional and non-proportional multiaxial vibrational stress for component optimisation based on the Modified Mohr-Mises-Hypothesis. *Int J Fatigue*, 137: 105643, 2020.
- [75] H. Bai, C. Zhu, Y. Zhou, X. Chen, H. Feng, and W. Ye. Study on Tooth Interior Fatigue Fracture Failure of Wind Turbine Gears. *Metals*, 10:1497, 2020.
- [76] C. Han, K. Liu, Y. Ma, P. Qin, and T. Zou. Multiaxial fatigue assessment of jacket-supported offshore wind turbines considering multiple random correlated loads. *Renew Energy*, 169:1252–1264, 2021.
- [77] B. Weber, B. Kenmeugne, J. C. Clement, and Robert J. L. Improvements of multiaxial fatigue criteria computation for a strong reduction of calculation duration. *Comp Mater Sci*, 15:381–399, 1999.



- [78] H. Wu, M. A. Meggiolaro, and J. T. P. de Castro. Validation of the multiaxial racetrack amplitude filter. *Int J Fatigue*, 87:167–179, 2016.
- [79] C. H. Wang and M. W. Brown. Life Prediction Techniques for Variable Amplitude Multiaxial Fatigue - Part 1: Theories. *J Eng Mater Technol*, 118:367–370, 1996.
- [80] C. H. Wang and M. W. Brown. Life Prediction Techniques for Variable Amplitude Multiaxial Fatigue - Part 2: Comparison With Experimental Results. *J Eng Mater Technol*, 118:371–374, 1996.
- [81] T. E. Langlais, J. H. Vogel, and T. R. Chase. Multiaxial cycle counting for critical plane methods. *Int J Fatigue*, 25:641–647, 2003.
- [82] A. Niesłony. Determination of fragments of multiaxial service loading strongly influencing the fatigue of machine components. *Mech Syst Signal Pr*, 23:2712–2721, 2009.
- [83] M. A. Meggiolaro and J. T. P. de Castro. An improved multiaxial rainflow algorithm for non-proportional stress or strain histories - Part II: The Modified Wang-Brown method. *Int J Fatigue*, 42:194–206, 2012.
- [84] V. Anes, L. Reis, B. Li, and M. de Freitas. New cycle counting method for multiaxial fatigue. *Int J Fatigue*, 67:78–94, 2014.
- [85] K. G. F. Janssens. Universal cycle counting for non-proportional and random fatigue loading. *Int J Fatigue*, 133:105409, 2020.
- [86] N. D. Bibbo, M. L. Larsen, J. Baumgartner, and V. Arora. An improved rainflow counting method for multiaxial stress states using the minimum circumscribed circle method to identify shear stress ranges. *Int J Fatigue*, 163:106997, 2022.
- [87] K. Dang Van, A. Le Douaron, and H.P. Lieurade. Multiaxial Fatigue Limit: A New Approach. ICF6, pages 1879–1885, 1984.
- [88] E. N. Mamiya, J. A. Araújo, and F. C. Castro. Prismatic hull: A new measure of shear stress amplitude in multiaxial high cycle fatigue. *Int J Fatigue*, 31:1144–1153, 2009.
- [89] N. Zouain, E. N. Mamiya, and F. Comes. Using enclosing ellipsoids in multiaxial fatigue strength criteria. *Eur J Mech - A/Solids*, 25:51–71, 2006.
- [90] C. Gaier, A. Lukacs, and K. Hofwimmer. Investigations on a statistical measure of the non-proportionality of stresses. *Int J Fatigue*, 26:331–337, 2004.
- [91] M. A. Meggiolaro and J. T. P. de Castro. An improved multiaxial rainflow algorithm for non-proportional stress or strain histories - Part I: Enclosing surface methods. *Int J Fatigue*, 42:217–226, 2012.
- [92] W. N. Findley. A Theory for the Effect of Mean Stress on Fatigue of Metals Under Combined Torsion and Axial Load or Bending. *J Eng Ind*, 81:301–305, 1959.
- [93] A. Carpinteri and A. Spagnoli. Multiaxial high-cycle fatigue criterion for hard metals. *Int J Fatigue*, 23:135–145, 2001.
- [94] A. Karolczuk and E. Macha. A Review of Critical Plane Orientations in Multiaxial Fatigue Failure Criteria of Metallic Materials. *Int J Fracture*, 134:267–304, 2005.
- [95] Y.-L. Lee, T. Tjhung, and A. Jordan. A life prediction model for welded joints under multiaxial variable amplitude loading histories. *Int J Fatigue*, 29:1162–1173, 2007.
- [96] J. Papuga and M. Růžička. Two new multiaxial criteria for high cycle fatigue computation. *Int J Fatigue*, 30:58–66, 2008.
- [97] J. Papuga. A survey on evaluating the fatigue limit under multiaxial loading. *Int J Fatigue*, 33:153–165, 2011.
- [98] K. Lorand. Review of high cycle fatigue models applied for multiaxial tension-torsion loading based on a new accuracy assessment parameter. *J Eng Studies Res*, 18:75–86, 2012.
- [99] H. Chen, D.-G. Shang, Y.-J. Tian, and J.-Z. Liu. Comparison of multiaxial fatigue damage models under variable amplitude loading. *J Mech Sci Technol*, 26:3439–3446, 2012.
- [100] Ø. A. Bruun and G. Härkegård. A comparative study of design code criteria for prediction of the fatigue limit under in-phase and out-of-phase tension-torsion cycles. *Int J Fatigue*, 73:1–16, 2015.
- [101] K. Barbash and W. Mars. Critical Plane Analysis of Rubber Bushing Durability under Road Loads. *SAE Technical Paper*, 01:0393, 2016.
- [102] P. S. van Lieshout, J. H. den Besten, and M. L. Kaminski. Comparative study of multiaxial fatigue methods applied to welded joints in marine structures. *Frattura ed Integrità Strutturale*, 37:173–192, 2016.
- [103] S.-P. Zhu, Z.-Y. Yu, J. Correia, A. De Jesus, and F. Berto. Evaluation and comparison of critical plane criteria for multiaxial fatigue analysis of ductile and brittle materials. *Int J Fatigue*, 112:279–288, 2018.
- [104] J. Papuga and R. Halama. Mean stress effect in multiaxial fatigue limit criteria. *Arch Appl Mech*, 89:823–834, 2019.
- [105] I. Portugal, M. Olave, I. Urresti, A. Zurutuza, A. López, M. Muñoz-Calvente, and A. Fernández-Canteli. A comparative analysis of multiaxial fatigue models under random loading. *Eng Struct*, 182:112–122, 2019.

- [106] A. Karolczuk, J. Papuga, and T. Palin-Luc. Progress in fatigue life calculation by implementing life-dependent material parameters in multiaxial fatigue criteria. *Int J Fatigue*, 134:105509, 2020.
- [107] B. Zhao, L. Xie, L. Wang, Z. Hu, S. Zhou, and X. Bai. A new multiaxial fatigue life prediction model for aircraft aluminum alloy. *Int J Fatigue*, 143:105993, 2021.
- [108] N. D. Bibbo, J. Baumgartner, and V. Arora. Comparative study of critical plane fatigue criteria on multiaxial variable amplitude loaded welded test specimens. *Int J Fatigue*, 158:106670, 2022.
- [109] J. Papuga, M. Nesládek, A. Hasse, E. Cízová, and L. Suchý. Benchmarking Newer Multiaxial Fatigue Strength Criteria on Data Sets of Various Sizes. *Metals*, 12:289, 2022.
- [110] T. Adam, N. Gathercole, H. Reiter, and B. Harris. Fatigue life prediction for carbon fibre composites. *Adv Compos Lett*, 1:23–26, 1992.
- [111] B. Harris. A parametric constant-life model for prediction of the fatigue lives of fibre-reinforced plastics. In Bryan Harris, editor, *Fatigue in Composites*, Woodhead Publishing Series in Composites Science and Engineering, pages 546–568. Woodhead Publishing, 2003.
- [112] G. K. Boerstra. The Multislope model: A new description for the fatigue strength of glass fibre reinforced plastic. *Int J Fatigue*, 29:1571–1576, 2007.
- [113] M. Kawai and T. Murata. A three-segment anisomorphic constant life diagram for the fatigue of symmetric angle-ply carbon/epoxy laminates at room temperature. *Compos Part A*, 41:1498–1510, 2010.
- [114] A. P. Vassilopoulos, B. D. Manshadi, and T. Keller. Piecewise non-linear constant life diagram formulation for FRP composite materials. *Int J Fatigue*, 32:1731–1738, 2010.
- [115] R. Sarfaraz, A. P. Vassilopoulos, and T. Keller. Experimental investigation and modeling of mean load effect on fatigue behavior of adhesively-bonded pultruded GFRP joints. *Int J Fatigue*, 44:245–252, 2012.
- [116] B. Oberwinkler. On the anomalous mean stress sensitivity of Ti-6Al-4V and its consideration in high cycle fatigue lifetime analysis. *Int J Fatigue*, 92:368–381, 2016.
- [117] Q. Ji, P. Zhu, J. Lu, and C. Zhu. Experimental study and modeling of fatigue life prediction of plain weave carbon/polymer composite under constant amplitude loading. *Adv Compos Mater*, 26:295–320, 2017.
- [118] M. Rosemeier and A. Antoniou. Probabilistic Approach for the Fatigue Strength Prediction of Polymers. *AIAA J*, 60:951–961, 2022.
- [119] M. A. Miner. Cumulative Damage in Fatigue. *J Appl Mech*, 12:159–164, 1945.
- [120] K. El-Tawil and A. A. Jaoude. Stochastic and nonlinear-based prognostic model. *Systems Science & Control Engineering*, 1:66–81, 2013.
- [121] H. Svärd. A branch and bound algorithm for evaluation of the Findley fatigue criterion. *Int J Fatigue*, 73:27–38, 2015.
- [122] M. Wentingmann, P. Noever Castelos, and C. Balzani. An adaptive algorithm to accelerate the critical plane identification for multiaxial fatigue criteria. ECCM, pages 1–10, 2018.
- [123] S. L. Sunde, F. Berto, and B. Haugen. Efficient implementation of critical plane for 3D stress histories using triangular elements. *Int J Fatigue*, 134:105448, 2020.
- [124] A. Chiocca, F. Frendo, and G. Marulo. An efficient algorithm for critical plane factors evaluation. *Int J Mech Sci*, 242:107974, 2023.
- [125] Y.-Y. Wang and W.-X. Yao. Evaluation and comparison of several multiaxial fatigue criteria. *Int J Fatigue*, 26:17–25, 2004.
- [126] Z. Lu, Y. Xiang, and Y. Liu. Crack growth-based fatigue-life prediction using an equivalent initial flaw model. Part II: Multiaxial loading. *Int J Fatigue*, 32:376–381, 2010.
- [127] V. Bonnard, J. L. Chaboche, P. Gomez, P. Kanouté, and D. Pacou. Investigation of multiaxial fatigue in the context of turboengine disc applications. *Int J Fatigue*, 33:1006–1016, 2011.
- [128] T. N. Chakherlou and B. Abazadeh. Estimation of fatigue life for plates including pre-treated fastener holes using different multiaxial fatigue criteria. *Int J Fatigue*, 33:343–353, 2011.
- [129] J. Li, Z.-P. Zhang, Q. Sun, and C.-W. Li. Multiaxial fatigue life prediction for various metallic materials based on the critical plane approach. *Int J Fatigue*, 33:90–101, 2011.
- [130] K. P. Subrahmanian and F. Dubouloz. Adhesives for bonding wind turbine blades. *Reinforced Plastics*, 53:26–29, 2009.
- [131] R. Stewart. Wind turbine blade production – new products keep pace as scale increases. *Reinforced Plastics*, 56:18–25, 2012.
- [132] C. Dörsch, H. Rosemann, J. Müssig, O. Bagemiel, R. Braun, and F. Sayer. On an integrated process and machinery concept for economic industrialized production of higher quality wind turbine rotor blades. ICCM20, 2015.
- [133] J. Franke, J.-H. Ohlendorf, and K.-D. Thoben. Automated production processes in the rotor blade industry – Solutions for a continuous direct textile layup. *Mater Sci Eng Technol*, 50:1326–1342, 2019.

- [134] J.-H. Ohlendorf, M. Richrath, J. Franke, M. Brink, and K.-D. Thoben. Towards automation of wind energy rotor blade production: a review of challenges and application examples. *Adv Manuf Polym Compos Sci*, 6:173–190, 2020.
- [135] P. Lux, A. G. Cassano, S. B. Johnson, M. Maiaru, and S. E. Stapleton. Adhesive curing cycle time optimization in wind turbine blade manufacturing. *Renew Energy*, 162:397–410, 2020.
- [136] A. G. Cassano, S. Dev, M. Maiaru, C. J. Hansen, and S. E. Stapleton. Cure simulations of thick adhesive bondlines for wind energy applications. *J Appl Polym Sci*, 138:49989, 2021.
- [137] V. Trappe. Fatigue life evaluation of composite wing spar cap materials. *Mater Test*, 61:1135–1139, 2019.
- [138] B. L. Ennis, C. L. Kelley, B. T. Naughton, R. E. Norris, S. Das, D. Lee, and D. Miller. Optimized Carbon Fiber Composites in Wind Turbine Blade Design. Technical report, Sandia National Laboratories, 2019.
- [139] R. Högel and U. Hilsenbek. The Colorful Side of Robotics. *Int Surface Technol*, 7:10–13, 2014.
- [140] B. Kjæside Storm. Surface protection and coatings for wind turbine rotor blades. In Povl Brøndsted and Rogier P.L. Nijssen, editors, *Advances in Wind Turbine Blade Design and Materials*, Woodhead Publishing Series in Energy, pages 387–412. Woodhead Publishing, 2013. ISBN 978-0-85709-426-1.
- [141] A. Sareen, C. A. Sapre, and M. S. Selig. Effects of Leading-Edge Protection Tape on Wind Turbine Blade Performance. *Wind Eng*, 36:525–534, 2012.
- [142] W. Hu, W. Chen, X. Wang, Z. Liu, J. Tan, and Y. Wang. Wind Turbine Blade Coating Fatigue Induced by Raindrop Impact. ASME 2020 Power Conference, page V001T08A010, 2020.
- [143] S. Doagou-Rad, L. Mishnaevsky Jr, and J. I. Bech. Leading edge erosion of wind turbine blades: Multiaxial critical plane fatigue model of coating degradation under random liquid impacts. *Wind Energy*, 23:1752–1766, 2020.
- [144] H. Mueller-Vahl, G. Pechlivanoglou, C. N. Nayeri, and C. O. Paschereit. Vortex Generators for Wind Turbine Blades: A Combined Wind Tunnel and Wind Turbine Parametric Study. ASME Turbo Expo, pages 899–914, 2012.
- [145] L. Mishnaevsky Jr., C. Bay Hasager, C. Bak, A.-M. Tilg, J. I. Bech, S. Doagou Rad, and S. Fæster. Leading edge erosion of wind turbine blades: Understanding, prevention and protection. *Renew Energy*, 169:953–969, 2021.
- [146] Z. Zhao, R. Jiang, J. Feng, H. Liu, T. Wang, W. Shen, M. Chen, D. Wang, and Y. Liu. Researches on vortex generators applied to wind turbines: A review. *Ocean Eng*, 253:111266, 2022.
- [147] 3M™. Technical Data Sheet - Wind Blade Bonding Adhesive W1101, 2012.
- [148] M. Wichmann and G. Rüb. Harnessing the wind: New technologies for longer, lighter rotor blades. *JEC Composites Magazine*, 78:27–29, 2013.
- [149] Gurit. Technical Data Sheet - Spabond™ 820HTA, 2022.
- [150] Gurit. Technical Data Sheet - Spabond™ 840HTA, 2022.
- [151] P. Noever Castelos, B. Haller, and C. Balzani. Validation of a modeling methodology for wind turbine rotor blades based on a full-scale blade test. *Wind Energy Sci*, 7:105–127, 2022.
- [152] F. Sayer, A. Antoniou, and A. van Wingerde. Investigation of structural bond lines in wind turbine blades by sub-component tests. *Int J Adhes Adhes*, 37:129–135, 2012.
- [153] J. M. Arenas, J. J. Narbón, and C. Alía. Optimum adhesive thickness in structural adhesives joints using statistical techniques based on Weibull distribution. *Int J Adhes Adhes*, 30:160–165, 2010.
- [154] K. Naito, M. Onta, and Y. Kogo. The effect of adhesive thickness on tensile and shear strength of polyimide adhesive. *Int J Adhes Adhes*, 36:77–85, 2012.
- [155] A. Akhavan-Safar, M. R. Ayatollahi, and L. F. M. da Silva. Strength prediction of adhesively bonded single lap joints with different bondline thicknesses: A critical longitudinal strain approach. *Int J Solids Struct*, 109:189–198, 2017.
- [156] J. Yeon, Y. Song, K. K. Kim, and J. Kang. Effects of Epoxy Adhesive Layer Thickness on Bond Strength of Joints in Concrete Structures. *Materials*, 12:2396, 2019.
- [157] Y. Liu, C. Carnegie, H. Ascroft, W. Li, X. Han, H. Guo, and D. J. Hughes. Investigation of Adhesive Joining Strategies for the Application of a Multi-Material Light Rail Vehicle. *Materials*, 14:6991, 2021.
- [158] M. Lindermann, I. Gebauer, and F. Sayer. Vorrichtung und Verfahren zum Auftragen einer Materialraupe, 2020. Patent Application, DE102019203819 A1.
- [159] D. Zarouchas and R. Nijssen. Mechanical behaviour of thick structural adhesives in wind turbine blades under multi-axial loading. *J Adhes Sci Technol*, 30:1413–1429, 2016.
- [160] G. Fernandez, D. Vandepitte, H. Usabiaga, and S. Debruyne. Static and cyclic strength properties of brittle adhesives with porosity. *Int J Fatigue*, 117:340–351, 2018.
- [161] A. I. M Foletti, J. S. Cruz, and A. P. Vassilopoulos. Fabrication and curing conditions effects on the fatigue behavior of a structural adhesive. *Int J Fatigue*, 139:105743, 2020.

- [162] A. T. Sears, D. D. Samborsky, P. Agastra, and J. F. Mandell. Fatigue Results and Analysis for Thick Adhesive Notched Lap Shear Test. In *Proc. AIAA SDM Wind Energy Session*, 2010.
- [163] T. Holst. Kennwerte zur Porosität und Porositätsverteilung für verschiedene Mischtechnologien. Technical report, Fraunhofer IWES, 2017. SmartBlades2, Deliverable 4.1.8.3.
- [164] J. Shewchuk, S. Y. Zamrik, and J. Marin. Low-cycle Fatigue of 7075-T651 Aluminum Alloy in Biaxial Bending. *Exp Mech*, 8:504–512, 1968.
- [165] T. J. George, J. Seidt, M.-H. H. Shen, T. Nicholas, and C. J. Cross. Development of a novel vibration-based fatigue testing methodology. *Int J Fatigue*, 26:477–486, 2004.
- [166] A. Makinde, L. Thibodeau, and K. W. Neale. Development of an Apparatus for Biaxial Testing Using Cruciform Specimens. *Exp Mech*, 32:138–144, 1992.
- [167] S. Demmerle and J. P. Boehler. Optimal design of biaxial tensile cruciform specimens. *J Mech Phys Solids*, 41:143–181, 1993.
- [168] A. Smits, D. Van Hemelrijck, T. P. Philippidis, and A. Cardon. Design of a cruciform specimen for biaxial testing of fibre reinforced composite laminates. *Compos Sci Technol*, 66:964–975, 2006.
- [169] J. V. Sahadi, R. J. H. Paynter, D. Nowell, S. J. Pattison, and N. Fox. Comparison of multi-axial fatigue parameters using biaxial tests of Waspaloy. *Int J Fatigue*, 100:477–488, 2017.
- [170] J.-Y. Zhao, Z. Lu, C.-Y. Zhou, L. Chang, and X.-H. He. In-plane biaxial ratcheting effect and low-cycle fatigue behavior of CP-Ti based on DIC method. *Fatigue Fract Eng M*, 45:1464–1479, 2022.
- [171] G. Tao and Z. Xia. Fatigue behavior of an epoxy polymer subjected to cyclic shear loading. *Mater Sci Eng A*, 486:38–44, 2008.
- [172] M. A. Eder and R. D. Bitsche. Fracture analysis of adhesive joints in wind turbine blades. *Wind Energy*, 18:1007–1022, 2015.
- [173] D. S. Zarouchas, A. A. Makris, F. Sayer, D. Van Hemelrijck, and A. M. Van Wingerde. Investigations on the mechanical behavior of a wind rotor blade subcomponent. *Compos Part B*, 43:647–654, 2012.
- [174] F. Sayer. *Sub-Component testing for structural adhesive joint assessment in wind turbine rotor blades: Dissertation*. 2020.
- [175] K. Branner, P. Berring, and P. U. Haselbach. Subcomponent testing of trailing edge panels in wind turbine blades. *ECCM17*, 2016.
- [176] A. Künzel and Y. Petryna. Parameter Identification based on quasi-continuous strain data captured by high resolution fiber optic sensing. *EWSHM*, 2016.
- [177] F. Lahuerta, M. J. de Ruiter, L. Espinosa, N. Koorn, and D. Smissaert. Assessment of wind turbine blade trailing edge failure with sub-component tests. *ICCM21*, 2017.
- [178] M. Rosemeier, G. Basters, and A. Antoniou. Benefits of subcomponent over full-scale blade testing elaborated on a trailing-edge bond line design validation. *Wind Energy Sci*, 3:163–172, 2018.
- [179] F. Belloni, M. A. Eder, and B. Cherrier. An Improved Sub-component Fatigue Testing Method for Material Characterization. *Exp Techniques*, 42:533–550, 2018.
- [180] I. Drisga, N. Glück, T. B. Block, and K. Ehrich. Fatigue behavior and climatic cycle testing of rotor blade components. *Lightweight Design worldwide*, 11:52–57, 2018.
- [181] M. Rosemeier, A. Antoniou, X. Chen, F. Lahuerta, P. Berring, and K. Branner. Trailing edge subcomponent testing for wind turbine blades—Part A: Comparison of concepts. *Wind Energy*, 22:487–498, 2019.
- [182] K. Ha, M. Bätge, D. Melcher, and S. Czichon. Development and feasibility study of segment blade test methodology. *Wind Energy Sci*, 5:591–599, 2020.
- [183] DNV GL AS. DNVGL-ST-0376 - Rotor blades for wind turbines, 2015.
- [184] M. Rosemeier, D. Melcher, A. Krimmer, W. Wroblewski, and A. Antoniou. Validation of crack initiation model by means of cyclic full-scale blade test. *J Phys Conf Ser*, 2265:032045, 2022.
- [185] A. E. Antoniou, M. M. Vespermann, F. Sayer, and A. Krimmer. Life Prediction Analysis of Thick Adhesive Bond Lines under Variable Amplitude Fatigue Loading. *ECCM18*, 2018.
- [186] D. Snowberg, S. Dana, S. Hughes, and P. Berling. Implementation of a Biaxial Resonant Fatigue Test Method on a Large Wind Turbine Blade. Technical report, National Renewable Energy Laboratory (NREL), 2014.
- [187] N. Post and F. Bürkner. Fatigue Test Design: Scenarios for Biaxial Fatigue Testing of a 60-Meter Wind Turbine Blade. Technical report, National Renewable Energy Laboratory (NREL), 2019.
- [188] F. Bürkner. *Biaxial dynamic fatigue tests of wind turbine blades: Dissertation*. 2020.
- [189] D. Melcher, H. Rosemann, B. Haller, S. Neßlinger, E. Petersen, and M. Rosemeier. Proof of concept: elliptical biaxial rotor blade fatigue test with resonant excitation. volume 942 of *IOP Conf Ser Mat Sci*, page 012007, 2020.
- [190] D. Melcher, E. Petersen, and S. Neßlinger. Off-axis loading in rotor blade fatigue tests with elliptical biaxial resonant excitation. volume 1618 of *J Phys Conf Ser*, page 052010, 2020.

- [191] D. Melcher, M. Bätge, and S. Neßlinger. A novel rotor blade fatigue test setup with elliptical biaxial resonant excitation. *Wind Energy Sci*, 5:675–684, 2020.
- [192] L. Lu, M. Zhu, H. Wu, and J. Wu. A Review and Case Analysis on Biaxial Synchronous Loading Technology and Fast Moment-Matching Methods for Fatigue Tests of Wind Turbine Blades. *Energies*, 15:4881, 2022.
- [193] O. Castro and K. Branner. Preliminary multi-axial strain analysis in wind turbine blades under fatigue test loads. volume 942 of *IOP Conf Ser Mat Sci*, page 012044, 2020.
- [194] X. Chen, A. Shihavuddin, S. H. Madsen, K. Thomsen, S. Rasmussen, and K. Branner. AQUADA: Automated quantification of damages in composite wind turbine blades for LCOE reduction. *Wind Energy*, 24:535–548, 2021.
- [195] M. Wentingmann, N. Manousides, A. Antoniou, and C. Balzani. Design and manufacturing optimization of epoxy-based adhesive specimens for multiaxial tests. *Mater Design*, 212:110213, 2021.
- [196] M. Wentingmann, N. Manousides, A. Antoniou, and C. Balzani. Yield surface derivation for a structural adhesive based on multiaxial experiments. *Polym Test*, 113:107648, 2022.
- [197] M. Kuhn, N. Manousides, A. Antoniou, and C. Balzani. Fatigue properties of a structural rotor blade adhesive under axial and torsional loading. *Fatigue Fract Eng M*, 46:1121–1139, 2023.
- [198] M. Kuhn, N. Manousides, A. Antoniou, and C. Balzani. Effects of non-proportionality and tension-compression asymmetry on the fatigue life prediction of equivalent stress criteria. *Fatigue Fract Eng M*, 46:3161–3178, 2023.
- [199] J. E. Bishop. Characterizing the non-proportional and out-of-phase extent of tensor paths. *Fatigue Fract Eng M*, 23:1019–1032, 2000.
- [200] M. A. Meggiolaro and de Castro J. T. P. Prediction of non-proportionality factors of multiaxial histories using the Moment Of Inertia method. *Int J Fatigue*, 61:151–159, 2014.
- [201] M. A. Meggiolaro, J. T. P. de Castro, and H. Wu. A fast algorithm to racetrack filter multiaxial histories preserving load shape. volume 300 of *ICMFF12*, page 17002, 2019.
- [202] D. C. Drucker and W. Prager. Soil Mechanics and Plastic Analysis or Limit Design. *Q Appl Math*, 10:157–165, 1952.
- [203] R. von Mises. Mechanik der festen Körper im plastisch- deformablen Zustand. *Nachrichten von der Gesellschaft der Wissenschaften zu Göttingen, Mathematisch-Physikalische Klasse*, 4: 582–592, 1913.
- [204] ASTM E1049-85. Standard Practices for Cycle Counting in Fatigue Analysis, 2017.
- [205] I. V. Papadopoulos. Long life fatigue under multiaxial loading. *Int J Fatigue*, 23:839–849, 2001.
- [206] A. Bernasconi. Efficient algorithms for calculation of shear stress amplitude and amplitude of the second invariant of the stress deviator in fatigue criteria applications. *Int J Fatigue*, 24: 649–657, 2002.
- [207] G. Petrucci. A critical assessment of methods for the determination of the shear stress amplitude in multiaxial fatigue criteria belonging to critical plane class. *Int J Fatigue*, 74:119–131, 2015.
- [208] J. Papuga, E. Cízová, and A. Karolczuk. Validating the Methods to Process the Stress Path in Multiaxial High-Cycle Fatigue Criteria. *Materials*, 14:206, 2021.
- [209] A. T. Schmidt and N. Pandiya. Extension of the static equivalent stress hypotheses to linearly vibrating systems using wave interference - The LiWi approach. *Int J Fatigue*, 147:106103, 2021.
- [210] H. E. Tresca. *Sur l'écoulement des corps solides soumis à de fortes pressions*. Gauthier-Villars, 1864.
- [211] W. J. M. Rankine. *A Manual on Applied Mechanics*. Richard Griffin and Company, Glasgow, Scotland, 1858.
- [212] F. Stüssi. Zur Theorie der Dauerfestigkeit. *IABSE congress report*, 5:229–234, 1956.
- [213] E. Haibach. The influence of cyclic material properties on fatigue life prediction by amplitude transformation. *Int J Fatigue*, 1:7–16, 1979.
- [214] K. Shiozawa, L. Lu, and S. Ishihara. S-N curve characteristics and subsurface crack initiation behaviour in ultra-long life fatigue of a high carbon-chromium bearing steel. *Fatigue Fract Eng M*, 24:781–790, 2001.
- [215] I. Marines, X. Bin, and C. Bathias. An understanding of very high cycle fatigue of metals. *Int J Fatigue*, 25:1101–1107, 2003.
- [216] B. Pyttel, D. Schwerdt, and C. Berger. Very high cycle fatigue - Is there a fatigue limit? *Int J Fatigue*, 33:49–58, 2011.
- [217] Y. Hong, A. Zhao, G. Qian, and C. Zhou. Fatigue Strength and Crack Initiation Mechanism of Very-High-Cycle Fatigue for Low Alloy Steels. *Metall Mater Trans A*, 43:2753–2762, 2012.
- [218] J. C. Jr. Newman. Fatigue and Crack-Growth Analyses under Giga-Cycle Loading on Aluminum Alloys. volume 101 of *Procedia Engineer*, pages 339–346, 2015.
- [219] C. M. Sonsino. Course of SN-curves especially in the high-cycle fatigue regime with regard to component design and safety. *Int J Fatigue*, 29: 2246–2258, 2007.

- [220] E. Castillo, R. Mínguez, A. J. Conejo, B. Pérez, and O. Fontenla. Estimating the parameters of a fatigue model using Benders' decomposition. *Ann Oper Res*, 210:309–331, 2013.
- [221] L. D'Angelo and A. Nussbaumer. Estimation of fatigue S-N curves of welded joints using advanced probabilistic approach. *Int J Fatigue*, 97:98–113, 2017.
- [222] J. F. Barbosa, J. A. Correia, R. Freire Júnior, S.-P. Zhu, and A. M. De Jesus. Probabilistic S-N fields based on statistical distributions applied to metallic and composite materials: State of the art. *Adv Mech Eng*, 11:1–22, 2019.
- [223] P. D. Toasa Caiza and T. Ummenhofer. Probabilistic relationships between strain range, stress range and loading cycles. Application on ASTM A969 steel. *Int J Fatigue*, 137:105626, 2020.
- [224] C. Li, S. Wu, J. Zhang, L. Xie, and Y. Zhang. Determination of the fatigue P-S-N curves – A critical review and improved backward statistical inference method. *Int J Fatigue*, 139:105789, 2020.
- [225] R. J. Morrissey, D. L. McDowell, and T. Nicholas. Frequency and stress ratio effects in high cycle fatigue of Ti-6Al-4V. *Int J Fatigue*, 21:679–685, 1999.
- [226] M. M. Shokrieh and M. J. Omid. Tension behavior of unidirectional glass/epoxy composites under different strain rates. *Compos Struct*, 88: 595–601, 2009.
- [227] A. Bozorg-Haddad, M. Iskander, and H.-L. Wang. Compressive Creep of Virgin HDPE Using Equivalent Strain Energy Density Method. *J Mater Civil Eng*, 22:1270–1281, 2010.
- [228] J. Richeton, S. Ahzi, K. S. Vecchio, F. C. Jiang, and R. R. Adharapurapu. Influence of temperature and strain rate on the mechanical behavior of three amorphous polymers: Characterization and modeling of the compressive yield stress. *Int J Solids Struct*, 43:2318–2335, 2006.
- [229] M. Zscheyge, R. Böhm, A. Hornig, J. Geritzen, and M. Gude. Rate dependent non-linear mechanical behaviour of continuous fibre-reinforced thermoplastic composites – Experimental characterisation and viscoelastic-plastic damage modelling. *Mater Design*, 193:108827, 2020.
- [230] A. Ahmed, M. Z. Rahman, Y. Ou, S. Liu, B. Mobasher, Guo S., and D. Zhu. A review on the tensile behavior of fiber-reinforced polymer composites under varying strain rates and temperatures. *Constr Build Mater*, 294:123565, 2021.
- [231] A. Dean, J. Reinoso, S. Sahraee, and R. Rolfes. An invariant-based anisotropic material model for short fiber-reinforced thermoplastics: Coupled thermo-plastic formulation. *Compos Part A*, 90:186–199, 2016.
- [232] R. Rafiee and M. R. Hashemi-Taheri. Failure analysis of a composite wind turbine blade at the adhesive joint of the trailing edge. *Eng Fail Anal*, 121:105148, 2021.
- [233] X.-Y. Miao, X. Chen, R. Lu, and M. A. Eder. Multi-site crack initiation in local details of composite adhesive joints. *Compos Part B*, 242: 110055, 2022.
- [234] Siemens Gamesa Renewable Energy via Medium. Close-up of B53 blades, 2022. Accessed: September, 2022.
- [235] MSC, 2022. Accessed: December, 2022.
- [236] V. Tchompalov. Tesla Model 3 Headlights, 2019. Accessed: December, 2022.
- [237] P. Platzer. Arch beim Highspeed-Slalom am Tauernwindpark, 2017. Accessed: December, 2022.
- [238] Siemens Gamesa Renewable Energy via Mace Group. A £310m renewable energy project, 2022. Accessed: December, 2022.
- [239] Fraunhofer IWES. Research rotor blade production at Fraunhofer IWES, 2021. Accessed: December, 2022.
- [240] Hawart. HAWART Stegsetzer, 2013. Accessed: December, 2022.
- [241] LM Wind Power. Building record-breaking blades to change the world through the power of wind, 2021. Accessed: December, 2022.
- [242] Motofil. Solutions for the solar and wind industry, 2022. Accessed: December, 2022.
- [243] Martina Buchholz for Fraunhofer IWES. Ganzblattprüfung, 2016.
- [244] F. Sayer. Rotor Blade | Material, Component and Structural Testing. Accessed: December, 2022.
- [245] A. Antoniou, C. Ueing, C. Lester, and N. Englisch. A damage approach on the fatigue degradation mechanism of biaxial Glass/Epoxy laminates. ISMEM, 2017.
- [246] S. Weeteling. Early morning windmill sunrise in the mist, 2021. Accessed: December, 2022.
- [247] Fraunhofer IWES. New test method: Biaxial rotor blade fatigue test, 2020. Accessed: December, 2022.

## Dissertations of the Institute for Wind Energy Systems

- 01 (2023) Updating structural wind turbine blade models via invertible neural networks, Dissertation, Pablo Noever Castelos, 2023
- 02 (2023) Non-Proportional Fatigue by Example of Fiber-Reinforced Rotor Blade Adhesive, Dissertation, Michael Kuhn, 2023









## Curriculum Vitae

Michael Kuhn 

Birth name: Wentingmann  
Born on 15<sup>th</sup> November 1990  
in Münster, Germany

### Awards

#### Preis d. Stiftung Bauindustrie Niedersachsen Bremen

*Award for excellent achievements within the standard period of study in Wind Energy Eng.*

#### Niedersachsenstipendium

*Scholarship provided by Leibniz University Hannover*

#### Deutschlandstipendium

*Scholarship provided by TÜV Hannover/Sachsen-Anhalt e.V. for Wind Energy Engineering*

#### Deutschlandstipendium

*Scholarship provided by Areva Wind for Maritime Technologies*

### Scientific Staff

Institute for Wind Energy Systems (IWES)  
Leibniz University Hannover

Jul  
2023

Involved Research Projects:  
SmartBlades2, ReliaBlade,  
Add2ReliaBlade

Jun  
2017

Tutorial Lecturer in:  
Rotor Blade Design for Wind Turbines  
Design and Installation of Wind Farms

May  
2017

### Wind Energy Engineering

Master of Science  
Leibniz University Hannover

Apr  
2015

Mar  
2015

### Maritime Technologies

Bachelor of Science  
Hochschule Bremerhaven

Sep  
2011

